Second harmonic generation (SHG) for contactless characterization of dielectric-semiconductor interfaces

Dimitrios Damianos

Communauté
UNIVERSITÉ Grenoble Alpes

THÈSE

Pour obtenir le grade de

DOCTEUR DE LA COMMUNAUTE UNIVERSITE GRENOBLE ALPES

Spécialité : **Nanoélectronique et Nanotechnologies (NENT)**

Arrêté ministériel : 25 mai 2016

Présentée par

Dimitrios DAMIANOS

Thèse dirigée par **Anne Kaminski-CACHOPO**, et
codirigée par **Irina IONICA** et **Danièle BLANC-PELISSIER**

préparée au sein du **Laboratoire IMEP-LAHC**
dans **l'École Doctorale EEATS**

Génération de seconde harmonique (SHG) pour la caractérisation des interfaces entre diélectriques et semiconducteurs

Thèse soutenue publiquement le **03 Octobre 2018**,
devant le jury composé de:

M. Jean-Pierre RASKIN
Professeur des Universités, Université Catholique de Louvain, Président
M. Yves JOURLIN
Professeur des Universités, Laboratoire Hubert-Curien, Rapporteur
M. Olivier PALAIS
Professeur des Universités, IM2NP Aix-Marseille, Rapporteur
M. Frédéric ALLIBERT
Docteur, Ingénieur R&D, SOITEC, Invité
M. Didier DUTARTRE
Docteur, Ingénieur R&D, STMicroelectronics, Invité
M. Guy VITRANT
Directeur de Recherche au CNRS, IMEP-LAHC, Invité
Mme. Anne KAMINSKI-CACHOPO
Professeur des Universités, IMEP-LAHC, Directrice de thèse
Mme. Irina IONICA
Maître de Conférences, IMEP-LAHC, Co-encadrante de thèse
Mme. Danièle BLANC-PELISSIER
Chargé de Recherche au CNRS, INL, Co-encadrante de thèse

Acknowledgments

While typically this “acknowledgments” section is considered to be an easy task, done at the very end of one’s thesis, I find it difficult to express my gratitude towards everyone being a part of my life and helping me reach this turn-point. And I describe it as difficult, not for being hard to put into words what I think, but mostly due to the endless feelings emerging in my heart and beautiful memories surging through my head when thinking back on these last 3 years.

First and foremost, I owe it to my family with all the constant love and support that I received. Mom and dad you have relentlessly tried to help me, my brother and sister flourish. You still have some way to go with the newest member of the family and I hope that you will be always proud and content for all of us.

I would like to thank all of the members of the jury for taking the time to read and evaluate my thesis as well as attend my PhD defence: Prof. Jean-Pierre Raskin, Prof. Olivier Palais, Prof. Yves Jourlin, Dr. Frédéric Allibert and Dr. Didier Dutartre.

I am really grateful and lucky to have had such amazing supervisors who always treated me with kindness and patience: Irina Ionica, Anne Kaminski and Danièle Blanc-Pelissier. They helped me a lot during my thesis, guiding me through the rough waves during this 3-year long trip in an unknown sea of knowledge. I finally reached the destination safe and sound, having improved professionally thanks to their advice and support.

I want to also express my profound gratitude to Guy Vitrant who was always answering my questions and has provided me with constant help and support for the modelling part of my thesis, despite his hellishly tight schedule and even though he was not one of my official supervisors. I also deeply thank Sorin Cristoloveanu who was always there to help me despite not being one of my official supervisors.

Many thanks are due to Xavier Mescot, Aude Bouchard, Martine Gri, Gregory Grosa for all their valuable technical support and outstanding availability throughout the IMEP-LAHC years. Furthermore, I kindly thank for the help that I received from all the HR team members: Isabelle, Fabienne, Dalhila, Brigitte, Valérie and Annaïck. I also thank everyone else in IMEP-LAHC that helped me both in direct and indirect ways.

I am happy and deeply grateful for spending cool and funny moments in the office with Licinus Benea (the Transylvanian wolf/gypsy), Giuseppe Acri (the Calabrese tiger), Mukta Singh Parihar (the Indian bride), Kyungwha “Lili” Lee and Hyungjin Park (the Korean mafia). The long hours in the lab were always delightful and alluring thanks to my office family.

Finally, to all of my friends in Grenoble: I am truly ecstatic and content to have met cool and awesome people like you. Thank you for being there for me, for all the merry and amusing times as well as the beautiful moments that I have created with you and which I vastly cherish.

Abstract/Résumé

Second harmonic generation (SHG) for contactless characterization of dielectric-semiconductor interfaces

This PhD work was developed in the context of research for novel characterization methods for ultra-thin dielectric films on semiconductors and their interfacial quality. Second harmonic generation (SHG) is a very promising non-invasive technique based on nonlinear optics. A laser emitting at the fundamental frequency is incident upon the sample which responds through its 2nd order polarization, generating a signal at twice the fundamental frequency. For centrosymmetric materials such as c-Si, amorphous SiO_2 or Al_2O_3, the SHG signal is mainly due to the defects and to the static electric field E_{dc} present at the interface (due to pre-existing charges Q_{ox} and/or photo-injected charge trapping/detrapping at interface traps D_{it}). Thus, SHG measurement gives access to the quality of dielectric/semiconductor interfaces. Nevertheless, the SHG signal is also dependent on multilayer optical propagation phenomena. For this reason, we have developed a simulation program which accounts for the optical phenomena and the static electric fields at the interfaces. We have used SHG to monitor the passivation quality of Al_2O_3/Si structures prepared with different processes and showed a correlation between SHG and minority carrier lifetime measurements. Q_{ox} and D_{it} were extracted from capacitance-voltage measurements and helped calculating the E_{dc} values. The optical simulation, fed with known E_{dc} values reproduced the experimental SHG data in these structures. The SHG was also used for Silicon-on-Insulator (SOI) substrates characterization. In thick SOI structures, both simulations and experimental results show that the SHG response is mainly given by optical interferences (E_{dc} has no impact). In ultrathin SOI, the interfaces are electrically coupled and E_{dc} is needed as input in the simulation in order to reproduce the experimental SHG data. This implies that in ultrathin SOI, SHG can access the interface electric fields in a non-destructive way.

Génération de seconde harmonique (SHG) pour la caractérisation des interfaces entre diélectriques et semiconducteurs

Cette thèse s'intéresse à une technique de caractérisation particulièrement bien adaptée à l'étude de couches diélectriques ultra-minces sur semiconducteurs. La génération de seconde harmonique (SHG) est une méthode très prometteuse, basée sur l'optique non-linéaire. Un laser est focalisé sur l'échantillon à caractériser et le signal à deux fois la fréquence fondamentale est mesuré. Pour les matériaux centrosymétriques comme c-Si, SiO_2 et Al_2O_3, le signal SHG est dû aux défauts et au champ électrique E_{dc} d'interface (induit par les charges préexistantes Q_{ox} et/ou piégées au niveau des pièges d'interface D_{it}). La SHG donne ainsi accès à la qualité des interfaces entre diélectriques/semiconducteurs. Néanmoins, le signal SHG dépend aussi des phénomènes de propagation optique dans les structures multicouches. Pour cette raison, nous avons développé un programme de simulation qui prend en compte les phénomènes optiques et les champs électriques statiques aux interfaces. Nous avons utilisé la SHG pour analyser la qualité de passivation de structures Al_2O_3/Si préparées avec des procédés différents et nous avons montré une corrélation entre SHG et mesure de durée de vie des porteurs de charges. Les valeurs de Q_{ox} et D_{it} ont été extraites par des mesures de capacité-tension et elles ont permis de calculer le champ E_{dc}. La simulation optique, avec les valeurs extraites de E_{dc} a permis de reproduire les données expérimentales de SHG dans ces structures. La SHG a été utilisée également pour la caractérisation des substrats Silicium-sur-Isolant (SOI). Pour les structures SOI épaisses, la simulation et les résultats expérimentaux ont montré que la réponse SHG est dominée par les interférences optiques (faible impact de E_{dc}). Pour les structures SOI ultraminces, les interfaces sont couplées électriquement et des valeurs de E_{dc} sont nécessaires pour reproduire les données expérimentales par simulation. Cela implique que pour les SOI ultraminces, la SHG pourrait donner accès aux champs électriques au niveau des interfaces d'une manière non-destructive.

Table of Acronyms

Acronym	Nomination
AFM	Atomic force microscopy
Al_2O_3	Alumina
ALD	Atomic layer deposition
AOI	Angle of incidence
ARC	Antireflective coating
BOX	Buried oxide
CMOS	Complementary metal-oxide-semiconductor
COCOS	Corona characterization of semiconductors
C-V	Capacitance-Voltage
EFISH or EFISHG	Electric field induced second harmonic generation
HF	Hydrofluoric acid
MOS	Metal-oxide-semiconductor
MOSFET	Metal-oxide-semiconductor field effect transistor
P-ALD	Plasma atomic layer deposition
(μ-)PCD	(Microwave) Photoconductance decay
PLD	Photoluminescence decay
SCR	Space charge region
SHG	Second harmonic generation
SOI	Silicon on insulator
T-ALD	Thermal Atomic Layer Deposition
TD-SHG	Time-dependent second harmonic generation
Ψ-MOSFET	Pseudo MOSFET

Table of Symbols

Symbol	Unit in SI	Description
ΔV_{FB}	V	Shift in flat band voltage
C_{ox}	F	Oxide capacitance
C_{Si}	F	Silicon capacitance
D_{it}	$cm^{-2}eV^{-1}$	Interface trap density
E_{dc}	V/m	Static dc electric field
$E_{dc}(0)$	V/m	Time-independent E_{dc}
$E_{dc}(t)$	V/m	Time-dependent E_{dc}
E_{ω}, $E_{2\omega}$	V/m	Optical electric field (at ω and 2ω frequencies)
I_{ω}, $I_{2\omega}$	W/m^2	Light intensity (at ω and 2ω frequencies)
n_{ω}, $n_{2\omega}$	-	Refractive index (at ω and 2ω frequencies)
Q_{ox}	cm^{-2}	Fixed oxide charge density
t_{BOX}	nm	Buried oxide thickness
t_{ox}	nm	Oxide thickness
t_{Si}	nm	Silicon (film) thickness
t_{SiO2}	nm	Silicon dioxide thickness
V_{FB}	V	Flat band voltage
V_G	V	Gate voltage
V_T	V	Threshold voltage
θ (θ_{exp}, $\theta_{simulated}$)	°	Angle of incidence (experimental/simulated)
τ_{eff}	μs	Minority carrier lifetime
φ	°	Azimuthal angle
$\chi^{(2)}$	m^2/V	Surface/interface 2nd order nonlinear susceptibility
$\chi^{(3)}$	m^2/V^2	Bulk 3rd order nonlinear susceptibility
ψ	°	Polarization angle

Table of Contents

Chapter 1:
General Introduction and Context

Contents of Chapter 1

1.1 Dielectrics on silicon

In modern microelectronics and photovoltaics, dielectrics are widely used as insulator layers in devices, for surface and interface functionalization, and passivation. Dielectrics are one of the main layers in Metal-Oxide-Semiconductor (MOS) devices and MOS field effect transistors (MOSFET), as well as in advanced substrates such as Silicon-On-Insulator (SOI) [1]. One of the existing challenges for very thin gate dielectrics in MOS devices is to insure their integrity and reliability. A typical MOSFET [2] structure is shown in Figure 1.1a. In MOSFETs, the oxide below the gate plays an important role in the electrostatic control of the transistor, allowing electrical insulation between the gate and the semiconductor. Having a high energy barrier, the dielectric prohibits charge movement through it. By controlling the body and gate potentials, charge (positive or negative, depending on substrate doping) can be induced in the semiconductor below the oxide. Therefore, by adjusting the source and drain potentials this charge can flow in the channel. In modern technology, it is imperative to decrease the transistor size [3], which inevitably influences its operation. As the oxide shrinks (typically SiO_2), undesired quantum effects (like tunnelling) increase gate leakage. Hence, alternative high-k oxides with higher oxide thicknesses must be employed.

Dielectrics are also used in complementary MOS (CMOS) imagers technology [4] and in solar cells [5] for passivation. In both applications, impinging photons are converted to electrons inside the devices. However, imperfect silicon surfaces can cause significant electronic losses due to charge carrier recombination. Passivation dielectrics (such as SiO_2, Al_2O_3, etc…) can reduce these recombination losses and increase the conversion efficiency. A widely commercialized standard solar cell is shown in Figure 1.1b [6], where the dielectric is deposited on top of a vertical p-n junction in order to supress recombination losses and act as an antireflection coating (ARC). Typically, high-k oxides (SiN_x, Al_2O_3, etc…) are used, allowing for better passivation of the solar cell's texturized surface while acting as ARC's. Passivation can be either chemical, or field-effect related: in the former, the interface trap density is reduced; in the latter, some pre-existing fixed charges create an electric field which repels the minority carriers from the semiconductor surface, reducing their recombination. In all the cases, dielectrics fill in their role if they and their interfaces with semiconductors are of a very good quality.

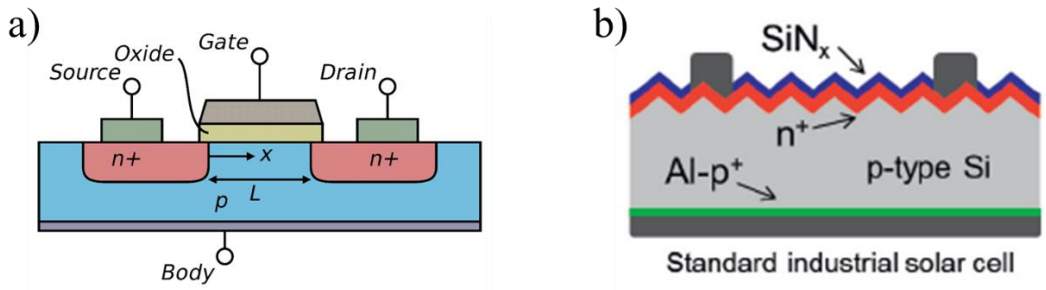

Figure 1.1: a) Typical MOSFET structure with its four terminals shown (Source, Drain, Gate, Body) [2]. b) Standard industrial solar cell [6].

1.2 Defects and characterization methods

The dielectric that is most widely used in semiconductor industry is SiO_2, due to its excellent quality and optimal control of the technological process. Its properties depend on the fabrication procedure and conditions. However, during manufacturing, defects can show up at the interface between the different materials [7] and in the dielectric itself, which can cause performance decrease and device failure, especially when downscaling the technology.

Typically, two main families of defect characterization exist: the physicochemical and the electrical methods. For instance, techniques such as X-Ray Diffraction [8], Total X-Ray Fluorescence [9], Atomic Force Microscopy [10], and many others, give information regarding chemical composition, metallic contamination, surface roughness, crystallography, stacking defects, etc… In this thesis we will only address electrical properties of dielectrics on Si. Therefore, we will focus on the electrical characterization techniques and electrical parameters such as fixed oxide charge (Q_{ox}) and interface trap (D_{it}) concentrations, as well as the effective lifetime of minority carriers τ_{eff} inside silicon, which quantify the quality of the dielectric/Si interface. Some of the most important defects shown in Figure 1.2 are:

- Contaminations either in the bulk of the dielectric or at the interface, typically metallic (Fe, Ni, Cu, etc…) [11]. For example, during thermal oxide growth, heating elements in the furnace can release volatile contaminants [12].
- Electrically active defects at the dielectric / Si interface that can be charges with concentrations in the range 10^{10} - 10^{13} cm^{-2} [13] or interface traps with different concentrations according to their energy level inside the bandgap.

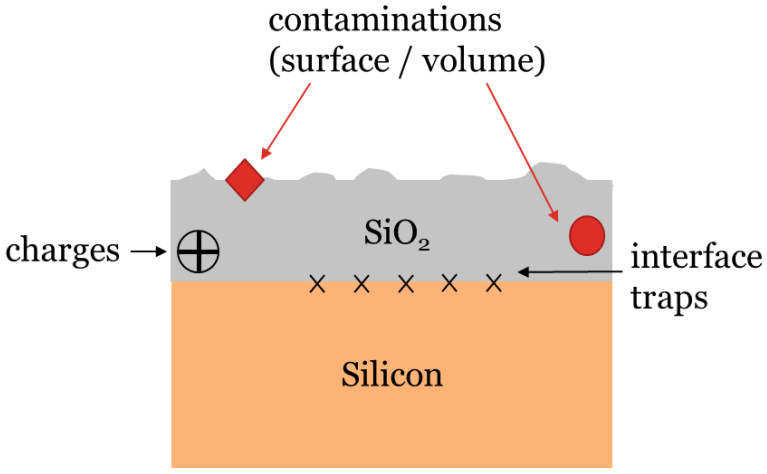

Figure 1.2: Typical SiO_2/Si defects: surface and volume contaminations, fixed charges (Q_{ox}) and interface traps (D_{it}) [11], [14], [15].

Specifically, the electrically active defects on which we will focus in this thesis, are present in all insulator/semiconductor systems and can be subcategorized as follows (Figure 1.3) [14], [15]:

- Interface trapped charges (D_{it}), which are located at the interface between the insulator and the semiconductor. They can be positive or negative in nature, induced by oxidation processes or they can be structural defects or metallic impurities. Furthermore, they can be caused by radiation or other bond-breaking processes. They are connected electrically with the Si substrate.
- Fixed oxide charges (Q_f, also noted as Q_{ox}), which are located near the interface. They are positive (in the case of SiO_2) and related to the oxidation process, oxidation temperature and silicon orientation. They are not electrically connected with the Si substrate.
- Oxide trapped charge (Q_{ot}), which is a charge trapped in the oxide that can either be positive or negative (holes or electrons). It is mainly caused by ionizing radiation, tunnelling or other mechanisms.
- Mobile oxide charge (Q_m), which is mainly caused by ionic impurities such as negative ions and heavy metals (Na^+, Li^+, etc…) that can move inside the oxide.

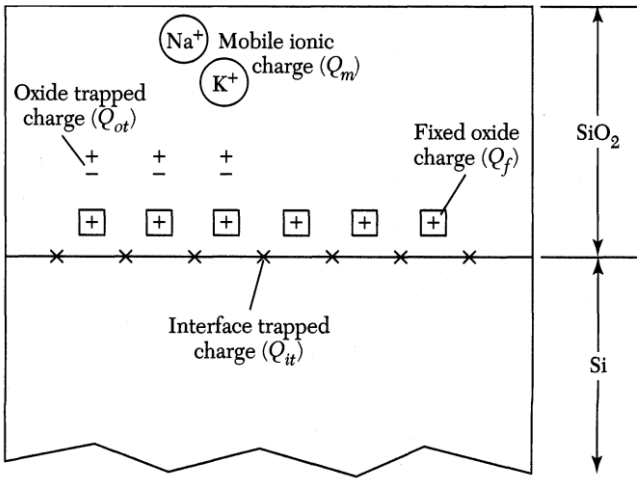

Figure 1.3: The 4 different types of traps and charges in SiO_2/Si systems [16].

These defects have to be minimized in order to achieve high quality substrates. The additional challenge is related to the reduced dielectric thicknesses, which are in the order of a few nm in the latest technology nodes [3]. In this context, dielectrics characterization is an important topic and sensitive, reliable, fast and non-destructive techniques are needed for material quality evaluation before full device processing. In addition, factory level metrology integration with real time in-situ and in-line tools are required. In the next section we will present some of the conventional electrical methods used in microelectronics and photovoltaics, which allow $Q_{ox}/D_{it}/\tau_{eff}$ extraction.

1.2.1 Fixed oxide charge and interface traps evaluation

The most common electrical measurement for dielectric characterization is capacitance-voltage (C-V) being widely used for MOS capacitors [15]. With the help of C-V measurements in different conditions it is possible to extract information regarding the semiconductor (flat band voltage V_{FB}, doping level in the substrate N_A/N_D, etc…) and the oxide (fixed oxide charge Q_{ox}, thickness t_{ox}, etc…), as well as the interface trapped density D_{it}. Different methods can be used to extract interface trap density such as Berglund (low frequency C-V) [17], Terman (high-frequency C-V) [18], etc… Additionally, quasi-static C-V [15] allows accessing slow D_{it}.

As all the conventional electrical characterization methods, C-V necessitates extra processing steps in order to fabricate specific test devices (here a metal must be deposited on top of the dielectric/silicon stack in order to create a gate for the MOS capacitor). Furthermore, the electrical measurements can cause dielectric breakdown of ultrathin dielectric films (<10 nm) used today [19]–[22] and they cannot be applied on a whole wafer.

A technique which can be applied on a whole silicon wafer with a dielectric deposited on top, is the corona discharge (Figure 1.4) [14], [23], [24]. A high DC voltage (around 10 kV) is applied on an electrode (typically a sharp needle) and causes a dielectric breakdown of the atmospheric air below it, creating ions (either positive H_3O^+ or negative CO_3^-, depending on the polarity of the DC voltage on the electrode). The ions diffuse toward the surface of the sample (dielectric on Si in our case) placed on a grounded chuck facing the corona electrode. The ions do not damage the samples since they lose their kinetic energy due to collisions with atmospheric particles (mean free path ~10^{-7} m in standard conditions). The corona charges deposited on top of the dielectric modify the surface potential which is monitored with a Kelvin probe (Figure 1.4) [14]. At the point where the surface potential is zero, the deposited corona charges counterbalance the pre-existing ones, which can be the fixed charges in the dielectric.

With the Corona Oxide Characterization of Semiconductors (COCOS) [25], it is possible to calculate the flat band voltage V_{FB}, the charge required to reach flat band condition Q_{tot} and the interface trap density D_{it} [25]. A drawback is that hysteresis effects (charging/discharging phenomena) cannot be monitored and a cleaning of the surface is mandatory after the measurement in order to remove the deposited corona charges.

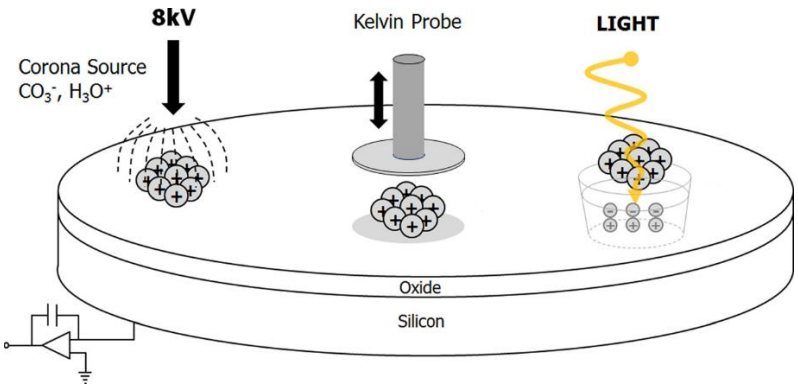

Figure 1.4: Corona discharge characterization [26]. Corona charges are deposited on top of the dielectric first and the surface potential is measured with a Kelvin probe in dark and later under light illumination.

1.2.2 Minority carrier lifetime measurement

Photoconductance decay (PCD) is a well-known contactless method for the evaluation of minority carrier lifetime in Si [14] which does not require specific device fabrication. A schematic of the measurement setup is shown in Figure 1.5a. An optical source (light pulse) in Figure 1.5b creates electron hole pairs in the semiconductor and increases the conductance of the sample. When the light source is shut-off, recombination processes occur and the excess minority carrier density (hence the conductance) decreases, which is monitored from the decrease of the microwave signal (Figure 1.5c). The exponential microwave signal in Figure 1.5c has a characteristic time τ, which is the lifetime of the minority carriers and its value indicates the quality of a passivation layer (higher values for better passivation). While the technique can work in transient mode for minority carrier lifetime higher than 200μs, another version exists: the quasi-steady-state PCD (QSS-PCD) [27].

The technique's strength is the contactless nature and rapid measurement but both sides of the sample must be passivated (extra processing step), in order to reduce surface recombination effects and allow extraction of the effective lifetime. However, this technique gives only a lifetime value and is not able to separate between the two passivation mechanisms (chemical and field-effect). In addition, the calculation of Q_{ox} and D_{it} is not possible.

Photoluminescence decay (PLD) is another method of monitoring the time dependence of excess minority carriers [14], [28]. Similar to PCD, excess carriers are generated by a short light pulse with a photon energy higher than the bandgap of the semiconductor. In contrast with PCD, the excess carrier density is monitored through the time-dependence of the light emitted from radiative recombination of electron-hole pairs, and not from conductance. Similar to PCD, it is only possible to extract the effective lifetime but not Q_{ox} and D_{it} values.

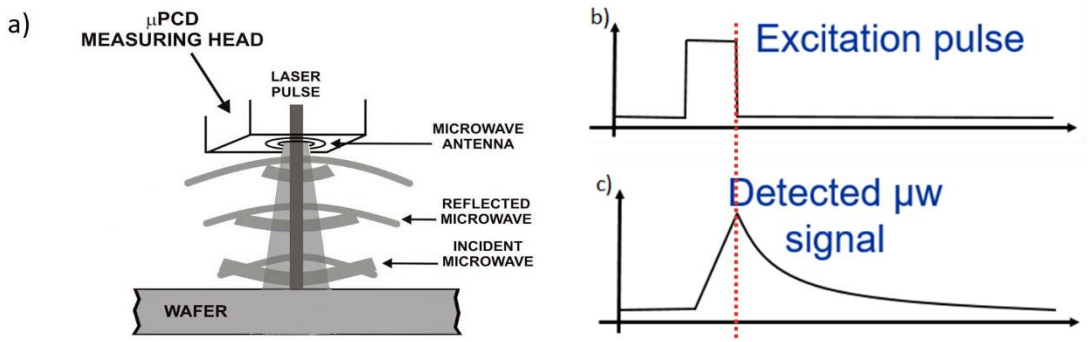

Figure 1.5: a) μ-PCD measurement setup schematic [29]. A laser pulse creates excess minority carriers in the sample under study and an antenna emits a microwave signal that gets reflected from the sample. The excitation pulse (b) increases the sample's conductance (c) which decays after the excitation stops. The decay is ultimately related to the material quality through the lifetime values.

1.2.3 Second Harmonic Generation

Apart from the regular techniques presented above, another one that is complementary to them, is surface Second Harmonic Generation (SHG) [30], [31]. SHG is a nonlinear optical technique based on the second order polarization generated from a material which is illuminated with a high-intensity laser light. Centrosymmetric materials such as Si and amorphous dielectrics like SiO_2, Al_2O_3, etc, do not allow second-order (and generally even-order) effects such as SHG, due to the presence of an inversion symmetry centre [30]. In a dielectric/semiconductor material stack like SiO_2/Si and SOI, the second harmonic is generated at the interfaces between the media where the inversion symmetry is broken due to lattice mismatch and the presence of static electric fields [32], [33].

The reflected SHG intensity from a dielectric/Si interface is described by [31], [32]:

$$I_{2\omega} \propto \left|\chi^{(2)} + \chi^{(3)} E_{dc}\right|^2 \left(I_{\omega}\right)^2 ,$$

where $\chi^{(2)}$ and $\chi^{(3)}$ are the second and third order nonlinear susceptibilities (which are material dependent), I_{ω} is the incident light intensity and E_{dc} is the static electric field at the interface arising from fixed charges, interface traps, space charge region, etc... Therefore, being both non-invasive and interface specific, SHG can give access to this interfacial electric field.

The preceding work ~20 years ago (synthesized in [34]) unfolded the ability of SHG to characterize interface electric fields, as well as structural properties like stress and strain at the interfaces of dielectric/silicon stacks. Table 1.1 shows the capabilities of the aforementioned measurement techniques for the electrical properties of dielectrics on semiconductors. Among them, the SHG appears very promising, provided that the extraction methods are developed.

Table 1.1: Dielectric on semiconductor characterization techniques: advantages (+) and disadvantages (-)

	CV-IV	µ-PCD	Corona (COCOS)	SHG
Sample processing	-	+	+	+
Non-invasive	-	+	-	+
Full wafer mapping	-	+	+	+
Q_{ox} and D_{it} extraction	direct	-	indirect	*to be improved*
τ_{eff} extraction	-	+	-	-

1.3 Framework and goal of this thesis

SHG characterization was used for investigating the interface quality of test materials like high-k dielectrics (Al_2O_3) on Silicon, and Silicon-on-Insulator (SOI) wafers by accessing the static electric field (owing to interface traps D_{it} and fixed charges Q_{ox}) present at interfaces between the media. The aim of this thesis is to utilize SHG for SOI and high-k passivation quality control and to take a step forward towards calibration. The structure of this thesis is as follows:

- Chapter 2 presents the SHG theory starting from an intuitive approach. Then the proper formalism to describe SHG from surfaces and interfaces of interest (in dielectrics on Si and SOI) is introduced. Furthermore, the concept of electric field induced SHG (EFISHG) is presented along with its application for a simple SiO_2/Si interface. The need for optical simulation reveals itself naturally as a must, in order to use SHG for material characterization.
- In Chapter 3 the optical simulation is introduced. SHG signals contain information about the electrical properties of the interface but are also affected by optical phenomena (interferences, absorption, etc…). A separation between optics and static electric field is therefore mandatory. The optical simulation is used to study propagation in multi-layered structures and check its impact on the SHG signal. We included the static electric field in our home-made simulator in order to study its impact.
- Chapter 4 presents the characterization done on Al_2O_3/Si samples. These samples are known to contain fixed charges (Q_{ox}) that can be activated or not, depending on how they are processed. The impact of these charges was investigated by other techniques (C-V, µ-PCD). We attempted to quantify them and subsequently correlate them with the SHG characterization. Additionally, the simulation from Chapter III is combined with the experimental SHG results for verification.
- In Chapter 5, SHG for SOI characterization is presented. SOI is a multilayer stack with many interfaces that might be electrically coupled (which is the case for ultra-thin SOI [35]). Furthermore, the multilayer geometry affects inevitably the observed SHG behaviour through multiple reflections, interferences, etc… For this reason, the home-made simulator is used to

study the impact of the static electric field from the top and buried interfaces on the SHG behaviour.

- Chapter 6 summarizes the results and presents the general conclusions. In addition, ongoing research and future prospects are discussed.

This thesis is therefore an interdisciplinary research between the fields of optical and microelectronic characterization techniques, at the interface between academia (physical principles) and industry (industrial scale in-line SHG characterization tool for ultimate use in wafer inspection inside the production line).

Chapter 2:
Introduction to Second Harmonic Generation

This chapter introduces Second Harmonic Generation (SHG) and shows some examples of its use for material and interface characterization. The SHG theory is presented step by step, starting from an intuitive approach, then specifying it in the dipolar approximation for centrosymmetric materials; supplementary contributions due to quadrupolar terms and presence of static electric fields at an interface are then considered. The conclusion of the theoretical part is that in SiO_2/Si samples, the SHG is mainly given by the interface and the static electric field present there. Finally, SHG experiments for the simple SiO_2/Si system are shown and basic parameters affecting the SHG signals are discussed.

Contents of Chapter 2

2.1 Theory of second harmonic generation from centrosymmetric materials

2.1.1 An intuitive approach of SHG

Second harmonic generation (SHG) is reported as the first nonlinear optical process [36], [37] which was discovered in a centrosymmetric quartz crystal after the invention of the first ruby laser in 1960. Second harmonic phenomenological theories were later developed for materials including metals and semiconductors [38], [39]. SHG is related to the response of a material under excitation through an electromagnetic field. For example, a dielectric material system can be regarded as a collection of valence electrons being bound to their ion cores. When an external electric field is applied, the electrons will get slightly displaced from their initial positions, while the ion cores are considered fixed. This creates a dipole which is associated to an induced polarization inside the material (Figure 2.1a) [40]. If the applied field is oscillating, the resulting electric dipole oscillates as well and emits a radiation at the oscillation frequency. The polarization of the material (P) versus the applied electric field (E) is shown schematically as a solid line in Figure 2.1b. If the electric field has a small enough amplitude, the induced polarization dependence can be approximated linearly:

$$\vec{P}^{(1)}(\omega) = \chi^{(1)}\vec{E}(\omega) \tag{2.1}$$

with $\chi^{(1)}$ the linear electrical susceptibility of the material.

High amplitude electric fields, such as those from lasers, can excite higher orders of the polarization response in the material (Figure 2.1c). The response becomes nonlinear and the polarization should be expressed as a Taylor expansion in a power series of the field strength:

$$\vec{P} = \chi^{(1)}\vec{E}(\omega) + \chi^{(2)}\vec{E}(\omega)^2 + \chi^{(3)}\vec{E}(\omega)^3 + \cdots = \vec{P}^{(1)} + \vec{P}^{(2)} + \vec{P}^{(3)} + \cdots \tag{2.2}$$

where $\chi^{(n)}$ is the n^{th} order nonlinear susceptibility of the medium and is a tensor of rank n+1. It defines the material response to the n^{th} order of the electric field. The second order polarization is related to the second order response:

$$\overrightarrow{P^{(2)}}(2\omega) = \chi^{(2)}\vec{E}(\omega)^2 \tag{2.3}$$

The intensity of the SHG is proportional to the square of the second order polarization:

$$I_{2\omega} \propto \left|\overrightarrow{P^{(2)}}\right|^2 = \left|\chi^{(2)}\right|^2 \left|\vec{E}(\omega)\right|^4 \tag{2.4}$$

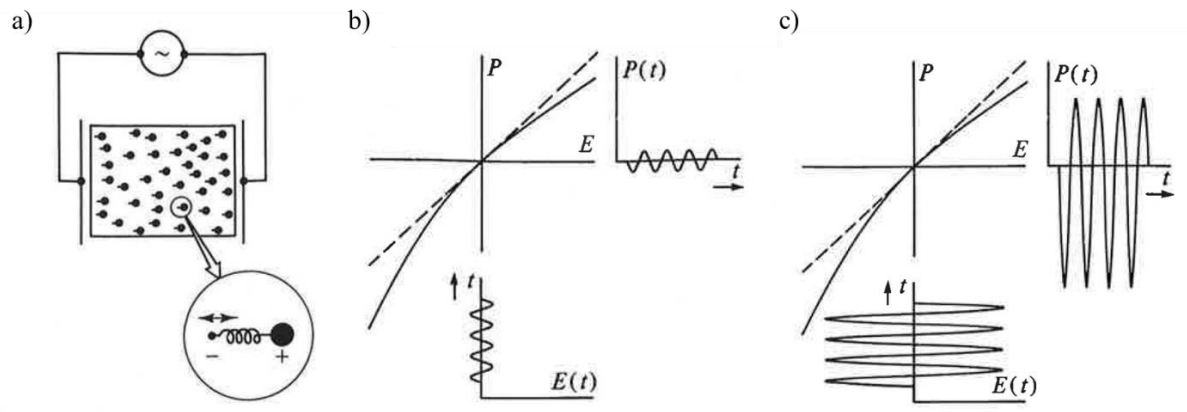

Figure 2.1: a) Schematic of the displacement of bound charges in a dielectric under the influence of an externally applied electric field. b) An electric field with a small amplitude oscillating at an optical frequency induces a linear polarisation. c) High amplitude electric fields can induce a nonlinear polarization response in the material [40].

In other words, in 2nd order nonlinear optics, an incident beam with a specific frequency ω interacts with the material through the second order susceptibility inducing a polarization which creates the second harmonic beam, with a frequency of 2ω (Figure 2.2a). Quantum mechanically, the SHG process can be visualized by considering, in the simplest case, the energy levels of an atom and its interaction with photons. Two photons of the same frequency ω are suppressed during the interaction with the atom and a single photon of frequency 2ω is emitted (Figure 2.2b).

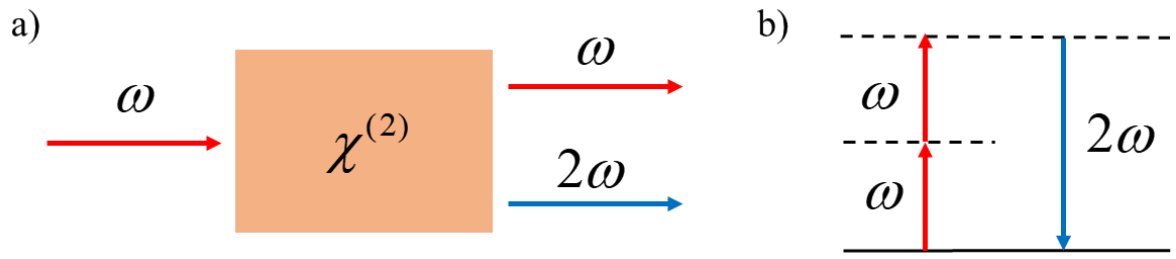

Figure 2.2: a) Second harmonic generation from a material described by $\chi^{(2)}$. b) Energy levels illustrating second harmonic generation.

2.1.2 SHG in centrosymmetric materials in the dipolar approximation

The incident electric fields that generate SH light inside a material are vectors with 3 components in cartesian coordinates:

$$\vec{E} = \begin{pmatrix} E_x \\ E_y \\ E_z \end{pmatrix} \tag{2.5}$$

Therefore, the "i" (= x,y,z) component of the 2nd order nonlinear polarization in a medium is written as a sum of all the possible combinations of the electric fields:

$$P_i(2\omega) = \sum_{j,k} \chi_{ijk}^{(2)} E_j(\omega) E_k(\omega) \tag{2.6}$$

where, the indices 'ijk' can be one of the x, y or z coordinates. In the previous expression, there are 3^2=9 possible combinations for the electric fields, while the second order susceptibility tensor is a 2nd rank tensor with 3^3=27 components. The full 2nd order polarization expression is [30]:

$$\begin{pmatrix} P_x^{(2)} \\ P_y^{(2)} \\ P_z^{(2)} \end{pmatrix} = \begin{pmatrix} \chi_{xxx}^{(2)} & \chi_{xxy}^{(2)} & \chi_{xxz}^{(2)} & \chi_{xyx}^{(2)} & \chi_{xyy}^{(2)} & \chi_{xyz}^{(2)} & \chi_{xzx}^{(2)} & \chi_{xzy}^{(2)} & \chi_{xzz}^{(2)} \\ \chi_{yxx}^{(2)} & \chi_{yxy}^{(2)} & \chi_{yxz}^{(2)} & \chi_{yyx}^{(2)} & \chi_{yyy}^{(2)} & \chi_{yyz}^{(2)} & \chi_{yzx}^{(2)} & \chi_{yzy}^{(2)} & \chi_{yzz}^{(2)} \\ \chi_{zxx}^{(2)} & \chi_{zxy}^{(2)} & \chi_{zxz}^{(2)} & \chi_{zyx}^{(2)} & \chi_{zyy}^{(2)} & \chi_{zyz}^{(2)} & \chi_{zzx}^{(2)} & \chi_{zzy}^{(2)} & \chi_{zzz}^{(2)} \end{pmatrix} \begin{pmatrix} E_x E_x \\ E_x E_y \\ E_x E_z \\ E_y E_x \\ E_y E_y \\ E_y E_z \\ E_z E_x \\ E_z E_y \\ E_z E_z \end{pmatrix} \tag{2.7}$$

Due to the invariance of the electric fields at frequency ω in eq. (2.6), their indices are interchangeable according to Kleinman symmetry [30]: E_kE_j can replace E_jE_k. Therefore, the second order susceptibility is symmetrical with respect to its last two indices. The nonlinear susceptibility tensor reduces to a form with 18 independent components, and the polarization expression is written as:

$$\begin{pmatrix} P_x^{(2)} \\ P_y^{(2)} \\ P_z^{(2)} \end{pmatrix} = \begin{pmatrix} \chi_{xxx}^{(2)} & \chi_{xyy}^{(2)} & \chi_{xzz}^{(2)} & \chi_{xyz}^{(2)} & \chi_{xxz}^{(2)} & \chi_{xxy}^{(2)} \\ \chi_{yxx}^{(2)} & \chi_{yyy}^{(2)} & \chi_{yzz}^{(2)} & \chi_{yyz}^{(2)} & \chi_{yxz}^{(2)} & \chi_{yxy}^{(2)} \\ \chi_{zxx}^{(2)} & \chi_{zyy}^{(2)} & \chi_{zzz}^{(2)} & \chi_{zyz}^{(2)} & \chi_{zxz}^{(2)} & \chi_{zxy}^{(2)} \end{pmatrix} \begin{pmatrix} E_x^2 \\ E_y^2 \\ E_z^2 \\ 2E_yE_z \\ 2E_xE_z \\ 2E_xE_y \end{pmatrix} \tag{2.8}$$

The above polarization expression is simplified even more in materials of interest for technological applications, such as those that we mainly study in this thesis: amorphous dielectrics (SiO_2, Al_2O_3) and silicon which are centrosymmetric, exhibiting inversion symmetry [30], [41]. In the dipolar approximation, the polarization vectors inside these materials are invariant under the inversion of the coordinate system. Assume an optical electric field $\vec{E}$ inducing an electron oscillation inside the material, which generates the 2nd order polarization $\overrightarrow{P^{(2)}}(\vec{E})$; if the field is inversed $(-\vec{E})$, the electron oscillation inside the material must be opposite to the one obtained in the previous case, i.e. $-\overrightarrow{P^{(2)}}(-\vec{E})$. Additionally, the inversion symmetry implies that the material response is the same in both cases:

$$\overrightarrow{P^{(2)}}(\vec{E}) = -\overrightarrow{P^{(2)}}(-\vec{E}) \Rightarrow \chi^{(2)}\vec{E}\vec{E} = -\chi^{(2)}(-\vec{E})(-\vec{E}) \Rightarrow \chi^{(2)}\vec{E}\vec{E} = -\chi^{(2)}\vec{E}\vec{E} \tag{2.9}$$

For this relation to be valid, the $\chi^{(2)}$ term must be zero, which means that inside the bulk of centrosymmetric materials:

$$\chi^{(2)}_{bulk} = 0 \tag{2.10}$$

Therefore, in the **dipolar approximation**, no second harmonic radiation is generated from the bulk of the material with inversion symmetry. Nevertheless, any breaking of the inversion symmetry (e.g. the presence of an interface) can give rise to a second order polarization.

2.1.3 SHG at an interface between two centrosymmetric materials

Even though for bulk centrosymmetric media, $\chi^{(2)}_{bulk} = 0$, at the interface between two such media the inversion symmetry is broken. Figure 2.3 shows an example of amorphous SiO_2 on Si; the inversion symmetry is broken along the z axis, while it holds for x and y axes (on the surface plane of the material).

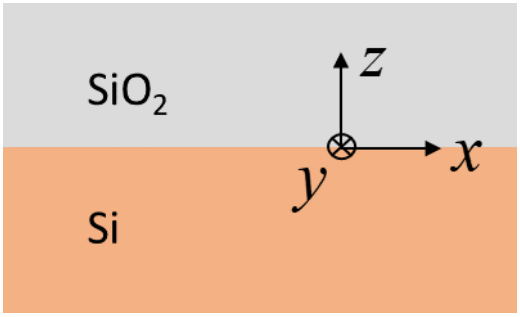

Figure 2.3: Interface between SiO_2 and Si (centrosymmetric materials) and the xyz coordinates.

Using the symmetries of the material properties we can reduce the number of elements in the general expression of the susceptibility tensor (eq. (2.8)). For example, we consider the case where the electric field is only along the x-axis $(E_x, 0, 0)$:

$$\begin{pmatrix} P_x^{(2)} \\ P_y^{(2)} \\ P_z^{(2)} \end{pmatrix} = \begin{pmatrix} \chi_{xxx}^{(2)} & \chi_{xyy}^{(2)} & \chi_{xzz}^{(2)} & \chi_{xyz}^{(2)} & \chi_{xxz}^{(2)} & \chi_{xxy}^{(2)} \\ \chi_{yxx}^{(2)} & \chi_{yyy}^{(2)} & \chi_{yzz}^{(2)} & \chi_{yyz}^{(2)} & \chi_{yxz}^{(2)} & \chi_{yxy}^{(2)} \\ \chi_{zxx}^{(2)} & \chi_{zyy}^{(2)} & \chi_{zzz}^{(2)} & \chi_{zyz}^{(2)} & \chi_{zxz}^{(2)} & \chi_{zxy}^{(2)} \end{pmatrix} \begin{pmatrix} E_x^2 \\ 0 \\ 0 \\ 0 \\ 0 \\ 0 \end{pmatrix} \tag{2.11}$$

Simply, we can write:

$$\begin{pmatrix} P_x^{(2)} \\ P_y^{(2)} \\ P_z^{(2)} \end{pmatrix} = \begin{pmatrix} \chi_{xxx}^{(2)} E_x^2 \\ \chi_{yxx}^{(2)} E_x^2 \\ \chi_{zxx}^{(2)} E_x^2 \end{pmatrix} \tag{2.12}$$

If we apply the inversion symmetry in the x axis, the polarization $(P_x^{(2)},0,0)$ produced by $(E_x,0,0)$ must be equal to $(-P_x^{(2)},0,0)$ produced by $(-E_x,0,0)$ and the susceptibility components will vanish:

$$\left.\begin{aligned} -P_x^{(2)} &= -\chi_{xxx}^{(2)}(-E_x)(-E_x) = -\chi_{xxx}^{(2)}E_x^2 \\ P_x^{(2)} &= \chi_{xxx}^{(2)}E_x^2 \end{aligned}\right\} \xrightarrow{-P_x^{(2)}=P_x^{(2)}} \chi_{xxx}^{(2)} = 0 \qquad (2.13)$$

Likewise, for the y-axis we can find that $\chi_{yyy}^{(2)} = 0$. With similar symmetry arguments, the 2nd order nonlinear susceptibility tensor for a Si (100) surface/interface with C_{4v} symmetry has only five non-vanishing components and the second order polarization takes the form [42], [43]:

$$\begin{pmatrix} P_x^{(2)} \\ P_y^{(2)} \\ P_z^{(2)} \end{pmatrix} = \begin{pmatrix} 0 & 0 & 0 & 0 & \chi_{xxz}^{(2)} & 0 \\ 0 & 0 & 0 & \chi_{yyz}^{(2)} & 0 & 0 \\ \chi_{zxx}^{(2)} & \chi_{zyy}^{(2)} & \chi_{zzz}^{(2)} & 0 & 0 & 0 \end{pmatrix} \begin{pmatrix} E_x^2 \\ E_y^2 \\ E_z^2 \\ 2E_yE_z \\ 2E_xE_z \\ 2E_xE_y \end{pmatrix} \qquad (2.14)$$

Additionally, $\chi_{xzx}^{(2)} = \chi_{yzy}^{(2)}$ and $\chi_{zxx}^{(2)} = \chi_{zyy}^{(2)}$.

2.1.4 Quadrupolar contribution from the bulk in SHG

In section 2.1.2, we showed that in the dipolar approximation, the dipolar contributions from bulk centrosymmetric materials is zero. However, higher order (multipole) contributions, such as magnetic dipole or electric quadrupole, can generate SHG from a few atomic layers of the bulk [44]. The leading order multipole contributions are the electric quadrupole and magnetic dipole contributions described by [31], [39], [45]:

$$\overrightarrow{P_Q}(2\omega) = \chi_Q^{(2)}\vec{E}(\omega)\vec{\nabla}\vec{E}(\omega) \qquad (2.15)$$

where $\chi_Q^{(2)}$ is the 2nd order quadrupolar susceptibility, which is a tensor of rank 4 with 81 components. The gradient in the above equation reflects the nonlocal nature of the quadrupolar polarization. Depending on the crystal class the medium belongs to, some elements of $\chi_Q^{(2)}$ are zero. For a cubic centrosymmetric medium (such as silicon), the only non-vanishing elements are $\chi_{Q,iiii}^{(2)}$, $\chi_{Q,iijj}^{(2)}$, $\chi_{Q,ijij}^{(2)}$, $\chi_{Q,ijji}^{(2)}$ which are usually represented by the phenomenological parameters β, γ, δ and ζ (linear combinations of $\chi_Q^{(2)}$ elements) [39], [45]–[47]. The nonlinear polarization is written with respect to these parameters as:

$$\overrightarrow{P_Q}(2\omega) = (\delta-\beta-2\gamma)\left(\vec{E}\cdot\vec{\nabla}\right)E_i + \beta E_i\left(\vec{\nabla}\cdot\vec{E}\right) + \gamma\nabla_i\left(\vec{E}\cdot\vec{E}\right) + \zeta E_i\nabla_i E_i \qquad (2.16)$$

For crystalline Si, the first 3 terms are isotropic, while the last one is anisotropic with respect to crystal orientation. The anisotropic term contributes in all polarization configurations of the fundamental and the SHG radiation [45]. Typically, the first term in eq. (2.16) vanishes in the plane wave approximation, the second term disappears in a homogeneous medium (due to the zero divergence of the electric field) and the third term always appears in linear combinations with the surface $\chi^{(2)}_{zxx}$ component (i.e. $\chi^{(2)}_{zxx}+\varepsilon^{-1}\gamma$) [45]–[47].

2.1.5 Geometry of SHG experiments

In general, the second order polarization from Si (100) surfaces/interfaces, besides the excitation laser characteristics, will also depend on the various experimental parameters such as the angle of incidence (θ) of the fundamental light, its polarization angle (ψ) relevant to the plane of incidence and the azimuthal angle (φ) shown in Figure 2.4. When ψ=0°, the incident light is polarized parallel (P) to the plane of incidence (xz-plane), while for ψ=90° its polarization is perpendicular to it (S). Likewise, SH light can be detected at either P- or S- polarization.

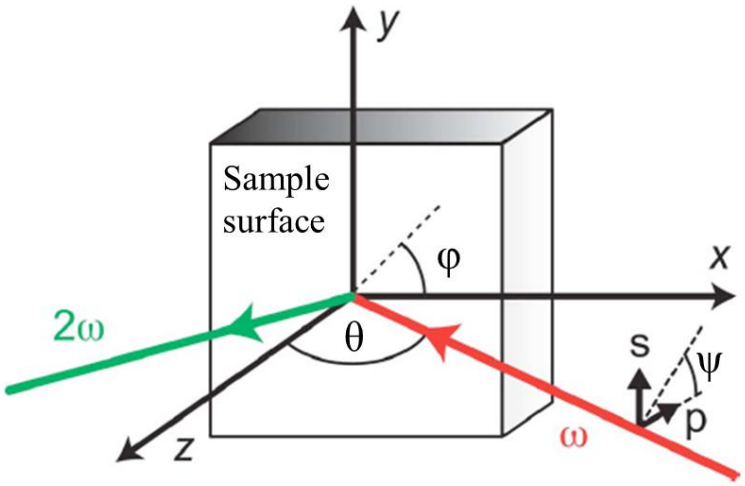

Figure 2.4: Typical angles of polarization (ψ) and azimuthal (φ) present in the nonlinear polarization expression. The plane of incidence is the xz-plane and θ is the angle of incidence [43].

For the two most common cases of P- and S- polarized SH light, the 2nd order nonlinear polarization for Si (100) surfaces/interfaces can be written as [42]:

a) For P-polarized SH:

$$\begin{aligned} P^{NL}_{P-out} = &\left\{\chi^{(2)}_{zxx}F_s\sin^2\psi+(\chi^{(2)}_{zxx}F_s f_c^2-\chi^{(2)}_{xzx}2F_c f_s f_c+\chi^{(2)}_{zzz}F_s f_s^2)\cos^2\psi+\right.\\ &+\gamma F_s-\frac{i}{4}\lambda_\omega n_\omega\zeta\left[F_c f_s\sin^2\psi+(3F_c f_c^2 f_s+4F_s f_s^2 f_c)\cos^2\psi+\right.\\ &\left.\left.+2F_c f_s f_c\cos\psi\sin\psi\sin 4\varphi+F_c f_s(f_c\cos^2\psi-\sin^2\psi)\cos 4\varphi\right]\right\}E_\omega^2 \end{aligned} \qquad (2.17)$$

b) For S-polarized SH:

$$P_{S-out}^{NL} = \left\{ \chi_{xzx}^{(2)} 2 f_s \cos\psi \sin\psi - \frac{i}{4} \lambda_\omega n_\omega \zeta \left[-2 f_s f_c \cos\psi \sin\psi \right.\right. \\ \left.\left. + f_s (\sin^2\psi - f_c^2 \cos^2\psi) \sin 4\varphi + 2 f_s f_c \cos\psi \sin\psi \cos 4\varphi \right] \right\} E_\omega^2 \quad (2.18)$$

where f_s, f_c, F_s, F_c are Fresnel coefficients for the fundamental and the SH waves defined as:

$$fundamental: f_s = \frac{\sin\theta}{n_\omega}, f_c = \frac{\cos\theta}{n_\omega}$$
$$SH: F_s = \frac{\sin\theta}{n_{2\omega}}, F_c = \frac{\cos\theta}{n_{2\omega}} \quad (2.19)$$

with n_ω being the refractive index of Si at the fundamental and $n_{2\omega}$ at the 2nd harmonic frequency.

In some cases, we might want to probe the bulk properties of the Si substrate. Therefore, we must be able to separate the surface/interface dipolar and the bulk quadrupolar contributions. This is possible for Si (100) substrates, where the total SHG intensity, including contributions from the surface and the bulk can be written in a more compact form. For either P- or S- polarized fundamental radiation (ψ=0° or ψ=90° in eq.(2.17) and eq.(2.18)), the SH intensity becomes [31], [42]–[44]:

a) For P-polarized SHG:

$$I_{2\omega}^{P-out} = \left| a + b\cos(4\varphi) \right|^2 \quad (2.20)$$

b) For S-polarized SHG:

$$I_{2\omega}^{S-out} = \left| c\sin(4\varphi) \right|^2 \quad (2.21)$$

where α includes isotropic dipolar contributions from the surface and b, c include only anisotropic quadrupolar contributions from the bulk [42], [44]. In addition, α, b, c, include linear optical properties. Typically, in Si (100) substrates α is much stronger than b and c (up to one order of magnitude) [44].

Typical rotational anisotropic SHG data from Si (100) substrates are shown in Figure 2.5. A 4-fold anisotropic pattern for P-polarized SHG is present, as theoretically predicted [44], [31] and as expected from eq.(2.20). The α term sets the isotropic level in the graph, while b describes the oscillation. The SHG anisotropy pattern changes to 8-fold when the S-polarized second harmonic is detected. This is also expected theoretically from eq.(2.21). Note that in the case of P-polarized SH, the surface/interface properties are mostly accessible via the α term which is prominent, while for S-polarized SH a few layers (nm) of the Si bulk properties are probed (c term in eq.(2.21) depends only on the bulk quadrupolar anisotropic component, characteristic of the bulk properties).

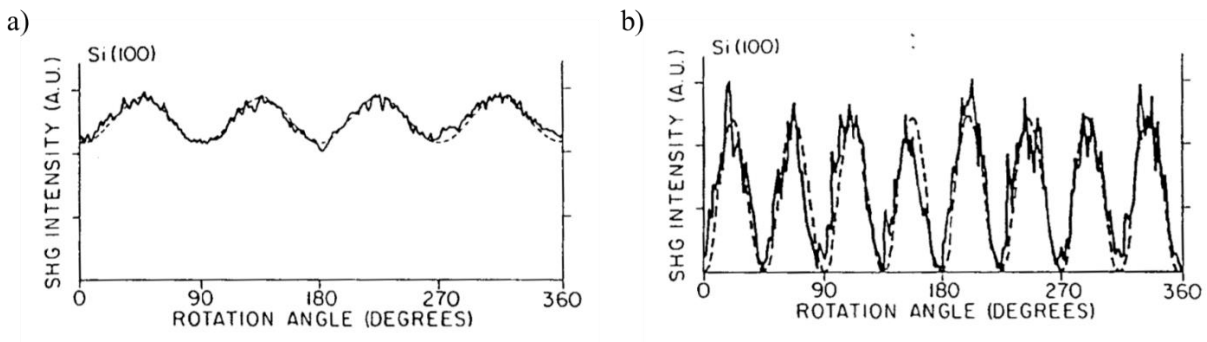

Figure 2.5: SHG versus azimuthal angle for Si (100) with P-polarized fundamental and: a) P-polarized SHG exhibiting a 4-fold symmetry, b) S-polarized SHG exhibiting 8-fold symmetry. The fundamental wavelength was 532 nm and the angle of incidence 45° [44], [31].

2.1.6 Electric field induced second harmonic (EFISH)

In centrosymmetric materials, the inversion symmetry can be lift-off in presence of a supplementary dc electric field E_{dc} (internal or applied). This situation is common at interfaces between materials. For example, between SiO_2 and Si, interface traps and charges give rise to such a static electric field (E_{dc}). E_{dc} could be slowly varying as compared to optical frequencies and can thus be considered as quasi-static. This quasi-static term is superposed on the optical electric field term and the total field becomes:

$$\overrightarrow{E_{tot}} = \vec{E}(\omega) + \overrightarrow{E_{dc}} \qquad (2.22)$$

When this electric field is used in the power series expansion of eq. (2.2), the 2nd order nonlinear polarization contains an extra term originating from the bulk 3rd order nonlinear susceptibility [43], [48]–[50]:

$$\overrightarrow{P^{(2)}}(2\omega) = \chi^{(2)}\vec{E}(\omega)\vec{E}(\omega) + \chi^{(3)}\vec{E}(\omega)\vec{E}(\omega)\overrightarrow{E_{dc}} \qquad (2.23)$$

In this case, the SHG intensity is written as:

$$I_{2\omega} = \left|\chi^{(2)} + \chi^{(3)}E_{dc}\right|^2 I_{\omega}^2 \qquad (2.24)$$

This E_{dc} contribution to SHG is called EFISH (electric field induced second harmonic). EFISH is generally modest because of the small values of $\chi^{(3)}$ (~10^{-24} m^2V^{-2} [30]) compared to $\chi^{(2)}$ (~10^{-18} mV^{-1} [51]), unless the electric field is high (on the order of MV/cm). In the case of Si/SiO_2 stacks, the electric field can be high enough to reveal an EFISH contribution.

Moreover, the electric field E_{dc} can evolve in time, either by varying the applied external field or due to internal field variation: laser photo generated charges can be trapped or de-trapped at the interface and modify E_{dc}. In this case, EFISH and SHG are time-dependent:

$$I_{2\omega}(t) = \left|\chi^{(2)} + \chi^{(3)}\left[E_{dc}(0) + E_{dc}(t)\right]\right|^2 I_{\omega}^2 \qquad (2.25)$$

where $E_{dc}(0)$ is a time independent term describing the pre-existing static electric field at the interface and $E_{dc}(t)$ is a time-dependent term describing charging/discharging phenomena occurring during the measurement.

2.2 Application of SHG to SiO_2/Si structures

The simplest and most-studied interface in microelectronics is the one between SiO_2 and Si. Numerous SHG experiments have been performed in this system regarding various properties such as surface/interface roughness [52]–[54], strain [55]–[58], electronic transitions and resonances [50], [56], [59]–[62], etc... In this work, we will focus on quality control of Si/SiO_2 interfaces through EFISH by evaluating the number of fixed charges and interface traps. EFISH has been specifically used as a sensitive probe of interface electric fields in:

- Simple SiO_2/Si interfaces [24]–[31] for studying the trapping/detrapping dynamics of electrons and holes induced by laser irradiation.
- Cr/SiO_2/Si(111) [49], [63]–[65] and Cr/SiO_2/Si(100) [66] MOS capacitors for studying the buried SiO_2/Si interface by varying the externally applied bias on the MOS.
- Integrated silicon circuits for detecting electrical signals in CMOS devices [67].

In this section, we will present some of the experimental results in order to show the capabilities of the technique in a well-studied structure.

Most of the previous studies start by analysing the SHG versus time curves (see Figure 2.7 later). Before moving forward, let us explain the phenomena that can induce such time dependencies in SHG curves. The initial SHG, $I_{2\omega}(t=0)$, can be associated to the interface structural properties ($\chi^{(2)}$ term) and the pre-existing static electric field ($\chi^{(3)}E_{dc}(0)$ term) in eq. (2.25). Therefore, this first data point (t=0) probes $E_{dc}(0)$ and consequently the fixed charges and some charged interface traps present at the interface before any significant laser-induced charge-trapping occurs. As the laser continues irradiating the sample two main phenomena give rise to time-dependent EFISH, $\chi^{(3)}E_{dc}(t)$ in eq. (2.25):

i. The fundamental beam, for typically used visible/NIR wavelengths at approximately 500-900 nm (1.38 – 2.48 eV) is absorbed by Si (E_g=1.12 eV) and creates electron-hole pairs which can be separated by the pre-existing interfacial dc field E_{dc} (Figure 2.6a), potentially screening it.
ii. The electrons from the Si valence band can be injected into the oxide conduction band with multiphoton processes (by overcoming the 4.41-4.54 eV band offset between Si and SiO_2 [16], [68]). The variable band offset values depend on the oxide growth (wet or dry) and thickness

of the top ultrathin SiO_2 [68]. The electrons can be trapped at interface or bulk states in the oxide, as well as at the surface of the oxide by ambient oxygen molecules, if the oxide is thin enough (Figure 2.6a and Figure 2.6b). Moreover, the holes in the Si conduction band can be injected into the oxide by overcoming the 5.48-5.61 eV band offset by a higher order multiphoton absorption process. However, the probability is lower than the electron injection process since more energy is needed to overcome the barrier. Nevertheless, if the laser power is high enough, hole injection occurs as well [69].

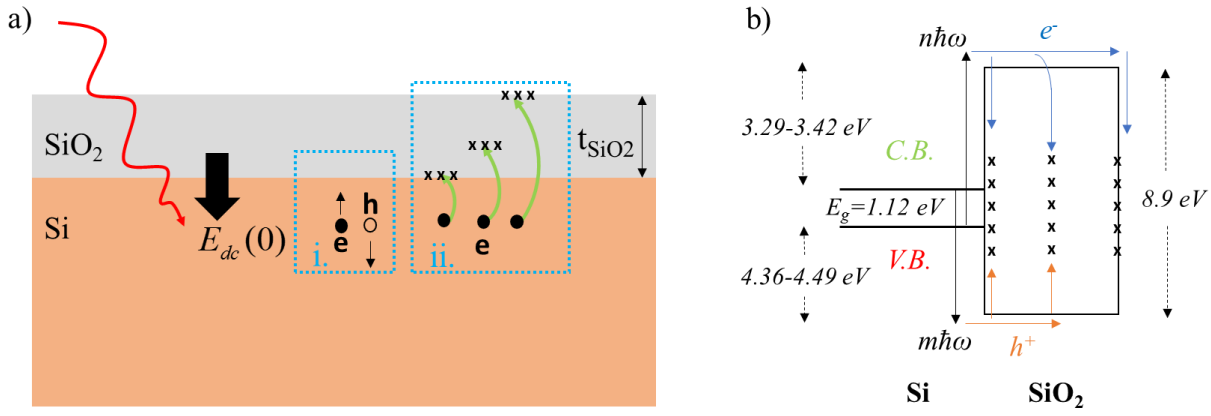

Figure 2.6: a) Electron-hole generation and subsequent separation due the pre-existing electric field (i) and electron injection into the oxide (ii). b) Energy band diagram of electron and hole injection from Si to various oxide trap states (interface, bulk and surface of the oxide).

Figure 2.7 shows a time-dependent second harmonic intensity (TD-SHG) curve obtained on native SiO_2/Si, using a pump laser operating at 770 nm (1.61 eV) with 10 kW/cm^2 average irradiance [70]. The photons do not have enough energy to interact with the oxide which has a 8.9 eV bandgap. However, they interact with Si which has a 1.12 eV bandgap resulting in absorption of the incident radiation (1.61 eV) and creation of electron-hole pairs. Furthermore, for high enough laser intensities as in this example (>kWcm^{-2} average irradiance), the electrons in the Si valence band can be excited to the oxide conduction band by a 3-photon process [71], [72], since the band offset is 4.41-4.54 eV (3 photons x 1.61 eV/photon=4.83 eV). Then they get trapped at different sites as shown in Figure 2.6b, altering the pre-existing static electric field $E_{dc}(0)$ at the interface.

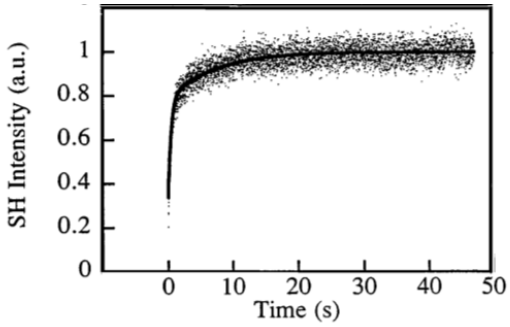

Figure 2.7: Time-dependent SHG from a native oxide covered Si (100) sample, irradiated with a 770 nm laser of 10 kWcm^{-2} average irradiance [70].

Before further analysis, we have to understand first the impact of various experimental parameters on the SHG signals. The SHG results will depend on:

1) The incident laser **wavelength**, which will cause multiphoton electron injection processes.
2) The incident laser **power:** higher power increases the probability of multiphoton processes.
3) The **thickness** of the SiO_2 layer: for thick oxides (>10 nm) the trapping mechanism at the surface is negligible [71].
4) The pre-existing interface electric field $\mathbf{E_{dc}(0)}$, which further depends on:
    a. Silicon substrate **doping** and doping-induced charge **traps**.
    b. **Externally applied bias** (for example in MOS structures).
    c. Eventual **fixed oxide charges**.

Next, we will address some of these parameters and their impact on the SHG characterization of the SiO_2/Si system.

2.2.1 Laser wavelength dependence of SHG

Marka et al. [73] quantified the number of photons needed for electron injection from the Si valence band to the SiO_2 conduction band. For this reason, they combined two lasers: an intense pump laser source with varying power (1-6 eV) to inject electrons at different photon energies; a lower intensity probe laser source at 800 nm and 45° angle of incidence for monitoring the time dependent SHG.

In the usual SHG expression, $I_{2\omega} = \left|\chi^{(2)} + \chi^{(3)} E_{dc}(t)\right|^2 I_\omega^2$, the quasi-static electric field could be proportional to the density of the charged electron traps at the surface, $E_{dc}(t) = \frac{e n_e(t)}{\varepsilon_{Si}}$ [74]. This trapped charged density can be described by a rate equation, which gives the rate at which electrons are getting trapped. The solution of the rate equation is a simple exponential:

$$n_e(t) = n_0\left[1 - \exp(-t / t^e_{pump})\right] \qquad (2.26)$$

where n_0 is the initial number of the unfilled traps, n_e is the number of filled traps and t^e_{pump} is the time constant for electron injection induced by the pump laser. Since the electric field is proportional to the density of trapped charges, the SHG can be fit by:

$$I_{2\omega}(t) \propto \left|y_0 + a\left[1 - \exp(-t / t^e_{pump})\right]\right|^2 \qquad (2.27)$$

where y_0 and α are phenomenological fitting constants.

By changing the pump laser power, the time-dependent SHG data will have different trapping rates [73], [74], since $1/t^e_{pump}$ is proportional to the probability of an n-photon interband transition [75]:

$$\frac{1}{t^{e}_{pump}} \propto \frac{K_n}{n\hbar\omega}\left(I_\omega\right)^n \qquad (2.28)$$

where K_n is the n-photon absorption coefficient.

By plotting $1/t^{e}_{pump}$ versus different incident pump intensities I_ω (laser power) in log-log scale, the number of photons participating in the injection process can be found by linear fitting (Figure 2.8a). The same procedure is done for various pump photon energies in order to find the number of photons participating in the injection process.

Figure 2.8b shows the order of the multiphoton excitation process versus the incident photon energy. At specific energies, jumps indicate the change in the number of photons required to inject an electron from the Si valence band to the oxide conduction band (their band offset is 4.5 eV). For energies 4.5 eV only one photon is needed to inject an electron; for lower energies between 2.25 eV and 4.5 eV two photons are needed; below 2.25 eV three photons are required.

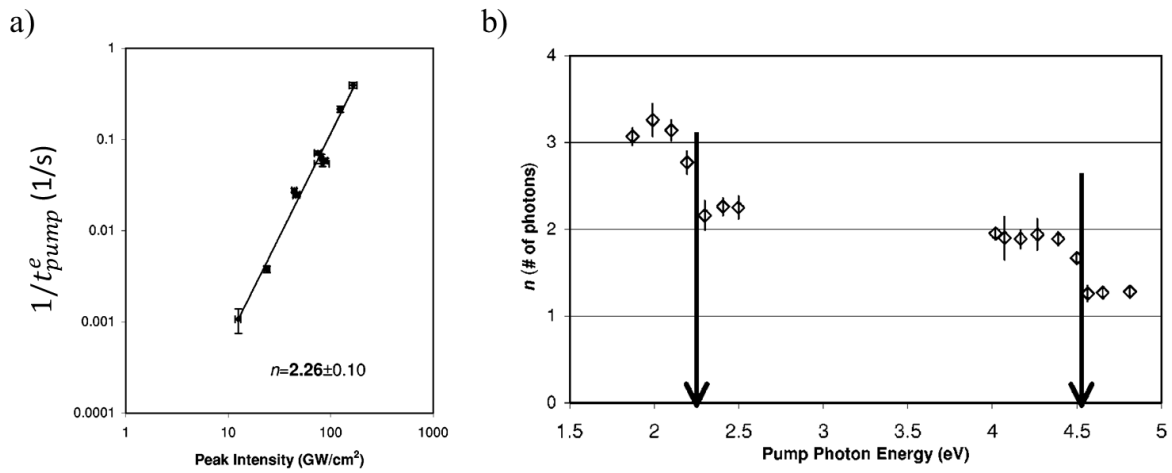

Figure 2.8: a) Electron injection rate ($1/t^{e}_{pump}$) versus the pump intensity for 512 nm radiation (2.43 eV). Two photons are needed for electron injection, as seen from the linear fit. b) Number of photons versus energy of the pump beam needed for injecting electrons from the Si valence band to the SiO_2 conduction band [73].

2.2.2 Laser power dependence of SHG

Another parameter that influences the SHG in SiO_2/Si systems is the laser power. For incident wavelengths greater than 550 nm, the rate of 3-photon induced charge injection depends on the 3rd power of the laser power [74]–[76]; the higher the laser power, the quicker the electron injection is. This is presented in Figure 2.9, where the time-dependent SHG is plotted for two different incident irradiances (laser irradiance is proportional to laser power): 3 $kWcm^{-2}$ (a) and 10 $kWcm^{-2}$ (b) [70]. By increasing the irradiance, the injection rate is increased and the charge traps fill up faster. This results

in a fast increase of the E_{dc} and consequently a faster rise time in SHG. After a certain time has passed, the charge injection saturates when the trap sites are filled, inducing a saturated SHG signal.

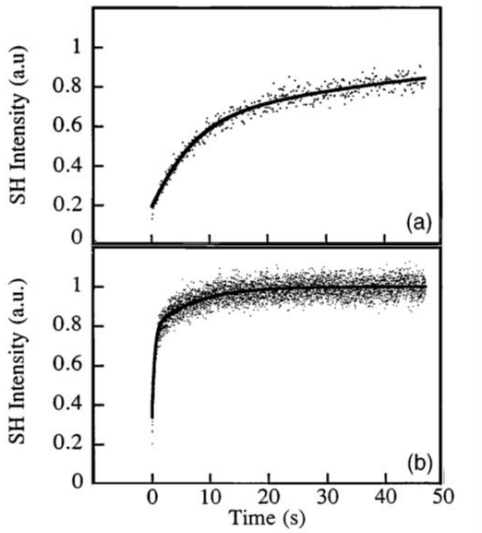

Figure 2.9: Time-dependent SHG from a native oxide (<5 nm) covered Si (100) sample, irradiated with a 770 nm laser having an irradiance of a) 3 kWcm^{-2} and b) 10 kWcm^{-2} [70].

2.2.3 SiO_2 thickness dependence of SHG

Bloch et al. [71] showed that the SHG signal from SiO_2/p-type Si (100) samples depends on the oxide thickness (Figure 2.10). In their experiment, they used a 800 nm laser with a 0.25 kWcm^{-2} irradiance, reporting that the ambient oxygen facilitates the trapping of photo-injected electrons at the surface of the oxide. The oxygen molecules have a high electron affinity, so they can trap the electrons at the oxide/ambient surface providing that its thickness is less than 10 nm [77]. The SHG results [71] showed that the saturation signal decreased with increasing oxide thickness, which was attributed to electron scattering as the electrons were travelling through the oxide. For thicknesses higher than 10 nm, the oxide is too thick for the electrons to get injected and trapped at the oxide/ambient surface.

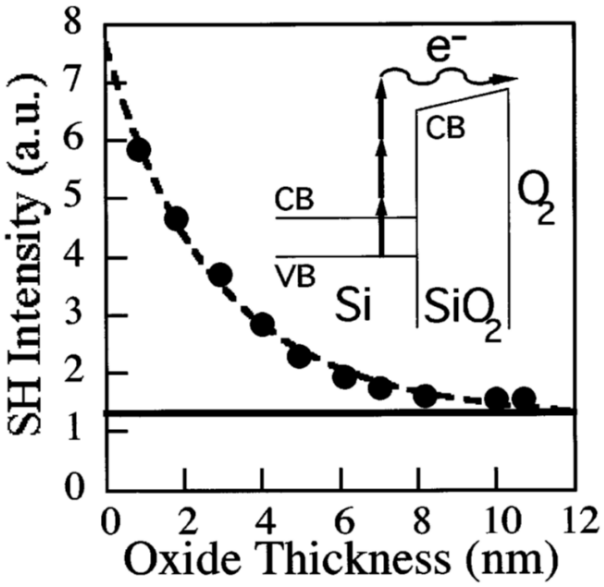

Figure 2.10: SHG intensity (at saturation level) versus oxide thickness on oxidized p-type Si (100) samples. The samples were illuminated with a 800 nm laser at a constant irradiance of 0.25 kWcm^{-2} [71].

2.2.4 Influence of Si-doping and boron-induced traps on SHG

The doping of Si plays a significant role in the space charge region (SCR) formation in the Si substrate, thus in the E_{dc} value, which can affect the SHG measurements. The electric field in the SCR is proportional to the substrate doping [16], [34]. Clearly, higher doping causes stronger E_{dc}, thus stronger initial SHG (at t=0).

Fiore et al. [78] investigated the effect of doping type and doping concentration on the SHG signals from Si(111)/SiO_2 samples illuminated by a 730 nm fs laser with 9.1 kWcm^{-2} average irradiance. Figure 2.11 shows the temporal evolution of SHG for: a) p-doped Si, highly doped with 9x10^{18} cm^{-3} density (circles) and lightly doped (triangles). b) n-doped Si, highly doped with 4x10^{19} cm^{-3} density (circles) and lightly doped (triangles).

In p-doped Si (Figure 2.11a), the initial SHG (first point) is higher in the heavily doped sample (circles) since a larger EFISH contribution is present, arising from positive charge accumulated at the interface. The TD-SHG signal initially drops and then slowly rises. The decrease is more prominent in the heavily doped p-Si (circles). The SHG decrease was attributed to the injection of photoexcited electrons that create an electric field opposite to the pre-existing one at the interface, until the two cancel each other out and SHG reaches a minimum. At that point, the total electric field is zero (E_{dc}=0) and the only SHG contribution is from the $\chi^{(2)}$ term. As the laser keeps illuminating, additional photoinjected electrons increase the total electric field, which is observed as a rise in SHG.

In n-doped Si (Figure 2.11b), the initial SHG (first point) is higher in the heavily doped sample (circles) since a larger EFISH contribution is present, arising from negative charge accumulated at the

interface. The monotonic time-dependent increase signifies that the photo-injected electrons create an electric field with the same direction as the pre-existing one. The relative change in TD-SHG magnitude during the first 200 s, becomes smaller as the dopant density increases (triangles→circles). For higher doping concentration, the difference between initial and saturation values is smaller. This is related probably to the increased charge density at the interface due to higher doping, creating a Coulomb barrier that reduces the electron photo-injection rate.

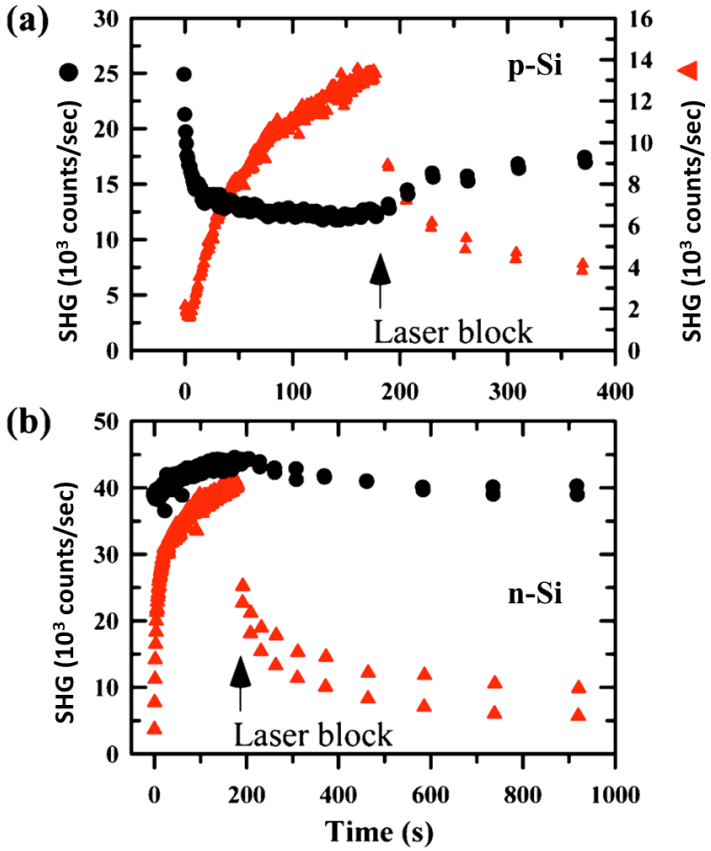

Figure 2.11: Time-dependent SHG from Si (111) samples covered with native SiO_2 at various doping levels and types: a) p-Si, $N_A=9x10^{18}$ cm^{-3} (circles, left axis) and p-Si, lightly doped (triangles, right axis). b) n-Si, $N_D=4x10^{19}$ cm^{-3} (circles) and n-Si, lightly doped (triangles) [78].

SHG has been used as a characterization tool of charge traps induced by boron doping in SiO_2/Si [79]–[82]. The samples had a 2 nm native oxide on top of the highly boron doped Si substrate (<0.01-0.02 Ωcm) and they were irradiated by a 800 nm fs laser with an average power of 400 mW. The SHG signal exhibits a sharp decrease followed by a minimum and later the signal starts increasing again (Figure 2.12a) [79]. The mechanisms explaining the change in time-dependent SHG are the following:

1) Before the laser starts irradiating the sample, there is a significant electric field at the SiO_2/Si interface, which can be attributed to the presence of B^- ions in the Si and B^+ ions in the SiO_2. Then, the initial SHG signal (at t=0) is $I_{2\omega}(0) = \left|\chi^{(2)} + \chi^{(3)} E_{dc}(0)\right|^2 I_\omega^2$ where $E_{dc}(0)$

is the initial static interface electric field. $E_{dc}(0)$ has a direction from the SiO_2 towards Si, as shown in Figure 2.12b (1) and originates from boron charge traps.

2) When the laser starts illuminating the sample, electrons are injected both in the B^+ traps and captured by the ambient oxygen at the surface of the oxide. The filling of B^+ traps causes the initial boron-trap induced field to drop; additionally, the electron injection at the surface creates an electric field opposite to the initial. This causes the net static electric field to drop which is manifested in the SHG signal as well.
3) As the laser keeps irradiating the sample, more B^+ traps get filled and the electric field due to electron injection at the surface keeps increasing, until the initial and the induced fields cancel each other out. A minimum is observed in the SHG.
4) Next, the SHG signal starts increasing as more electrons are injected in the B^+ traps and on the oxygen molecules at the surface.
5) The traps fill completely and the SHG signal saturates.

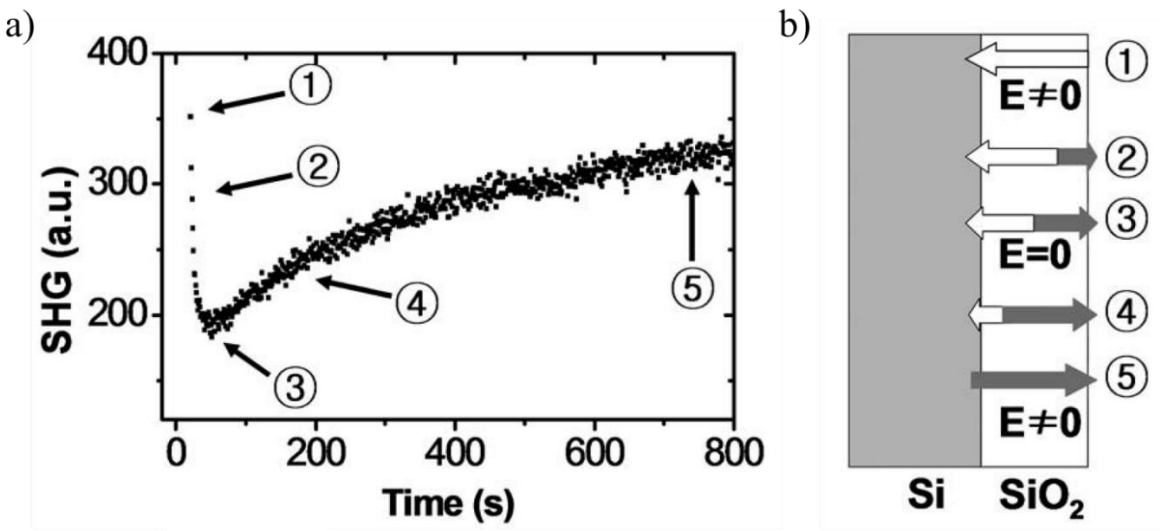

Figure 2.12: a) Time-dependent SHG in a p-doped Si substrate (0.01-0.02 Ωcm) with 2 nm native oxide. b) Schematic diagram with the initial and induced static electric fields at the interface [79].

Since the oxide is thin, the electrons that are trapped from the oxygen molecules are released easily. For this reason, when the laser beam is blocked, electrons trapped in the oxygen molecules and/or in the B^+ traps tunnel back to the empty states in the Si valence band, decreasing the interface dc field [69], [83]. Normally, the initial SHG from the same sample as before should be recovered after laser blocking, but this was not the case (Figure 2.13). When the beam was blocked for ~100s, no initial SHG decrease was observed, as before. Only a monotonic increase of SHG was present. The same occurred with blocking periods of more than 1h. Only for several hours of beam blocking, a slight (but not complete) recovery of the initial SHG was reported. This means that the boron traps did not release the electrons back to the Si, therefore the initial static electric field did not revert to its original value. For

this reason, it was speculated that the electron detrapping rate for boron charge traps is less than the electron detrapping rate for the surface oxygen traps.

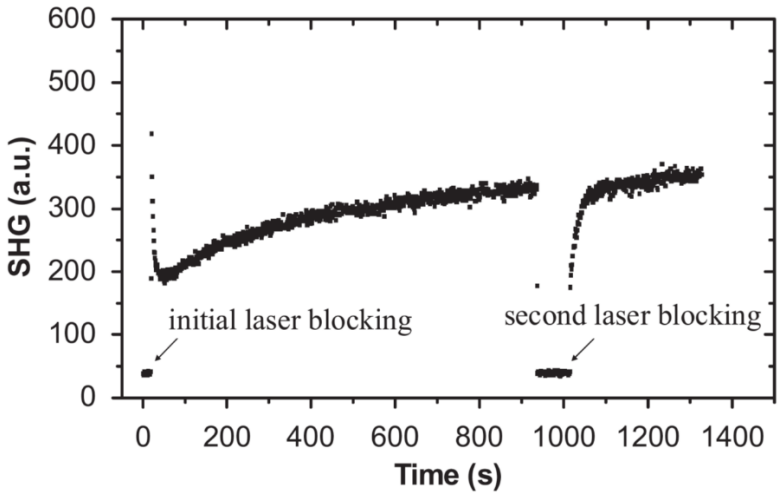

Figure 2.13: Time dependent SHG in a highly boron doped Si (0.01-0.02 Ωcm). After a long exposure (~900s), the laser beam is blocked for ~100s [79].

2.2.5 External bias effect on SHG from MOS structures

The electric field E_{dc} at the SiO_2/Si interface can also be modified by applying an external bias V, as in MOS capacitors. The SHG intensity can be written as a function of applied bias [64]:

$$I_{2\omega}(V) \propto \left| A + B(V - V_{FB}) e^{i\psi} \right|^2 \qquad (2.29)$$

with A and B being constants, while ψ is the phase difference between A and B, and V_{FB} is the flat band voltage. SHG experiments in Cr/SiO_2/Si MOS structures have been performed in order to study the impact of the interface electric field [49], [63]–[65], [66].

Aktsipetrov et al. [84] studied the mechanism of dc-electric field induced SHG at the buried Si/SiO_2 interface by applying a bias in a 3 nm Cr/234 nm SiO_2/Si (111) MOS structure. The Si substrate was p-type (boron doped) with a concentration of $5x10^{15}$ cm^{-3}. The dependence of the SHG intensity on the applied bias is shown (Figure 2.14). The minimum point in these curves corresponds to V_{FB}. A quadratic fit near the minimum is done based on eq. (2.29) and it describes well the observed behaviour. As expected, the applied bias alters the electric field in the space charge region of Si:

i. For $V<V_{FB}$, holes accumulate in the SCR as the applied bias acquires more negative values and $I_{2\omega}$ in eq. (2.29) increases.
ii. For $V=V_{FB}$, the bands are flat and the SHG response reaches a minimum, $I_{2\omega} \sim |A|^2$.
iii. For $V>V_{FB}$, electrons accumulate in the SCR as the applied bias acquires more positive values and $I_{2\omega}$ in eq. (2.29) increases.

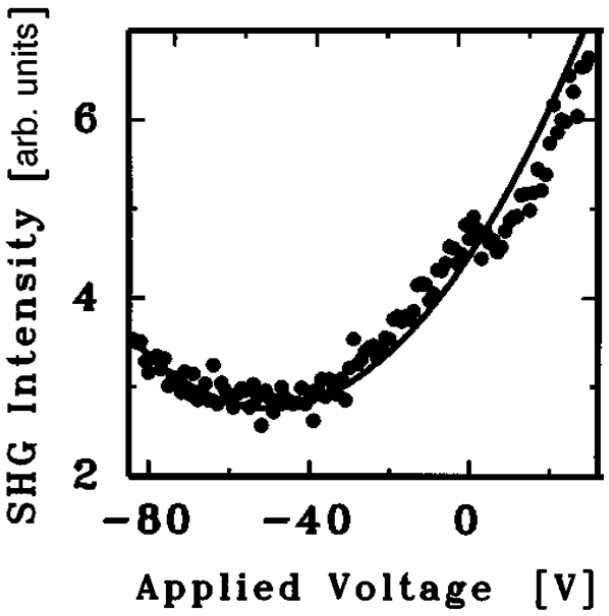

Figure 2.14: SHG intensity versus an applied voltage (V) from a 3 nm Cr/234 nm SiO_2/Si MOS sample. The solid line represents a model parabolic curve [84].

2.3 Conclusions

The interest of SHG for centrosymmetric materials characterization comes from its dependence on the interface electric field, $I_{2\omega}(t) = \left|\chi^{(2)} + \chi^{(3)}\left[E_{dc}(0) + E_{dc}(t)\right]\right|^2 I_{\omega}^2$. The constant term $E_{dc}(0)$ gives information regarding the fixed charges in the oxide (Q_{ox}) and the initially trapped charges. The time-dependent term $E_{dc}(t)$ reveals the charging/trapping mechanisms. In SiO_2/Si interfaces, the mechanisms giving rise to $E_{dc}(t)$ are:

- Separation of charges (photo-induced electron hole pairs) due to $E_{dc}(0)$.
- Injection of electrons and/or holes from the Si bands into/onto SiO_2, through multiphoton processes.

Depending on the experimental SHG parameters we can decrease the probability of a specific mechanism with respect to the others. Typical electric field induced SHG results showed that:

- The number of photons required for multiphoton injection depends on the laser wavelength. Typically, for wavelengths in the optical/NIR region 3 photons are needed.
- The multiphoton injection rate increases for higher incident laser power.
- The multiphoton injection rate decreases for increasing oxide thicknesses. The SHG time-dependence disappears for t_{SiO2}>10 nm and charges cannot be trapped on the SiO_2 surface.
- SHG is influenced by any parameter that affects E_{dc}: doping type and density, externally applied bias, etc…

However, since SHG is an optical technique, I_{ω} and $I_{2\omega}$ (in the usual expression) exhibit optical propagation phenomena in thin film systems (absorption, multiple reflections, interferences). If we want to extract information about E_{dc} only (therefore Q_{ox} and D_{it}), we need to properly account for these optical effects. The next chapter will introduce the modelling of the optical phenomena.

Chapter 3:
SHG Optical Modelling

In this chapter we present the SHG optical simulation. First, we describe linear optical phenomena (propagation of radiation inside a layer, boundary conditions for transmission at an interface between two media). The simulation performed at the incident wavelength allows the calculation of the electromagnetic fields at the fundamental frequency at every point in the structure. Based on the fundamental fields, the nonlinear polarization generated at each interface is explicitly written for the most common experimental input/output polarization combinations. Additionally, the static electric field (E_{dc}) is incorporated in the nonlinear polarization expression. The second harmonic fields are calculated at each interface using specific boundary conditions (with source terms). Finally, the simulator is validated by comparison with experimental data in SiO_2/Si structures.

Contents of Chapter 3

3.1 Introduction

When analysing data from SHG experiments in systems that are comprised of multiple stacked layers, it is important to consider the propagation of radiation throughout them. The fundamental and SH electric fields are both affected by linear optical phenomena such as absorption, refraction, and interference due to multiple reflections. In order to underline the interest of the simulation, Figure 3.1 shows experimental time-dependent SHG results on Silicon on Insulator (SOI) with different geometries. The three samples give very different SHG signatures but are these variations only related to charging/discharging dynamics at the interface, or does the geometry of each SOI structure play a role as well? In order to answer the question, we developed a home-made program to simulate the geometry related optical phenomena. Then, we added a time-independent static electric field related to charged interface states (D_{it}) and trapped charge (Q_{ox}), before any significant laser-induced charge trapping occurs. The static electric field in the simulation does not include charging/discharging phenomena. The objective is to determine the theoretical output field at the second harmonic frequency (2ω) from a multilayer structure, in order to compare it with the first point in time-dependent SHG experimental data.

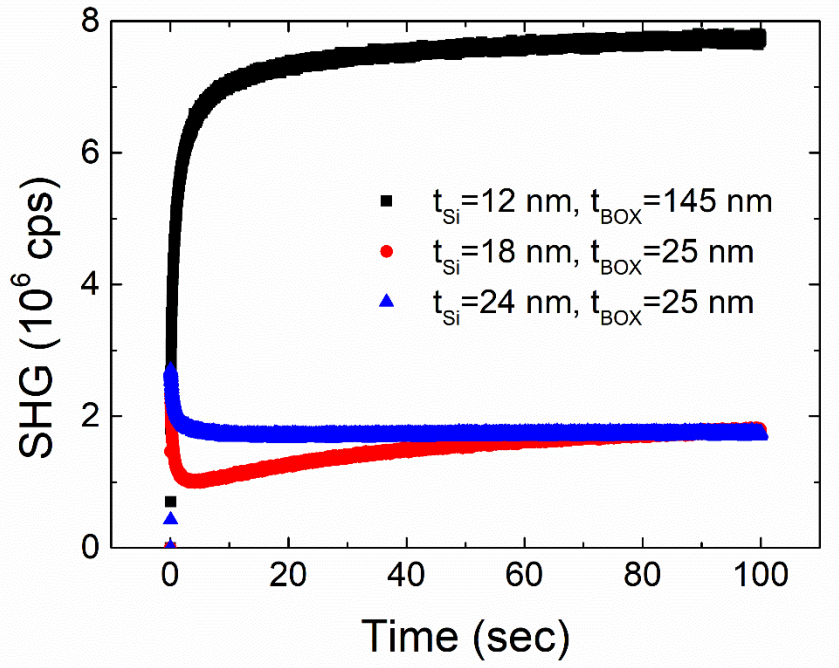

Figure 3.1: SHG versus time measured on SOI samples with different geometries.

Generally, as previously seen, SHG is written as:

$$I_{2\omega} \propto \left|\chi^{(2)} + \chi^{(3)} E_{dc}\right|^2 \left(I_{\omega}\right)^2 \qquad (3.1)$$

When light travels through a multilayer structure, it can be absorbed and partially reflected/transmitted at the different interfaces inside the structure. This is true for both the incident light of intensity I_{ω} and

for the generated second harmonic light of intensity $I_{2\omega}$ (see Figure 3.2). Thus, the modelled phenomena are:

- propagation through a layer.
- transmission and reflection at an interface, without source terms in order to describe the incident light at frequency ω (I_ω).
- transmission and reflection at an interface, with source terms in order to describe the second harmonic generation at frequency 2ω ($I_{2\omega}$).

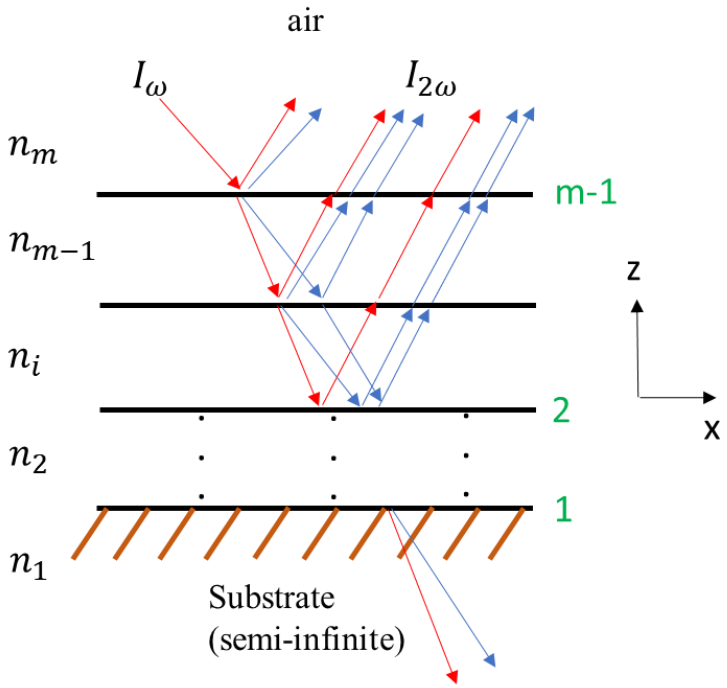

Figure 3.2: Multilayer structure, comprising m layers (with refractive indices n_m) and m-1 interfaces. The incident fundamental I_ω (in red) propagates throughout the structure and generates at each interface the SH radiation $I_{2\omega}$ (in blue), which also propagates. Both beams are refracted at interfaces, absorbed in layers and exhibit interferences.

For a better visual understanding of the simulation, the program flow as well as the optical phenomena inside the structure are described by blocks in Figure 3.3. An overview of the program flow is given in Figure 3.3a:

1. Initially, we set all of the simulation parameters (incident wavelength, refractive indices, angle of incidence, input/output polarization, etc…).
2. The program runs the main function (Figure 3.3b) for the fundamental field. The main function calculates the output electric field (E_ω at every point across the structure) and works as follows:
    i. The value of the electric field at the bottom of the structure (substrate) is used as input. This is done in order to have a simulation tool which works for any number of layers: a numerical procedure of calculating the bottom input field from the actual incident field E_ω is given later.

ii. the field is propagated up to the first interface.

iii. the boundary conditions are imposed at the interface and the transmitted electric field in the new medium is calculated.

iv. This is repeated for all layers until the electric field at the top layer (air) is acquired.

3. A physical boundary condition is imposed: no reflected light from the bottom of the substrate (physically the radiation propagates in the thick substrate and is absorbed, therefore it does not reach the bottom). The electric field at the fundamental frequency is then computed in the whole structure with a numerical procedure that is explained later (section 3.4).
4. The electric field spatial distribution obtained from this previous step is used for the calculation of the nonlinear polarization at each interface.
5. The main function runs again, as in step b, but for the second harmonic field (the nonlinear polarization has now to be included in the boundary conditions).
6. The physical boundary condition is imposed, considering that there is no incident light at 2ω. The SH field is calculated with a numerical procedure.
7. The results are plotted.

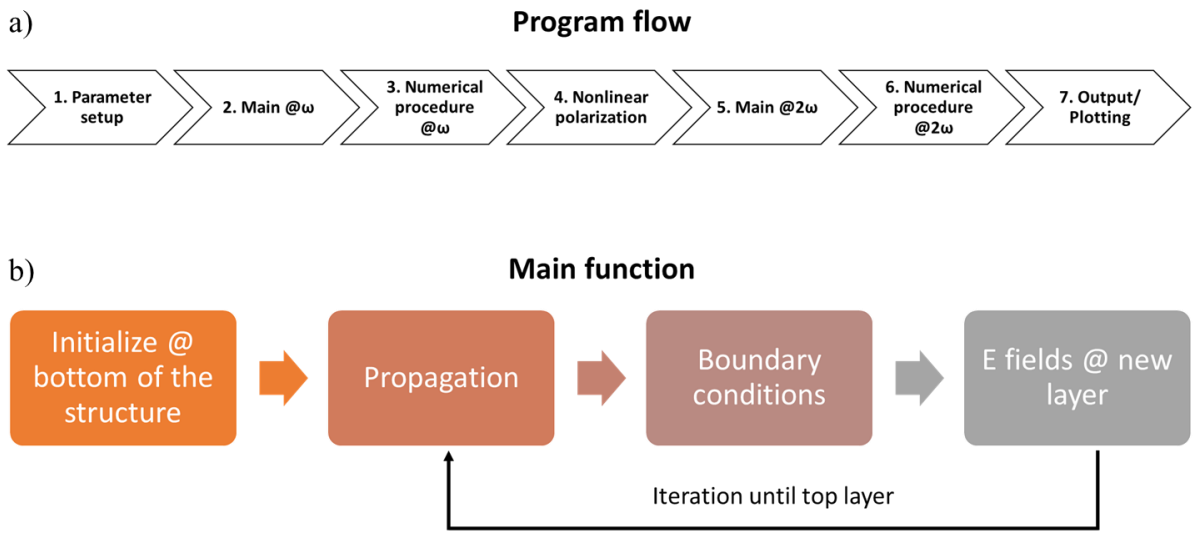

Figure 3.3: Block description of the simulation: a) the program flow and b) the main function are shown.

3.2 Linear optical phenomena

In this part, we present how propagation inside each layer and transmission/reflection at the interface are included in the simulation in the main function (Figure 3.3).

3.2.1 Propagation inside a layer

In the most general case, when light is incident at an arbitrary angle at the interface between two media, it will get refracted as it enters the new medium (Figure 3.4). Snell's law [85] describes the relation between the refractive indices of the two media (n_i and n_{i+1}) and the angles of incidence (θ_i) and refraction (θ_{i+1}):

$$n_i \sin\theta_i = n_{i+1} \sin\theta_{i+1} = \cdots = n_{air}\theta_{air} \tag{3.2}$$

where θ_{air} is the incident angle for light coming from the air (top layer) and $n_{air}=1$. Note that θ_{air} is the angle of incidence set experimentally.

For the particular case of light being incident from the air ($n_{air}=1$), the angle of refraction in medium i is:

$$\sin\theta_i = \frac{\sin\theta_{air}}{n_i} \tag{3.3}$$

For absorbing media, the refractive index is complex and its imaginary part describes the absorption. Therefore, the angles will be complex numbers as well.

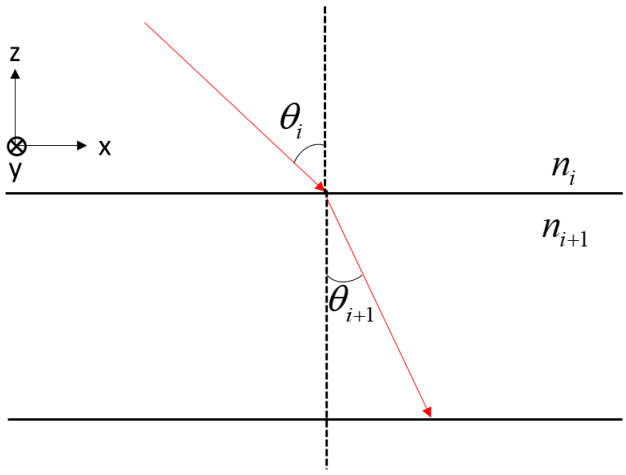

Figure 3.4: Incident light at an interface between two adjacent media. The angles of incidence and refraction, as well as the refractive indices of each layer are shown.

Let us consider that the field E_i is known when it enters a layer ($E_{initial}$). From this starting point, we calculate its value at each position inside the layer, as it propagates towards the next layer (Figure 3.5a) as:

$$E_i(z) = E_i^{initial} \exp(\pm i k_{z,i} z) \tag{3.4}$$

where $k_{z,i}$ is the vertical projection of the wavevector of the radiation and z is the position inside the layer i. The exponential term describes the propagation in the positive (+) or negative (-) z-direction.

Note that all fields are assumed to have the $e^{-i\omega t}$ time dependence. For example, if a field enters from the bottom of a layer, which has a thickness d_i, at the top of the layer the value of the electric field will be:

$$E_i^{final} = E_i^{initial} \exp(+ik_{z,i}d_i) \tag{3.5}$$

Figure 3.5b shows the wavevector in the i-th layer k_i, with its vertical $k_{z,i}$, and parallel $k_{x,i}$ components. Using Snell's law (eq. (3.2)), the k_x values in every layer can be written as:

$$k_{x,i} = k_i \sin\theta_i = k_0 n_i \sin\theta_i = k_0 n_{air} \sin\theta_{air} \Rightarrow k_{x,i} = k_0 \sin\theta_{air} \tag{3.6}$$

where $k_0 = 2\pi/\lambda$ is the wavevector of the radiation in vacuum (n_{air}=1). For the vertical component k_z in each layer we get:

$$k_{z,i} = \sqrt{k_i^2 - k_{x,i}^2} = \sqrt{n_i^2 k_0^2 - k_0^2 \sin^2\theta_{air}} \Rightarrow k_{z,i} = k_0 \sqrt{n_i^2 - \sin^2\theta_{air}} \tag{3.7}$$

where n_i is the complex refractive index of the i-th layer. Therefore, the wavevector is a complex number: its real part describes the propagation of radiation, while its imaginary part describes the absorption inside a layer [85].

If k_0 is adapted, formula (3.7) applies for both fundamental, $k_{0,\omega} = 2\pi/\lambda_\omega$, and second harmonic beams, $k_{0,2\omega} = 2\cdot(2\pi/\lambda_\omega)$.

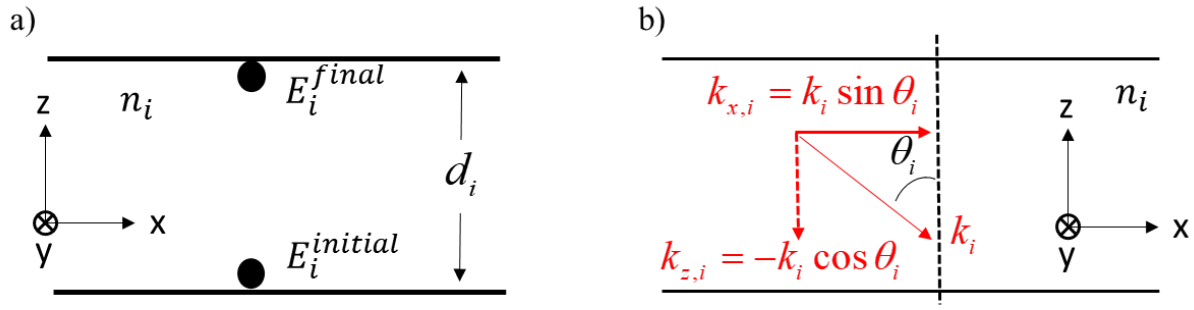

Figure 3.5: a) Initial and final field amplitudes inside an arbitrary layer with refractive index n_i. b) Real part of wavevector in medium "i", describing the propagation of the radiation, and its projections on each of the x- and z- axis. Only the real part of the wavevector is shown for understanding the propagation effects. The minus sign denotes that the direction of propagation in the z-direction is downward.

3.2.2 Fundamental radiation transmission at an interface

In the most general case, the electric fields are **incident** from both sides onto a planar interface separating two media with refractive indices n_i and n_{i+1} (Figure 3.6). Both cases of parallel and perpendicular polarizations are shown [86]:

a. P-polarization or transverse magnetic (TM) mode, where the electric fields lie in the incidence plane and the magnetic fields are perpendicular to it (along the y-direction),
b. S-polarization or transverse electric (TE) mode, where the magnetic fields are parallel to the incidence plane and the electric fields are perpendicular to it.

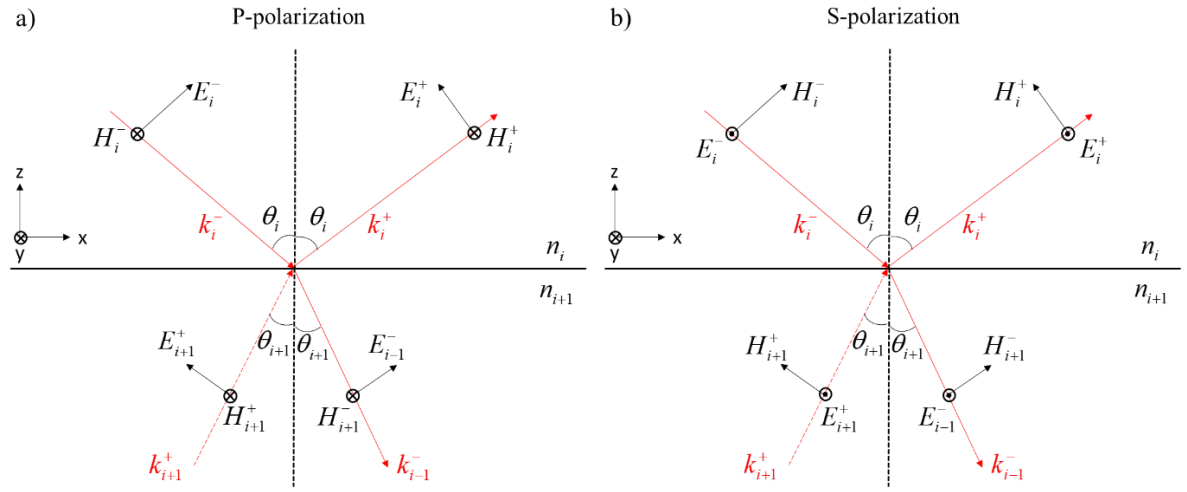

*Figure 3.6: Electric and magnetic fields **incident** from both sides at an interface between two media for: a) P-polarization (TM mode) and b) S-polarization (TE mode). In P-polarization the magnetic fields are directed towards the page, while in S-polarization the electric fields are directed outside of the page (towards the reader).*

The electromagnetic fields should be continuous across the interface and should obey the boundary conditions of Maxwell's equations in the absence of surface charges and currents [85], [87]. This means that the electric "normal" components of the displacement (D) and of the magnetic induction (B) to the interface, as well as "parallel" components of the electric field (E) and magnetic field (H), must be continuous across the interface:

$$\begin{aligned} &1) D_i^{\perp} = D_{i+1}^{\perp} \\ &2) B_i^{\perp} = B_{i+1}^{\perp} \\ &3) E_i^{//} = E_{i+1}^{//} \\ &4) H_i^{//} = H_{i+1}^{//} \end{aligned} \qquad (3.8)$$

and in the case of non-magnetic materials they become:

$$\begin{aligned} &1) \varepsilon_i E_i^{\perp} = \varepsilon_{i+1} E_{i+1}^{\perp} \\ &2) B_i^{\perp} = B_{i+1}^{\perp} \\ &3) E_i^{//} = E_{i+1}^{//} \\ &4) B_i^{//} = B_{i+1}^{//} \end{aligned} \qquad (3.9)$$

By using the expressions for the electromagnetic fields in the Appendix and by taking the 1st and 3rd boundary conditions for the normal ($E^{\perp}$) and tangential ($E^{//}$) electric fields in the case of P-

polarization, and the 2nd and 4th boundary conditions for the normal ($B^{\perp}$) and tangential ($B^{//}$) magnetic fields in the case of S-polarization, we find:

a) For P-polarization:

$$\begin{aligned} n_i\left(E_i^- + E_i^+\right) &= n_{i+1}\left(E_{i+1}^- + E_{i+1}^+\right) \\ \cos\theta_i\left(E_i^- - E_i^+\right) &= \cos\theta_{i+1}\left(E_{i+1}^- - E_{i+1}^+\right) \end{aligned} \tag{3.10}$$

b) For S-polarization:

$$\begin{aligned} E_i^+ + E_i^- &= E_{i+1}^+ + E_{i+1}^- \\ n_i\cos\theta_i\left(E_i^+ - E_i^-\right) &= n_{i+1}\cos\theta_{i+1}\left(E_{i+1}^+ - E_{i+1}^-\right) \end{aligned} \tag{3.11}$$

If the fields at the interface E_i^+ and E_i^- inside medium i are known, it is possible to calculate the fields in the other medium $i+1$ through the above relations, by simply solving the system of 2 equations with two unknowns (E_{i+1}^+ and E_{i+1}^-) for each polarization case. After calculating the fields at the new medium, we use the new wavevectors (calculated for medium $i+1$) in order to compute the fields at the end of the same layer, right before the next interface. Then the new boundary conditions are taken into account, with the known fields being E_{i+1}^+ and E_{i+1}^-, while the unknown fields are E_{i+2}^+ and E_{i+2}^-. This process is repeated until the electric fields are calculated at the final layer. With this numerical method, there is no need to search for analytical solutions and expressions for boundary conditions at each interface, which is cumbersome for arbitrarily big structures with many layers. Through this method, the electric and magnetic field values throughout the whole structure are accessed, which will be useful for the computation of the nonlinear polarization in the next section.

3.3 Nonlinear optical phenomena: Second harmonic generation at the interface

Second harmonic generation occurs when light at a fundamental frequency ω incident on a material, induces a 2nd order nonlinear polarization at the double frequency 2ω:

$$P(2\omega) = \chi^{(2)}\left|E(\omega)\right|^2 \tag{3.12}$$

with E(ω) being the incident electric field. In our case, the $\chi^{(2)}$ term exists only at the interface between the adjacent centrosymmetric materials, and in order to compute the nonlinear polarization at that interface we need to know the value of the electric field as well as the $\chi^{(2)}$ susceptibility tensor components. Initially, we will detail the new boundary conditions including an extra term due to the nonlinear polarization source and later we will give the full expression of the nonlinear polarization including all dependencies on geometrical parameters for each output polarization.

3.3.1 Boundary conditions with source terms

A similar analysis that was used for the fundamental fields regarding transmission at the interface will be employed here as well. In this case however, the wavevector component in eq. (3.7) changes, since we have to take into account the refractive indices at the SH frequency. Furthermore, the boundary conditions at the interface in presence of a nonlinear polarization become [41], [88]:

a) For P-polarization:

$$\begin{aligned} n_i^{2\omega}\left(E_i^{2\omega,+}+E_i^{2\omega,-}\right)+n_i^{\omega}\frac{P_i^{NL}}{\left(n_i^{\omega}\right)^2-\left(n_i^{2\omega}\right)^2}&=n_{i+1}^{2\omega}\left(E_{i+1}^{2\omega,+}+E_{i+1}^{2\omega,-}\right)\\ \cos\theta_i^{2\omega}\left(E_i^{2\omega,+}-E_i^{2\omega,-}\right)+\frac{P_i^{NL}\cos\theta_i^{\omega}}{\left(n_i^{\omega}\right)^2-\left(n_i^{2\omega}\right)^2}-\frac{P_i^{NL}\sin\theta_i^{\omega}}{\left(n_i^{2\omega}\right)^2}&=\cos\theta_{i+1}^{2\omega}\left(E_{i+1}^{2\omega,+}-E_{i+1}^{2\omega,-}\right)\end{aligned} \tag{3.13}$$

b) For S-polarization:

$$\begin{aligned} E_i^{2\omega,+}+E_i^{2\omega,-}+\frac{P_i^{NL}}{n_{\omega}^2-n_{2\omega}^2}&=E_{i+1}^{2\omega,+}+E_{i+1}^{2\omega,-}\\ n_i^{2\omega}\cos\theta_i^{2\omega}\left(E_i^{2\omega,+}-E_i^{2\omega,-}\right)+n_i^{\omega}\cos\theta_i^{\omega}\frac{P_i^{NL}}{\left(n_i^{\omega}\right)^2-\left(n_i^{2\omega}\right)^2}&=n_{i+1}^{2\omega}\cos\theta_{i+1}^{2\omega}\left(E_{i+1}^{2\omega,+}-E_{i+1}^{2\omega,-}\right)\end{aligned} \tag{3.14}$$

Based on them, we can calculate the SH electric fields in the new medium. Note that the $E_i^+, E_i^-, E_{i+1}^+, E_{i+1}^-$ amplitudes in the above relations refer to the fields at the SH frequency, and the nonlinear polarization term P_i^{NL} is calculated using the fundamental fields computed in the previous step. If there is a perfect matching of the values of n_{ω} and $n_{2\omega}$, a Brewster angle appears and the above expressions change [88] in order to have finite limits. However, in our experiments the denominator cannot be zero since the refractive indices for Si at frequencies ω and 2ω are complex (we give their values in section 3.4).

3.3.2 Polarization terms

The nonlinear polarization term P_i^{NL} is different depending on the polarization of the incident and outgoing light. P_i^{NL} has two forms, depending on which polarization we detect the SH light [89],[42]:

i. For P-output polarization:

$$\begin{aligned} P_{P-out}^{NL}=&\left\{\chi_{zxx}^{(2)}F_s\sin^2\psi+(\chi_{zxx}^{(2)}F_s f_c^2-\chi_{xzx}^{(2)}2F_c f_s f_c+\chi_{zzz}^{(2)}F_s f_s^2)\cos^2\psi+\right.\\ &+\gamma F_s-\frac{i}{4}\lambda_{\omega}n_{\omega}\zeta\left[F_c f_s\sin^2\psi+(3F_c f_c^2 f_s+4F_s f_s^2 f_c)\cos^2\psi+\right.\\ &\left.\left.+2F_c f_s f_c\cos\psi\sin\psi\sin 4\varphi+F_c f_s(f_c\cos^2\psi-\sin^2\psi)\cos 4\varphi\right]\right\}E_{\omega}^2\end{aligned} \tag{3.15}$$

ii. For S-output polarization:

$$P_{S-out}^{NL} = \left\{ \chi_{xzx}^{(2)} 2 f_s \cos\psi \sin\psi - \frac{i}{4} \lambda_\omega n_\omega \zeta \left[-2 f_s f_c \cos\psi \sin\psi + \right. \right. \\ \left. \left. + f_s (\sin^2\psi - f_c^2 \cos^2\psi) \sin 4\varphi + 2 f_s f_c \cos\psi \sin\psi \cos 4\varphi \right] \right\} E_\omega^2 \quad (3.16)$$

where ψ is the polarization angle of the incident light (fundamental); φ is the azimuthal angle of rotation around the normal axis of the structure (Figure 3.7), typically measured from a reference direction on the Si wafer (the wafer notch, indicating the [001] direction); E_ω is the electric field at the interface which is computed in the previous step; $\chi_{ijk}^{(2)}$ are the elements of the interface dipole susceptibility tensor and γ, ζ are bulk quadrupole components [42]; f_s, f_c, F_s, F_c are Fresnel coefficients for the fundamental and the SH waves (defined already in Chapter 2):

$$fundamental: f_s = \frac{\sin\theta}{n_\omega}, f_c = \frac{\cos\theta}{n_\omega} \\ SH: F_s = \frac{\sin\theta}{n_{2\omega}}, F_c = \frac{\cos\theta}{n_{2\omega}} \quad (3.17)$$

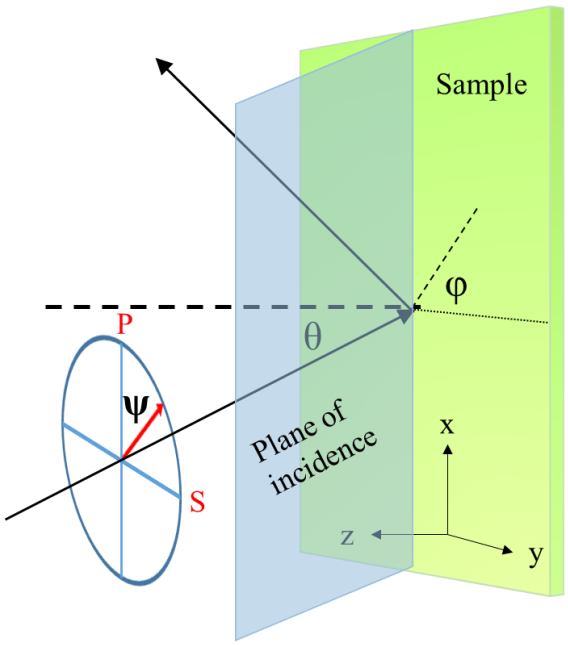

Figure 3.7: Typical angles (polarization, incidence, azimuthal) showing up in the nonlinear polarization expression. The plane of incidence is also shown.

In a typical experiment, the incident light is either P- or S- polarized. Therefore, we usually have four main polarization configurations, namely P-input/P-output, S-input/P-output, P-input/S-output and S-input/S-output. In the expressions (3.15)-(3.16), we use ψ=0° (cosψ=1, sinψ=0) for P-input and ψ=90° (cosψ=0, sinψ=1) for S-input polarization and we find:

a) for P-input/P-output:

$$P_{P-in/P-out}^{NL} = \left[\chi_{zxx}^{(2)} F_s f_c^2 - \chi_{xzx}^{(2)} 2F_c f_s f_c + \chi_{zzz}^{(2)} F_s f_s^2 + \gamma F_s - \right. \\ \left. - \frac{i}{4} \lambda_\omega n_\omega \zeta (3F_c f_c^2 f_s + 4F_s f_s^2 f_c + F_c f_s f_c \cos 4\varphi) \right] E_\omega^2 \quad (3.18)$$

b) for S-input/P-output

$$P_{S-in/P-out}^{NL} = \left[\left(\chi_{zxx}^{(2)} + \gamma \right) F_s - \frac{i}{4} \lambda_\omega n_\omega \zeta F_c f_s (1 - \cos 4\varphi) \right] E_\omega^2 \quad (3.19)$$

c) for P-input/S-output:

$$P_{P-in/S-out}^{NL} = \frac{i}{4} \lambda_\omega n_\omega \zeta f_s f_c^2 \sin 4\varphi E_\omega^2 \quad (3.20)$$

d) for S-input/S-output:

$$P_{S-in/S-out}^{NL} = -\frac{i}{4} \lambda_\omega n_\omega \zeta f_s \sin 4\varphi E_\omega^2 \quad (3.21)$$

3.3.3 DC Electric field inclusion

The expressions (3.18)-(3.21) are available in absence of static electric fields that are typically present at interfaces between dielectrics and silicon. How are they modified when E_{dc} is accounted for? In order to include it in the polarization expressions, E_{dc} is added to the $\chi_{zzz}^{(2)}$ component only, since it is the prominent interface susceptibility term which creates a 2nd order polarization in the vertical z-direction. The $\chi_{zzz}^{(2)}$ component is only present in the case of P-output polarization (eq. (3.15)), so the new expression becomes:

$$P_i^{NL} = \left\{ \chi_{zxx}^{(2)} F_s \sin^2\psi + \left[\chi_{zxx}^{(2)} F_s f_c^2 - \chi_{xzx}^{(2)} 2F_c f_s f_c + \left(\chi_{zzz}^{(2)} + \chi^{(3)} E_{dc} \right) F_s f_s^2 \right] \cos^2\psi \right. \\ + \gamma F_s - \frac{i}{4} \lambda_\omega n_\omega \zeta \left[F_c f_s \sin^2\psi + (3F_c f_c^2 f_s + 4F_s f_s^2 f_c) \cos^2\psi \right. \\ \left. \left. + 2F_c f_s f_c \cos\psi \sin\psi \sin 4\varphi + F_c f_s (f_c \cos^2\psi - \sin^2\psi) \cos 4\varphi \right] \right\} E_\omega^2 \quad (3.22)$$

The 3rd order susceptibility $\chi^{(3)}$ is typically very low, so the question is how important the E_{dc} contribution is. For example a SiO_2/Si interface has a $\chi^{(2)}$ in the order of 10^{-18} m^2/V [51] while $\chi^{(3)}$ (in the order of 10^{-24} m^3/V^2 [30]) when multiplied by E_{dc} (in the order of 10^4-10^5 V/cm), it has the same order of magnitude with $\chi^{(2)}$ and its contribution becomes significant. However, care must be taken each time when including the E_{dc} values since their sign and values can also cancel out the $\chi_{zzz}^{(2)}$ term in eq.(3.22).

3.4 Numerical procedure for the initial field calculation

In the simulation, we start numbering the layers (thus the electric fields) from the bottom, since it is easier to set as many layers as desired (Figure 3.2). However, in the experiment the incident field is known at the top layer. Therefore, a numerical procedure is needed in order to find the correct input electric field at the bottom layer from the actual incident field amplitude. For this reason, we treat the whole multilayer structure under study as a "black box" (Figure 3.8a), for which we want to know only the fields in the first layer (air) and in the bottom layer (substrate). This "black box" includes all of the propagation phenomena and the boundary conditions described previously. The analytical problem in the most general case can be described by the matrix formalism [90]:

$$\begin{pmatrix} E_m^+ \\ E_m^- \end{pmatrix} = \begin{pmatrix} A & B \\ C & D \end{pmatrix} \begin{pmatrix} E_1^+ \\ E_1^- \end{pmatrix} \tag{3.23}$$

where, the matrix ABCD describes the transmission and reflection of waves at each interface (including the boundary conditions) as well as the propagation inside each layer. The physical boundary condition of no incident light from the bottom of the structure is imposed (Figure 3.8b), since the substrate is treated as semi-infinite, and there will be only a transmitted wave.

$$\begin{pmatrix} E_m^+ \\ E_m^- \end{pmatrix} = \begin{pmatrix} A & B \\ C & D \end{pmatrix} \begin{pmatrix} 0 \\ E_1^- \end{pmatrix} \Rightarrow \begin{matrix} E_m^+ = BE_1^- \\ E_m^- = DE_1^- \end{matrix} \tag{3.24}$$

Figure 3.9 presents schematically the numerical treatment procedure for the calculation of the realistic input E_1^- field (one-step solving matricial approach). Initially, the main function runs for an arbitrary E_1^- and determines E_m^- and E_m^+; the parameters B, D are then calculated. Since these quantities are now known, we enter the right value to E_m^- (the incident field on the structure) and the appropriate E_1^- is determined. This is used as the new initial field for the simulation; the main function runs again, correct values of the fundamental electric field throughout the structure are obtained and are used for the SH computation.

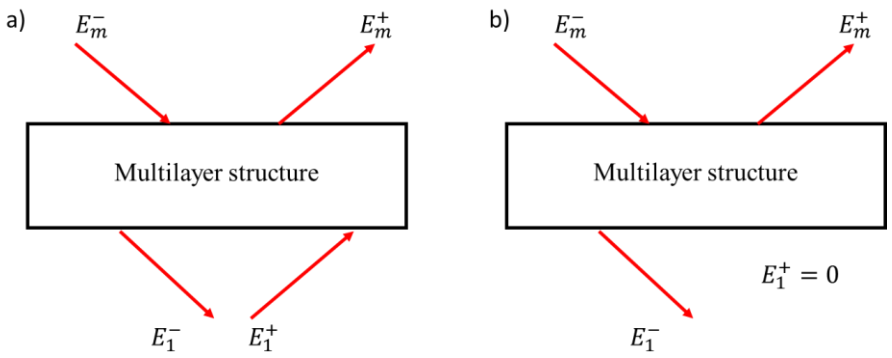

Figure 3.8: a) Incident and outgoing fundamental fields in a multilayer structure considered as a "black box". b) Boundary condition: no upward travelling light from the bottom (no reflection from the bottom of the thick substrate).

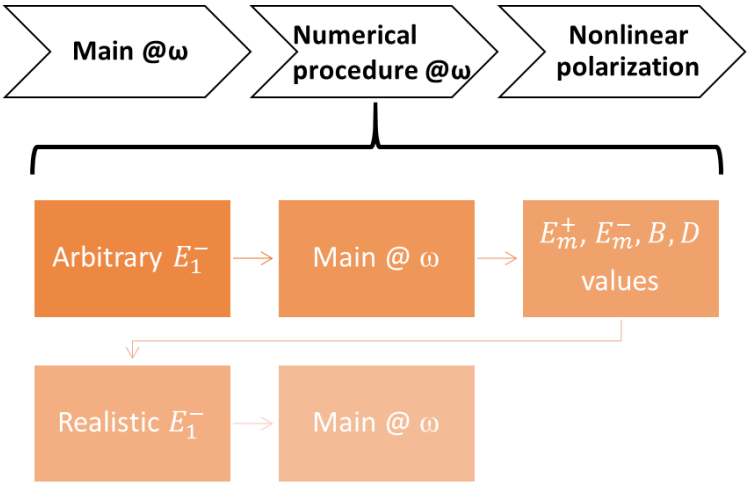

Figure 3.9: Schematic of the numerical procedure for calculating the fundamental electric field.

In the case of the SH fields, the matrix takes the form:

$$\begin{pmatrix} E_m^+ \\ E_m^- \end{pmatrix} = \begin{pmatrix} U \\ V \end{pmatrix} + \begin{pmatrix} A & B \\ C & D \end{pmatrix} \begin{pmatrix} E_1^+ \\ E_1^- \end{pmatrix} \tag{3.25}$$

which differs from (3.23) by an extra vector U,V that describes the nonlinear polarization term calculated from the fundamental waves and located at interfaces. When imposing the physical boundary condition of no light incident from both the bottom and the top of the structure, shown in Figure 3.10b, then the matrix takes the form:

$$\begin{pmatrix} E_m^+ \\ E_m^- \end{pmatrix} = \begin{pmatrix} U \\ V \end{pmatrix} + \begin{pmatrix} A & B \\ C & D \end{pmatrix} \begin{pmatrix} 0 \\ E_1^- \end{pmatrix} \Rightarrow \begin{matrix} E_m^+ = U + BE_1^- \\ E_m^- = V + DE_1^- \end{matrix} \tag{3.26}$$

Figure 3.11 shows a schematic of how the numerical procedure works. Initially, the first run of the main function for $E_1^- = 0$ will give us the values of U and V while the second run for an arbitrary E_1^- will

give us the values of B and D. Furthermore, we impose the extra (physical) boundary condition that there is no incident light E_m^- at 2ω, shown in Figure 3.10c (since the SH is generated from the fundamental fields inside the "black box"). Finally, we compute the field amplitude E_1^- that will be used as an input in the final run of the main function in the simulation.

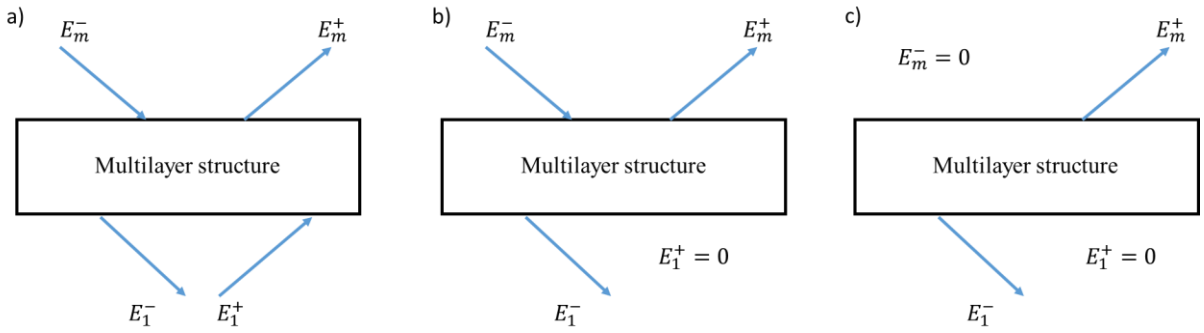

Figure 3.10: a) All incident and outgoing SH fields in a multilayer structure. Boundary conditions for: b) no light travelling upwards from the bottom (no reflection from the bottom of the thick substrate), c) no incident light at 2ω travelling downwards to the structure (SH light is only generated inside the structure at the interfaces due to the nonlinear polarization).

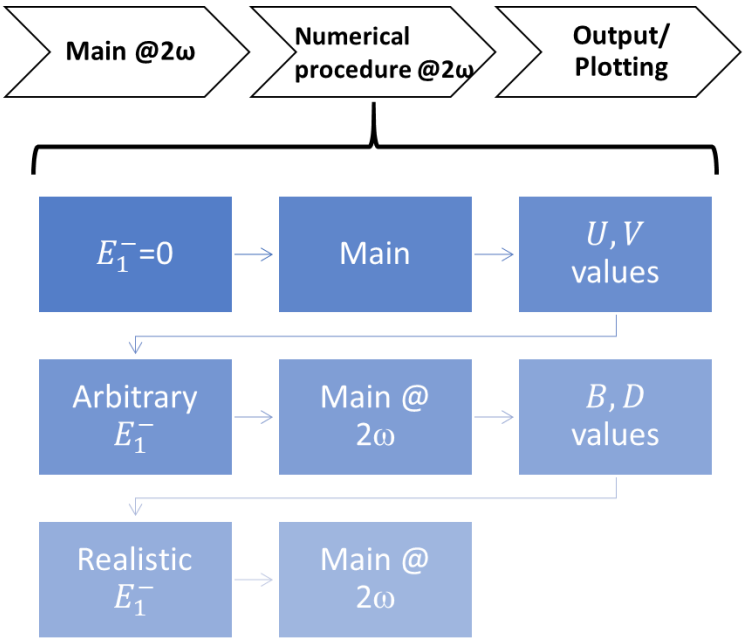

Figure 3.11: Schematic of the numerical procedure for calculating the second harmonic field.

Note that analytical expressions of SH fields for few layer structures exist in the literature [91]. However, in our case we want to solve the problem numerically (including cases of many layer structures), so we followed the previous approach. In the next section, we will verify the simulator by comparison with experimental data for simple structures.

3.5 Validation of the simulation procedure on a SiO_2/Si structure

We used our simulation on simple SiO_2/Si structures in order to validate its capability to reproduce experimental data. The refractive indices for Si and SiO_2 at 780 nm (fundamental) and 390 nm (second harmonic) and typical nonlinear susceptibility were taken from the literature [92] and [51] respectively (Table 3.1). It should be noted that $\chi^{(2)}$ values depend on the material preparation and can vary by one order of magnitude [93]. However, we used the values from [51], being a more recent reference. For $\chi^{(3)}$ only the typical order of magnitude will be used [30] in the next chapters; in this section no E_{dc} field was taken into account.

Table 3.1: Material properties of Si/SiO_2

Material property	Values used in the simulation	Alternative values
Si: n_ω	3.696+0.006i [92]	
Si: $n_{2\omega}$	5.976+0.465i [92]	
SiO_2: n_ω	1.4610 [94]	
SiO_2: $n_{2\omega}$	1.4767 [94]	
χ_{zzz} (m^2/V)	5.8×10^{-18} [51],	6.5×10^{-18} [93]
χ_{xzx} (m^2/V)	1.2×10^{-18} [51],	0.35×10^{-18} [93]
χ_{zxx} (m^2/V)	0.043×10^{-18} [51],	0.13×10^{-18} [93]
ζ (m^2/V)	4.4×10^{-18} [51],	0.23×10^{-18} [93]
$\chi^{(3)}$ (m^3/V^2)	10^{-24} [30]	

Before validating the simulation by comparison with experiments, we will first investigate the impact of the layer thickness, which can also be responsible for changes in the SHG signal. Theoretically, in our 3-layer model (air/oxide/substrate) we treat the substrate (and the air) as a semi-infinite plane and therefore its thickness should not play a significant role. This is the case in Figure 3.12a, where the simulated SHG versus the angle of incidence is shown, for varying the silicon substrate thickness below SiO_2 (t_{SiO2}=2 nm). The substrate thickness does not affect the overall SHG behaviour. For all the next simulations carried out, we use a value of 1 nm for the substrate thickness.

The oxide layer thickness can also be modified. In Figure 3.12b, the simulated SHG versus the oxide thickness shows an interference pattern. The parameters used in the simulation were 0° azimuthal angle, 45° angle of incidence and P-input/P-output polarization configuration.

For validating the simulation, we use experimental data from Si wafers covered with native SiO_2. In the next simulations, we consider t_{SiO2}=2 nm.

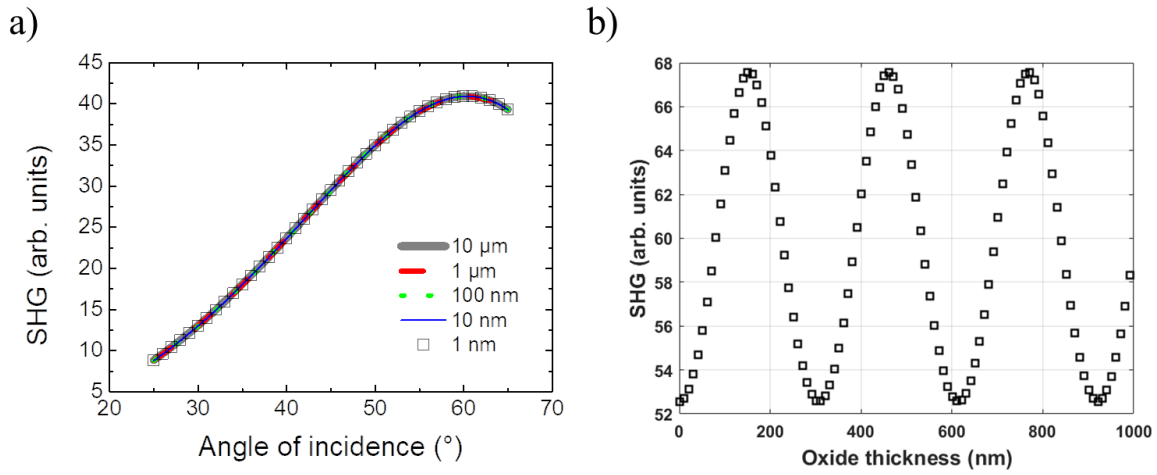

Figure 3.12: a) Simulated SHG intensity versus angle of incidence in a SiO_2/Si structure, for varying substrate thickness (t_{SiO2}=2 nm). There is no effect from the substrate thickness. b) SHG intensity versus the SiO_2 thickness on a Si substrate. An interference pattern is visible.

3.5.1 SHG versus input polarization

Figure 3.13a shows the experimental results of both P- and S- polarized detected SH signal with varying input polarization. The measured sample was a lightly doped Si (100) wafer covered with native oxide (SiO_2). Figure 3.13b shows the simulation results, which reproduce well the experiment. The input geometrical parameters that were used in the simulation were the same as in the experiment (45° angle of incidence, 0° azimuthal angle).

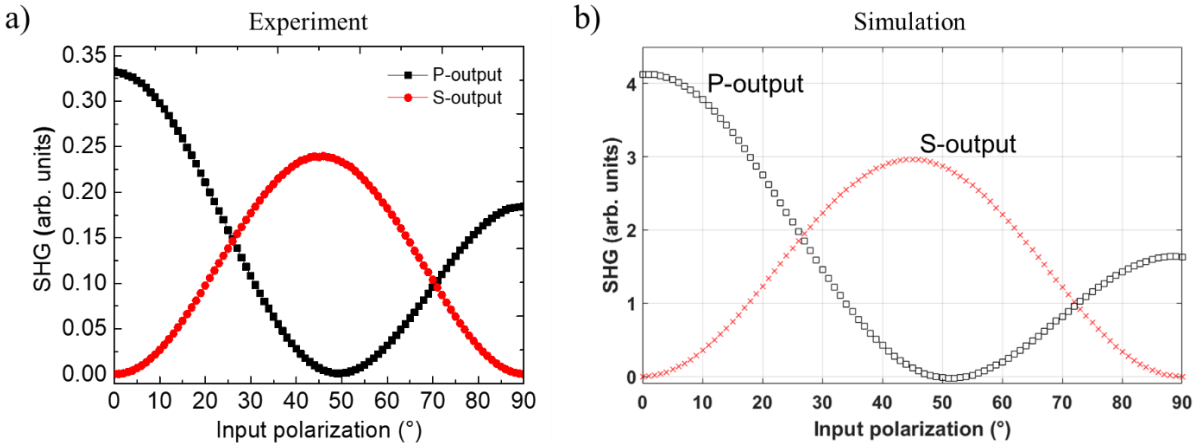

Figure 3.13: SHG intensity versus input polarization for the two SH polarization cases of P-output and S-output. a) Experimental results on Si covered with native oxide. b) Simulation results with t_{SiO2}=2 nm.

3.5.2 SHG versus angle of incidence

A change in the angle of incidence (AOI) modifies the optical path in the structure, which inevitably impacts the SHG. Figure 3.14 shows an excellent correlation between experiment and simulation, with a SHG peak appearing at 60° angle of incidence in both cases.

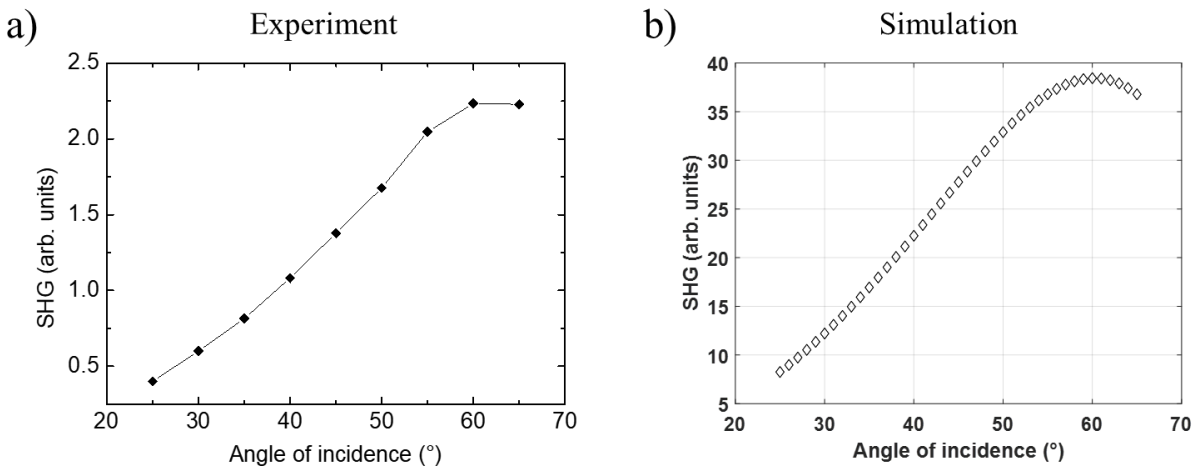

Figure 3.14: SHG intensity versus angle of incidence for P-input/P-output polarizations at 0° azimuthal angle. a) Experimental results on Si covered with native oxide. b) Simulation results with t_{SiO2}=2 nm.

3.5.3 SHG versus azimuthal angle

Finally, we study the SHG versus the azimuthal angle on the same sample (see Figure 3.15 (a) experiments and (b) simulations. Again, there is a good agreement between them, enhancing the fact that the polarization expressions that we use, in conjunction with the values of the different parameters are correct.

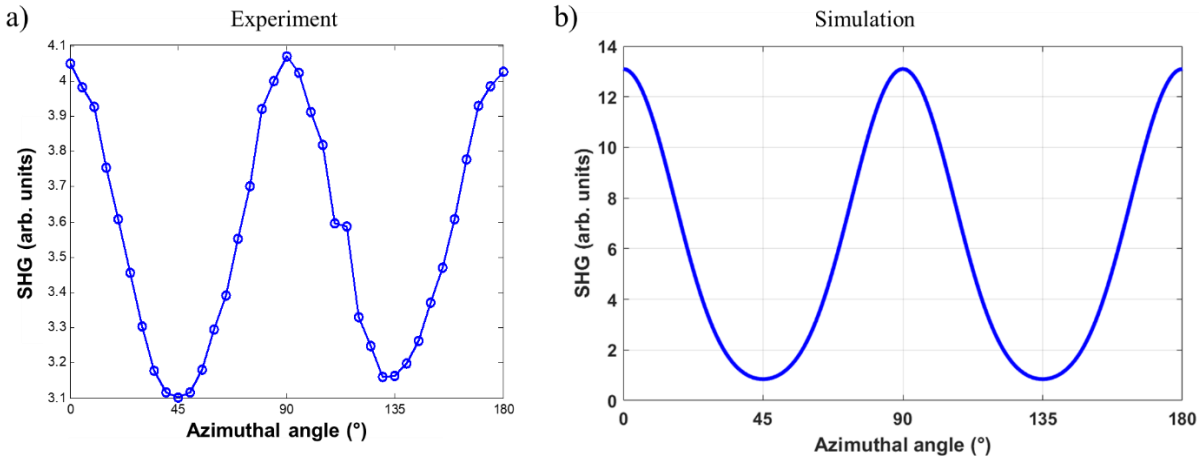

Figure 3.15: SHG intensity versus azimuthal angle for P-input/P-output polarizations at 45° angle of incidence. a) Experimental results on Si covered with native oxide. b) Simulation results with t_{SiO2}=2 nm.

Measurements and corresponding simulations were also performed on 50 nm and 500 nm thick SiO_2 on Si, exhibiting excellent correlation as well (results not shown).

3.6 Conclusions

In this chapter we described our home-made simulation. We presented how the electric fields at the fundamental and the SH frequency were calculated numerically. At each interface, appropriate boundary conditions for each field were considered and the transmitted fields in the new medium were calculated. The new fields were propagated up to the next interface and new boundary conditions were taken. This process was repeated for all layers in the system. Furthermore, the E_{dc} field, which is of paramount importance in characterizing the interface, was incorporated in the prominent $\chi^{(2)}_{zzz}$ component of the nonlinear polarization. We also accounted for the actual physical conditions of no reflected light from the bottom of the semi-infinite absorbing substrate, and no incident 2ω light (since it is generated inside the system). Finally, the simulation tool was verified by using experimental data from Si covered with a native SiO_2. The SHG was simulated versus the incident polarization, the angle of incidence and the azimuthal angle, and a good correlation with the experiments was observed.

Chapter 4:
SHG Characterization of Al_2O_3 on Si

This chapter investigates the ability of second harmonic generation (SHG) to probe the passivation of Si with an atomic layer deposited (ALD) Al_2O_3. Samples with various oxide charges (Q_{ox}) and interface state densities (D_{it}) were fabricated, using different deposition parameters. The samples are characterized by C-V and μ-PCD measurements in order to evaluate Q_{ox} and D_{it} as well as the effective minority carrier lifetime τ_{eff}. SHG results are subsequently correlated with τ_{eff}. Q_{ox} and D_{it} values. The simulations support the experiments and open the way for the estimation of fixed charges through stand-alone SHG.

Contents of Chapter 4

4.1 SHG experimental setup

The experimental setup used throughout this thesis is an optical SHG wafer inspection system developed by FemtoMetrix (Harmonic F1x®) [95] and its configuration is schematically shown in Figure 4.1. A pump laser operating at 780 nm, delivers femtosecond pulses to the sample under study, with 95 fs pulse duration and 80 MHz repetition rate. The average power is 360 mW. A rotating half wave plate (HWP) allows the selection of the polarization angle of the linearly polarized incident light, from 0° (P-polarized, parallel to the plane of incidence) to 90° (S-polarized, vertical to the incidence plane). Furthermore, the angle of incidence of the incoming beam can be controlled between 25° to 65° with respect to the sample surface normal (Figure 4.2). A lens with a 15 cm focal length focuses the beam on the sample's surface and the minimum spot size diameter is approximately 50 µm for a 45° angle of incidence. The actual beam size on the wafer obviously affects the spatial resolution of the measurement, which can go down to 50 µm. Additionally, the sample can be rotated around its surface normal (azimuthal angle).

The reflected fundamental and the generated second harmonic beam from the sample pass through a collimator, a rotating polarizer (which allows to choose the polarization of the second harmonic light) and some filters (single pass and band pass filters) which separate the two beams. The collimated, filtered SH light is detected and measured by a photomultiplier tube (PMT) coupled with a gated photon counter.

The sample is put on a metallic chuck with a capability of accepting wafers up to 300 mm diameter. Metallic probes can be placed on top of the wafer surface and a bias voltage can be applied between the chuck and the probes in order to modify externally the electric fields in the stacks. Figure 4.1b, depicts the inside of the Harmonic F1X machine, with a 200 mm diameter wafer placed on the chuck. A reflectometer is integrated inside the Harmonic F1X tool allowing the measurement of layer thicknesses at the same location of the samples as the SHG measurements.

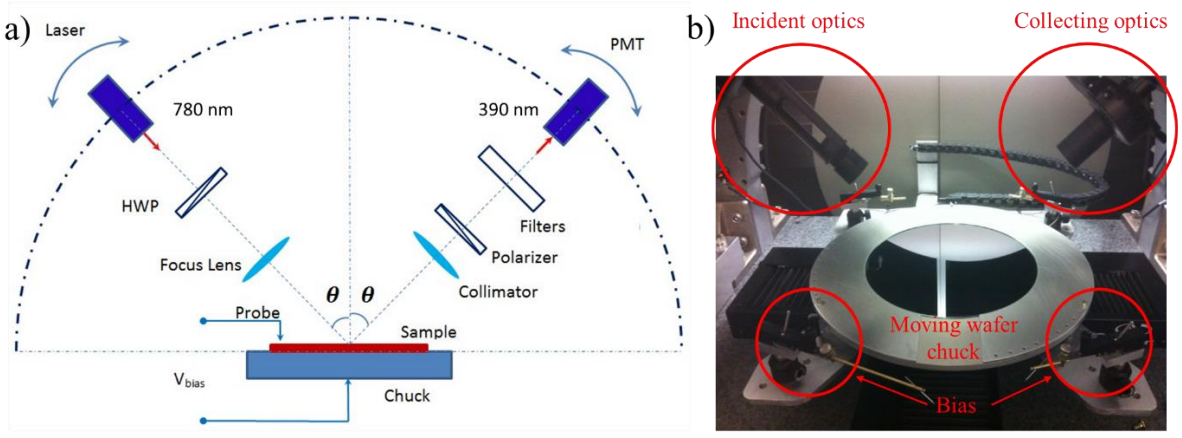

Figure 4.1: a) Schematic of the SHG measurement configuration from FemtoMetrix. b) Inside look in the Harmonic F1X system with a 200 mm wafer placed on the chuck.

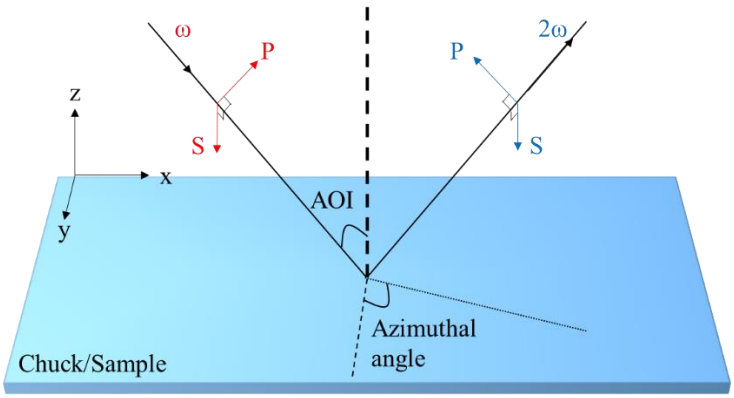

Figure 4.2: Schematic of the experimental geometry showing the polarizations of incident and SH beams, as well as the incidence and azimuthal angles.

4.2 Al_2O_3 on Si

The performance of silicon-based structures like CMOS imagers and solar cells depend largely on the defects and residual charges at their surface and interface. Structurally, defects can be dangling bonds like P_{b0}- (trivalently bonded Si atom $Si_3 \equiv Si\circ$) or E'- type centres ($O \equiv Si\circ$) typical in SiO_x/Si interfaces [7], [96]–[99] (as shown in Figure 4.3a). The surface/interface passivation of silicon structures is mandatory for ensuring proper functionality and is one of the main technological challenges.

The quality of the passivation is affected by the number of defects (traps) D_{it}, which can trap either electrons or holes. Normally D_{it} is a function of the energy level in the bandgap but for simplification we refer to a specific trap energy level (E_t) which determines the localisation of the trap energy in the bandgap. An acceptor-type trap (with its energy level close to E_c) can capture electrons, while donor-type traps (with energy levels close to E_v) can capture holes. The capture cross-sections for electrons and holes σ_n and σ_p are depicted in Figure 4.3b.

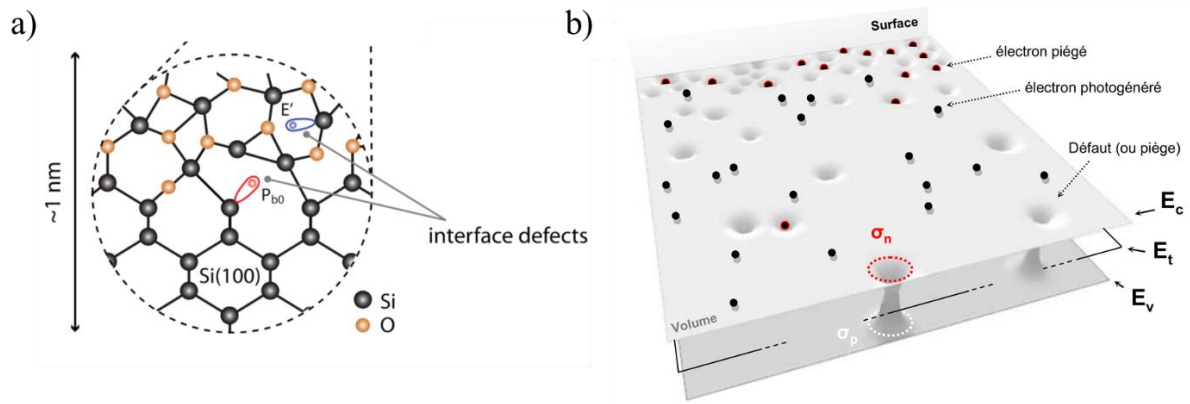

Figure 4.3: a) Atomic structure of the interface which shows two main electronically active defects (taken from [100]*). b) Visualization of energy bands close to the surface/interface, as well as trapping of electrons by typical defects* [101].

The trapped electrons shown in Figure 4.3 can either be re-emitted in the conduction band or recombine with a hole in the valence band. Passivating the silicon surface reduces this unwanted recombination, and it is typically achieved through the use of dielectrics (like SiO_2 and high-k [13], [102]) due to two main mechanisms:

- Chemical passivation, through the formation of Si-O and Si-H bonds which chemically neutralize dangling bonds on the surface of silicon and reduces D_{it} (Figure 4.4a).
- Field-effect passivation, achieved by fixed charges present in the oxide Q_{ox} that induce an electric field at the dielectric/Si interface, which repels one type of charges (either positive or negative) away from it (Figure 4.4b).

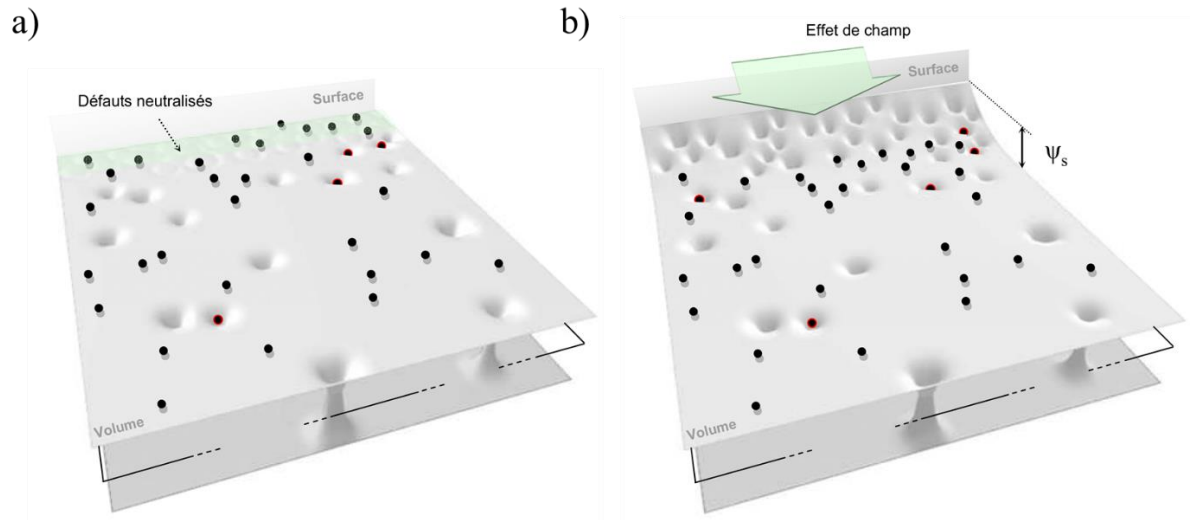

Figure 4.4: Schematic views of: a) chemical passivation which neutralizes defects and reduces D_{it}, b) field-effect passivation which pushes electrons away from the surface (holes, which are not shown, are attracted close to the surface/interface in this example) [101].

Within this context, Al_2O_3 is known to provide excellent surface passivation of crystalline silicon which is critical for the performance of devices such as photodetectors and high-efficiency solar cells [13]. Al_2O_3 is an interesting passivation dielectric due to its combined capabilities of:

- chemical passivation which is attributed to H diffusion from Al_2O_3 towards the interface with silicon [13].
- field-effect passivation by negative charges [13], related to aluminium vacancies (V_{Al}) and oxygen interstitials (O_i) [103], which produce levels below mid gap in the Al_2O_3 bandgap [104].
- low interface defect density and the ability to use nm thick films while achieving an excellent stability during different processing steps [13].

SHG is an interesting tool for characterization of the electronic properties of Al_2O_3 films on Si. It would be ideal though to extract pure electrical information (i.e. Q_{ox} and D_{it}) from a contactless SHG experiment, without actually proceeding to extra processing steps for electrical characterization. In

order to achieve this goal, SHG should be calibrated for quantitative information extraction. First, we will present the fabrication procedure of the samples as well as preliminary lifetime and electrical characterization with photoconductance decay (PCD) and capacitance-voltage (C-V) respectively, which we correlate with SHG measurements. The propagation of radiation in thin film/Si stacks exhibits multiple reflections and interferences, which may conceal the relevant information and must be taken into account. We will then show how the SHG technique associated with simulation could lead to quantification of electric fields at dielectric/semiconductor interfaces.

4.3 Literature review on SHG characterization of Al_2O_3 on Si

Previous studies have demonstrated the great capabilities of SHG characterization for dielectrics (SiO_2 and high-k) on Si bringing remarkable insights into surface and buried interface studies. It has been reported, that during SHG measurements the trapping process for dielectrics on Si occurs via injection of photoexcited electrons from the Si valence band into the oxide conduction band [71], [72]. For high-k dielectrics (Al_2O_3, ZrO_2 and HfO_2) on Si, SHG has been applied for the study of the interfacial defects capable of charge trapping, using rotational angle SHG [72], as well as for monitoring the charge-trapping dynamics. In the same paper, detrapping was evidenced by a decrease of the SHG signal with time, and was significantly reduced in high-k films, in contrast to SiO_2, due to a reduced tunnelling efficiency of electrons back to Si. Charge trapping defects in high-k stacks such as $Si/SiO_2/HfO_2$, have been characterized by spectroscopic SHG and time-dependent EFISH generation [105]: oxygen vacancy defects in HfO_2 films were identified and charge trapping in Hf-silicate samples was shown to be dominated by oxide surface defects.

For the particular case of Al_2O_3, spectroscopic and time-dependent SHG revealed a fixed negative charge concentration in thin Al_2O_3 layers that increases after annealing (from 10^{11} cm^{-2} before anneal, up to 10^{12}-10^{13} cm^{-2} after anneal) [106]. SHG was shown to be directly sensitive to the electric field in the space charge region induced by the fixed negative charges and was used to distinguish between the influence of field-effect and chemical passivation [106]. Moreover, both the amount of charges that can be injected into Al_2O_3 and their net rates increased after annealing [106]. Spectroscopic SHG was also used to distinguish field-effect and chemical passivation for different thicknesses (2-20 nm) of Al_2O_3 on Si [107]. In the same work, they demonstrated that the field-effect passivation was virtually unaffected by the Al_2O_3 thickness down to 2 nm for the plasma-assisted ALD and 5 nm for the thermal ALD process. In another study [108], the differences between the passivation mechanisms of H_2O-based and plasma-based ALD processes for Al_2O_3 deposition were analysed: EFISH suggested significant differences in pre-existing charge density leading to different levels of field-effect passivation between the films deposited by the two ALD processes.

It must be noted that when depositing Al_2O_3 on Si, even at an H-terminated surface (after HF etch), there is always an interfacial native SiO_x layer [109] in the 0.1-1 nm range. Studies including spectroscopic SHG, time-dependent SHG, and rotational angle SHG have shown that the interfacial oxide layer thickness plays an important role in the density and polarity of the interface charges [110], [111]. With around 5-10 nm of interfacial deposited SiO_2, the polarity of the total fixed charge changed from negative to positive, although the resulting density was negligible.

The particularity of our work is that we correlate electrical parameters (τ_{eff}. Q_{ox} and D_{it}) extracted from other techniques (PCD, C-V) with SHG parameters for various samples. Moreover, we use in our simulator E_{dc} values calculated from previously extracted Q_{ox} in order to explain the experimental SHG behavior.

4.4 Sample fabrication and preliminary characterization

In this section, we present the procedure for fabricating samples followed by preliminary characterization with conventional techniques such as PCD and C-V measurements which give initial information regarding electrical properties: carrier lifetime, Q_{ox} and D_{it} that will be necessary for comparison with SHG signals later.

4.4.1 Sample fabrication

The samples fabricated at INL were Al_2O_3 on silicon wafers. The silicon substrates were double-sided polished FZ p-type (boron doped) with [100] or [111] surface orientation and resistivity of 0.8 Ω.cm. The substrates were subsequently treated using a standard cleaning process to remove organic residuals (Piranha [H_2SO_4, H_2O_2]) and diluted HF etch to remove the top native and chemical oxide. Ultrathin Al_2O_3 films were deposited using either thermal or plasma atomic layer deposition (ALD) in an Ultratech Fiji F200 reactor. For the thermal ALD (T-ALD) samples, trimethyaluminium ($Al(CH_3)_3$) – TMA) and water (H_2O) were used as reactants, while for the plasma ALD (P-ALD) samples, oxygen radicals were generated by a plasma source. In both cases, the sample holder and reactor chamber temperature was 250°C. For both processes each ALD cycle consists of TMA dosing followed by a purge, then exposure to an oxidant (either water or plasma) followed again by a purge. After the deposition, some of the samples were subjected to extra processing by annealing at 400°C for 10 min. The annealing step was done in order to reduce the interfacial trap density (chemical passivation) and activate the negative charges inside Al_2O_3 (field-effect passivation).

Initially a sample batch with the same T-ALD process (Table 4.1) was prepared in order to have a first comparison of SHG measurements and average lifetime values measured through µ-PCD. These

samples had the same 15 nm Al_2O_3 on either Si (100) or Si (111) substrate. Each sample was subsequently cut in half, and one half was kept intact while the other half was subjected to the extra annealing step.

For the goal of passivation monitoring through SHG, we intentionally chose low and high-quality samples, in order to have a panel of materials with very different passivation quality. In the as-deposited plasma ALD samples, a high density of negative charges is already present and the impact of annealing on the field-effect passivation is moderate [112]. This 2nd batch (Table 4.2) comprised 15 nm T-ALD or P-ALD Al_2O_3 on either Si (100) or Si (111) substrates, both as-deposited and annealed, resulting in 8 samples. They were used to confirm results from the 1st batch and allowed us to proceed further into passivation monitoring through SHG. By combining conventional CV measurements and SHG characterization on the 4 samples with Si (100) substrate, we evidenced the connection of the interfacial electric field and SHG.

Finally, the last batch (Table 4.3) was created for verifying some hypothesis regarding the impact of the thickness of the Al_2O_3 ultrathin film on the optical propagation effects mentioned in Chapter 3. Therefore, this last set of samples was only studied with SHG.

In the following tables we present all of the fabricated samples, their code-name, along with the corresponding characterization that was carried out on each one (indicated with the "+" sign).

Table 4.1:1st sample batch and performed characterization

Sample	Process	μ-PCD	C-V	SHG
A0	T-ALD on Si (100), as deposited (15 nm)	+	-	+
A1	T-ALD on Si (100), annealed (15 nm)	+	-	+
B0	T-ALD on Si (111), as deposited (15 nm)	+	-	+
B1	T-ALD on Si (111), annealed (15 nm)	+	-	+

Table 4.2: 2nd sample batch and performed characterization

Sample	Process	μ-PCD	C-V	SHG
P0	P-ALD on Si (100), as deposited (15 nm)	+	+	+
P1	P-ALD on Si (100), annealed (15 nm)	+	+	+
T0	T-ALD on Si (100), as deposited (15 nm)	+	+	+
T1	T-ALD on Si (100), annealed (15 nm)	+	+	+
Px0	P-ALD on Si (111), as deposited (15 nm)	-	-	+
Px1	P-ALD on Si (111), annealed (15 nm)	+	-	+
Tx0	T-ALD on Si (111), as deposited (15 nm)	+	-	+
Tx1	T-ALD on Si (111), annealed (15 nm)	+	-	+

Table 4.3: 3rd sample batch and performed characterization

Sample	Process	µ-PCD	C-V	SHG
T5	5nm T-ALD on Si (100), annealed	-	-	+
T15	15 nm T-ALD on Si (100), annealed	-	-	+
T25	25 nm T-ALD on Si (100), annealed	-	-	+

4.4.2 µ-PCD characterization

The surface passivation of silicon was evaluated before and after annealing by measuring the effective minority carrier lifetime (τ_{eff}). Generally, τ_{eff} is expressed as a bulk lifetime term (τ_{bulk}) and a surface contribution (S) that is described by the following relation [13], [113]:

$$\frac{1}{\tau_{eff}} = \frac{1}{\tau_{bulk}} + \frac{2S}{W} + \cdots \qquad (4.1)$$

where S is the surface recombination velocity and W is the wafer thickness. For Si substrates with high bulk lifetimes and passivated on both surfaces, S can be directly related to τ_{eff} by $S = W / 2\tau_{eff}$.

Spatially resolved effective minority carrier lifetime mapping was performed by microwave photo-conductance decay (with the "Semilab WC-2000 µW-PCD" equipment [29] at INL) on the passivated samples, before and after annealing. The equipment is using a laser source emitting at 904 nm with a short light pulse of 200 ns to create electron-hole pairs in Si. The excess carriers modify the conductivity, which is monitored by microwave reflectivity as a function of time. The decay of the photoconductivity with time allows determining the minority carrier lifetime. The mapping step was of 500 µm.

Figure 4.5 shows the maps obtained on the first batch of samples, namely 15nm T-ALD Al_2O_3 coated Si(100) and Si(111), as-deposited and annealed. The averaged τ_{eff} value was 57 µs for Al_2O_3/Si(100) and 81 µs for Al_2O_3/Si(111) before annealing. After annealing, these values increased to 140 µs and 250 µs respectively (Table 4.4). The higher values of lifetime measured after annealing for each case confirm the reduction of surface recombination mainly due to the field-effect passivation by activation of the negative charges at the Al_2O_3/Si interface. Additionally, higher lifetime values are obtained when the alumina is deposited on Si(111) rather than on Si(100), suggesting a better chemical passivation. The effect can be related to a higher quality substrate, since the Si(111) is known to produce better free surfaces than Si(100) [98].

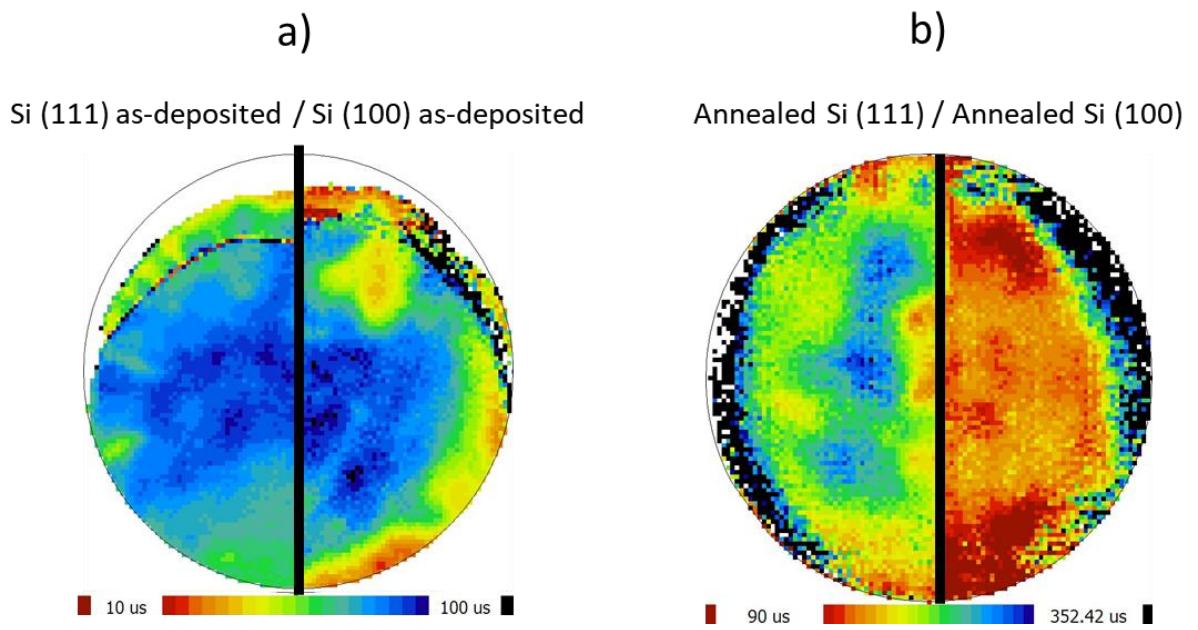

Figure 4.5: Carrier lifetime measured with μ-PCD on the first batch of samples in Table I: a) as-deposited thermal ALD Al_2O_3 on Si (111) and Si (100); b) annealed thermal ALD Al_2O_3 on Si (111) and Si (100).

Table 4.4: μ-PCD lifetime values for the 1st batch of Si samples passivated with Al_2O_3

Sample	Process	τ_{eff} (μs)
A0	T-ALD on Si (100), as deposited (15 nm)	57
A1	T-ALD on Si (100), annealed (15 nm)	140
B0	T-ALD on Si (111), as deposited (15 nm)	81
B1	T-ALD on Si (111), annealed (15 nm)	250

Table 4.5 shows the effective lifetime values from the second batch of samples, namely 15 nm Al_2O_3 either prepared with the T-ALD or P-ALD process on either Si(100) or Si(111) substrates, both as-deposited and annealed. The averaged τ_{eff} value for the as-deposited samples was 3.5 μs for P0 [P-ALD Al_2O_3/Si(100)], 120 μs for T0 [T-ALD Al_2O_3/Si(100)], 140 μs for Tx0 [T-ALD Al_2O_3/Si(111)], while Px0 [P-ALD Al_2O_3/Si(111)] had a very low value, which was not recorded. After annealing, these values increased for all samples regardless of their ALD process or substrate. As previously, Si (111) substrates exhibit better τ_{eff} hence better chemical passivation.

In the next section, we will mainly focus on the characterization of samples P0, P1, T0, T1 with Si (100) substrates, since we know all of their τ_{eff} values.

Table 4.5: µ-PCD lifetime values for the 2nd batch of Si samples passivated with Al_2O_3

Sample	Process	τ_{eff} (µs)
P0	P-ALD on Si (100), as deposited (15 nm)	3.5
P1	P-ALD on Si (100), annealed (15 nm)	65
T0	T-ALD on Si (100), as deposited (15 nm)	120
T1	T-ALD on Si (100), annealed (15 nm)	520
Tx0	T-ALD on Si (111), as deposited (15 nm)	140
Tx1	T-ALD on Si (111), annealed (15 nm)	460
Px0	P-ALD on Si (111), as deposited (15 nm)	-
Px1	P-ALD on Si (111), annealed (15 nm)	660

4.4.3 C-V characterization

In order to investigate the impact of the fixed charges and interface traps on SHG, we need a complementary method to quantify them. The most established way to monitor fixed oxide charge concentration Q_{ox} and interface trap density D_{it} is the conventional C-V technique [14], [15]. An additional step was necessary for the fabrication of circular MOS capacitors: ~200 nm thick Al was evaporated through a shadow mask with circular holes of various diameters (500 µm down to 200 µm). CV measurements were performed on the samples, where the total capacitance C_m was measured as a function of the gate voltage V_G in the parallel C_p-G_p model [15] with a Keysight (Agilent) B1500A equipment. The bias was swept from negative to positive values with a step of 100 mV. The ac signal level was set at 30 mV for frequencies ranging from 1 kHz up to 1 MHz.

Figure 4.6a shows the total capacitance C_m versus the gate voltage V_G for a 500 µm diameter MOS measured at 1 MHz. The 3 characteristic regions of a typical CV curve from the literature [14], [15] are shown in Figure 4.6b:

- the accumulation region for negative V_G, where C_m is given by the oxide capacitance C_{ox} (maximum capacitance).
- The depletion region, where C_m starts to drop due to the silicon capacitance C_{Si} which is connected in series with C_{ox} ($C_m^{-1} = C_{ox}^{-1} + C_{Si}^{-1}$). The value of V_G at which the transition between accumulation and depletion takes place is the flat band voltage V_{FB}.
- The inversion region for positive V_G, where C_m saturates since the depletion width in Si reaches its maximum.

Our measured curve (Figure 4.6a) resembles a deep depletion capacitance (C_{dd}) instead of a typical high frequency one (C_{hf}) in Figure 4.6b. C_{dd} can be obtained when measuring in high frequencies

if the sweeping voltage is too fast and the structure is not in thermal equilibrium. When moving fast from flatband to threshold voltage and beyond, the inversion layer is only partially formed since the generation of minority carriers cannot keep up with the amount needed to form the inversion layer. Therefore, the depletion layer keeps increasing beyond its maximum thermal equilibrium value, resulting in a total capacitance that further decreases with increasing voltage. In order to approach equilibrium conditions for each measurement point, the delay time for the bias sweep was set to 1s for the following measurements.

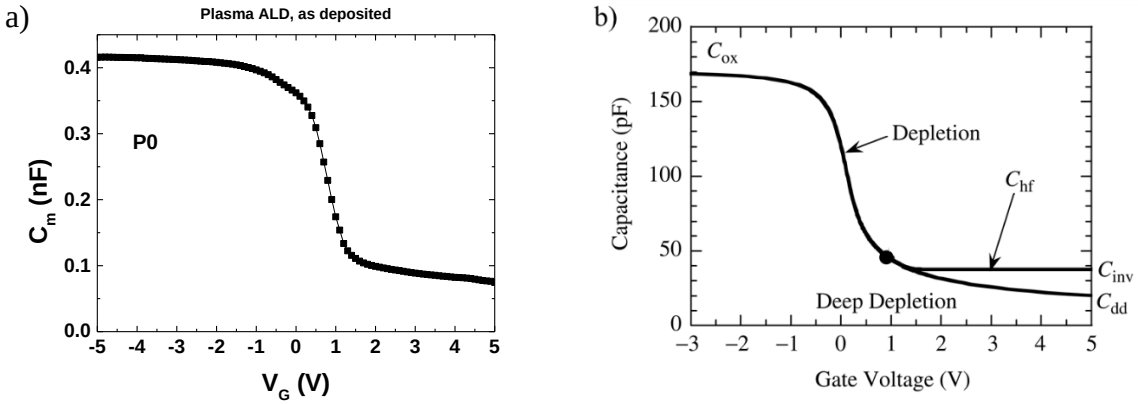

Figure 4.6: a) C-V measured at 1 MHz on a Al/Al_2O_3/Si MOS capacitor with 500 µm diameter. b) Theoretical MOS-CV curve showing the oxide C_{ox}, the high frequency C_{hf}, the inversion C_{inv} and the deep depletion C_{dd} capacitances (Figure 2.9 from [14]*).*

Figure 4.7 shows the C-V results on 200 nm Al/15 nm Al_2O_3/Si (100) circular capacitors with 500 µm diameter (for both plasma and thermal ALD) where V_G was swept initially from negative to positive values (trace) and then from positive to negative (retrace). A hysteresis effect is visible in the depletion region when the voltage sweeping direction is reversed. The effect is more prominent for P0 than for the T0 sample indicating that the plasma sample has a higher charge trapping capability (electrons and holes). This is consistent with the fact that the as-deposited plasma ALD samples exhibit more surface defects mostly due to the lower hydrogen concentration in the process (use of O_2 as oxidant instead of H_2O for the thermal ALD process). The smaller hysteresis in T0 indicates the better interface of thermal ALD Al_2O_3 on Si.

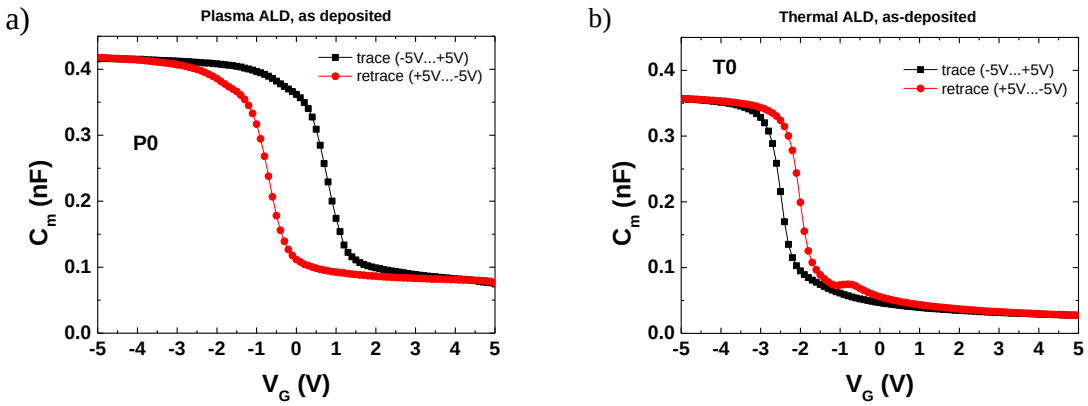

Figure 4.7: C-V measured at 1MHz on the 200 nm Al/15 nm Al_2O_3/Si (100) capacitors with 500μm diameter: a) plasma ALD Al_2O_3 as-deposited and b) thermal ALD Al_2O_3 as deposited.

In Figure 4.8 the total capacitance was measured as a function of the gate voltage (from accumulation to inversion) for different frequencies ranging from 1 kHz to 1 MHz. We observe a frequency variation in the depletion region for the P0 sample but not for T0. The presence of trap states localized in the oxide/semiconductor interface account for this frequency dispersion (plasma ALD is known to induce more traps). We also observe a surprising variation in the maximum capacitance in accumulation for different frequencies and the effect is more prominent for T0. The capacitance in accumulation is supposed to be given by C_{ox} and it should be constant for different frequencies. It is typically expressed as [14], [15]:

$$C_{ox} = \frac{\varepsilon_{ox}}{t_{ox}} S \qquad (4.2)$$

with ε_{ox} being the dielectric permittivity, S the surface of the capacitor and t_{ox} the oxide thickness. In most cases [14], [15], the variation of the maximum capacitance with frequency is associated with series resistance. We tried correcting our data with typical procedures [14], [15] but the effect was not removed. In order to investigate this, next we will measure samples with varying MOS surface area and at different frequencies.

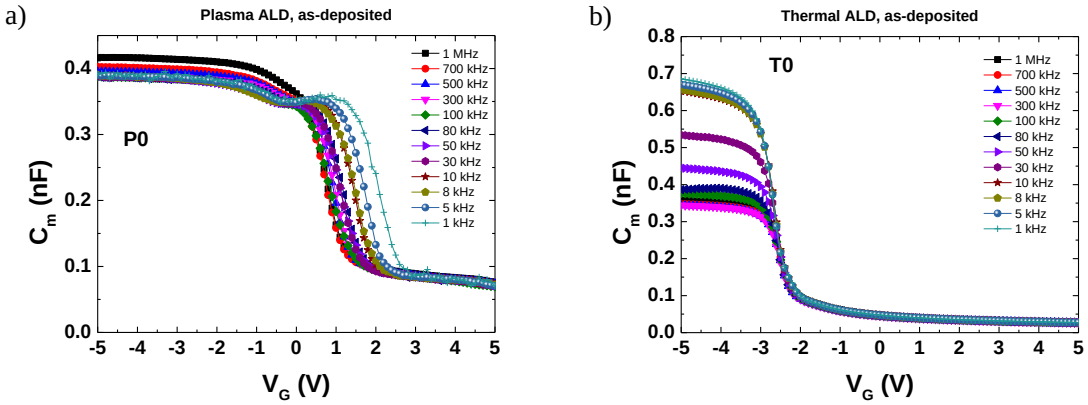

Figure 4.8: C-V measurements on 200 nm Al/15 nm Al_2O_3/Si (100) capacitors with 500μm diameter: a) plasma ALD Al_2O_3 and b) thermal ALD Al_2O_3.

In Figure 4.9 we show the accumulation capacitance (C_{ox}) versus the surface of the MOS capacitor for high (1 MHz) and low (1 kHz) frequencies for: (a) P0 and (b) T0 samples. The theoretically expected oxide (maximum) capacitances are drawn as lines, calculated from eq. (4.2), with t_{ox}=15 nm and $\varepsilon_{ox} = 9\varepsilon_0$ for plasma ALD and $\varepsilon_{ox} = 7\varepsilon_0$ for thermal ALD (ε_0 is the vacuum permittivity). The solid blue line corresponds to a 15 nm Al_2O_3 film only, while the dashed green line corresponds to a combined 15 nm Al_2O_3/1 nm thin interfacial SiO_2 layer (which is always present as discussed previously). The model with the interfacial layer seems to be more appropriate, at least for the thermal ALD sample in the low frequency limit. Nevertheless, there are discrepancies between the measured capacitance values and the theoretical ones, at least for MOS with large surfaces (diameters). Since the MOS capacitors were fabricated by Al evaporation through a shadow mask, some possible explanations for this effect are:

- the precision when measuring the surface of the capacitors might not be good.
- the quality of the interface between Al and Al_2O_3 might not be the best, since before the Al evaporation, the sample was stored in an ambient environment for a prolonged time period and possible contamination from the air could be present (for example moisture).
- higher surface areas are more inclined to exhibit defects that dramatically affect C-V curves.

In order to avoid the problem, we proceed to perform the C-V measurements on the smallest diameter (200 μm) MOS capacitors.

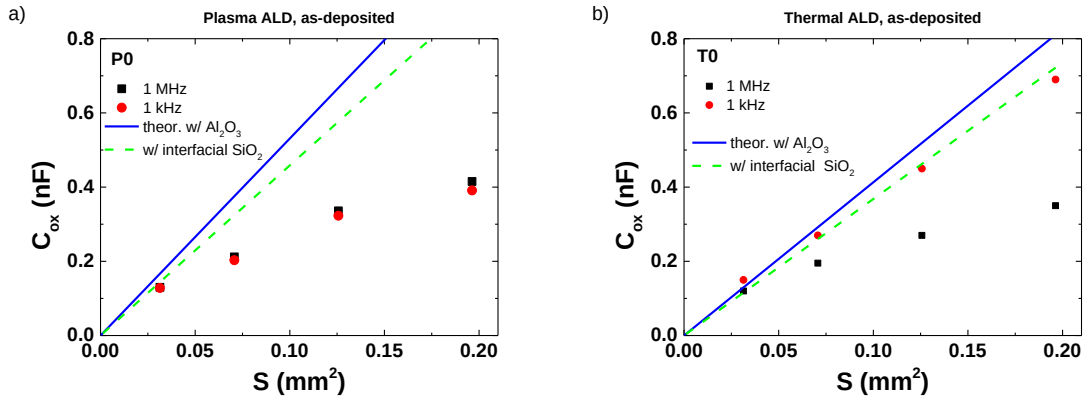

Figure 4.9: Accumulation (maximum) capacitance versus the MOS surface size for a) plasma ALD Al_2O_3 and b) thermal ALD Al_2O_3. Two models were used to fit the data, one with a 15 nm Al_2O_3 film only and another with a combined 15 nm Al_2O_3 / 1 nm thin interfacial SiO_2 layer, as explained in the text.

C-V measurements were performed on 200 μm MOS structures including both as-deposited and annealed samples from the two different ALD processes (thermal and plasma), for frequencies ranging from 1 kHz to 1 MHz. The capacitance of plasma samples exhibits stronger frequency dependence in the depletion region than the thermal ones, which is expected since the former has more interface traps able to respond to the ac field at lower frequencies. Additionally, after annealing of the

as-deposited samples (P0, T0), the impact of the frequency in the depletion capacitance is lower (P1, T1), since the annealing is known to reduce interface traps [13], [112], [114], [115].

After this qualitative description of the CV curves, we can proceed to a more quantitative analysis in order to extract values of Q_{ox} and D_{it} which will be compared with SHG data.

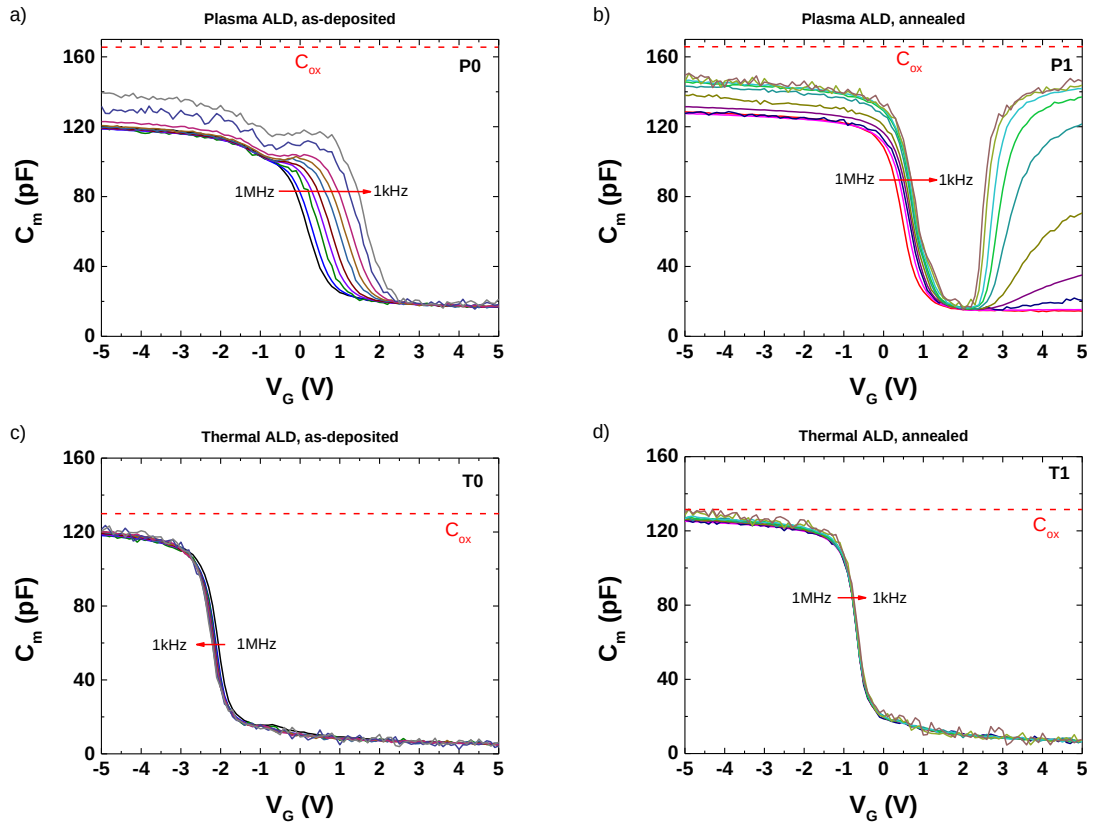

Figure 4.10: C-V measurements between 1 MHz and 1 kHz on a) plasma ALD as-deposited (P0), b) plasma ALD annealed (P1), c) thermal ALD as-deposited (T0) and d) thermal ALD annealed (T1), all on Si (100) substrates. The theoretical maximum oxide capacitance in accumulation is shown as well.

4.4.4 Extraction of the fixed oxide charges Q_{ox} and of the interface field E_{dc}

In order to extract the number of fixed charges after annealing, C-V was plotted on the same graph for the as-deposited and the annealed samples at the highest frequency (1 MHz) where the response of interface traps is minimum (Figure 4.11). The C-V curves of both plasma ALD (P0) and thermal ALD (T0) as-deposited samples are shifted towards more positive V_G values after annealing, which indicates the activation of negative charges. As expected, the ΔV_{FB} shift is larger for thermal ALD (T0) since negative charges are already present in as-deposited plasma ALD (P0) and the impact of annealing on the field-effect passivation is moderate [112].

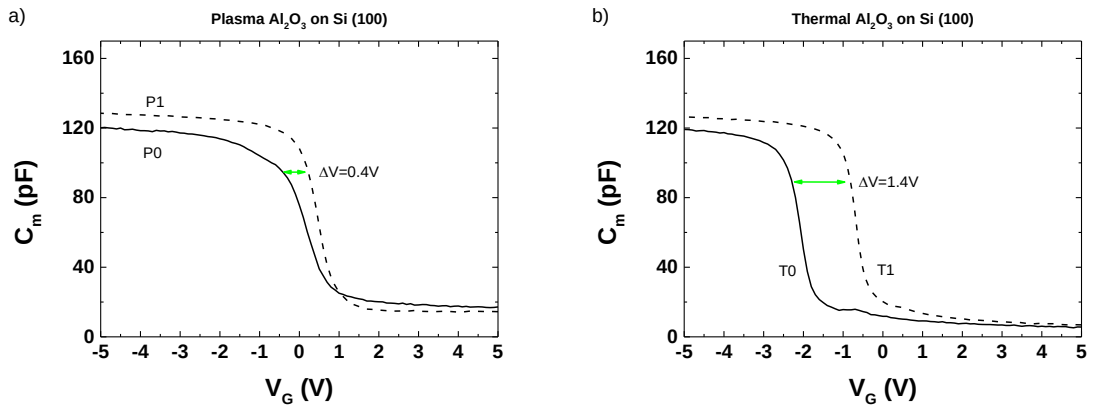

Figure 4.11: C-V scan at 1 MHz. The V_{FB} shift is visible between as-deposited and annealed thermal ALD sample (a) and plasma ALD sample (b). The shift towards more positive values indicates the activation of negative charges after annealing.

The flat band voltage is related to the fixed oxide charges (Q_{ox}) through [14], [15]:

$$Q_{ox} = \left(\varphi_{ms} - V_{FB}\right) C_{ox} \tag{4.3}$$

where φ_{ms} is the work function difference between the metal gate and the semiconductor and C_{ox} is the oxide capacitance. The work function φ_{ms} was calculated to be -0.94 V (for Al gate and p-doped Si with $2x10^{16}$ cm^{-3} carrier concentration which corresponds to our samples resistivity of 0.8 Ωcm [116]). In order to extract V_{FB} we plot $1/C^2_m$ [14]; the total capacitance in the depletion regime follows V_G linearly:

$$\frac{1}{C_{total}^2} = \frac{1}{C_{ox}^2} + \frac{2}{S^2 N_A q \varepsilon_{Si}} (V_G - V_{FB}) \tag{4.4},$$

where N_A is the acceptor doping level, q is the elementary charge and $\varepsilon_{Si} = 11.7\varepsilon_0$ the dielectric permittivity of silicon. By plotting $1/C_m^2$ versus V_G (eq. (4.4)) we can find V_{FB} and C_{ox}, and Figure 4.12 shows the result for the P0 sample. Subsequently, we can calculate Q_{ox} from Equation (4.3), which is then used to estimate the electric field in the SCR of Si from the Gauss equation:

$$E_{dc} = \frac{Q_{ox}}{\varepsilon_{Si}} \tag{4.5}$$

The same method was used for the calculation of the parameters for other samples and the results are reported in Table 4.6. These electric field values will be correlated later with the SHG signals.

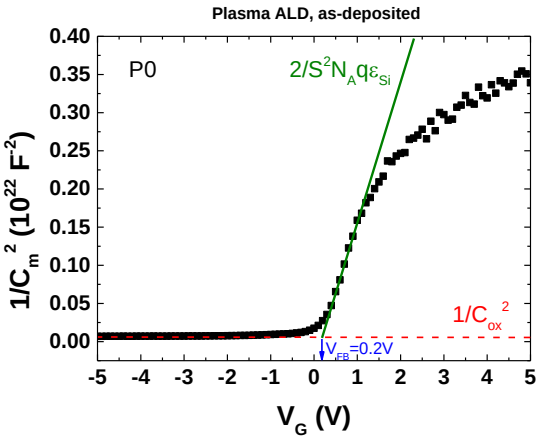

Figure 4.12: $1/C_m^2$ versus V_G at 1MHz and extraction of V_{FB} and C_{ox} from Equation (4.4) for the plasma ALD as-deposited sample (P0).

Table 4.6: Electrical quantities from C-V characterization results

Sample	V_{FB} (V)	Q_{ox} (x 10^{12} cm^{-2})	E_{dc} (x 10^5 V/cm)
P0	0.2	-2.64	+4.04
P1	0.5	-3.58	+5.48
T0	-2.1	+2.85	-4.36
T1	-0.4	-0.5	+0.77

4.4.5 D_{it} extraction

The technique used for the extraction of D_{it} from C-V measurements is the high-low frequency C-V technique [17]. With this method, two measurements are taken at two different frequencies, one being very high (typically 1 MHz) and another being low (1-10 kHz). At high frequency when the device is at equilibrium, minority carriers (electrons) do not respond to the external oscillating field. Therefore, electrons cannot be trapped by interface states and the interface trap response is prevented [14]. The equivalent capacitance C_{HF} is simply the oxide and the semiconductor capacitance C_{Si} in series (equivalent circuit shown in Figure 4.13a).:

$$\frac{1}{C_{HF}} = \frac{1}{C_{ox}} + \frac{1}{C_{Si}} \tag{4.6}$$

The second measurement is taken at low frequency, in order to permit trap response:

$$\frac{1}{C_{LF}} = \frac{1}{C_{ox}} + \frac{1}{C_{Si} + C_{it}} \tag{4.7}$$

In this case, the semiconductor and interface trap capacitances are in parallel and their product is in series with the oxide capacitance. The equivalent circuit is shown in Figure 4.13b.

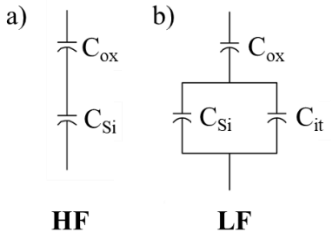

Figure 4.13: Equivalent circuit capacitances for a) high frequency and b) low frequency CV measurements of MOS structures [14].

By normalizing Equations (4.6), (4.7) with the oxide capacitance, we can rewrite them as:

$$\frac{C_{HF}}{C_{ox}} = \frac{C_{Si}}{C_{ox} + C_{Si}} \tag{4.8}$$

$$\frac{C_{LF}}{C_{ox}} = \frac{C_{Si} + C_{it}}{C_{ox} + C_{Si} + C_{it}} \tag{4.9}$$

By solving Equation (4.8) for C_{Si} and replacing to Equation (4.9), we find for the effective trap capacitance C_{it}:

$$\frac{C_{it}}{C_{ox}} = \frac{C_{LF}}{C_{ox} - C_{LF}} - \frac{C_{HF}}{C_{ox} - C_{HF}} \tag{4.10}$$

Then we can calculate the interface trap density as:

$$D_{it} = \frac{C_{it}}{qS}(cm^{-2}eV^{-1}) \tag{4.11}$$

where q is the electron charge and S is the area of the MOS capacitor.

Figure 4.14 shows the interface trap density D_{it} versus the gate voltage for all samples. D_{it} was calculated using the high-low frequency technique as described previously, from the C-V measurements at two different frequencies (1 MHz and 10 kHz). Since the interface trap density is normally given in depletion or at the onset of inversion [14], we identified the D_{it} value corresponding to $V_G=V_{FB}+5\%V_{FB}$ for each sample (marked by arrows in Figure 4.14). Sample P0 has a D_{it} value of approximately ~10^{13} $cm^{-2}eV^{-1}$, P1 ~$3x10^{12}$ $cm^{-2}eV^{-1}$, T0 ~$5x10^{10}$ $cm^{-2}eV^{-1}$ and finally T1 ~$2x10^{10}$ $cm^{-2}eV^{-1}$. We observe lower values of D_{it} for the thermal ALD (T0, T1) than the plasma ALD (P0, P1) process as expected, due to the higher hydrogen concentration from the H_2O oxidant (present during the thermal ALD process) which better passivates the surface [117]. Additionally, the high D_{it} values for the annealed plasma samples is consistent with the very low minority carrier lifetime.

The D_{it} concentration decreases after annealing for both processes because of the diffusion of H atoms present in the dielectric layer towards the dielectric/Si interface [115]. All of the electrical parameters extracted from the CV measurements are summed up in Table 4.7.

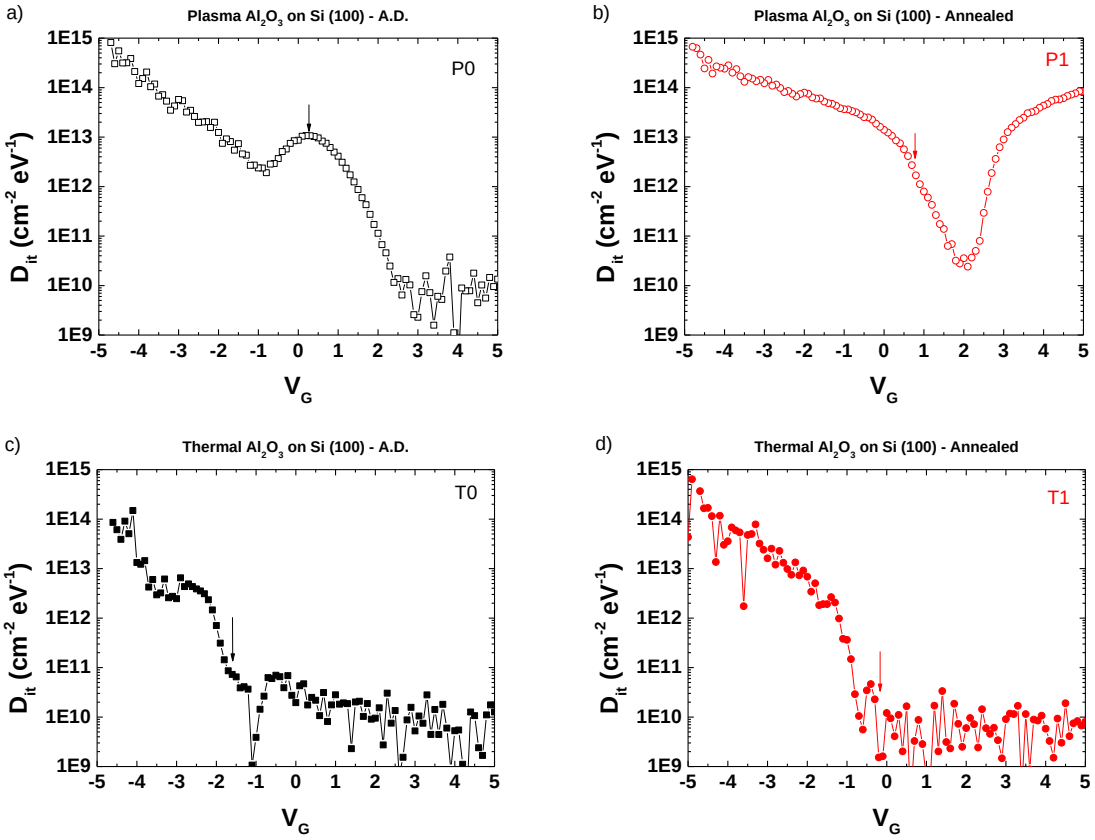

Figure 4.14: D_{it} vs V_G for all 4 samples. In depletion, approximate values of D_{it} (in $cm^{-2}eV^{-1}$) are: a) ~10^{13}, b) ~$3x10^{12}$, c) ~10^{11}, d) ~$2x10^{10}$.

Table 4.7: D_{it} values for Si samples passivated with a 15 nm Al_2O_3 film

Sample	D_{it} (eV^{-1} cm^{-2})
P0	10^{13}
P1	$3x10^{12}$
T0	10^{11}
T1	$2x10^{10}$

Q_{ox} and D_{it} values extracted from C-V measurements are consistent with the different sample processing and the literature results [115]. After annealing, Q_{ox} values are large and negative. The D_{it} concentration decreases after annealing for both plasma and thermal processes because of the diffusion of H atoms present in the dielectric layer towards the dielectric/Si interface. Furthermore, the high D_{it} values for the annealed plasma sample (P1) is consistent with its very low minority carrier lifetime that may be due to contamination during the cleaning procedure.

4.5 SHG characterization of Al_2O_3/Si samples

In this section, SHG characterization of Al_2O_3/Si is carried out. Initially, we present typical time-dependent SHG signals for two different ALD processes and subsequent annealing. We compare the time constants extracted from TD-SHG curves with the D_{it} values from C-V measurements. Later, the initial SHG signal (t=0), relevant to Q_{ox} and initially charged D_{it}, are correlated with τ_{eff} and E_{dc} from μ-PCD and C-V measurements correspondingly. We include the E_{dc} field values in the optical simulation in order to reproduce the experimental data. Finally, some precautions when explaining SHG data will be presented, such as Si substrate orientation, dielectric film thickness, etc…

4.5.1 Impact of the ALD process and annealing conditions measured with SHG

4.5.1.1 Time-Dependent SHG: phenomenological analysis

As already mentioned, the ALD process and subsequent annealing may have a significant impact on the interface properties in Al_2O_3/Si stacks. This impact can be probed qualitatively by time-dependent (TD) SHG measurements. Figure 4.15a shows the TD-SHG signals from the thermal and plasma ALD Al_2O_3 on Si(100) samples (from Table 4.2), recorded for 1000 s with 10 ms time resolution (the photon counting gate was integrating the signal every 10 ms). The monotonous increase of the signal was attributed to the electric field-induced second harmonic (EFISH) effect [70], [71], [74], [118]. Plasma ALD samples (P0, P1) exhibit higher initial (t=0) and saturation (t=1000s) values than thermal ALD samples (T0, T1). The first data point on each curve $I_{2\omega}(t=0)$ can be associated to the interface structural properties and its static electric field $\chi^{(2)}$ and $\chi^{(3)}E_{dc}(0)$ correspondingly. Therefore, this first point probes the fixed charges and some charged interface traps present at the interface before any laser-induced charge-trapping occurs (Figure 4.15b). As the laser keeps illuminating the sample (Figure 4.15c), two competing phenomena give rise to time-dependent EFISH:

- The fundamental beam creates electron-hole pairs in Si which can be separated by the pre-existing interface dc field. In the case of Al_2O_3 with negative charges this would decrease the SHG intensity (which is not the case in Figure 4.15a).
- The electrons from the Si valence band can be injected into the conduction band of Al_2O_3 and get trapped in interface or bulk states in the oxide. This happens when the electrons overcome the energy barrier at the oxide/Si interface by 2- or 3- photon absorption processes or alternatively through tunnelling [111], therefore increasing the initial electric field (Figure 4.15d). After the trap sites are filled, SHG reaches saturation.

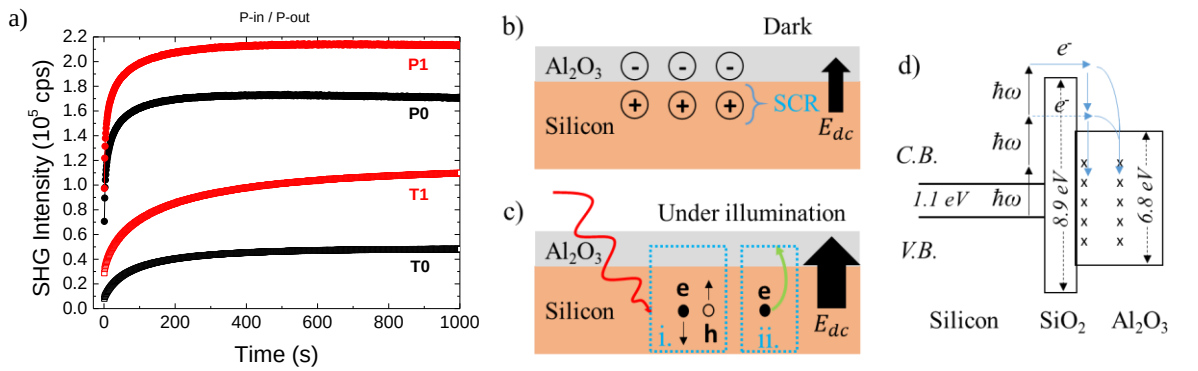

Figure 4.15: (a) Time-dependent SHG measurements on 15nm thermal and plasma ALD Al_2O_3 on Si (100) samples (as-deposited in black and annealed in red). b) Static electric field at the interface caused by negative fixed charges in Al_2O_3 under dark conditions. The negative charges induce positive charges in the Si and a static $E_{dc}(0)$ appears. c) Under illumination the dc electric field can be modified by: i) electron-hole pairs created inside Si and separated due to the pre-existing field, ii) electrons from the Si valence band injected into the oxide via a multi-photon process. d) The 3-photon-assisted electron injection into interface or bulk oxide traps is depicted schematically with the energy band diagram (adapted from [111]*).*

TD-SHG can give information on the charge trapping kinetics. Generally, the time-dependent behaviour of SHG can be fitted by one or more exponentials which are associated with one or more charging mechanisms attributed to different kinds of traps [70], [83]. In the case of Al_2O_3 on Si, charging occurs from photo-generated electrons inside the silicon substrate which are injected at the interface or inside the bulk of the oxide [72] (Figure 4.15d). In our case, injection of charges at the Al_2O_3/air interface is unlikely to occur since the thickness of the film is 15 nm. The SiO_x intermediate layer (0.5-1 nm thickness in our case) present at the Al_2O_3/Si interface is thin enough to play a lesser role in the charge transfer [111]. In order to compare the time dependencies between our samples, the experimental data were fitted by two exponentials:

$$\sqrt{I_{2\omega}(t)} \propto a_0 + a_1(1-e^{-t/\tau_1}) + a_2(1-e^{-t/\tau_2}) \qquad (4.12)$$

where a_i are constants and τ_i are the time constants associated to charging mechanisms. An example of the fitting curves is shown in Figure 4.16 for sample T1 and the fitting parameters are reported in Table 4.8 for all four samples.

Table 4.8: Time constants extracted from TD-SHG exponential fitting and D_{it} values from C-V measurements

Sample	D_{it} (eV^{-1} cm^{-2})	τ_1 (s)	τ_2 (s)
P0	10^{13}	5	63
P1	$3x10^{12}$	6	90
T0	10^{11}	29	172
T1	$2x10^{10}$	35	268

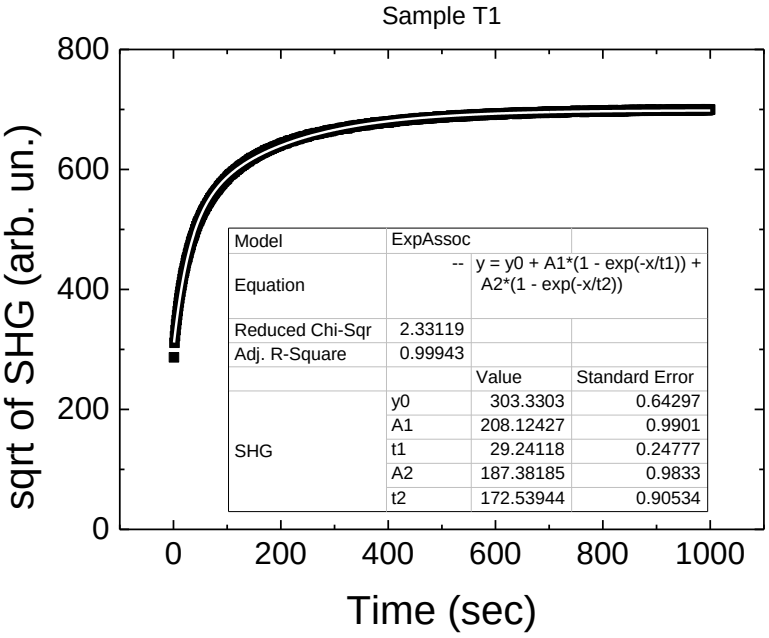

Figure 4.16: Square root of the SHG signal versus time and fitting curve with two exponentials for the as-deposited thermal ALD sample.

In all cases an initial fast signal increase is followed by a slower time variation ($\tau_1 < \tau_2$). Comparing the two processes, we see that T0-T1 samples have higher time constants than P0-P1 samples, indicating faster trapping for plasma ALD samples, which is consistent with the much larger values of D_{it}. Generally, the higher D_{it} concentrations are associated with the smaller time constants. Annealing the as-deposited samples (P0, T0) caused an increase in both time constants. The larger time constants τ_2 related to the slow increase of SHG, can be associated to the saturation of trapping sites [111]. The fact that annealing passivates the interface traps (verified by a noticeable decrease of the D_{it} values in Table 4.8 and by the increase of field-effect passivation) can explain the increase in both time constants.

Another way to monitor the trapping/detrapping dynamics is to irradiate the sample for some time so that electrons can get trapped, then block the laser letting the traps discharge, and finally re-irradiate the sample on the same spot, in order to observe any residual trapped charges. Figure 4.17 shows the SHG response measured on the same samples with the following sequence: irradiation time of 50 minutes, subsequent blocking of the laser for 435 minutes and re-irradiation for 60 minutes. For P0 and P1 samples, SHG intensity initially increases for around 8 minutes until it reaches a maximum and then it starts decreasing. Similar decreasing SHG signals after a maximum value were observed in the Si/SiO_2 system [83]: this behaviour was attributed to hole-injection processes and photo-induced generation of new hole trap sites. After blocking the laser, some of the trapped electrons are transferred back to silicon where they recombine with holes. The elevated initial point after re-irradiation reflects the residual laser-induced trapped charges. We can quantify the detrapping by estimating the percentage

of the drop in the SHG signal between the last SHG intensity value before blocking the laser and the first SHG intensity value after re-irradiation. After annealing, the detrapping channels are reduced, so the percentage drop is lower compared to the as-deposited samples.

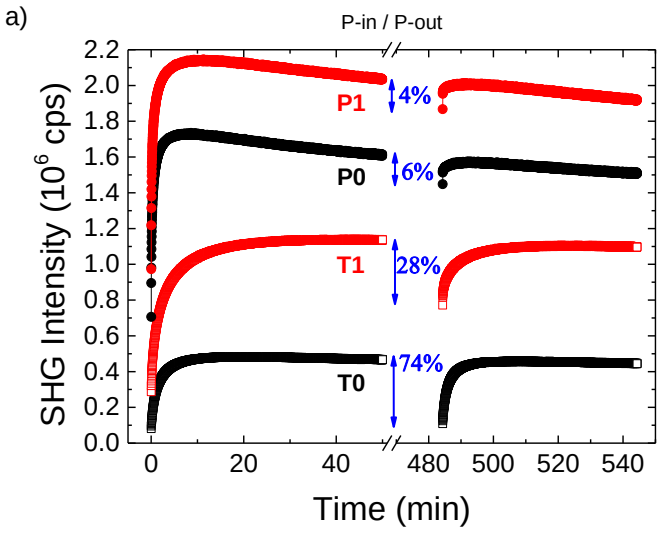

Figure 4.17: TD-SHG for thermal and plasma ALD Al_2O_3 on Si (100). The irradiation time was initially 50 minutes, then the laser was blocked for ~435 minutes and the same spots were re-irradiated for 60 minutes.

4.5.1.2 SHG mapping

Another capability of SHG is to measure the inhomogeneity of the surface properties of the samples (similar to µ-PCD maps in Figure 4.5). When a sample is irradiated at a specific point, the SHG signal will depend on the local interface properties, such as the fixed charges and interface traps. Although the ALD process is uniform, it strongly depends on the substrate surface and the final passivation treatment, which does not necessarily provide the exact same values of Q_{ox} and D_{it} across a wafer. In order to perform SHG mapping, the first batch of thermal-ALD samples was used (A0, A1, B0, B1) and the results were compared to their minority carrier lifetime mapping (Table 4.1, Figure 4.5). The angle of incidence was set at 45° and the irradiation time was short (1 s). P-polarization was used for both incident and detected beam. Figure 4.18 was obtained on the A0, A1 samples (thermal ALD Al_2O_3 on Si(100)), while Figure 4.19 on B0, B1 samples (thermal ALD Al_2O_3 on Si(111)). Each map was normalized with its own maximum value. We calculated approximately 20% signal variation for sample A0, 40% for A1, 10% for B0 and 40% for B1. Annealing seems to increase the non-uniformity of the surface which could be attributed to inhomogeneous surface termination from the wet chemical cleaning. However, in-depth analysis would be necessary to investigate this effect.

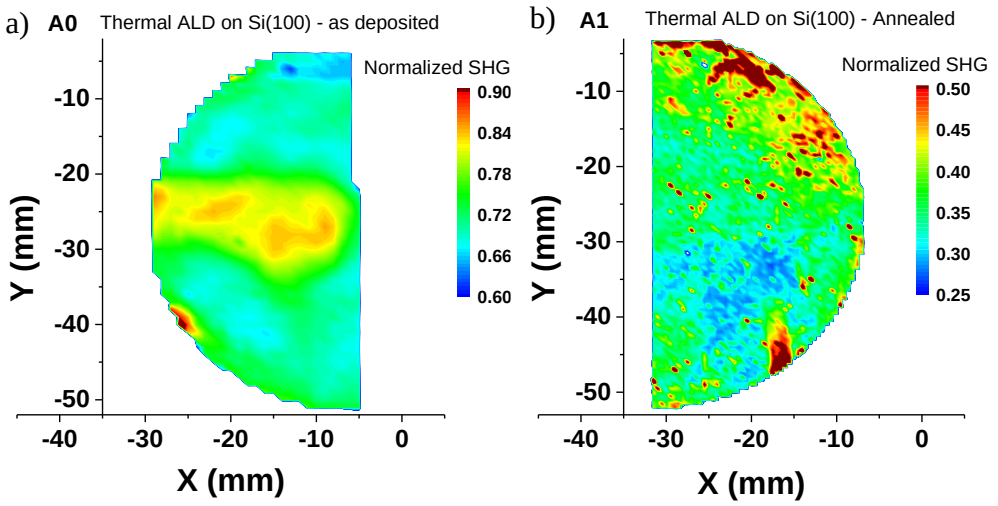

Figure 4.18: Normalized SHG maps on Al_2O_3 deposited of Si (100): (a) as-deposited and (b) after annealing. Each contour is normalized with its own maximum SHG signal. The spatial resolution of the measurements is 1mm.

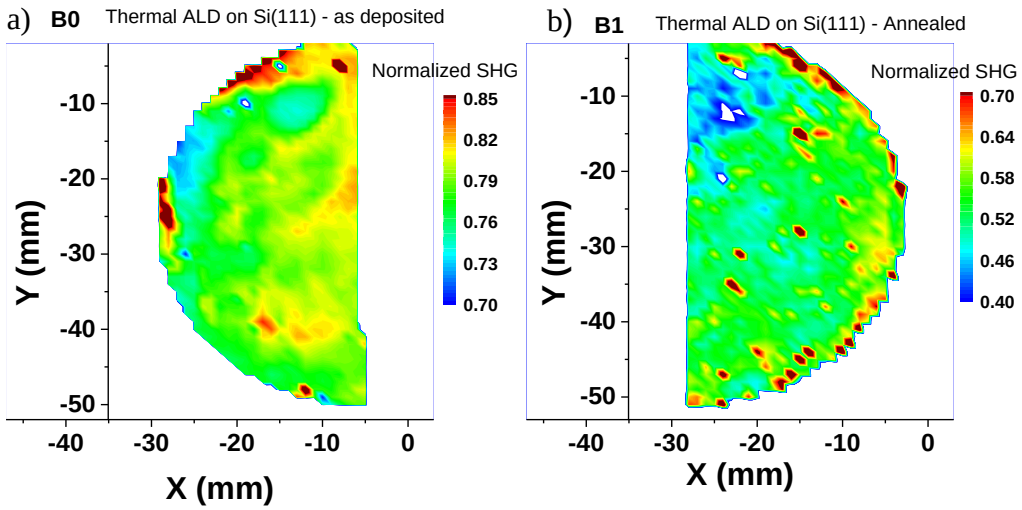

Figure 4.19: Normalized SHG maps on Al_2O_3 deposited on Si (111): (a) as-deposited and (b) after annealing. Each contour is normalized with its own maximum SHG signal. The spatial resolution of the measurements is 1mm.

4.5.2 Initial SHG (at t=0)

In this section we focus on the initial SHG values at t=0 which we correlate with the minority carrier lifetime τ_{eff} extracted from µ-PCD and with the E_{dc} values calculated from C-V curves.

4.5.2.1 Correlation with τ_{eff}

As explained previously, the first data point on each SHG curve in Figure 4.15 (at t=0) can be associated to the fixed charges Q_{ox} present at the interface and initially charged D_{it}, before any significant laser-induced charge-trapping can occur. We observe higher initial SHG for the plasma ALD

(P0, P1) than for the thermal ALD (T0, T1) process, which can be accredited to the higher D_{it} concentration and/or higher Q_{ox} density for the former. Furthermore, for each process, the SHG intensity increases after annealing, which is consistent with the increase of fixed negative Q_{ox}, causing the enhancement of the dc field.

Figure 4.20 compares the normalized initial SHG values (at t=0) with the normalized lifetime values (from Table 4.5). It is clear that both carrier lifetime and SHG increase after annealing. Minority carrier lifetime is proportional to Q_{ox}^2/D_{it} [109], [13], and SHG is proportional to Q_{ox}^2, since the SHG signal depends quadratically on E_{dc}: $I_{2\omega} \propto \left|\chi^{(2)}_{\text{interface}} + \chi^{(3)}E_{dc}\right|^2 (I_\omega)^2$, with $E_{dc} = Q_{ox}/\varepsilon_{Si}$. Annealed samples have more negative charges and exhibit higher SHG signal since the E_{dc} term is higher.

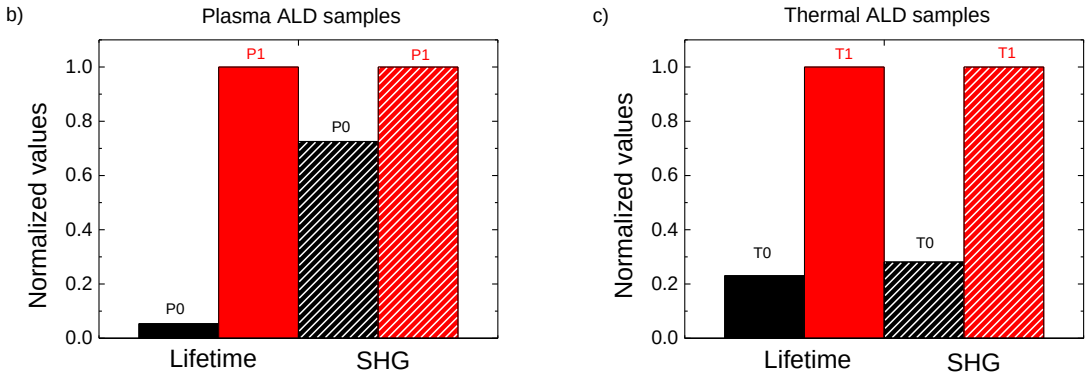

Figure 4.20: Normalized carrier lifetimes measured by µ-PCD and normalized SHG signals for as-deposited and annealed samples prepared with a) plasma ALD and b) thermal ALD processes. The normalization was done for each set with the respective maximum of each measurement technique.

4.5.2.2 Correlation with E_{dc}

Rewriting $I_{2\omega} \propto \left|\chi^{(2)} + \chi^{(3)}E_{dc}\right|^2 (I_\omega)^2$ we obtain that the square root of the SH intensity (at t=0) is roughly proportional to E_{dc}:

$$\sqrt{I_{2\omega}} \propto \left|\chi^{(2)} + \chi^{(3)}E_{dc}(0)\right| I_\omega \qquad (4.13)$$

In order to associate the initial SHG signal with the static electric field E_{dc} induced by pre-existing Q_{ox} and charged D_{it}, the square root of the initial SHG for each sample is plotted versus E_{dc}, calculated from the C-V curves (Figure 4.21). The linear relationship between $\sqrt{I_{2\omega}}$ and E_{dc}, announced by eq. (4.13) agrees well with the SHG experimental data. This corroborates the fact that SHG can probe the oxide/Si interface electric field and that EFISH is the main contribution to the initial second harmonic signal in our samples.

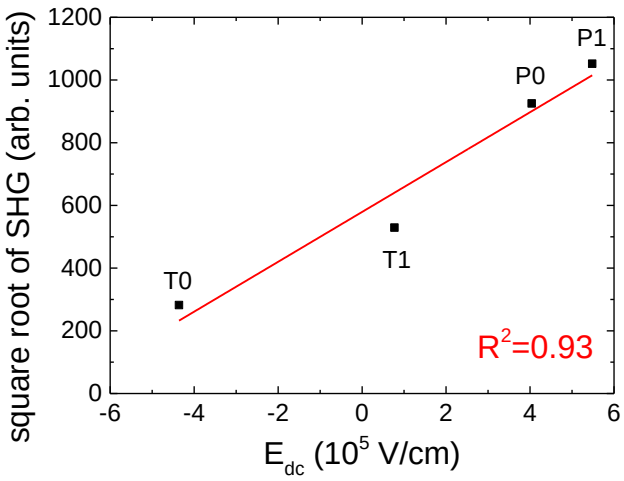

Figure 4.21: Square root of initial value of SHG signal versus the value of static electric field calculated from Q_{ox} extracted in C-V measurements (see Table 4.6).

In order to move towards a method of extracting E_{dc} by using SHG, we return to modelling in order to understand the impact of the geometry and/or of the electric field and to imagine an SHG experiment for obtaining E_{dc}.

4.5.3 SHG modelling in Al_2O_3

4.5.3.1 Geometry effect

In order to access electrical parameters, one must anticipate the impact of optical effects on SHG by using proper simulation, as mentioned in Chapter 3. Therefore, when comparing structures with different film thicknesses or even when choosing the angle of incidence in SHG experiments, the optical path is modified and these effects will eventually influence the measurements.

We used the 3rd batch of samples (Table 4.3) to investigate the thickness impact. SHG was measured on three samples with thicknesses 5, 15 and 25 nm, after annealing (Figure 4.22). The optical simulation reproduces the experimental thickness dependence trend of the SHG. It should be noted that an electric field of 10^5 V/cm was included in the simulation (the same order of magnitude as in Table 4.6). The good agreement validates our simulator for the Al_2O_3 case.

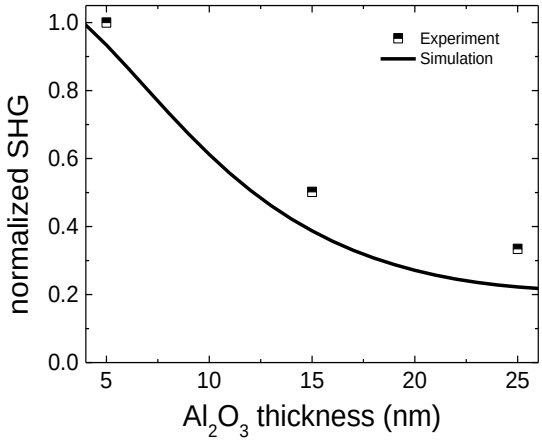

Figure 4.22: Experimental and simulated SHG intensity versus Al_2O_3 thickness. The measurements were performed at 45° angle for P-input/P-output polarizations. The normalization was done by dividing each set (experimental and simulated) with its corresponding maximum value.

Another way to verify the impact of the optical effects is to vary the angle of incidence (AOI). The AOI is ideal since it alters the propagating path of the fundamental and harmonic beams, which inevitably affect the interference pattern. In Figure 4.23 we compare the experimental (a) and simulated (b) SHG versus AOI for the 5, 15 and 25 nm Al_2O_3 samples. The same value of E_{dc} (10^5 V/cm) was used for all simulations. The relative changes between the samples can be mainly explained through thickness effects.

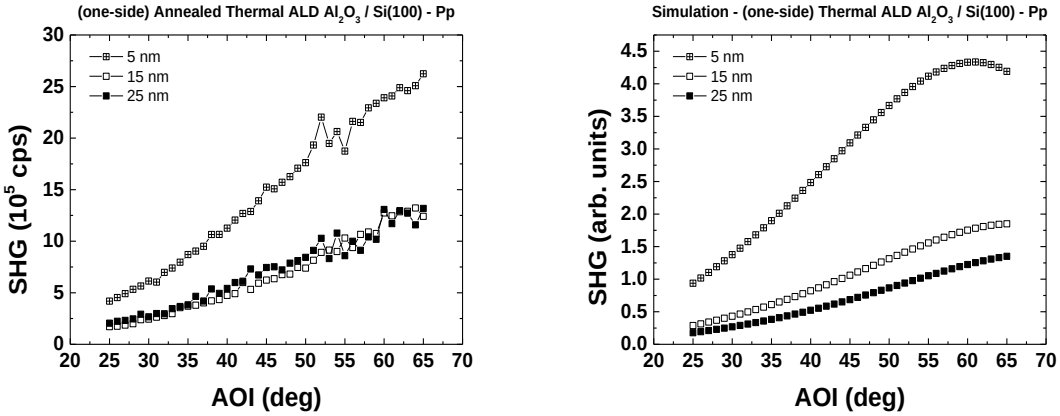

Figure 4.23: a) experimental and b) simulated SHG vs AOI for P-input / P-output polarization combinations, for 3 different sample thicknesses. The change in the layer thickness is appropriate enough to explain the differences in observed SHG.

4.5.3.2 SHG modelling including E_{dc}

An approach of finding the E_{dc} field without resorting to electrical techniques is to measure the SHG versus AOI for both as-deposited and annealed samples with the same film thicknesses in order to remove the thickness effects shown previously (samples from 3rd batch). Figure 4.24 shows the initial SHG signal (at t=0) versus the angle of incidence (data points), and an offset is observed between the

two samples for each ALD process. We attribute this difference to the change in the dc field after annealing. In order to investigate this, we could simulate the SHG using the polarization expression from Chapter 3 with the electric field term:

$$P_{P-in/P-out}^{NL} \propto \left[\left(\chi_{zzz}^{(2)} + E_{dc} \right) F_s f_s^2 + \chi_{zxx}^{(2)} F_s f_c^2 - \chi_{xzx}^{(2)} 2 F_c f_s f_c - \frac{i}{4} \lambda_\omega n_\omega \zeta (3 F_c f_c^2 f_s + 4 F_s f_s^2 f_c + F_c f_s f_c) \right] E_\omega^2 \quad (4.14)$$

The values for each $\chi^{(2)}$ component used in the model were taken from ref. [51] while for $\chi^{(3)}$ the typical order of magnitude was used for bulk 3rd order susceptibilities [30] (Table 3.1 in Chapter 3).

However, the real values of $\chi^{(2)}$ could be different from the ones used in the simulation, since the material preparation and process varies. Additionally, the sign and value of the E_{dc} term can cancel out the $\chi_{zzz}^{(2)}$ term in Equation (4.14). Therefore, since absolute values of $\chi^{(2)}$ and $\chi^{(3)}$ were difficult to obtain, we used a "differential" approach for simulating the AOI experiments:

1. We consider the as-deposited sample as a reference, which we simulated using eq. (4.14) with E_{dc}=0 and the $\chi^{(2)}$ values from the literature [51].
2. We calculated the algebraic difference between the dc field magnitudes of as-deposited and annealed samples ΔE_{dc} from Table 4.6, which we added in the simulation using eq. (4.14). This curve was considered to correspond to the annealed sample.
3. Finally, a normalization was done by dividing each set (experimental and simulated) with its corresponding maximum values.

As seen in Figure 4.24, the optical simulation (solid lines) of SHG versus the angle of incidence agrees well with the actual experiment (symbols). This illustrates the potential of the simulation which includes optical phenomena to investigate indirectly the electrical properties or passivation quality (E_{dc} and thus Q_{ox}) through contactless SHG experiments.

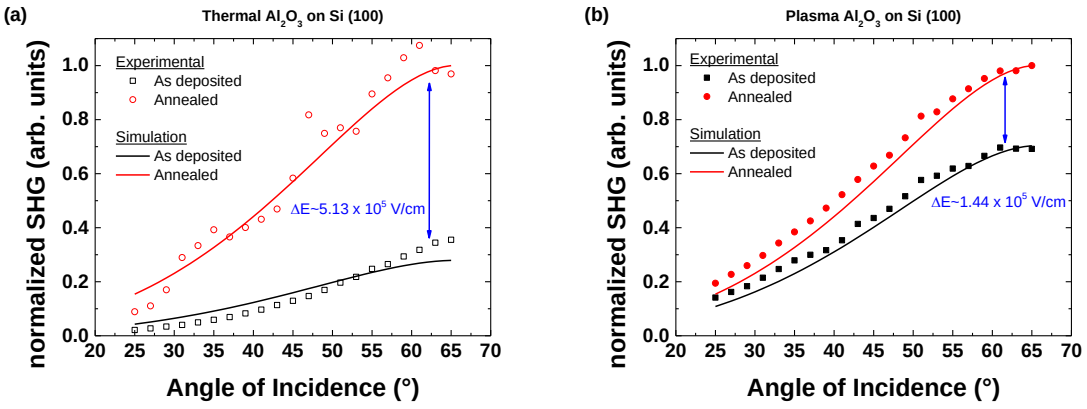

Figure 4.24: Normalized SHG intensity vs angle of incidence for thermal (a) and plasma (b) ALD Al_2O_3. The black (open, filled) and red (open, filled) symbols are the experimental data for as-deposited and annealed samples respectively. The black and red lines are the simulated data for an electric field variation at the interface which was calculated from the V_{FB} shift in the C-V curves. The normalization is done by dividing each set (experimental and simulated) with its corresponding maximum values.

4.5.4 Rotational anisotropic SHG

In order to investigate if the annealing causes any structural changes to the samples, we monitor the SHG versus the azimuthal angle for a 45° angle of incidence. As already seen in Chapter 2, the rotation of the samples around the vertical z-axis gives information regarding the symmetry properties either of the surface/interface (P-in/P-out configuration) or a few nm of the bulk silicon substrate (P-in/S-out configuration). In Figure 4.25, the SHG intensity is monitored versus the azimuthal angle for the P0-P1 samples in a) P-in/P-out and b) P-in/S-out polarization configurations, where we observe the following:

- The intensity in P-in/S-out configuration is 2 orders of magnitude lower than P-in/P-out. This is consistent with the fact that the SH generated from a few layers in bulk Si, $P^{NL}_{P-in/S-out} = (i/4)n_\omega \zeta f_c^2 f_s \sin 4\varphi E_\omega^2$, is weaker than the SH generated from surfaces with large susceptibility components:

$$P^{NL}_{P-in/P-out}(\varphi) = \left[\chi^{(2)}_{zzz} F_s f_s^2 + \chi^{(2)}_{zxx} F_s f_c^2 - \chi^{(2)}_{xzx} 2F_c f_s f_c - \right. \\ \left. -(i/4)\lambda_\omega n_\omega \zeta \left(3F_c f_c^2 f_s + 4F_s f_s^2 f_c + F_c f_s f_c \cos 4\varphi\right)\right] E_\omega^2 \qquad (4.15)$$

- The 4-fold symmetry in P-in/P-out configuration is typical for Si(100) surfaces. This is supported by the simplified expression of the SHG intensity given by [31], [34], [43]: $I^{Pp}_{2\omega} \propto \left| a_0 + a_4 \cos 4\varphi \right|^2$.
- The 8-fold symmetry of the bulk in P-in/S-out configuration is in agreement with the simplified expression [31], [34], [43]: $I^{Ps}_{2\omega} \propto \left| b_4 \sin 4\varphi \right|^2$.
- The annealing influences only the amplitude of the surface/interface component, evidenced by the increase in SHG intensity between P0 and P1 due to the enhanced EFISH contribution (Figure 4.25a), and annealing has no effect on the bulk (Figure 4.25b).

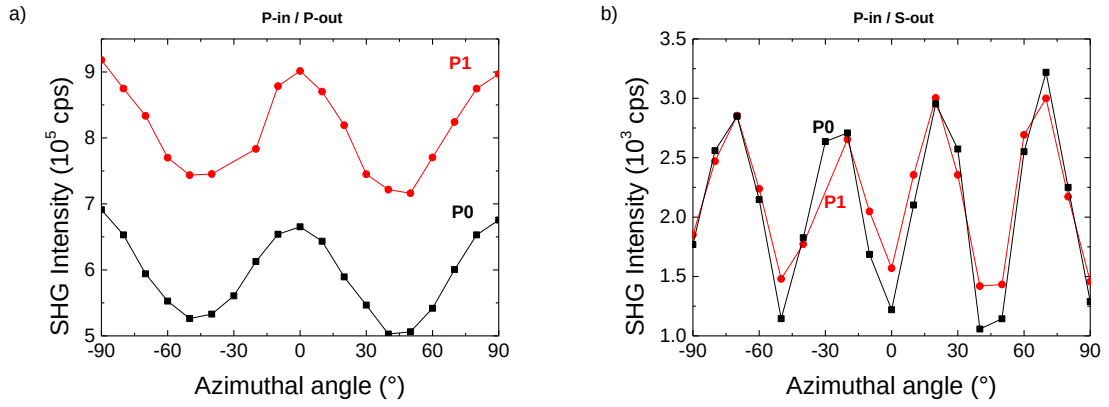

Figure 4.25: SHG vs azimuthal angle for 15 nm P-ALD Al_2O_3 on Si (100). Black square symbols are for as-deposited samples while red circles are for annealed ones. b) P-input/P-output polarization configuration showing the 4-fold symmetry of the surface, b) P-input/S-output polarization configuration showing the 8-fold symmetry of the substrate.

We use the simulation tool to verify the SHG versus azimuthal angle experiments. In Figure 4.26, we simulate the SHG response for a) P-in/P-out and b) P-in/S-out polarization configurations by keeping all the parameters in the simulation the same for the two samples. For the as-deposited sample eq. (4.15) was used, while for the annealed one the E_{dc} is only added in the $\chi^{(2)}_{zzz}$ component (as explained in Chapter 3). Note that the polarization expression for P-in/S-out, $P^{NL}_{P-in/S-out} = (i/4)\lambda_\omega n_\omega \zeta f_c^2 f_s \sin 4\varphi E_\omega^2$, does not include the $\chi^{(2)}_{zzz}$ component. Even though the simulated amplitude ratio for P-in/P-out seems to be affected by the E_{dc} value (Figure 4.26a), which is not the case in the experiment (Figure 4.25a), the experimental azimuthal angle dependency is fairly well simulated.

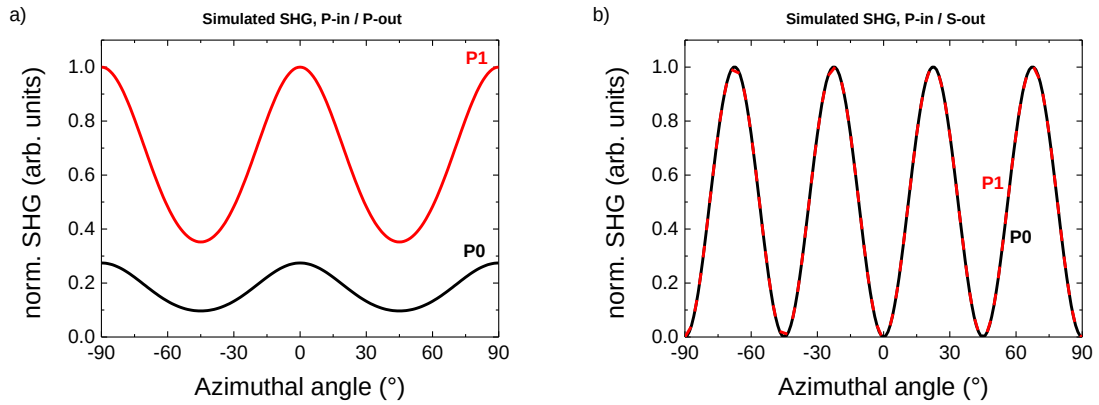

Figure 4.26: Simulated SHG vs azimuthal angle for plasma ALD Al_2O_3 on Si (100). a) P-input/P-output polarization configuration, corresponding to surface response, exhibiting typical 4-fold symmetry. b) P-input/S-output polarization configuration, corresponding to bulk quadrupole response, exhibiting typical 8-fold symmetry. Each data set was normalized by its corresponding maximum value.

In the case of the thermal ALD samples we expect similar azimuthal dependencies, since the symmetry properties emerge from the Si (100) substrate which is the same. In Figure 4.27, the SHG intensity is monitored versus the azimuthal angle for the T0-T1 samples in a) P-in/P-out and b) P-in/S-out polarization configurations, as before. It is clearly seen that the general behaviour is the same as in the case of plasma ALD samples, and similar comments can be made regarding the symmetry and the effect of passivation. However, the surface/interface component of the T1 sample (Figure 4.27a) exhibits a noisy behaviour which could be attributed to a variation of the native oxide layer upon annealing. Furthermore, for the thermal ALD process the bulk contribution (Figure 4.27b) seems to be slightly affected as well after the annealing step. We speculate that since the hydrogen concentration at the interface is higher for the thermal ALD processes due to the H_2O reactant [115], [117], and since the hydrogen diffuses away from the interface with Si after annealing, it could possibly lead to a small structural change in the first few atomic layers inside bulk Si. Nonetheless, an exhaustive study must be done in the future for consolidating the causes behind this noisy behaviour.

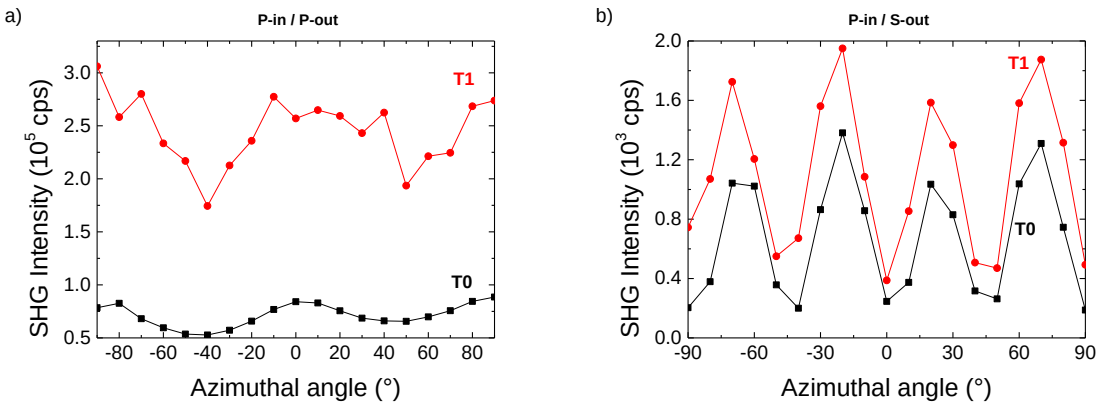

Figure 4.27: SHG vs azimuthal angle for 15 nm T-ALD Al_2O_3 on Si (100). Black square symbols are for as-deposited samples while red circles are for annealed ones. b) P-input / P-output polarization configuration showing the 4-fold symmetry of the surface, b) P-input / S-output polarization configuration showing the 8-fold symmetry of the substrate.

4.5.5 Impact of the Si substrate crystallography

All of the previous experiments and discussion were done for Al_2O_3 films deposited on Si (100) substrates. Figure 4.28 shows that the time dependent behaviour measured on Al_2O_3/Si(111) is similar to Al_2O_3/Si(100) but the SHG levels (initial and saturation) are behaving differently. For both plasma and thermal processes, the as-deposited samples (Px0, Tx0) exhibit higher SHG than the annealed ones (Px1, Tx1), in contrast to what was observed for Si (100) substrates (Figure 4.15a). The question is whether this result is unexpected or not.

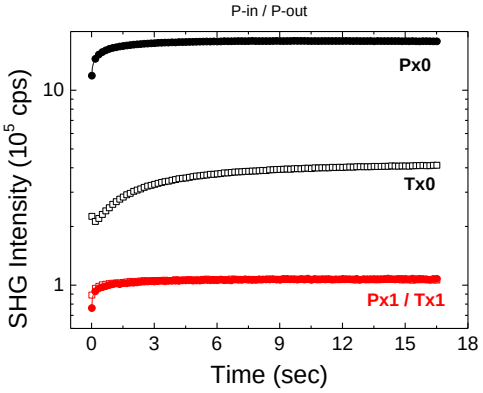

Figure 4.28: TD-SHG for thermal and plasma ALD Al_2O_3 on Si (111). The annealed samples (Px1, Tx1) show higher SHG than the as-deposited ones (Px0, Tx0).

Note that the interfaces between dielectrics and Si (111) substrates have different susceptibility components than Si (100) comprising the 2nd order polarization [42]. By changing the azimuthal angle of the sample, we can highlight the different symmetries of the Si (111) substrates which could possibly explain the discrepancies. In Figure 4.29 and Figure 4.30 we plot experimental SHG versus azimuthal angle for the plasma and thermal ALD Al_2O_3 (15 nm) respectively, on Si (111) substrates. Indeed, for

the P-in/P-out polarization configuration, we clearly see the anisotropy of the rotational SHG signals when comparing as-deposited and annealed samples. In contrast to the Si (100) substrates, the as-deposited samples (Px0, Tx0) at 0° azimuthal angle have stronger SHG signals than the annealed ones (Px1, Tx1), although we would normally expect to measure a higher SHG signal after annealing.

Furthermore, the P-in / S-out signals have the same order of magnitude as the P-in/P-out case. This is attributed to the fact that in the polarization expression for silicon with (111) orientation there is an extra surface susceptibility term $\chi_{xxx}^{(2)}$ superimposed on the bulk anisotropic term ζ, $P_{2\omega}^{Ps} = \left[\chi_{xxx}^{(2)} f_c^2 + \lambda_\omega n_\omega \zeta (i\sqrt{2}/6)\left(f_c^2 - 2 f_s^2 f_c \right) \right] \sin 3\varphi E_\omega^2$. For this reason, the SHG isotropic level is set by the strong surface term $\chi_{xxx}^{(2)}$ (same order of magnitude as the other surface elements), while the weak bulk anisotropic term ζ modulates the response, thus exhibiting the 6-fold symmetry of the bulk.

The validation step through simulation would need to accommodate the correct polarization expression for Si (111) substrates. We must keep in mind that the nature of the substrate and its relevant position (regarding rotation) when characterizing it with SHG, are of paramount importance, and care must be taken when SHG signals from different samples are studied.

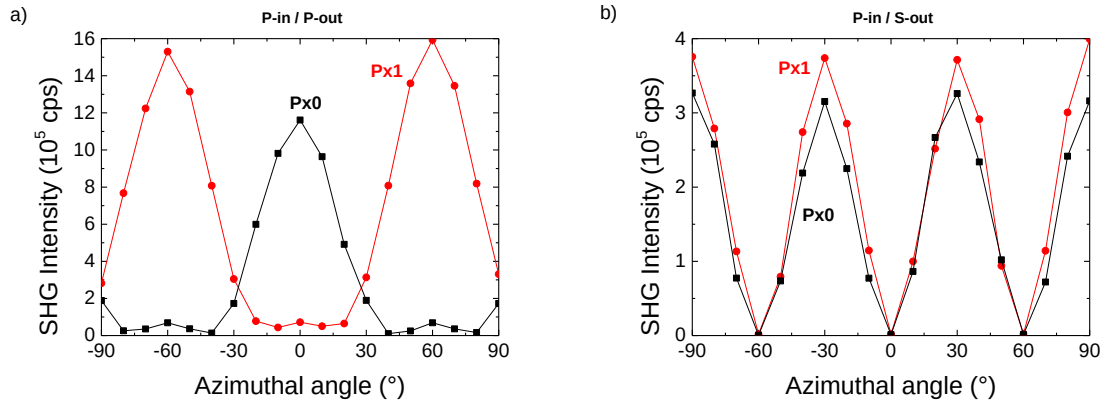

Figure 4.29: SHG vs azimuthal angle for 15 nm plasma ALD Al_2O_3 on Si (111). Black square symbols are for as-deposited samples while red circles are for annealed ones. b) P-input/P-output polarization configuration showing the 6-fold symmetry of the surface, b) P-input/S-output polarization configuration showing the 6-fold symmetry of the substrate.

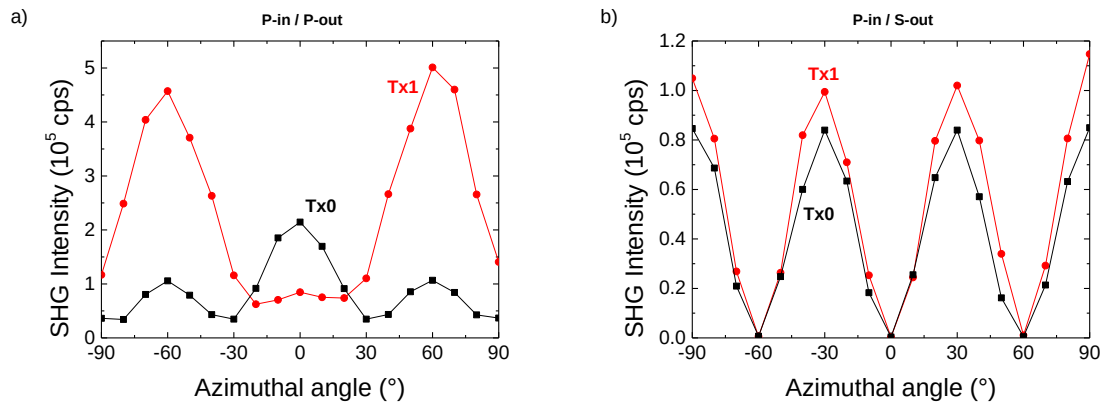

Figure 4.30: SHG vs azimuthal angle for 15 nm thermal ALD Al_2O_3 on Si (111). Black square symbols are for as-deposited samples while red circles are for annealed ones. b) P-input/P-output polarization configuration showing the 6-fold symmetry of the surface, b) P-input/S-output polarization configuration showing the 6-fold symmetry of the substrate.

4.6 Conclusions

In this chapter, we investigated the capacity of SHG to monitor the field effect passivation due to fixed oxide charges in Al_2O_3 on Si. Conventional μ-PCD and C-V measurements revealed the minority carrier lifetime (τ_{eff}), the interface trap density (D_{it}) and the fixed oxide charge density (Q_{ox}) which helped estimating the static electric field (E_{dc}) at the interface between Si and Al_2O_3. The time-dependent dynamics of EFISH showed the SHG time evolution is fast (slow) for high (low) D_{it} values. Afterwards, the initial SHG was correlated with the quantities obtained from the conventional characterization techniques:

a) SHG measurements were compared with minority carrier lifetime values corroborating the possibility for contactless probing of Al_2O_3/Si interfacial quality.
b) We showed that the square root of the SHG intensity scales linearly with the electric field value as expected.
c) SHG simulations fed with the shifts in values of the electric fields inside Si, could reproduce the experimental data.

By coupling SHG versus angle of incidence experiments in samples with unknown E_{dc} fields, and a simulation tool we could eventually estimate the electric field values from the data. By decorrelating optical phenomena, the combination of experiment and simulation paves the way for a pragmatic oxide charge quantitative analysis via SHG. In the future, optimized ALD procedures will be used to create a range of samples in order to examine the sensitivity limits of the technique as well as variability issues.

Chapter 5:
SHG Characterization of SOI Structures

In this chapter we investigate SHG as a non-invasive, non-destructive characterization technique for monitoring the quality of film, oxide and interfaces in silicon-on-insulator (SOI) wafers. The experimental parameters such as polarization angles, angle of incidence, and azimuthal angle were optimized for experiments on SOI. The influence of SOI geometry (Si film/BOX thicknesses), dc electric fields at each interface, as well as surface post-treatment (passivation) will be explored and compared with theoretical simulations performed with our home-made simulation tool.

Contents of Chapter 5

5.1 Silicon-on-insulator: fabrication, defects & Ψ-MOSFET characterization

Silicon-on-insulator (SOI) technology was born with the introduction of silicon-on-sapphire [119] wafers, which were interesting for military and space applications due to their increased resistance to radiation, but were very costly to produce. SOI structures consist of a top silicon layer, separated from the bulk substrate by an insulating layer which provides a good electrostatic control on the future device. There exist several technologies to fabricate SOI wafers such as Separation by IMplantation of OXygen (SIMOX [120], [121]), bond and etch-back SOI (BESOI [122]), Epitaxial Layer Transfer Wafer (Eltran [123]). However, their low-quality interface was a limiting factor but the development of the SmartCut™ process [124] allowed production of SOI materials of the highest quality.

5.1.1 SmartCutTM fabrication process

SmartCut™ technology is a technique based on implantation of light ions and direct bonding of two wafers in order to define and transfer ultrathin single-crystal layers from one substrate to another. It works like an atomic scalpel and allows active layers to be managed independently from the supporting mechanical substrate [125]. Generally, it consists of the following basic steps (Figure 5.1):

- Initially two Si wafers are required: a donor wafer A and a handle wafer B.
- SiO_2 is grown on wafer A through thermal oxidation; this will become the buried oxide (BOX) layer of the final SOI wafer.
- Ions are implanted in wafer A through the oxide: they induce a buried weak zone in the Si (microcavities depicted with dashed lines in Figure 5.1) that will define where the fracture will take place later.
- Wafer A is cleaned and directly bonded to wafer B. Bonding occurs after a conditioning process which makes the wafer surfaces hydrophilic, thus well suited to spontaneous direct adhesion at room temperature.
- The bonded wafers are annealed in order to increase the pressure of the implanted ions in the microcavities, which cause a horizontal fracture in wafer A. The two wafers are separated.
- Wafer B undergoes annealing and chemical-mechanical polishing (CMP) and is the SOI substrate. Wafer A can be reused for another SmartCut™ fabrication process.

This technology has several advantages such as excellent Si film and BOX thickness control, high quality interfaces, low density of defects at the interface, and recycling of the handle wafer which reduces costs.

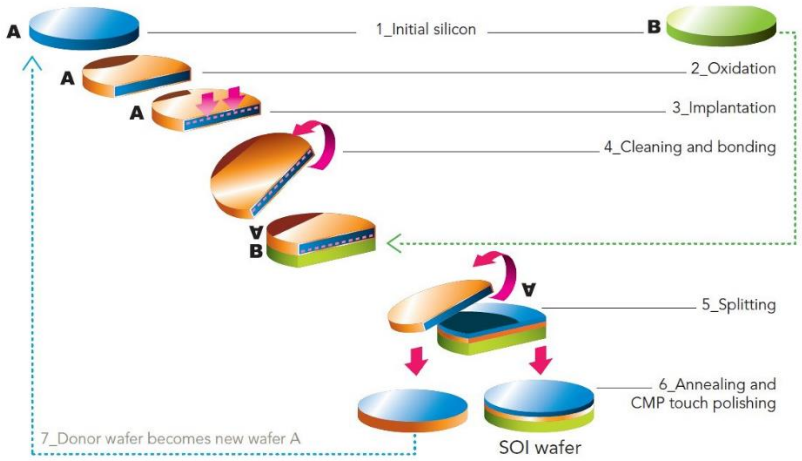

Figure 5.1: Schematic with basic steps in SOI wafer manufacturing with the SmartCut™ process [125].

5.1.2 SOI defects

During the various process steps of SOI manufacturing, defects can show up at the interface or in the different layers, which can cause performance decrease and device failure, especially when downscaling the technology. Typical defects include (Figure 5.2) [126]:

- "Pipes", which are conductive paths caused by defects in the BOX or Si film that can induce leakage currents and affect device and transistor performance.
- Surface roughness.
- Residual oxygen or carbon in the silicon film from the fabrication procedure, which also decrease the breakdown voltage.
- Fixed charges in the BOX (Q_{ox}), which eventually affect leakage and shift the threshold voltage of transistors.
- Interface trapped charge (D_{it}) at the SiO_2/Si interfaces, which can eventually decrease the carrier mobility and increase the subthreshold swing, limiting transistor performance.
- Contaminations (metal or alkaline ions) typically metallic (either at the bulk of the Si film or BOX or their interfaces), which affect the electrical properties of the structure and decrease the mobility and minority carrier lifetime.

We will focus here on Q_{ox} and D_{it}. Both have an impact on the electrical characteristics of the SOI and on the device that will be fabricated eventually, hence they must be minimized. For this reason, electrical characterization techniques are needed for material quality evaluation before MOSFET manufacturing.

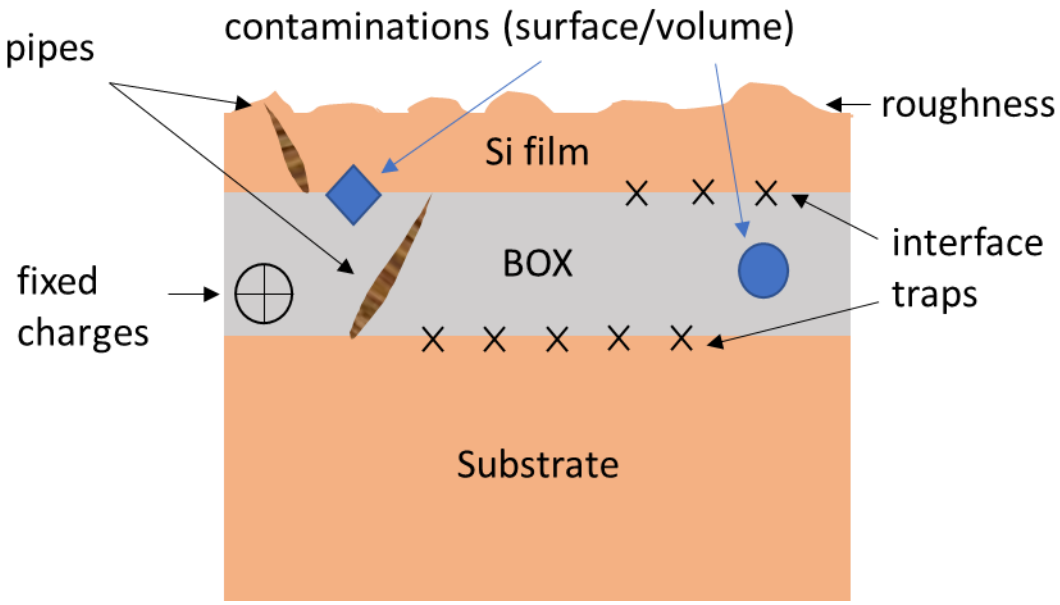

Figure 5.2: Typical SOI defects such as pipes, surface and volume contaminations, fixed charges (Q_{ox}) and interface traps (D_{it}).

5.1.3 Ψ-MOSFET characterization

The pseudo-MOS transistor (Ψ-MOSFET) technique [127], [128], was specifically developed for SOI characterization, without necessitating fabrication of MOS test structures, since the BOX serves as a gate dielectric. The substrate is placed on a metallic chuck and is biased as a back-gate (Figure 5.3a). Two metallic probes placed on the top silicon film play the role of source and drain. The current flowing between source and drain (I_D) is controlled by the voltage applied on the back-gate (V_G). The particularity of the Ψ-MOSFET for a lightly doped silicon film (~10^{15} cm^{-3}), is that channels of electrons or holes can be induced in the same SOI structure, thanks to the metallic source and drain that can provide both. Consequently, both electrons and holes are tested with the same structure. This technique characterizes efficiently reliability, yield, and variability due to charge traps and associated defects at interfaces [129], [130]. In fully depleted SOI transistors, these charge traps can cause significant bias temperature instabilities (degradation of V_{th} with changing bias at elevated temperatures) [130], [131] as well as hot carrier stress which can have a detrimental impact in device reliability [132].

A typical measured I_D-V_G curve (in semi-log scales) for a Ψ-MOSFET configuration, is shown in Figure 5.3b. The sample had a 88 nm Si film and 145 nm BOX thickness, exhibiting electrical characteristics similar to those in fully-processed MOSFET's.

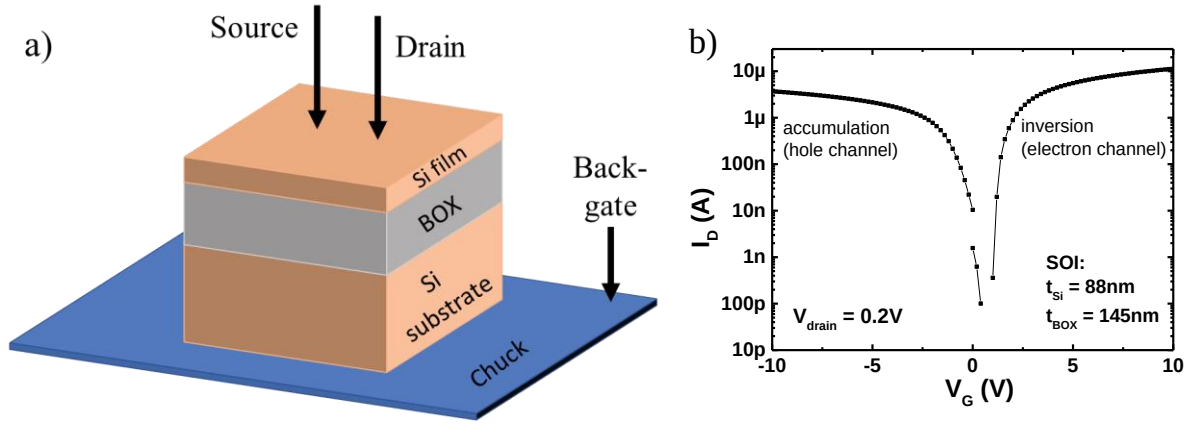

Figure 5.3: a) Schematic of the Ψ-MOSFET technique in SOI structures. b) Drain current versus gate voltage in a SOI with 88 nm of Si film thickness and 145 nm of buried oxide thickness.

At V_G=0, the Si film can be depleted due to Q_{ox} and D_{it} present in the BOX. At V_G=V_{FB} we have the flat-band condition. In the case of V_G<V_{FB}, the Si film will be accumulated with holes, which form a conduction channel (left side in Figure 5.3b and Figure 5.4a). For V_{FB}< V_G<V_T (threshold voltage), the Si film is depleted, while for V_G>V_T, a conductive channel of electrons is created (right side in Figure 5.3b and Figure 5.4b).

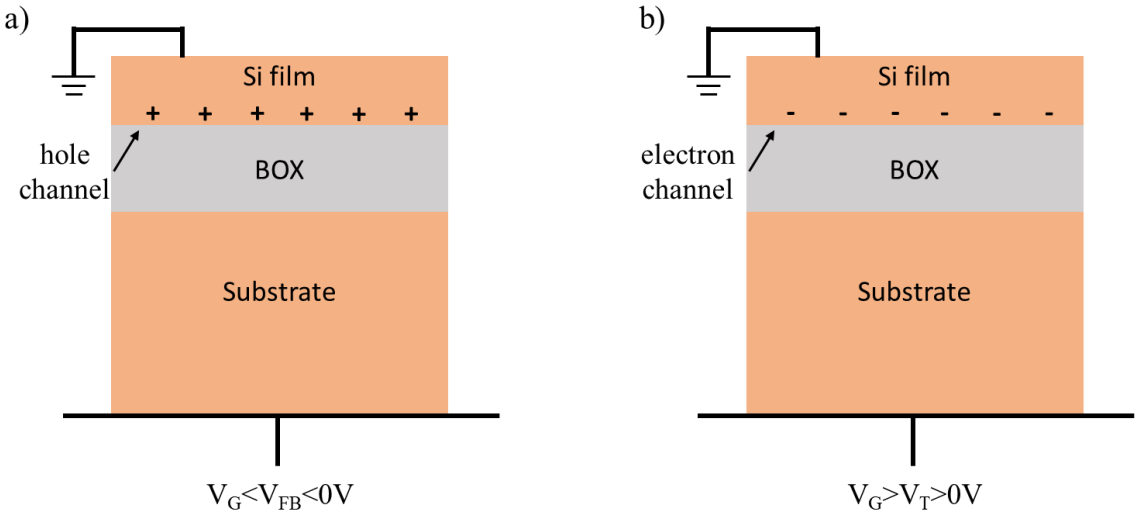

Figure 5.4: a) Hole channel for negative bias (V_G<V_{FB}<0V) and b) electron channel for positive bias (V_G>V_T>0V).

It should be noted that the use of electrical probes can damage the ultrathin Si film layer [126]. In Figure 5.5 we probe with Atomic Force Microscopy (AFM) the surface morphology of the Si film in a 88 nm Si film/145 nm BOX structure. The scanned area is where one of the Ψ-MOSFET probes was in contact and clearly there is some damage (scratches) reaching ~30 nm depth for a probe pressure of 100 g (probe radius is ~40 μm). This shows that the technique can damage the surface, especially in ultrathin SOI. For this reason, non-invasive characterization techniques such as SHG, able to give access to electrical parameters are very promising.

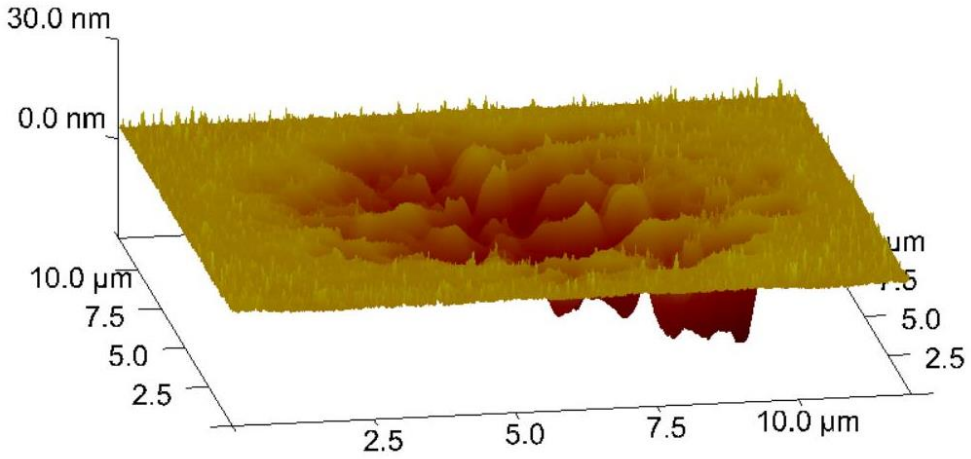

Figure 5.5: Probe scratches on a 88 nm/145 nm SOI, imaged by AFM.

5.2 SHG characterization of SOI: state of art

SHG was already used for non-destructive and contactless characterization of SOI. Jun et al. [32] have demonstrated that the SHG signal from SOI depends on time due to laser-induced charge trapping and varies if there is a native oxide on top of the structure. Figure 5.6 shows the time-dependent SHG in SOI structures with:

a) Native oxide on top of the Si film.
b) No oxide on top of the Si film (etched).

For both cases two regions on the same sample were scanned: one from the exposed BOX (where the Si film was etched) and one from the full SOI structure (denoted as "island" in the figure).

In the case of naked BOX, the electrons are photoinjected to interface traps but not at the surface of the oxide since it is thick. The induced electric field originates mostly from the electron hole separation which screens the pre-existing field, thus reducing it. This is similar to the discussion in Chapter 2 (§2.2). This is the origin of the decrease in temporal SHG signals from the naked BOX. For the same reason, the time dependence is weaker (A→B, D→E in Figure 5.6a). Even after blocking the beam and re-irradiating on the same spot, no significant changes are visible (B→C). Meanwhile, between the sample with the native oxide (Figure 5.6a) and the one without (Figure 5.6b), the BOX values do not vary significantly (A, Q and B, R), which is expected since the same BOX/substrate interface is probed in both cases.

The SHG signal from a Si island increases monotonically (F→G) as electrons are injected from the Si film to the native oxide and to the oxide surface (getting trapped by ambient oxygen molecules); SHG reaches saturation (G) when the trap sites are filled. At some point the beam is blocked for a period of time (G→H) and the electron photo-injection stops; previously trapped electrons are tunnelling back

to the Si film and recombine with holes. When the same spot is re-irradiated, the SHG signal starts from a lower level (H) compared with the previous saturation level (G). The initial point in the SHG data after re-irradiation is higher than the first initial point (H>F) since not all electrons are detrapped. Furthermore, SHG measurements on new islands (fresh measurement points) confirmed the repeatability of the process (J→K). The SHG intensity from the etched native oxide SOI (L, M in Figure 5.6b) is much smaller than the SHG from the sample with a native oxide (F, G in Figure 5.6a), which means that the SHG signal is dominated by the native oxide/Si film interface.

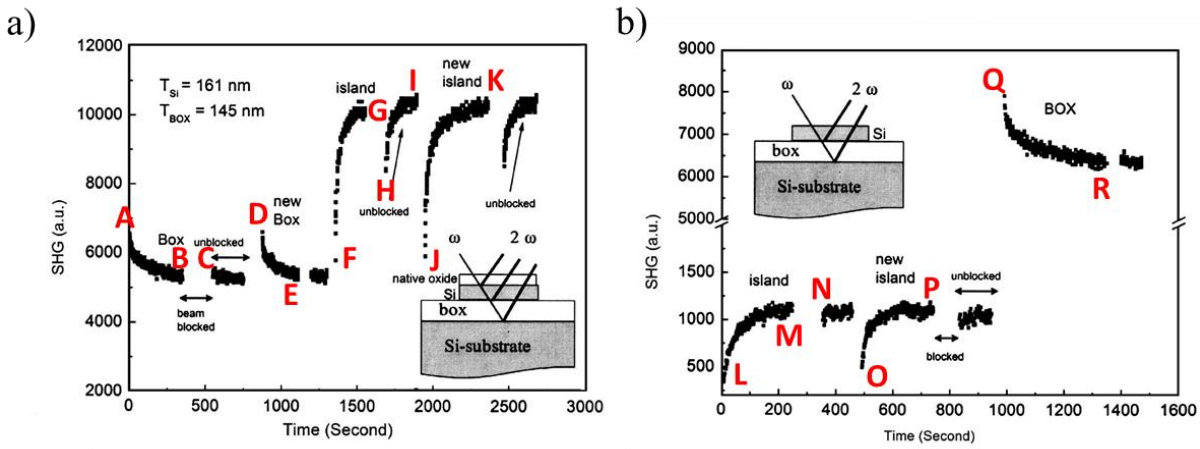

Figure 5.6: Time-dependent SHG signals from a SOI with t_{Si}=161 nm and t_{BOX}=145 nm having either: a) 3 interfaces (with top native oxide) and b) 2 interfaces (without top oxide) [32]. *The fundamental beam wavelength was 800 nm with an average power of 730 mW.*

Alles et al. [133]–[135], [33] have demonstrated that the time-dependent SHG from SOI is affected by thermal processing steps (Figure 5.7a) and metallic contaminations, such as Ni (Figure 5.7b). Regarding the thermal treatment, various temperatures affect electrical properties of the SiO_2/Si interfaces (Q_{ox}, D_{it}) directly impacting SHG. Regarding the metal contamination, Ni diffuses extremely fast during high temperature process steps, while during cool-down it precipitates at the top oxide/Si film and Si film/BOX interfaces. The more contaminated sample (10^{14} cm^{-2}) induced a stronger SHG than the less contaminated (10^{12} cm^{-2}) and the reference samples. Moreover, the SHG was correlated with μPCD measurements since metallic contaminations affect the minority carrier lifetime as well (Figure 5.8). The inset of Figure 5.8 shows the contaminated regions as areas of low lifetime (in red). For higher contamination levels, the lifetime is lower and the SHG is higher. These experimental results showed that SHG can be used as a qualitative method for process control metrology.

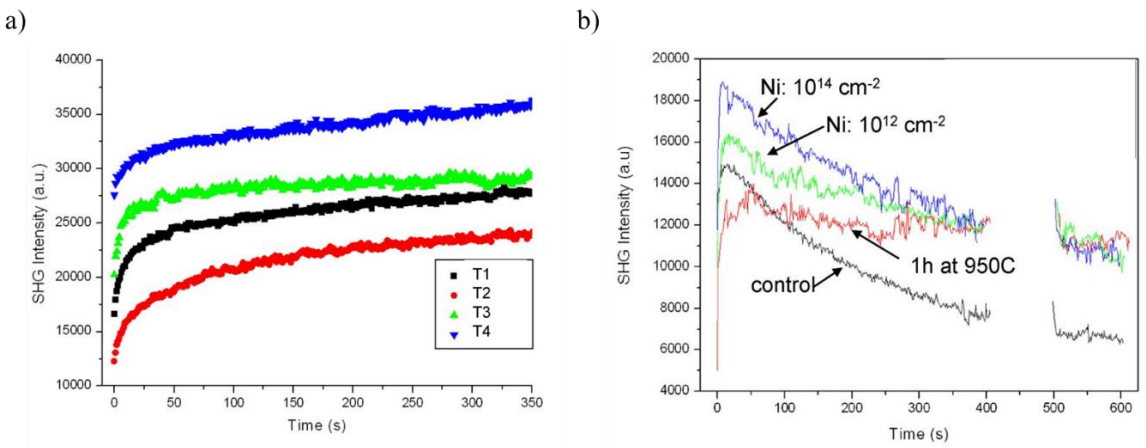

Figure 5.7: SHG measurements on SOI wafers with thicknesses in the range 140-150 nm for the Si film and 50-85 nm for the BOX. a) TD-SHG for different thermal treatments (at various temperatures). b) TD-SHG for two different Ni contamination levels, for an annealed sample at 950°C and a control sample [33].

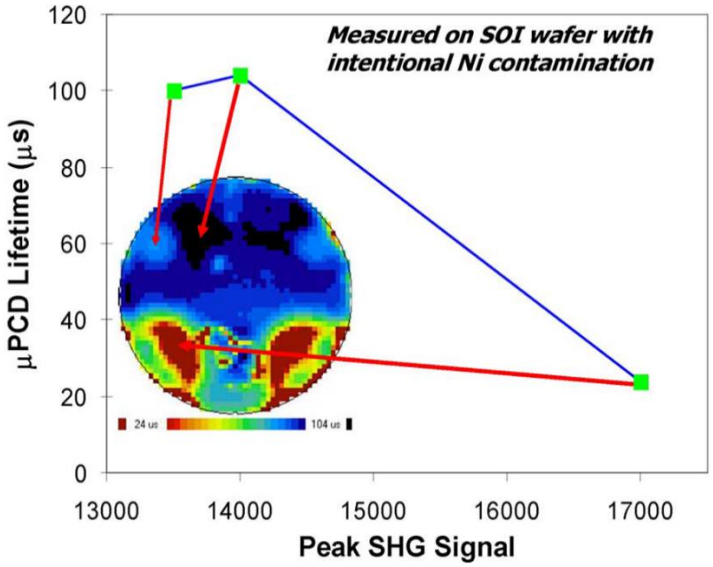

Figure 5.8: Minority carrier lifetime correlation with peak SHG for Ni-contaminated sample, following annealing. The inset shows the lifetime map (µPCD) and the spots where the SHG peak signal was acquired [33].

In another work [136], the SHG response with substrate bias was studied and the effects of x-ray irradiation were illustrated as a potential application of SHG measurement. A schematic diagram of how the bias was applied on the SOI is shown in Figure 5.9a. A metallic grounded tip is in contact with the Si film, while a voltage is applied on the substrate. The total field at each interface is modulated by the external field which modifies the SHG response as:

$$I^{2\omega}(t) \propto \left|\chi^{(2)} + \chi^{(3)} \cdot \left(E_{dc} + E_{ext}\left(V_{sub}\right) + E(t)\right)\right|^2 \cdot \left(I^{\omega}\right)^2 \qquad (5.1)$$

where E_{dc} is the pre-existing interface electric field (due to D_{it} and/or Q_{ox}), E_{ext} is the applied electric field (due to V_{sub}) and E(t) is the time-dependent electric field due to charge trapping/detrapping.

In Figure 5.9b the bias dependence of a normalized SHG signal (by its maximum saturation value) is correlated with I_D-V_G curves from typical Ψ-MOSFET measurements on two SOI substrates:

a) t_{Si}=160 nm and t_{BOX}=145 nm (squares),
b) t_{Si}=72 nm and t_{BOX}=230 nm (circles).

The minimum SHG intensity occurred for nonzero applied bias in the case of thinner Si film and/or thicker BOX (circles), since the Q_{ox} and D_{it} influence has to be cancelled out from the externally applied field. The flatband voltages calculated from the I_D-V_G curves were -1.8V for t_{Si}=160 nm and -14.2V for t_{Si}=72 nm. The minimum SHG for both SOI occurred near the flatband voltages, since the electric field at the interfaces is smallest when the bands in the Si film are flat.

Furthermore, the effect of x-ray irradiation on SHG is shown in Figure 5.10a, where the saturation SHG is monitored versus an applied substrate bias. Two samples were measured which had the same geometry (t_{Si}=72 nm and t_{BOX}=230 nm) but one was irradiated with 5Mrad total dose while the other was a reference. After irradiation the SHG shifts to higher values, caused by the higher interface electric field due to radiation-induced oxide charges (E_{dc} term in eq. (5.1)). The shift of SHG intensities after irradiation is consistent with the shift in I_D-V_G curves obtained from Ψ-MOSFET (in Figure 5.10b). The flatband voltage has lower values with increasing dose (Figure 5.10b). These changes in SHG could be useful for obtaining information about oxide trapped charges in devices subjected to ionizing radiation.

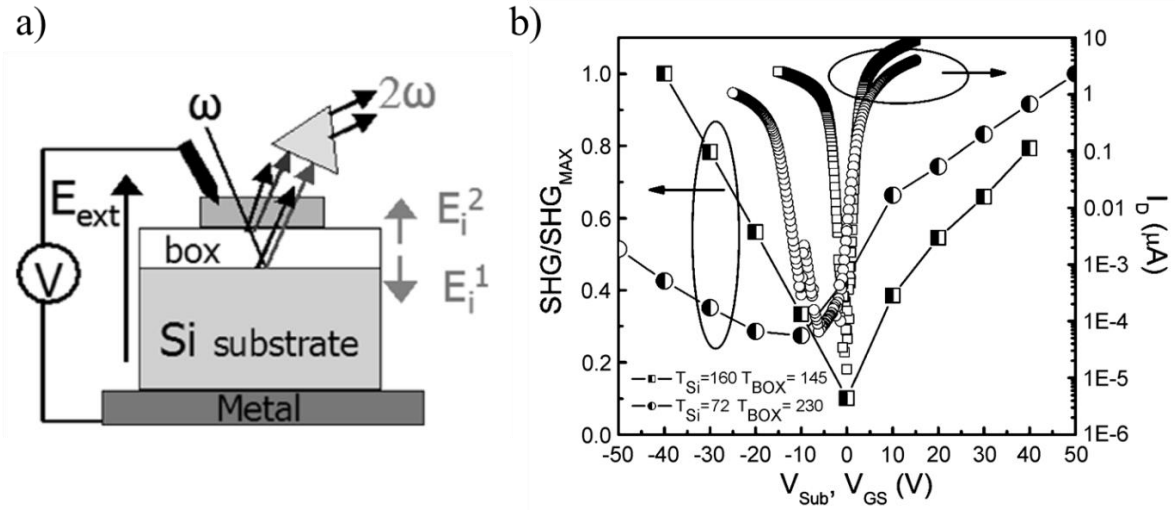

Figure 5.9: SHG (left axis) and drain current (right axis) versus substrate bias for two SOI structures (squares: t_{Si}=160 nm and t_{BOX}=145 nm, circles: t_{Si}=72 nm and t_{BOX}=230 nm) [136].

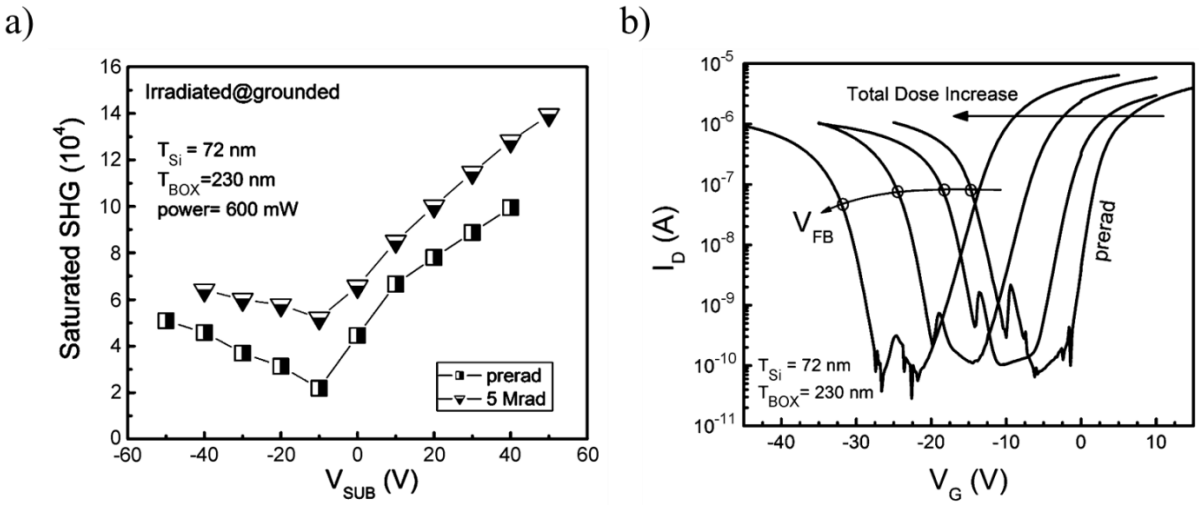

Figure 5.10: a) Saturated SHG signal versus substrate bias before and after x-ray irradiation (5Mrad dose) on a SOI with t_{Si}=72 nm and t_{BOX}=230 nm. B) I_D-V_G curves obtained for the same SOI for an increasing dose [136].

From all these studies, we understand the interest of SHG characterization for SOI but we also see how difficult it is to compare results obtained on different samples. Indeed, SHG in multilayer structures such as SOI is affected by optical phenomena such as interferences, multiple reflections, etc… Moreover, the electric field from each separate interface has an impact on the total SHG. In this chapter we address the optical phenomena by studying the impact of the layer thicknesses (Si film and BOX), as well as the effect of the static electric field from the various interfaces on SHG, using optical simulation.

5.3 SHG characterization: Impact of experimental parameters

Before studying the impact of various parameters on SHG, we first present a typical SHG curve. Figure 5.11a shows the SHG intensity versus time measured on a SOI wafer with t_{Si}= 88 nm, t_{BOX}= 145 nm and a non-passivated surface (*i.e.*, covered with native oxide). The silicon film on the top of the SOI was selectively etched, creating small Si islands, separated by exposed BOX areas (Figure 5.11b). This enables separate measurement of SHG on both the Si film and the exposed BOX. The experimental configuration was P-polarized fundamental beam and P- polarized SH beam, 45° angle of incidence, and 0° azimuthal angle. As shown on Figure 5.11a, the signal coming from the exposed BOX is about one order of magnitude lower than the one measured directly on the silicon film. This indicates that the total SHG signal is dominated by native oxide/Si film and Si film/BOX contributions.

The second remark concerns the time evolution observed while probing the silicon film, which looks similar to a charging phenomenon. The SiO_2/Si interfaces are always charged (Q_{ox}, D_{it}), so a built-in electric field is present. When the laser shines upon the material, electron-hole pairs are generated and separated by the existing interface field. The electrons can be injected in the oxide, modifying the

internal electric field. Depending on the relative signs of the contributions $\chi^{(2)}$ and $\chi^{(3)}E$ in the usual expression, $I_{2\omega} \propto \left|\chi^{(2)} + \chi^{(3)} E_{dc}\right|^2 (I_\omega)^2$, the SHG signal can have either charging or discharging behaviour.

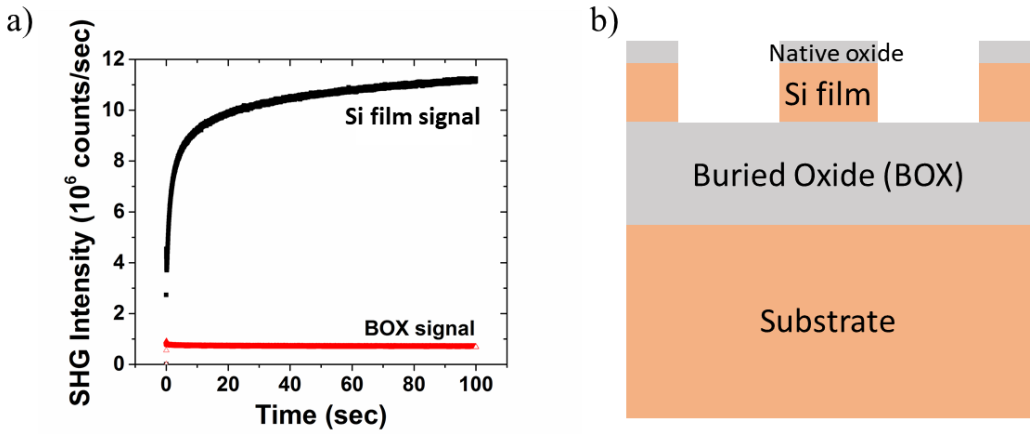

Figure 5.11: a) Typical SHG intensity vs. time measured on the BOX region and on the silicon film. The SOI under test had an 88 nm film, a 145 nm BOX and a non-passivated top surface (native oxide). The experimental configuration used was: P-in for incident beam polarization, P-out for the SHG polarization; 45° angle of incidence and 0° azimuthal angle. b) Etched SOI structure, with Si islands and exposed BOX regions.

SHG being an optical technique, its signal depends on various experimental parameters such as the angle of incidence, the polarization of the incident fundamental and detected SH radiation, as well as the azimuthal angle. Before further detailing any physical explanation or modelling of the SHG signal from SOI, the experimental SHG parameters have to be chosen in order to have the most relevant measurement configuration. Next, we examine the optimum parameters for SHG signal maximization from a SOI with 88 nm thick Si film and 145 nm BOX.

5.3.1 Input/output polarization configurations

Figure 5.12 shows, in semi-logarithmic scale, the different in/out polarization pairs from silicon film (Figure 5.12a) and exposed BOX (Figure 5.12b), for the same SOI structure as before (88 nm Si film/145 nm BOX). The lowest signals are obtained in both cases with the S-out configuration, as theoretically expected [10]. For the S-in/P-out configuration, the signal from the exposed BOX has the same order of magnitude as the one from the silicon film. Furthermore, the S-out configurations (P-in/S-out, S-in/S-out) have a very low signal (2-3 orders of magnitude lower than P-in/P-out) since the the bulk quadrupolar susceptibilities are smaller than the interface dipolar ones, as already mentioned in Chapter 2. However, the aim of these measurements is to have a tool characterizing the interface between the top Si film and BOX, so we prefer using the P-in/P-out configuration, which gives the strongest signal from the film and for which the BOX contribution is one order of magnitude lower.

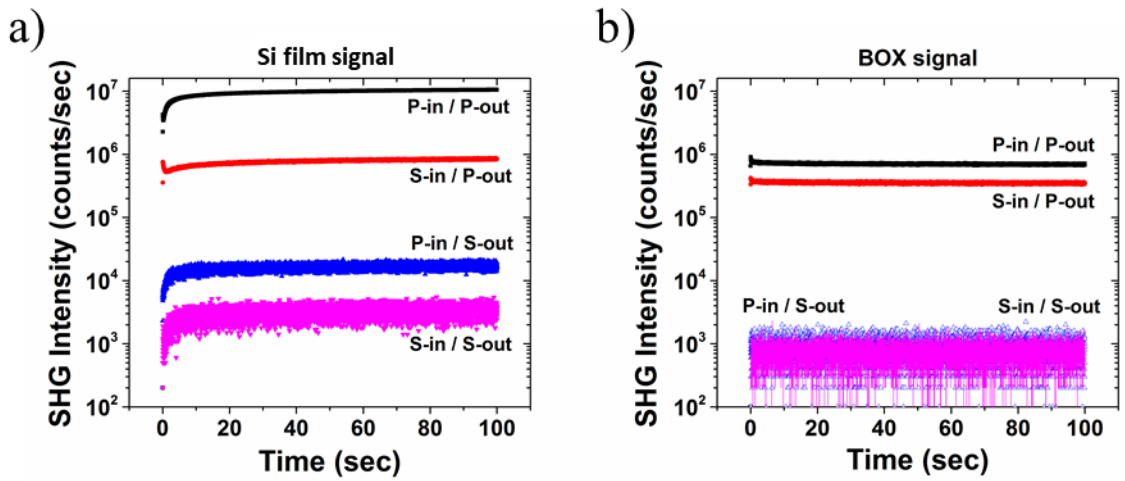

Figure 5.12: Polarization configurations of the incident and the SHG beams for SOI wafer with non-passivated surface, 88nm film and 145 nm BOX thicknesses. The angle of incidence was 45°. (a) Signal from the Si film island (full SOI structure). (b) Signal from the exposed BOX region.

5.3.2 Angle of incidence

The angle of incidence (AOI) is another important experimental parameter that must be optimized, since it alters the travelling path of the fundamental and harmonic beams inside the multilayer structure which inevitably induces interferences that changes the SHG signal. Figure 5.13 shows the impact of the angle of incidence on the SHG intensity from the same sample (88 nm Si film/145 nm BOX). The signal was collected on both the Si film and the exposed BOX for different angles of incidence for P-in/P-out polarization configuration. The maximum for the SOI signal appears at 45°. The BOX signal peak is shifted and, more importantly, it is at least one order of magnitude lower than the Si film signal (as already seen from time-dependent SHG graphs before). This peak shift originates from the changes in the interference pattern, depending on the various layers of the structure. Subsequent experiments used a 45° incidence angle in order to maximize signal from the silicon film.

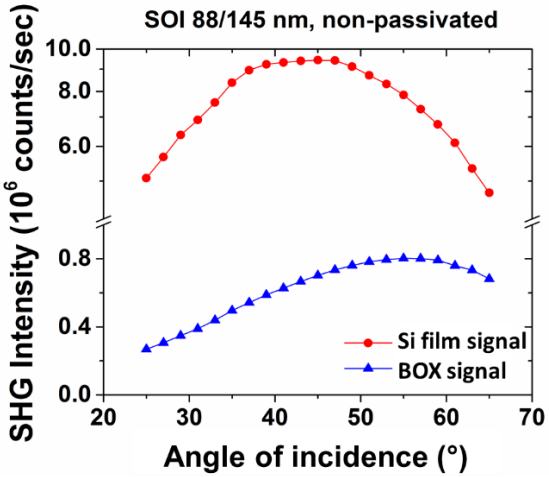

Figure 5.13: Dependence of the SHG signal on the angle of incidence. Both incident and reflected SHG beams were P-polarized. The sample had a 88 nm Si film and 145 nm BOX.

5.3.3 Azimuthal angle

In a crystal, the SHG intensity depends on the angular orientation of the sample with respect to the beam's direction, which is described by the azimuthal angle (as already mentioned in Chapter 2). For silicon (100) samples, it is known that the SHG shows a 90° periodicity versus the azimuthal angle, which results from 4-fold symmetry [44]. Figure 5.14a shows our measurement results on an 88 nm/145 nm SOI, using P-in/P-out polarizations and 45° angle of incidence. The 4-fold symmetry is apparent, albeit the signal variation is less than 10%. For validation, we have performed measurements on non-SOI reference wafers (thermally oxidized bulk Si with 4 nm thick oxide) which show the same trend as the exposed BOX region (Figure 5.14b). Furthermore, a 45° shift between SHG signals coming from the Si film (full SOI) and the BOX region (BOX/substrate interface only) is visible. This could be possibly attributed to the different electric fields at the interfaces: similar 45° phase shifts have been observed in the literature due to changes in the interface electric field, altering the EFISH contribution, which in turn impacts the azimuthal SHG [66], [82], [137].

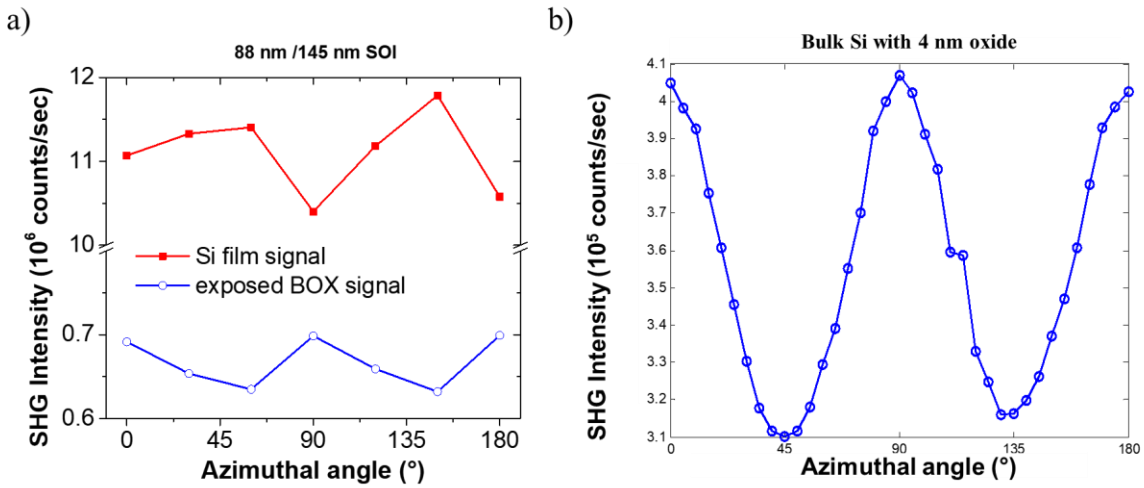

Figure 5.14: a) SHG signals versus angle of rotation of the sample (azimuthal angle) in 88nm/145nm SOI. The probed areas were a Si island and an exposed BOX region. b) SHG signal originating from p-type bulk Si (100) with thermal oxide on top.

From the above analysis, we chose the following parameters for our subsequent experiments: 45° angle of incidence, P-in/P-out polarization configuration and 0° azimuthal angle.

5.4 SHG characterization and simulation: dependence on geometry and interface fields

Before using SHG for contactless characterization of electric fields in SOI, we need to understand and take into account the thickness of the structure under test. The impact of the BOX and Si layer thicknesses is discussed and the need for optical simulation is introduced. Afterwards, we will use the optical simulator to study how the static electric fields from different interfaces affect the SHG

behaviour. Finally, we will present the experimental SHG results on samples before and after passivation (a process which alters the electric fields at the interface) and compare them to the simulation. The parameters shown schematically in Figure 5.15 are studied in the next paragraphs:

- t_{BOX} in section 5.4.1
- t_{Si} in sections 5.4.2-5.4.4.
- E_{dc} and passivation in section 5.4.5-5.4.6.

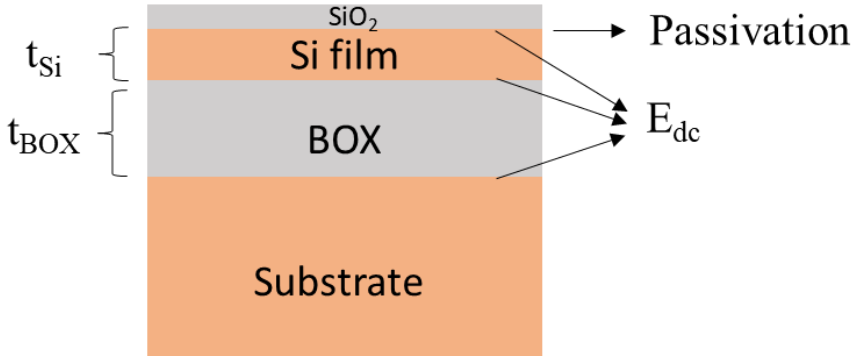

Figure 5.15: Main parameters that affect SHG in a SOI structure.

5.4.1 BOX thickness impact

Initially, we investigate the impact of the BOX thickness from SOI structures whose Si film has been etched-off. Figure 5.16a depicts an exposed BOX where the main contribution to SHG is from the BOX/substrate interface. Figure 5.16b shows the time dependent SHG signals from measured structures with variable BOX thicknesses (15 nm, 20 nm, 25 nm and 145nm). Note that SiO_2 is transparent at the incident and SH wavelengths (as mentioned in Chapter 2); consequently, in theory, SHG should not depend on the BOX thickness itself. However, we observe some differences between the various BOX thicknesses. In reality, the reflectance of the fundamental beam is smaller from the 145 nm SiO_2 film [138], meaning that more fundamental light reaches the BOX/substrate interface. Furthermore, fabrication steps for each BOX are slightly different, which can induce changes in the interface between the BOX and the silicon substrate (for example oxide charges and interface traps). Regardless of the fabrication, the SHG variation due to the BOX thickness is relatively small: increasing the BOX thickness by ~10 times causes a 35% change in SHG.

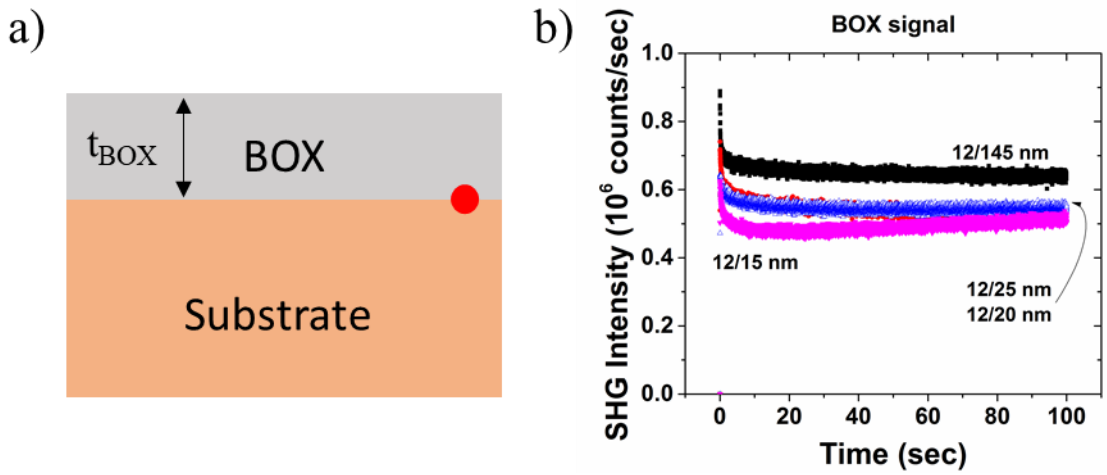

Figure 5.16: SHG signal originating from the SiO_2/Si substrate interface (red dot). a) The probed areas were exposed BOX regions with variable thickness. b) TD-SHG from the exposed BOX region of SOI wafers with various BOX thicknesses (15, 20, 25, 145 nm); the 12 nm Si film layer was etched-off.

Next, we will compare the SHG results from SOI wafers with the same Si film thickness (12 nm) and native oxide on top but variable BOX thickness (15 nm, 20 nm, 25 nm and 145nm). Figure 5.17a shows the measured structure where all of the interfaces can contribute in the SHG signal. As presented in Figure 5.17b, the SHG intensity is similar in all samples with thin BOX layers (15, 20 and 25 nm). However, we note a significant increase in SHG signal (~40-45%) between the samples with the thin BOX and the one with a thick BOX (145nm). In order to verify if this effect is attributed to potential interferences caused by thickness changes, we simulate the SHG versus the BOX layer thickness without considering E_{dc} and associate it with the experimental data (Figure 5.17c). The initial SHG intensity (at t=0) was used, in order to avoid significant laser induced charging. The data set and the simulation are normalized by their corresponding maximum values. The simulation reproduces well the experiment, indicating that the significant change in SHG intensity between thin and thick BOX structures originates mostly from layer thickness-related interferences.

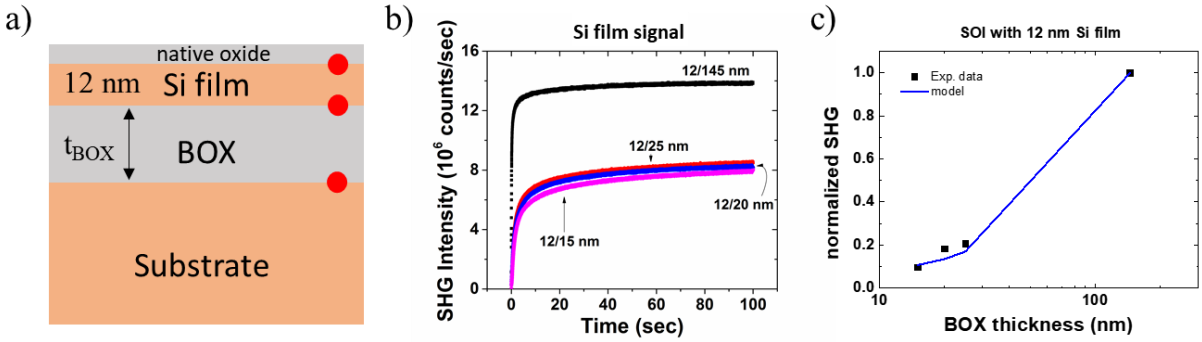

Figure 5.17: BOX thickness impact on SHG signal from non-passivated SOI. The top Si film thickness was 12 nm in all cases. The SOI structure under study is shown in (a) along with the contributions from each interface (indicated with red circles). The TD-SHG signals are shown in (b) and the dependence of the initial SHG (at t=0) versus the BOX thickness (experiments and simulation) is shown in (c). No E_{dc} was taken into account for the simulation.

5.4.2 Si film thickness impact

In a multi-layered SOI stack, the Si film thickness can critically affect the SHG intensity through absorption, reflection and transmission of the fundamental and second harmonic (SH) frequencies. Figure 5.18 shows the simulated response of the Si film thickness on the SHG signal (b) from a SOI structure with a fixed BOX thickness of 145 nm (a). The SHG intensity exhibits a periodic, oscillating behaviour with high amplitude variations which depend on the geometry of the SOI stack. Two points should be considered:

- SOI with different t_{Si} can give very different SHG values (see the red circles indicating the SOI structures with 12 nm and 88 nm Si film in Figure 5.18b).
- Thickness variation within the same wafer are not as large as the scale in Figure 5.18b but might have an impact as well. For example, for 6 to 12 inch diameter SOI wafers already in the market, the Si film thickness fluctuations (less than 5%) are much smaller than the scale depicted in Figure 5.18.

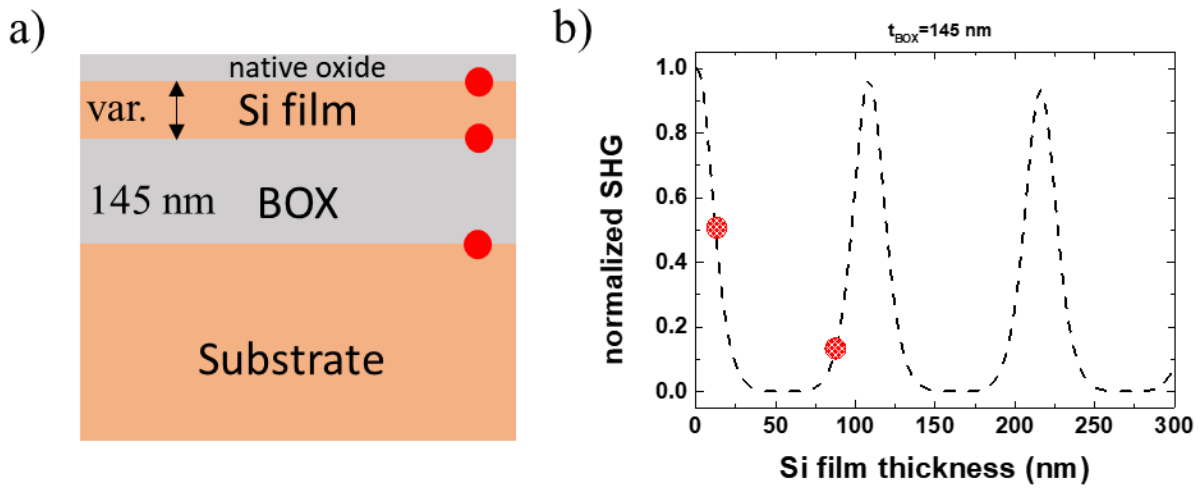

Figure 5.18: a) Schematic of simulated SOI structure t_{BOX} = 145 nm and varying Si film thickness. b) Simulated SHG signal versus Si film thickness. The angle of incidence was 45° and the fundamental beam wavelength was 780 nm.

In order to evaluate the impact of the Si film thickness, we tested SOI wafers with two different Si film thicknesses (12 nm and 88 nm) and the same 145 nm thick BOX layer. The SHG results are presented in Figure 5.19. Figure 5.19a shows the TD-SHG signal from the exposed BOX regions of the two samples (Si film was etched off). The differences between them are small (< 5%, probably caused by process differences during wafer manufacturing). Indeed, the signal is coming from the BOX/substrate interface which is similar across the two samples. For this reason, we can assume that when comparing the SHG from the Si film on these wafers, the differences will not be related to the BOX/substrate interface.

Figure 5.19b shows the measured SHG signal from the full SOI structures; SHG is noticeably higher for the thinner silicon film (12 nm). Initially, we attributed this result to the absorption by the silicon layer of the SH generated at the buried interfaces, as it propagates upwards towards the air (Figure 5.18a). The absorption is related to the film thickness t_{Si}, and for normal incidence the SHG intensity at the surface of the Si film is given by:

$$I = I_0 \exp(-Kt_{Si}) \tag{5.2}$$

where I_0 is the initial SH intensity generated at the Si film/BOX interface and K is the absorption coefficient of Si at 390nm SHG wavelength. The value of K is $1.43*10^5$ cm^{-1} [13]. The BOX is transparent to a wavelength of 390nm and does not absorb the SH generated at the BOX/substrate interface, as it propagates upwards. In a first approximation, the reflections at various interfaces inside the structure were not taken into account. The theoretical value for the ratio of the SHG intensities, due to absorption in Si films with different thicknesses, is:

$$\frac{I_{88/145}}{I_{12/145}} = \frac{I_0 \exp(-Kt_{Si1})}{I_0 \exp(-Kt_{Si2})} \approx 0.34 \tag{5.3}$$

From Figure 5.19b we calculated the ratio of the SHG intensities and found a value of 0.24 which differs by ~30% from the theoretical absorption ratio, showing the importance of a full simulation of the optical phenomena on the two structures, eventually adding the interface electric fields (which will be presented in §5.4.5).

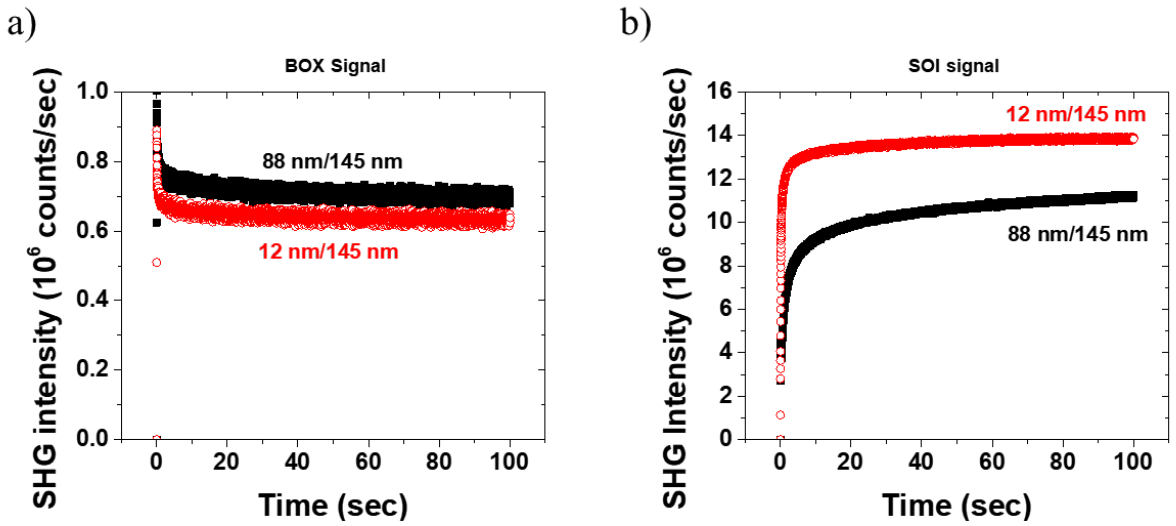

Figure 5.19: TD-SHG signals from 12 nm/145 nm and 88 nm/145 nm SOI samples measured on a) exposed BOX and b) Si film.

5.4.3 SHG correlation with Si film thickness variations within the same wafer

In order to analyse more extensively the Si film thickness influence on the SHG, it is necessary to have many SOI structures with different geometries, but their fabrication process would not be exactly the same, inevitably. An alternative way is to study the Si film thickness variations within the same wafer and connect it directly with the SHG signal.

In these series of experiments, a mapping of the Si film and BOX thicknesses, as well as of the SH signal, was done across different SOI wafers. The layer thicknesses were measured by using a reflectometer which was integrated inside the SHG equipment. The thicknesses were acquired at the same spots as the SHG measurements. In Figure 5.20a the comparison between Si film thickness and SHG intensity is shown for a thick SOI wafer with t_{Si}=145 nm and t_{BOX} =1000 nm (200 mm wafer diameter); a correlation is visible between the two quantities. In Figure 5.20b the same measurements are shown but for a thinner structure with t_{Si}=88 nm and t_{BOX}=145 nm (300 mm wafer diameter). Again, the SHG measurements are correlated with the Si film variations. However, different trends are obtained for thick and thinner structures and in order to understand this difference we need the simulation tool.

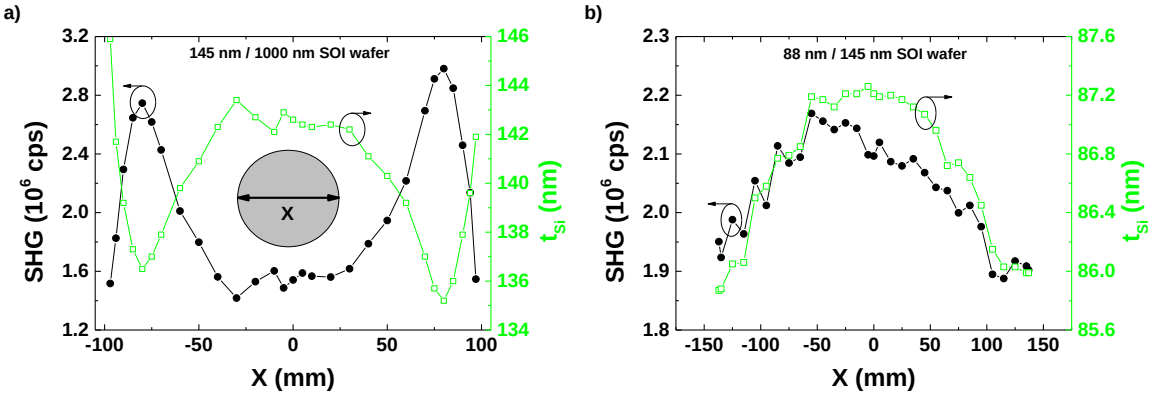

Figure 5.20: Si film thickness (open squares) and SHG signal (filled circles) for thick (a) and thinner (b) SOI wafers. The X-axis corresponds to different measurement locations on the wafer, across its diameter (as shown in the inset). The angle of incidence was set at 45° and the input/output polarizations at P/P.

For the simulation, we varied the layer thickness of the Si film, adapting the thickness range from the actual experiments in Figure 5.20 (keeping constant the BOX thickness of each structure: 1000 nm and 145 nm respectively). The simulation parameters were the same as the experimental ones (P-in/P-out polarizations, 45° AOI, 0° azimuthal angle), while the material parameters of the simulation were the ones described in Chapter 3 (Table 3.1).

Figure 5.21 presents the SHG intensity versus the Si film thickness from the measurements (data points from Figure 5.20) along with the corresponding simulation results (lines), for the two SOI wafers. It should be noted that these simulations were performed with no electric field E_{dc} taken into account. The agreement between simulation (with E_{dc}=0) and experiment is good, for both SOI. However, the thickness and the SHG variations are small (x-axis) and the experimental points look

dispersed for the thinner SOI (Figure 5.21b). If we add an electric field 10^4 V/cm (green dashed line in Figure 5.21b) the simulation is slightly modified but the change is insignificant.

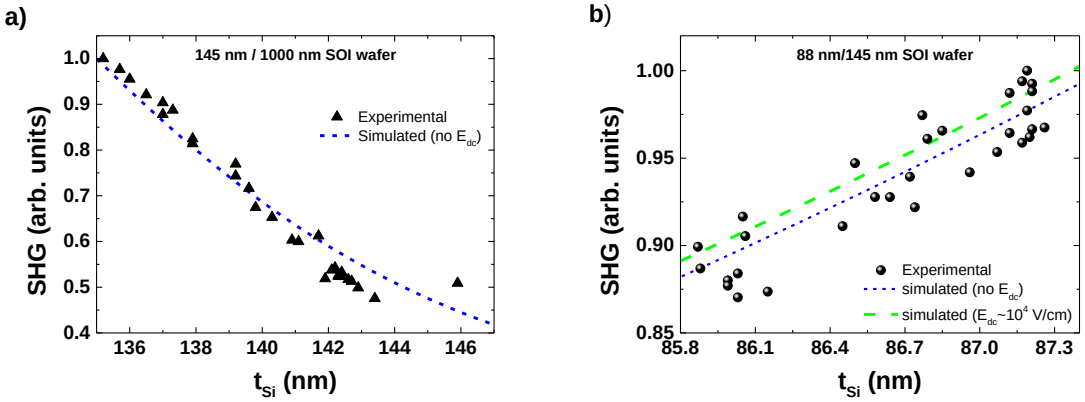

Figure 5.21: Model (lines) and experiment (data points) comparison of SHG signal versus Si film thickness for thick (a) and thin (b) SOI. The normalized experimental data points were calculated from Figure 5.20 for both cases. The normalization was done by dividing each set (experimental and simulated) by its corresponding maximum value.

With our reflectometer it was difficult to extract reliable SOI/BOX thicknesses for very thin films. Even though its resolution is on the order of 1 nm, the fit models were insufficient for ultrathin SOI. Instead of t_{Si} variation, another way to alter the optical path through a multilayer is to modify the angle of incidence as we will present in the next section.

5.4.4 SHG versus AOI: experiments and simulations

SHG experiments were performed for various angles of incidence of the fundamental beam. Figure 5.22a presents the SHG versus AOI measurements on the thicker SOI wafer (t_{Si}=145 nm and t_{BOX} =1000 nm) at two locations with different Si film thicknesses (as measured in Figure 5.20a). Figure 5.22b presents the simulated SHG (with no E_{dc} field taken into account) showing that the experimental data are well reproduced (shape and peak position) by adapting the thickness of the Si film layer in the simulation.

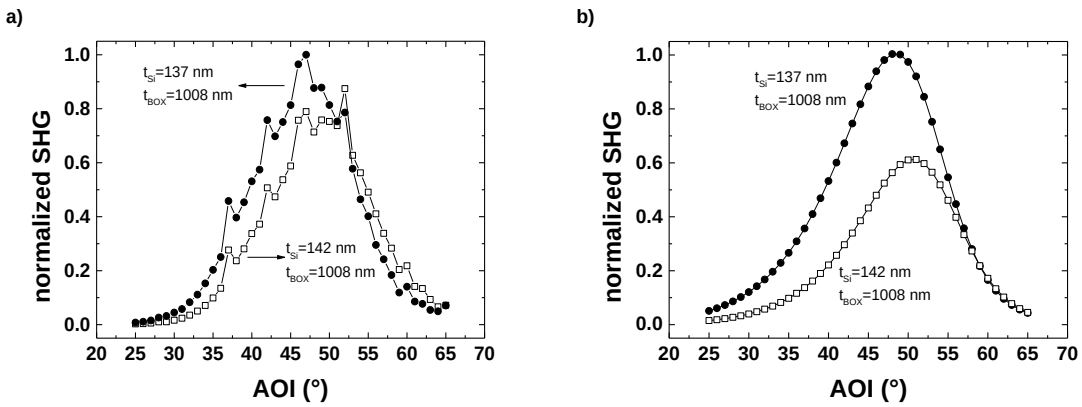

Figure 5.22: a) Experimental SHG versus angle of incidence (AOI) at two different locations on the same wafer as in Figure 5.20 (measured Si layer thicknesses are 137 nm and 142 nm respectively and measured BOX thickness is 1008 nm). b) SHG vs AOI from the simulations obtained with the corresponding Si film thicknesses. The normalization was done by dividing each set (experimental and simulated) by its corresponding maximum value.

For thinner SOI with t_{Si} = 88 nm and t_{BOX} = 145 nm (Figure 5.23a) the model reproduces also the observed behaviour (black solid line). This good correlation with the simulation for both geometries (without including the dc electric field) implies that the SHG is mainly given by the $\chi^{(2)}$ interface terms. Note that even if an electric field value of 10^4 V/cm is added in the simulation, its impact on the SHG intensity is small and the correlation does not change significantly (red dotted line in Figure 5.23a).

The correlation between experimental and simulated values of SHG intensity versus AOI observed on the previous samples is not evident for ultra thin SOI substrates: in Figure 5.23b the maxima of the experimental and the simulated SHG with no electric field are shifted by more than 20° for a 24 nm Si film/25 nm BOX sample. For a thin film, the model based exclusively on linear optical propagation phenomena appears not to be sufficient to explain the experimental results because of the presence of electric fields at the interfaces. Hence the vertical dc field (in the z-direction) must be added in the simulation at every Si/SiO_2 interface by including the extra term $\chi^{(3)}E_{dc}$ in the $\chi_{zzz}^{(2)}$ component, as discussed in Chapter 3 (§3.3.3).

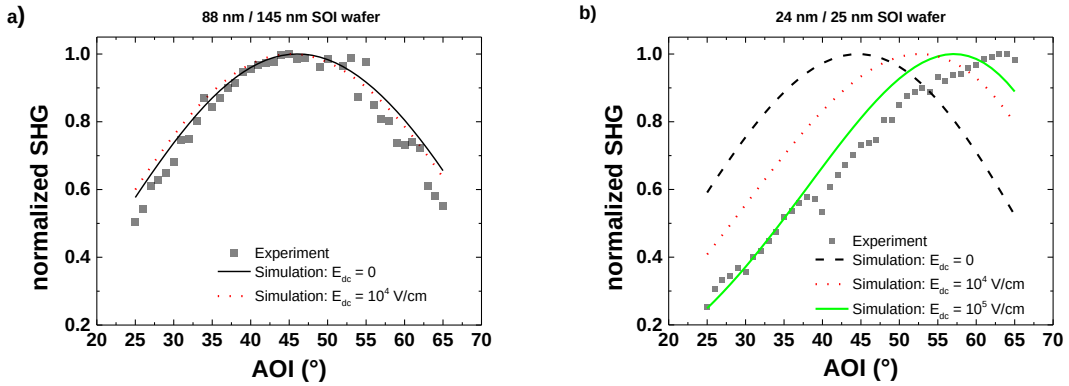

Figure 5.23: (a) SHG versus angle of incidence for the 88 nm/145 nm SOI. Comparison of experimental data (filled squares) and simulation without E_{dc} (solid black line) and with E_{dc} at all interfaces. (b) SHG versus AOI for an ultrathin SOI structure with 24 nm Si film and 25 nm BOX thicknesses. The value of the electric field included at all interfaces in the simulation was E_{dc} = 10^4 V/cm (red dotted line) and E_{dc} = 10^5 V/cm (green solid line).

With the incorporation of a dc field of 10^4 V/cm (at each interface) for the thin SOI with t_{Si} = 88 nm/t_{BOX} = 145 nm (red dotted line in Figure 5.23a) the change in the simulated SHG is negligible. However, for the ultrathin SOI with t_{Si} = 24 nm/t_{BOX} = 25 nm a dc field value of 10^4 V/cm (red dotted line in Figure 5.23b) changes significantly the SHG but is not enough to explain the experimental data. A field of 10^5 V/cm (green solid line in Figure 5.23b) simulates better the experimental behaviour. The aforementioned E_{dc} values are typical at ultrathin SiO_2/Si interfaces (up to 1 MV/cm) [139]. The higher E_{dc} value needed for the ultrathin SOI in Figure 5.23b is in agreement with the well-known increase of the electric field for decreasing Si film thickness due to stronger electrical coupling between the top SiO_2/Si film and Si film/BOX interfaces [140].

Nevertheless, we have used the same value of E_{dc} at each interface in the simulation but it is critical to understand how each interface contributes to the SHG response.

5.4.5 Impact of interfacial dc fields on simulated SHG

In order to understand the impact of the different electric fields at each interface on the total SHG response, we adjusted the E_{dc} value separately at each interface with our simulation tool. In SOI stacks the different interfaces do not have the same properties, i.e. interface state density and trapped charges [141]. Therefore, the strength of the dc electric field at the top and buried interfaces will be different, hence the generated second order polarization will be interface dependent and the global SHG response will vary.

It is important to note that the penetration depth of the fundamental light and the SH are different (Table 5.1). The absorption coefficient of Si at 300 K [92] is shown in this table and from its inverse we calculated the penetration depths. This means that for Si films with thicknesses higher than 70 nm, the fundamental radiation traverses the film, but for the SH radiation only the very top interface (top SiO_2/Si film) contributes significantly to the SH signal (the SH from buried interfaces is mostly absorbed). For much thinner films (<70 nm), the buried interfaces (Si film/BOX, and BOX/Si substrate) will influence the SH response as well, even if they are partially absorbed. The BOX is transparent to 390 nm light, so even the SH from the very bottom interface (BOX/Si substrate) might have an impact. In order to investigate where the dominant contribution comes from, simulations were done with different electric fields independently varied at each interface (only one is varying while the others are kept zero).

Table 5.1: Absorption coefficients of Si

Wavelength	Absorption coefficient	Penetration depth
780 nm	1030 cm^{-1}	10 µm
390 nm	$1.43*10^5$ cm^{-1}	70 nm

Primarily, the thicker 88 nm/145 nm passivated SOI was investigated. As observed in Figure 5.24a, the change of the E_{dc} value at the top interface (SiO_2/Si film, E_1) influences the simulated SH signal. We did not add any other E_{dc} since in our case the 88 nm Si film absorbs most of the SH contributions from the buried interfaces (Si film/BOX, E_2 and BOX/substrate, E_3), and only the top one is important (E_1). It is visible that as the electric field increases from 0 to 10^5 V/cm with a step of 0.1 MV/cm, the peak of the AOI curves shifts to lower angles. For more quantitative comparisons between the experimental and simulated curves, the relative positions of the AOI peaks are calculated. Specifically, θ_{exp} is the position of maximum SHG intensity (peak) in the experimental data while $\theta_{simulated}$ is the position of maximum in the simulated data. Figure 5.24b shows the relative position (θ_{exp}-$\theta_{simulated}$) versus the electric field value at the top interface. The straight line at y=0 gives the value of the E_{dc} field for which the simulated and experimental AOI peaks coincide. The best match here is achieved for a field of 10^4 V/cm. This relatively small value for the electric field is supported by the fact that the sample had a passivated Si film and consequently small D_{it} values.

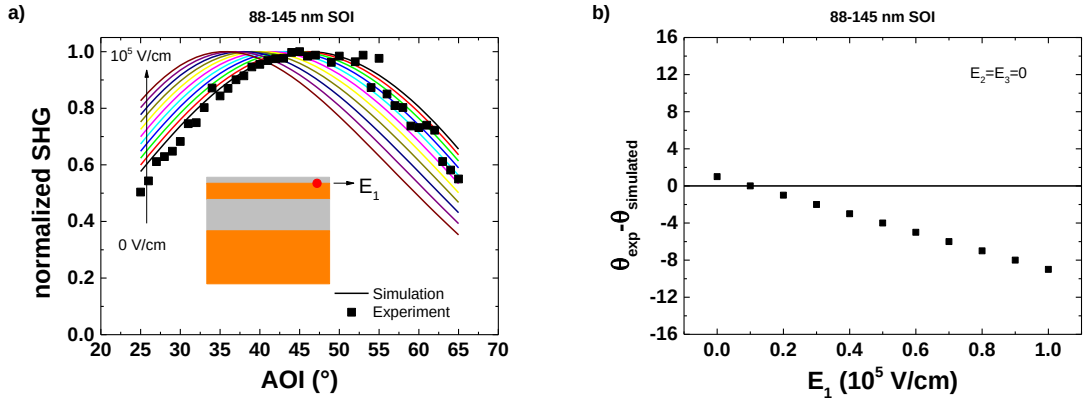

Figure 5.24: a) Variable E_1 field for the thicker SOI structure (t_{Si}=88 nm/t_{BOX}= 145 nm). b) Difference between experimental and simulated AOI peak position (θ_{exp}, $\theta_{simulated}$ respectively) versus the static electric field at the first interface, between the passivation layer and the Si film.

In thinner SOI structures, we expect that E_{dc} at the bottom interfaces (E_2, E_3) might also influence the SHG behaviour. In Figure 5.25 the impact of the dc electric field for the thin 12 nm/145 nm SOI structure is depicted. Specifically, Figure 5.25a shows the effect of varying only the very top field (E_1) at the top SiO_2/Si film interface, while the other two fields were neglected (E_2=E_3=0). From Figure 5.25b the best match is achieved when the top field has a value of ~9x10^4 V/cm. This E_{dc} value is higher than the one needed for the simulation of the thicker SOI, which is consistent with the fact that the thinner Si film couples more efficiently the top and buried interfaces [140].

Figure 5.25c shows the results for varying only the middle field (E_2), at the Si film/BOX interface, while the others were kept at zero (E_1=E_3=0). A relatively small variation of the simulated SHG curve is evidenced, but it is less significant compared to the previous case. The position of the peak is modified by the electric field at the film/BOX interface (Figure 5.25d), but it cannot be adjusted to fit the experiments because E_1=0, which is not realistic.

Finally, Figure 5.25e, f present the effect of varying only the bottom field (E_3), at the buried BOX/Si substrate interface, while keeping the others zero (E_1=E_2=0). The variation between the curves simulated with different E_3 values is hardly visible and the position of the simulated peak is practically constant. The absence of match between experimental and simulated peaks confirms that the 3rd interface (buried) has minimal influence on the SHG measured on such samples. This is consistent with the measurements in Figure 5.16b.

When comparing all of the curves together, it is clear that the top interfacial field plays the most critical role; this originates from the fact that the SH generated at the buried interfaces is partially absorbed (~13% from each buried interface) as it travels through the 12 nm Si film. Moreover, the quality of the Si film/BOX interface is better than the top SiO_2/Si film, which has more D_{it} and higher electric field.

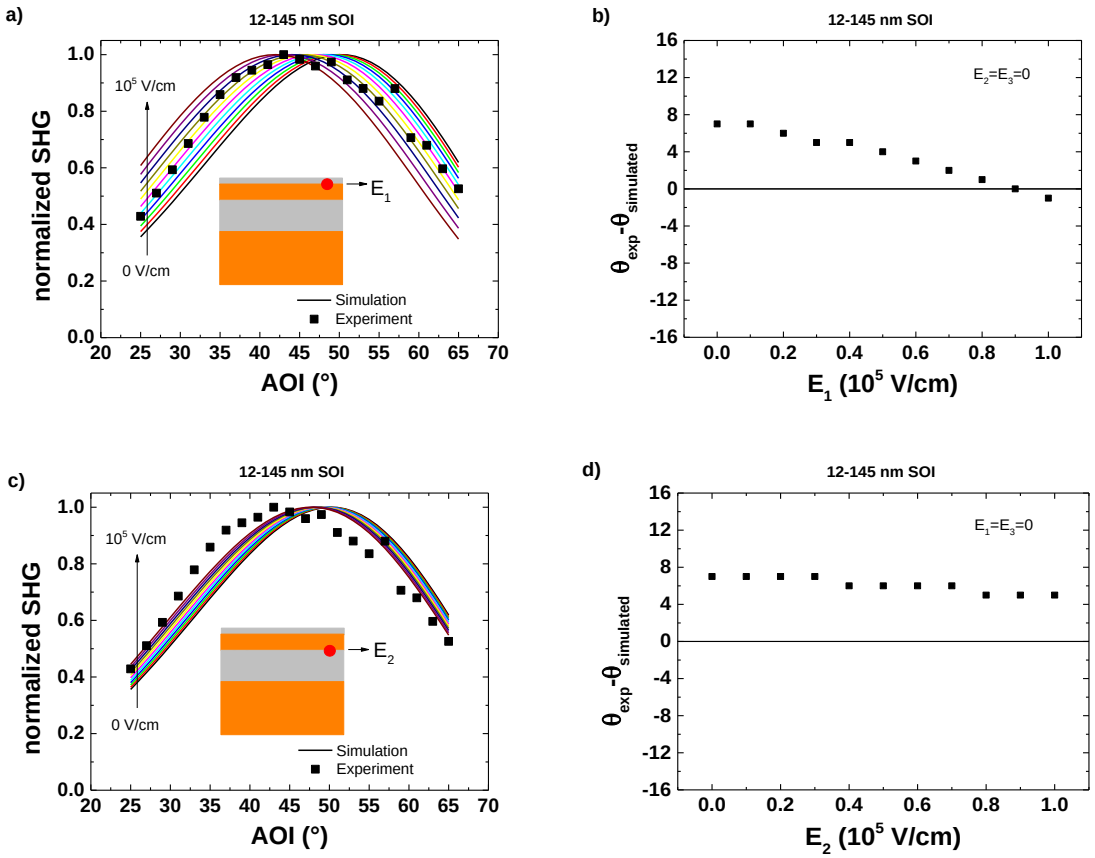

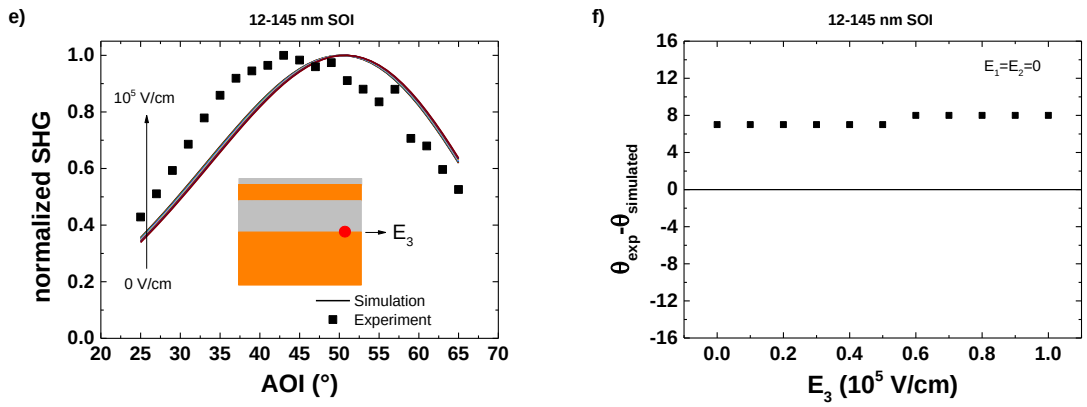

Figure 5.25: Simulated SHG versus angle of incidence (a, c, e) and relative maximum position versus electric field for a 12 nm/145 nm SOI structure. a,b) E_1 variable, $E_2=E_3=0$. c,d) E_2 variable, $E_1=E_3=0$. e,f) E_3 variable, $E_1=E_2=0$.

A way to probe the buried interfaces would be, for example, "fixing" a non-zero value of the electric field at the top interface (E_1), which is prominent, and tune the value of the field from the buried interface (E_2). Figure 5.26 shows the simulated SHG versus the electric field E_2 for two different values of the electric field at the top interface, $E_1=0$ and $E_1=0.9\text{x}10^5$ V/cm. The last value was taken from Figure 5.25b, since it is the best match to the maximum AOI. The square root of the SHG signal is preferably used here since it is directly proportional to the value of the electric field:

$$\sqrt{I_{2\omega}} \propto \left|\chi^{(2)} + \chi^{(3)} E_{dc}\right| I_{\omega} \qquad (5.4)$$

We observe that for both E_1 values, the SHG signal increases as we increase the value of E_2. We can conclude that if we have SOI structures with the same top interface quality (E_1 fixed), the fabrication variations that impact the buried interface will be measurable with SHG.

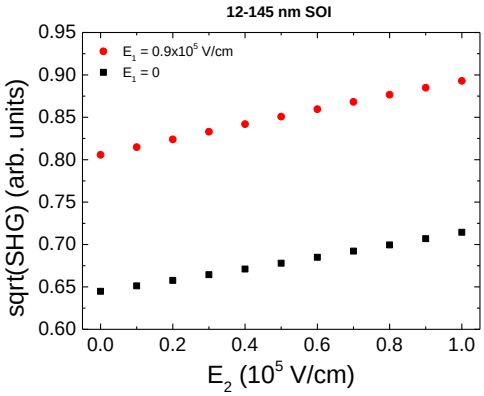

Figure 5.26: Simulated square root of SHG signal from a 12 nm/145 nm SOI structure versus the electric field at the buried interface E_2, for two different values of the electric field at the top interface, $E_1=0$ and $E_1=0.9\text{x}10^5$ V/cm.

5.4.6 Impact of interface electric fields on experimental SHG: passivated/non-passivated SOI samples

In this section, we investigate the effect of passivation on SOI structures. The passivation process resulted in a 4nm thick dry thermal oxide which is known to reduce the top interface states density [35] thus changing the interface electric field. In Figure 5.27, a typical I_D-V_G curve was measured by pseudo-MOSFET for a passivated and a non-passivated SOI with the same geometry. For each sample, the interface state density (D_{it}) was extracted from the subthreshold swing (S_S) of the I_D-V_G curve. S_S is calculated for $V_G<V_T$ (subthreshold region) and is simply defined as the inverse of the curve slope (green dashed lines). It is related to D_{it} through [127]:

$$S_S = \left(\frac{d \log I_D}{dV_G} \right)^{-1} = 2.3 \frac{kT}{q} \left(1 + \frac{C_{Si} + qD_{it}}{C_{ox}} \right) \qquad (5.5)$$

where kT/q is the thermal voltage with a value of 25.8 mV at room temperature, and C_{Si} and C_{ox} are the capacitances of the Si film in depletion and the BOX respectively. In Figure 5.27 we observe that the slope increases after passivation, hence S_S and D_{it} decrease: their calculated values are shown in Table 5.2.

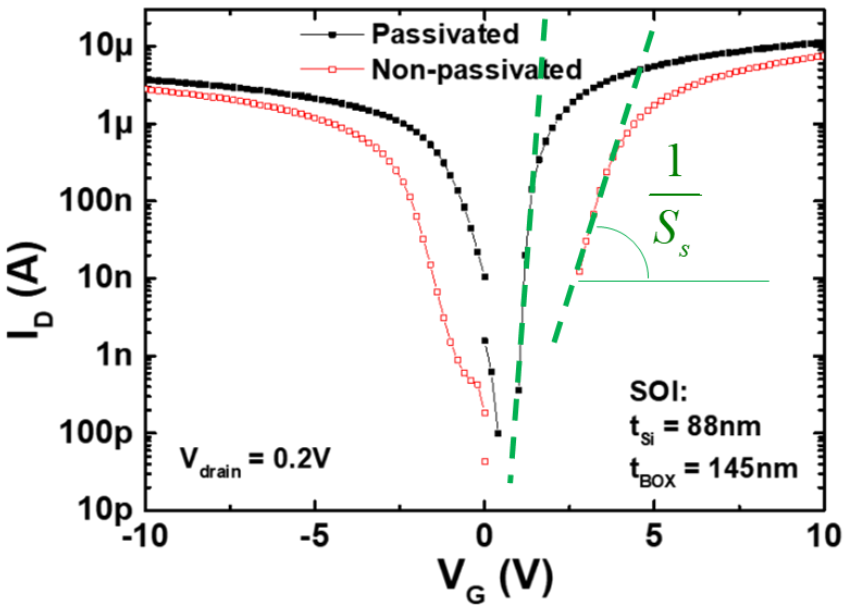

Figure 5.27: Drain current versus gate voltage in a passivated (thermal oxide on top) and non-passivated (native oxide on top) SOI with 88 nm of Si film thickness and 145 nm of buried oxide thickness.

Table 5.2: Subthreshold swing and D_{it} values for non-passivated and passivated 88/145 nm SOI.

88/145 nm SOI	S_S (V/decade)	D_{it} ($cm^{-2}eV^{-1}$)
non-passivated	0.6	$6*10^{11}$
passivated	0.4	$1*10^{11}$

Passivated (thermal oxide) and non-passivated (native oxide) samples were both tested with SHG in order to verify the results from the previous simulations where we altered the various E_{dc}. In Figure 5.28 the TD-SHG curves are shown for both passivated and non-passivated samples in 88/145 nm and 12/145 nm SOI geometries. There is a significant difference between passivated and non-passivated samples for both Si film thicknesses. Passivated SOI generates less SHG signal, which is consistent with the reduction of the interface trap states during the passivation process. The improved interface quality results in a smaller E_{dc} in the SOI and consequently a lower SHG signal (depicted schematically in Figure 5.29 for both geometries). There is also a slower time evolution for the passivated sample (visible for the 88nm film), presumably related to a reduced electron injection rate due to the lower D_{it}.

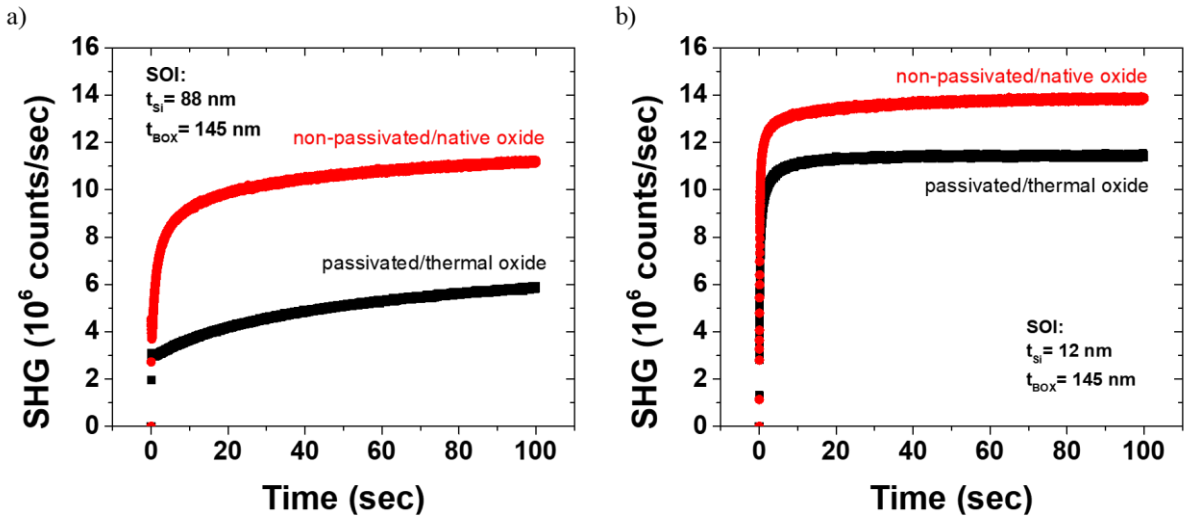

Figure 5.28: TD-SHG signals from passivated and non-passivated samples in a) 88 nm/145 nm and b) 12 nm/145 nm SOI geometries.

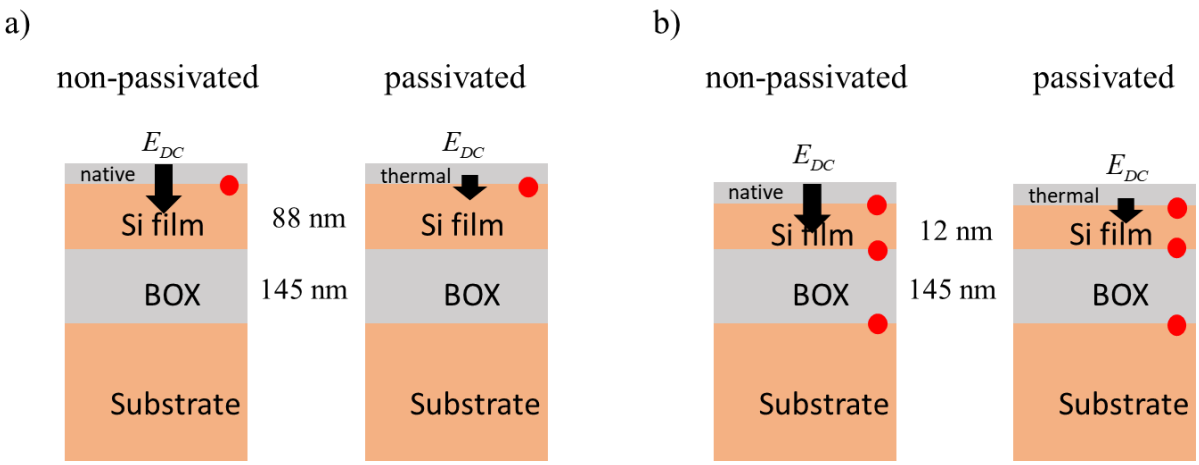

Figure 5.29: a) 88 nm/145 nm and b) 12 nm/145 nm SOI geometry schematics. The red circles indicate the interfaces that contribute to the detected SHG signal.

In order to investigate the effect of the passivation on the buried interface (BOX/substrate), the Si film was etched leaving the exposed BOX (Figure 5.30a) and the SHG was measured for all four samples. The results are shown in Figure 5.30b. The passivation process has a minimal effect on the buried interface since it should mainly modify the signal from the top silicon film (etched off). Nevertheless, a 10% variation in SHG is measured between samples which were passivated and those which were not passivated. This is probably attributed to the supplementary high temperature process step associated with the passivation process that may have affected the BOX (and the corresponding buried interface). Therefore, the electric field from the bottom interface does not affect noticeably the observed SHG. This was demonstrated previously in section 5.4.5, where the greatest impact on simulated SHG originated from the top interface E_{dc} (E_1); changing the E_{dc} from the buried interfaces (E_2, E_3) had minimal impact.

The exposed BOX demonstrates a decreasing SHG time dependence (Figure 5.30b), while for the full SOI structure TD-SHG increases (Figure 5.28). In the case of the full SOI structure, electrons are injected from the Si film via a 3-photon process to the interface and bulk states as well as to the ambient surface of the top ultrathin native or thermal SiO_2 (Figure 5.29), where electrons are captured by oxygen molecules. As we already saw in Chapter 2 in the case of simple ultrathin SiO_2/Si structures this injection mechanism to the ambient surface is more prominent. Furthermore, photogenerated electron-hole pairs in Si are separated from the pre-existing electric field, which would cause its screening, therefore decreasing the SHG. However, we observe a monotonically increasing behaviour (for the full SOI structures) meaning that the injection of electrons to trap sites creates an electric field much stronger than the pre-existing field. In the case of exposed BOX, the signal decreases: electrons cannot be injected on the oxide surface since the oxide is very thick. Injection to trap sites at the interface and bulk of the oxide, as well as charge separation, create an electric field which screens the pre-existing one.

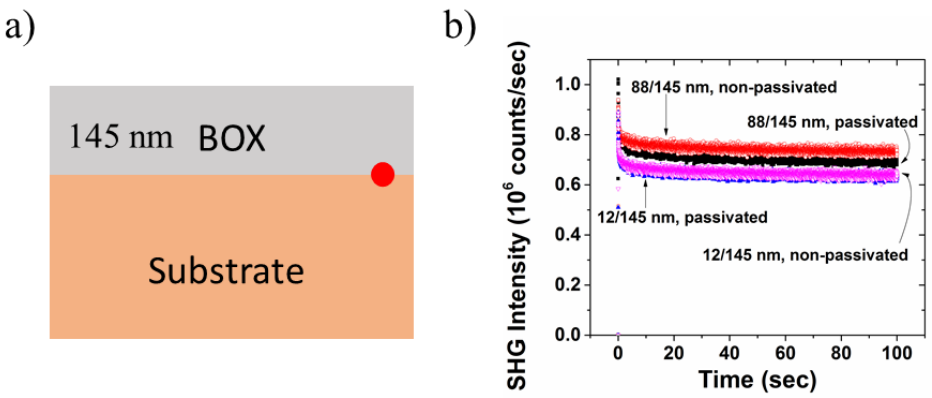

Figure 5.30: SHG signal originating from the SiO_2/Si substrate interface. a) The probed area was an exposed BOX region of 145 nm thickness (the Si layer was etched-off). b) TD-SHG from the exposed BOX region of passivated and non-passivated SOI wafers having initially 88 nm or 12 nm Si film.

To sum up, we observed that the electric field at the buried interface in both structures does not affect significantly the SHG signal. The main contribution is coming from the top interface (top oxide/Si film). Passivated top surface has reduced D_{it} (identified from conventional Ψ-MOSFET measurements), therefore lower E_{dc}, which translates to smaller SHG signal, as theoretically expected from:

$$I_{2\omega} \propto \left| \chi^{(2)}_{\text{interface}} + \chi^{(3)} E_{dc} \right|^2 \left(I_{\omega} \right)^2 \qquad (5.6)$$

5.5 Conclusions

Second Harmonic Generation was demonstrated as a non-destructive method to monitor the quality of SOI wafers. The experimental parameters leading to the strongest SHG signal from SOI samples with 88/145 nm geometry are P-in, P-out for the incident and SHG polarizations, 45° angle of incidence and a rotation angle of the sample of 0°. The SHG depends on the layer thickness of the Si film and the BOX, verified by simulation. The simulation tool also demonstrated the importance of the top electric field E_{dc} (top oxide/Si film interface) which was also observed experimentally from passivated and non-passivated samples, inherently having different top E_{dc}. This implies that the SHG technique corrected for thickness variations presents a great potential to access information about the interfacial electric fields (E_{dc}), leading to characterization of interface states (D_{it}) and quality control of SOI wafers.

Chapter 6:
General Conclusions and Prospects

Contents of Chapter 6

6.1 General conclusions

Integrated circuit and electronics components manufacturers need to know the wafer material quality before proceeding to device fabrication, in order to enhance yield and reduce costs. Various characterization methods are used for revealing information about the electrical interface quality between dielectrics and Si, by electrical parameters such as fixed charges in the oxide (Q_{ox}) and interface traps (D_{it}). Among these methods, SHG is a very interesting, non-invasive method that could be integrated in fab lines for real time monitoring. The technique's capability to probe electrical properties of interfaces comes from its dependence on interface structural defects and electric fields. Indeed, the SHG intensity $I_{2\omega}(t)$ from a material stack is generally described by:

$$I_{2\omega}(t) = \left|\chi^{(2)} + \chi^{(3)}\left[E_{dc}(0) + E_{dc}(t)\right]\right|^2 I_{\omega}^2 \qquad (6.1)$$

where $\chi^{(2)}$ and $\chi^{(3)}$ are the second and third order nonlinear susceptibilities (which are material dependent), I_{ω} is the incident light intensity. The constant term $E_{dc}(0)$ is the static electric field at the interface arising from Q_{ox} and initially charged D_{it}. The time-dependent term $E_{dc}(t)$ reveals the charging/trapping mechanisms such as:

- Separation of charges (photo-induced electron hole pairs) due to $E_{dc}(0)$.
- Injection of electrons and/or holes from the Si bands into/onto a dielectric layer, through multiphoton processes.

The aim of this thesis was to use SHG for material and interface electrical characterization on Al_2O_3/Si and Silicon-on-insulator (SOI). The development of a home-made simulator was mandatory in order to describe the optical nonlinear phenomena in presence of internal electric fields and eventually separate the optical phenomena from electrical properties.

- **Home-made simulator development**

Since SHG is an optical technique, I_{ω} and $I_{2\omega}$ in eq. (6.1) exhibit optical propagation phenomena in thin film systems, such as absorption and multiple reflections that cause interferences. In order to extract information about $E_{dc}(0)$ only (therefore Q_{ox} and D_{it}), we properly accounted for these optical effects by developing a home-made simulator. We took into account the electromagnetic radiation propagation at both ω and 2ω frequencies through Maxwell's equations. The simulation calculates first the electric fields everywhere in the multilayer structure, at the fundamental frequency (ω). Then, the nonlinear polarization is calculated at each interface which is used for the calculation of the electric fields at the second harmonic frequency (2ω). Furthermore, the essential $E_{dc}(0)$ term was incorporated in the nonlinear polarization. Finally, the simulation tool was validated by using experimental data from

Si covered with a native SiO_2. It was used in Chapters 4 and 5 to explain experimental data from Al_2O_3/Si and SOI.

- **SHG for evaluation of Al_2O_3 passivation quality**

Using both SHG simulations and experiments, we monitored the chemical and the field effect passivation due to fixed oxide charges in Al_2O_3/Si stacks fabricated with various deposition and annealing parameters. µ-PCD measurements revealed the effective carrier lifetime (τ_{eff}) in these stacks and a qualitative correlation with SHG was found as both τ_{eff} and the SHG intensity increased after annealing. Indeed, annealing improves the surface passivation of Si through hydrogen diffusion and negative charges activation which increases τ_{eff}, while the negative charges in Al_2O_3 increase $E_{dc}(0)$, therefore increase SHG (eq. (6.1)).

In order to extract more quantitative results from SHG measurements, a calibration is necessary. For that purpose, we fabricated MOS capacitors and extracted D_{it} and Q_{ox} from conventional C-V measurements; the static electric field $E_{dc}(0)$ at the interface between Si and Al_2O_3 was then estimated. We demonstrated that the square root of the SHG intensity scales linearly with $E_{dc}(0)$ (calculated from C-V), as expected from eq. (6.1). SHG simulations fed with the shifts of $E_{dc}(0)$ between as-deposited and annealed samples (for a thermal and a plasma ALD process), could reproduce the experimental data. This was done for 2 different experimental parameters: both SHG versus angle of incidence (AOI) and SHG vs azimuthal angle, exhibiting the importance of including the electric field in the optical simulation. The time-dependent dynamics of SHG, $E_{dc}(t)$, showed that the initial signal is related mostly to the fixed Q_{ox} and its time evolution is faster for higher D_{it} values. Finally, Si (111) substrates produce different results than Si (100), which is expected theoretically since the nonlinear polarizations are different.

- **SHG for SOI interface characterization**

Using SHG for characterization of multilayers such as SOI is more complicated due to the interferences coming from radiation propagation at multiple interfaces, as well as due to the possibility that the SOI interfaces are electrically coupled (especially in thin film SOI). The layer thicknesses of the Si film and the BOX both impact the SHG signals. For thick SOI with t_{Si}=145 nm/t_{BOX}=1000 nm, the SHG decreased with the increase of t_{Si} (measured by reflectometry) but for the thinner SOI with t_{Si}=88 nm/t_{BOX}=145 nm, the trend was opposite (SHG increased with the increase of t_{Si}). Our home-made simulation explained both trends by optical interferences. Moving a step further, we also experimented with the angle of incidence of the fundamental radiation, which effectively alters the optical path of the light travelling inside the multilayer structure. Both of the two SOI structures

exhibited a characteristic peak in SHG vs AOI experiments, which was reproduced by the simulation. While in thicker Si film/BOX structures no E_{dc} was introduced in the simulation, for ultrathin SOI (t_{Si}=24 nm/t_{BOX}=25 nm), an electric field value of 10^5 V/m was necessary in order to reproduce the experimental results. This indicates that SHG can access the interface electric fields present in ultrathin SOI interfaces.

Through the simulations for ultrathin Si film SOI, we could demonstrate that even though the static electric field at the top oxide/Si film interface is dominant, the electric field at the Si film/BOX and BOX/substrate interfaces can be accessed as well. This was also investigated experimentally with SHG characterization from non-passivated SOI (native top oxide) and passivated SOI (thermal top oxide) which reduces D_{it} (thus reduces E_{dc}). The SHG signals were stronger for the non-passivated SOI which has higher E_{dc} field. From this SOI study, our results imply that if the thickness variations are decorrelated from the SHG signals, we can access information regarding the interface electric fields, leading to characterization of interface states (Q_{ox} and D_{it}) of SOI wafers.

6.2 Prospects

- **Simulator development**

In this thesis, we mainly studied and simulated the static electric field, $E_{dc}(0)$ (initial, constant term). In the future, the time-dependent EFISH could be incorporated in the simulator by accounting for drift-diffusion and generation-recombination in Si, which could separately calculate the $E_{dc}(t)$ values. Furthermore, inside the simulation, we accounted for a single effective value of the electric field exactly at the interface. However, in reality, the electric field has a spatial distribution in the space charge region inside Si and as we move further away from the interface, the electric field drops rapidly. Therefore, for a more realistic approach, we could include:

- the electric field distribution in the Si SCR.
- SH radiation sources from a few nm (~escape depth of SHG) inside bulk Si.
- the time dependency of the static electric field.

- **SHG for future Al_2O_3 characterization**

In Chapter 4 we investigated the ability to acquire electrical information through SHG. However, interface electric field values extracted from CV measurements were used as input in the simulator in order to reproduce the experimental SHG. The goal is actually to deduce E_{dc} from stand-alone SHG measurements. For this reason, a calibration procedure needs to be developed in order to remove the optical phenomena from the Al_2O_3/Si stack using the experimental SHG data combined with the simulator in order to deduce E_{dc}.

- **SHG for future SOI characterization**

Being a fast, optical and non-invasive technique, SHG has the ability to map SOI wafers without surface contact. Given the sensitivity of SHG to the quality of interfaces, these spatial maps are of utility for semiconductor process monitoring and quality control. Furthermore, the conventional electrical tests for SOI wafers are based on the Ψ-MOSFET technique, from which the key material parameters are extracted, but the probes locally damage the Si film surface (and even the buried oxide in the case of ultrathin Si film/BOX). Measuring an SHG signal modulated by the bias voltage applied on the substrate is a highly promising method to achieve a contactless Ψ-MOSFET. SHG would then monitor the variation of the channel charge with the back-gate bias.

6.3 Other possible applications: preliminary results

The use of SHG for characterization of semiconductor/dielectric stacks could go further than the two studies shown here (Al_2O_3/Si and SOI). During this thesis we opened other possible applications of SHG and we will show some of the preliminary results in the following sections.

6.3.1 Cu contamination detection with SHG

Metallic contaminations can be induced on wafers during microelectronics processes and their presence limits the final device performance. SHG can detect non-invasively the contaminations at the interface between SiO_2/Si. For the proof of concept, we induced Cu contaminations intentionally on Si wafers [142] and then we studied the SHG signals in P-out polarization, which is interface specific (as mentioned in Chapter 2). Figure 6.1a shows SHG maps from Cu contaminated samples with different concentrations (10^{10}, 10^{11} at/cm^2). Both contaminated samples present higher SHG signal than the reference, with the higher contamination level having a stronger SHG. Furthermore, the time-dependence of the reference and the contaminated samples (Figure 6.1b) are different: the contaminated samples exhibit a faster time response towards saturation. We should note that the contamination procedure includes dipping the samples in a high temperature bath at ~80°C, which could cause some Cu diffusion in Si. The SHG could be able to identify the surface/bulk contaminants by using different input/output polarization combinations. This study needs to be completed with an optimized and reproducible contamination protocol, as well as benchmark tests with other measurement techniques (µ-PCD, TXRF, resistivity, etc…).

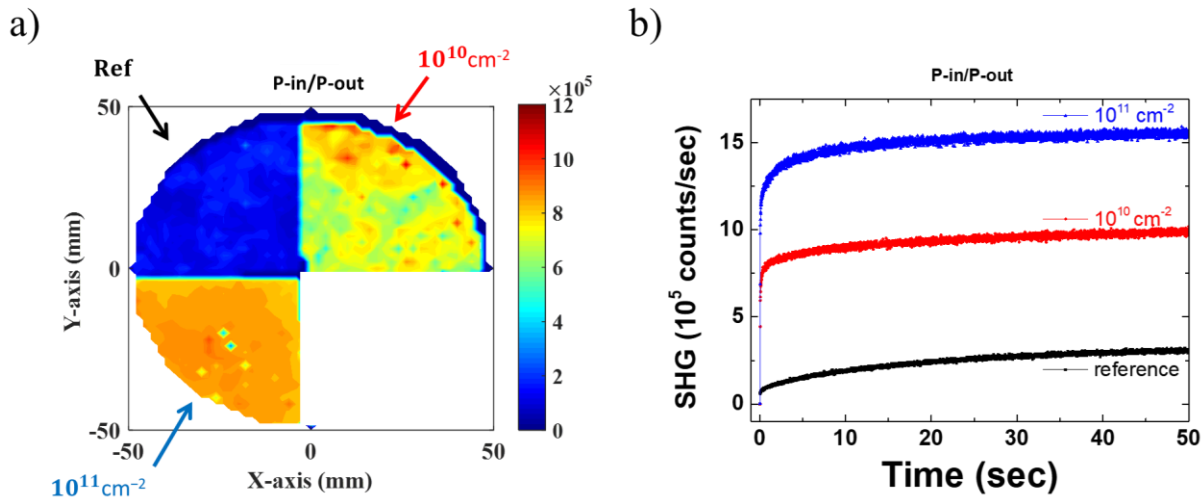

Figure 6.1: a) SHG map from Si samples contaminated with Cu with various concentrations (10^{10} cm^{-2}, 10^{11} cm^{-2}), as well as the reference sample. b) Time-dependent SHG from the same samples as in (a).

6.3.2 SHG for other high-k dielectrics

High-k dielectrics are used in photovoltaics and microelectronics for surface passivation. Chapter 4 showed a detailed SHG study of Al_2O_3/Si that can be extended to other high-k dielectrics (for example, HfO_2 passivation analysis with SHG is scheduled for a new project). However, since SHG is an optical technique, the results will also depend on the optical properties of each dielectric as well as the sign of the fixed charges in the oxide. Therefore, it is not possible to simply transpose the conclusions on any dielectric material. Let us show an example for SiN_x.

Two samples were fabricated: Si (100) passivated with a) 80 nm **standard SiN_x** layer and b) 80 nm **Si-rich SiN_x** layer. In Figure 6.2a, the minority carrier lifetime maps show higher lifetime for the Si-rich SiN sample (averaged τ_{eff} ~ 420 µs, while for standard SiN_x τ_{eff} ~ 265 µs). Figure 6.2b shows higher SHG signal for the standard SiN sample (almost one order of magnitude higher than the standard SiN). Hence, the sample with the higher minority carrier lifetime has a smaller SHG signal. The trend was opposite for Al_2O_3 (Chapter 4), where samples with higher effective lifetime (after annealing), showed higher SHG as well. The main reason for this difference is the large absorption coefficient of Si-rich SiN_x - particularly at 390 nm. Furthermore, the time-dependence of the SHG signal from SiN_x samples is exhibiting a decreasing behaviour, in contrast to the monotonous increase of the Al_2O_3 samples in Chapter 4. This difference is probably attributed to the known fixed positive charges in SiN_x layers on Si (against the negative charges in Al_2O_3).

Therefore, SHG is able to study many high-k dielectrics on Si, however each time the optical properties of the materials as well as the sign of the fixed charges should be taken into account when interpreting the data.

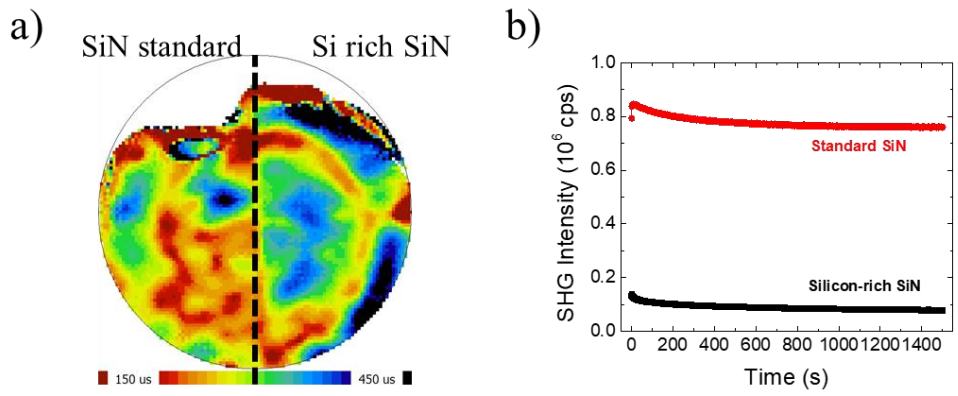

Figure 6.2: a) Minority carrier lifetime and b) time-dependent SHG for two samples passivated with SiN, one standard and the other Si-rich.

6.3.3 Surface roughness monitoring

Another application of SHG could potentially be the surface roughness monitoring. Dadap et al [143] already showed that rotational anisotropic SHG is impacted by the surface roughness of Si/SiO_2 samples. Based on a similar process, we produced samples with different roughnesses using HF etching for various etch times: 10 s, 1 min, 3 min, 9 min. In Figure 6.3 we plot the SHG versus the azimuthal angle for the fabricated SiO_2/Si (100) samples:

a) In Figure 6.3a, P-in/P-out polarization configuration (which probes the surface properties), the phase shifts by ~45° for all etched samples when compared with the reference. Furthermore, the longer the etch time, the higher the isotropic SHG level is. Similar results were obtained in [143].
b) In Figure 6.3b, the SHG from P-in/S-out polarization configuration (which probes the bulk properties), does not seem to change significantly. This is expected since HF affects only the oxide and does not attack the bulk Si.

However, we should note that after etching, the samples were measured with SHG in an ambient environment which promotes native oxide regrowth. An important aspect is the surface uniformity of each sample. In Figure 6.4 we clearly see from the P-in/P-out SHG signal contours that the surface layer is non-uniform. The AFM images from the 9 min and 1 min HF etched samples are also shown on the left for comparison, but the difference is small (as shown from the average R_a, and root mean square R_q roughness values). Again, SHG is obviously sensitive to the roughness but a more robust sample fabrication protocol must be established, in order to have a more quantitative analysis.

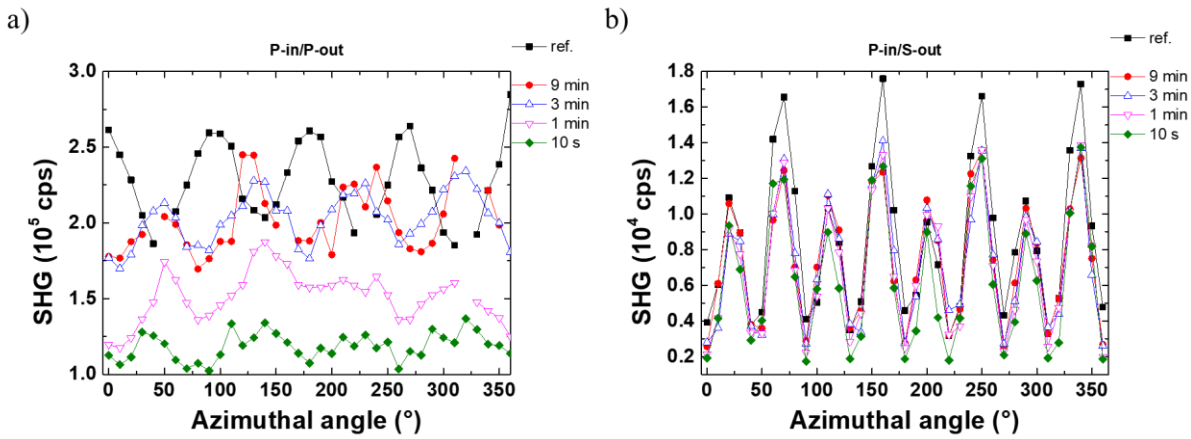

Figure 6.3: SHG versus azimuthal angle for samples etched for different times (10s, 1min, 3min, 9min) and the reference sample. a) P-in/P-out polarization configuration. b) P-in/S-out polarization configuration.

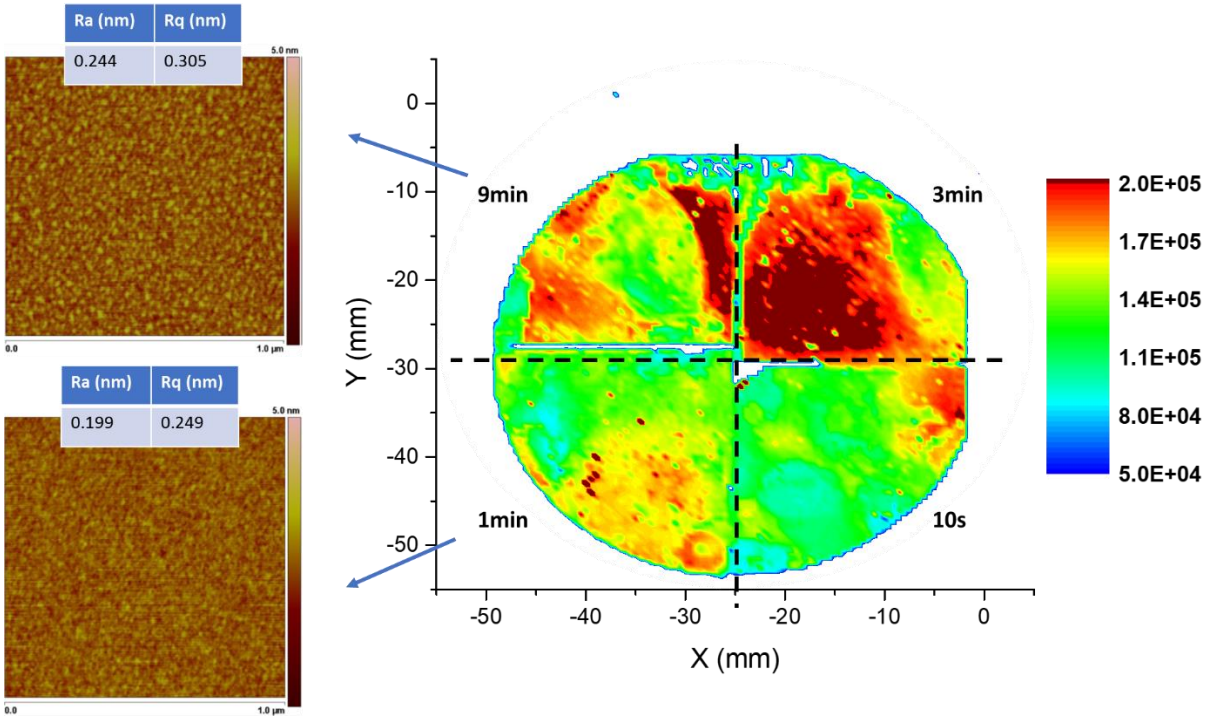

Figure 6.4: SHG color mapping of surface nonuniformity in Si samples with regrown native oxide in ambient environment following HF etch. The AFM images on the left for the 9 min and 1 min HF etched samples are shown.

6.3.4 SHG from non-centrosymmetric materials (GaN)

All the materials studied in this thesis were centrosymmetric; they do not produce any dipolar SH from their bulk (dipole forbidden), which makes the SHG technique highly sensitive to the interface properties. In the case of non-centrosymmetric materials though, bulk dipolar SHG is present. For the wurtzite crystal structure (GaN), the same expressions hold for the SHG intensity as in Chapter 2, with the only difference being that the second order dipolar susceptibility is stronger since it originates from the bulk of the material. The analysis of these kind of materials must take into consideration this bulk dipolar contribution. For example, in Figure 6.5 the SHG versus the azimuthal angle is monitored for a GaN/AlGaN/AlN/Si(111) stack. GaN produces a weak azimuthal SHG response for the P-in/P-out configuration, while a 6-fold symmetry is observed for P-in/S-out which is typical of Si (111) substrates. According to a previous work on these kind of materials [144], the SHG signals include:

- bulk dipolar sources from the GaN, AlGaN, and AlN films
- dipolar sources from the interface between the films due to strain
- a bulk quadrupolar source from the Si(111) substrate.

The weak anisotropic response from P-in/P-out configuration indicates that the bulk isotropic dipolar sources of SHG are a lot stronger than the bulk anisotropic quadrupolar component coming from Si (111). For the P-in/S-out configuration, the isotropic and anisotropic bulk and interface

contributions are comparable, revealing the 6-fold symmetry of Si (111). However, the various sources of SHG must be more thoroughly examined and the feasibility of separating dipolar interface and dipolar bulk contributions must be investigated in order to adapt the technique to each material under study.

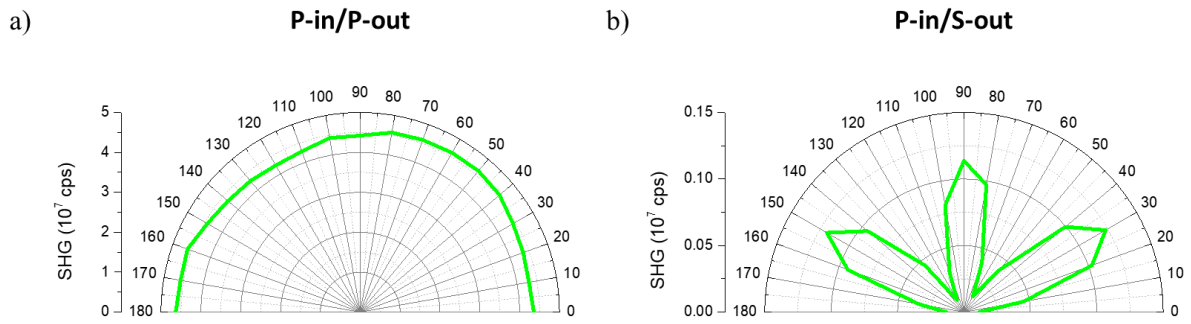

Figure 6.5: Azimuthal SHG from a GaN/AlGaN/AlN/Si(111) sample for a) P-in/P-out and b) P-in/S-out polarization configurations.

… All these preliminary results demonstrate the large potential of SHG for material/interface characterization, consisting a huge playground for the future PhD students …

Appendix

The general forms of the electric and magnetic fields used in the calculation of the boundary conditions in Chapter 2 are:

A) For P-polarization (no y component for E):

$$\overrightarrow{E_i^-}(z) = \left(E_i^- \cos\theta_i \vec{x} + E_i^- \sin\theta_i \vec{z}\right)\exp(-ik_{z,i}z + ik_{x,i}x)$$
$$\overrightarrow{E_i^+}(z) = \left(-E_i^+ \cos\theta_i \vec{x} + E_i^+ \sin\theta_i \vec{z}\right)\exp(+ik_{z,i}z + ik_{x,i}x)$$
$$\overrightarrow{E_{i+1}^-}(z) = \left(E_{i+1}^- \cos\theta_{i+1} \vec{x} + E_{i+1}^- \sin\theta_{i+1} \vec{z}\right)\exp(-ik_{z,i+1}z + ik_{x,i+1}x)$$
$$\overrightarrow{E_{i+1}^+}(z) = \left(-E_{i+1}^+ \cos\theta_{i+1} \vec{x} + E_{i+1}^+ \sin\theta_{i+1} \vec{z}\right)\exp(+ik_{z,i+1}z + ik_{x,i+1}x)$$

$$\overrightarrow{H_i^-}(z) = c\varepsilon_0(n_i E_i^- \cos\theta_i \vec{y})\exp(-ik_{z,i}z + ik_{x,i}x)$$
$$\overrightarrow{H_i^+}(z) = c\varepsilon_0(n_i E_i^+ \cos\theta_i \vec{y})\exp(+ik_{z,i}z + ik_{x,i}x)$$
$$\overrightarrow{H_{i+1}^-}(z) = c\varepsilon_0(n_{i+1} E_{i+1}^- \cos\theta_{i+1} \vec{y})\exp(-ik_{z,i+1}z + ik_{x,i+1}x)$$
$$\overrightarrow{H_{i+1}^+}(z) = c\varepsilon_0(n_{i+1} E_{i+1}^+ \cos\theta_{i+1} \vec{y})\exp(+ik_{z,i+1}z + ik_{x,i+1}x)$$

The magnetic fields were calculated from the usual expression $\vec{H} = -(1/i\omega\mu_0)\left(\vec{\nabla} \times \vec{E}\right)$.

B) For S-polarization, the magnetic and electric fields are:

$$\overrightarrow{H_i^-}(z) = c\varepsilon_0\left(n_i \cos\theta_i E_i^- \vec{x} + n_i \sin\theta_i E_i^- \vec{z}\right)\exp(-ik_{z,i}z + ik_{x,i}x)$$
$$\overrightarrow{H_i^+}(z) = c\varepsilon_0\left(-n_i \cos\theta_i E_i^+ \vec{x} + n_i \sin\theta_i E_i^+ \vec{z}\right)\exp(+ik_{z,i}z + ik_{x,i}x)$$
$$\overrightarrow{H_{i+1}^-}(z) = c\varepsilon_0\left(n_{i+1} \cos\theta_{i+1} E_{i+1}^- \vec{x} + n_{i+1} \sin\theta_{i+1} E_{i+1}^- \vec{z}\right)\exp(-ik_{z,i+1}z + ik_{x,i+1}x)$$
$$\overrightarrow{H_{i+1}^+}(z) = c\varepsilon_0\left(-n_{i+1} \cos\theta_{i+1} E_{i+1}^+ \vec{x} + n_{i+1} \sin\theta_{i+1} E_{i+1}^+ \vec{z}\right)\exp(+ik_{z,i+1}z + ik_{x,i+1}x)$$

$$\overrightarrow{E_i^-}(z) = \left(-E_i^- \vec{y}\right)\exp(-ik_{z,i}z + ik_{x,i}x)$$
$$\overrightarrow{E_i^+}(z) = \left(-E_i^+ \vec{y}\right)\exp(+ik_{z,i}z + ik_{x,i}x)$$
$$\overrightarrow{E_{i+1}^-}(z) = \left(-E_{i+1}^- \vec{y}\right)\exp(-ik_{z,i+1}z + ik_{x,i+1}x)$$
$$\overrightarrow{E_{i+1}^+}(z) = \left(-E_{i+1}^+ \vec{y}\right)\exp(+ik_{z,i+1}z + ik_{x,i+1}x)$$

where $\vec{x}, \vec{y}, \vec{z}$ are unit vectors.

References

[1] O. Kononchuk and B.-Y. Nguyen, Eds., *Silicon-on-insulator (SOI) Technology: Manufacture and Applications*. Woodhead Publishing, 2014.

[2] "MOSFET schematic." [Online]. Available: http://indexxit.com/mosfets/gorgeous-mosfets-rig-nitc-explained-mosfet-reactions-inside/.

[3] "ITRS," 2013. [Online]. Available: http://www.itrs2.net/2013-itrs.html.

[4] E. R. Fossum, S. Mendis, and S. E. Kemeny, "ACTIVE PIXEL SENSOR WITH INTRA-PIXEL CHARGE TRANSFER," Patent no. 5471515, 1995.

[5] A. G. Aberle, "Surface passivation of crystalline silicon solar cells: a review," *Prog. Photovoltaics Res. Appl.*, vol. 8, no. 5, pp. 473–487, 2000.

[6] J. Kruegener and N.-P. Harder, "Weak Light Performance of PERC, PERT and Standard Industrial Solar Cells," *Energy Procedia*, vol. 38, pp. 108–113, 2013.

[7] C. R. Helms and E. H. Poindexter, "The silicon-silicon-dioxide system: its microstructure and imperfections," *Rep. Prog. Phys*, vol. 57, pp. 791–852, 1994.

[8] B. D. Cullity, *Elements of X-Ray diffraction*, 2nd ed. Addison-Wesley, 1978.

[9] D. Hellin, S. De Gendt, N. Valckx, P. W. Mertens, and C. Vinckier, "Trends in total reflection X-ray fluorescence spectrometry for metallic contamination control in semiconductor nanotechnology," *Spectrochim. Acta Part B*, vol. 61, pp. 496–514, 2006.

[10] D. Rugar and P. Hasma, "Atomic Force Microscopy," *Phys. Today*, vol. October 1990, pp. 23–30.

[11] V. Gorodokin and D. Zemlyanov, "Metallic contamination in silicon processing," in *2004 23rd IEEE Convention of Electrical and Electronics Engineers in Israel*, pp. 157–160.

[12] M. E. Rodríguez, A. Mandelis, G. Pan, J. A. García, V. Gorodokin, and Y. Raskin, "Minority carrier lifetime and iron concentration measurements on p-Si wafers by infrared photothermal radiometry and microwave photoconductance decay," *J. Appl. Phys.*, vol. 87, no. 11, pp. 8113–8121, 2000.

[13] G. Dingemans and W. M. M. Kessels, "Status and prospects of Al2O3-based surface passivation schemes for silicon solar cells," *J. Vac. Sci. Technol. A*, vol. 30, p. 040802, 2012.

[14] Dieter K Schroder, *Semiconductor Material and Device Characterization*, 3rd ed. Wiley & Sons, 2006.

[15] E. H. Nicollian and J. R. Brews, *MOS (Metal Oxide Semiconductor) Physics and Technology*. New York, USA: John Wiley & Sons, 1982.

[16] S. M. Sze, *Physics of Semiconductor Devices Physics of Semiconductor Devices*, 3rd ed. Wiley & Sons, 2007.

[17] C. N. Berglund, "Surface States at Steam-Grown Silicon-Silicon Dioxide Interfaces," *IEEE Trans. Electron Devices*, vol. 13, no. 10, pp. 701–705, 1966.

[18] L. M. Terman, "An Investigation of Surface States at a Silicon/Silicon Oxide Interface employing Metal-Oxide-Silicon Diodes," *Solid. State. Electron.*, vol. 5, pp. 285–299, 1962.

[19] P. Solomon, "Breakdown in silicon oxide−A review," *J. Vac. Sci. Technol.*, vol. 14, no. 5, pp. 1122–1130, Sep. 1977.

[20] J. Kolodzey, E. A. Chowdhury, T. N. Adam, G. Guohua Qui, I. Rau, J. O. Olowolafe, J. S. Suehle, and Y. Yuan Chen, "Electrical conduction and dielectric breakdown in aluminum oxide insulators on silicon," *IEEE Trans. Electron Devices*, vol. 47, no. 1, pp. 121–128, 2000.

[21] Ih-Chin Chen, S. E. Holland, and Chenming Hu, "Electrical breakdown in thin gate and tunneling oxides," *IEEE Trans. Electron Devices*, vol. 32, no. 2, pp. 413–422, Feb. 1985.

[22] G. Besnard, X. Garros, P. Nguyen, F. Andrieu, P. Reynaud, W. Van Den Daele, K. K. Bourdelle, W. Schwarzenbach, a. Toffoli, R. Kies, D. Delprat, G. Reimbold, and S. Cristoloveanu, "Reliability of ultra-thin buried oxides for multi-VT FDSOI technology," *Solid. State. Electron.*, vol. 97, pp. 8–13, 2014.

[23] C. Huyghebaert, T. Bearda, E. Rosseel, J. L. Everaert, E. Don, and T. Pavelka, "Use of Corona Charge Photo-Conductance Decay (Charge-PCD) for fast metal contamination monitoring of high temperature processes," *ASMC (Advanced Semicond. Manuf. Conf. Proc).*, no. 1, pp. 397–401, 2008.

[24] S. Dauwe, "Low-Temperature Surface Passivation of Crystalline Silicon and its Application to the Rear Side of Solar Cells," PhD Thesis, Hannover, 2004.

[25] M. Wilson, J. Lagowski, L. Jastrzebski, A. Savtchouk, and V. Faifer, "COCOS (corona oxide characterization of semiconductor) non-contact metrology for gate dielectrics," *AIP Conf. Proc.*, vol. 550, p. 220, 2001.

[26] J. E. De Vries and Y. Rosenwaks, "Measuring the concentration and energy distribution of interface states using a non- contact corona oxide semiconductor method," *Appl. Phys. Lett*, vol. 100, p. 082111, 2012.

[27] R. A. Sinton, A. Cuevas, and M. Stuckings, "Quasi-steady-state photoconductance, a new method for solar cell material and device characterization," in *Conference Record of the Twenty Fifth IEEE Photovoltaic Specialists Conference - 1996*, 1996, pp. 457–460.

[28] J. Dziewior and W. Schmid, "Auger coefficients for highly doped and highly excited silicon," *Appl. Phys. Lett.*, vol. 31, pp. 2473–2510, 1977.

[29] "Semilab." www.semilab.hu.

[30] R. W. Boyd, *Nonlinear Optics*, 3rd ed. Academic Press, 2008.

[31] T. F. Heinz, "Second-Order Nonlinear Optical Effects at Surfaces and Interfaces," *Nonlinear Surface Electromagnetic Phenomena*. pp. 353–416, 1991.

[32] B. Jun, Y. V. White, R. D. Schrimpf, D. M. Fleetwood, F. Brunier, N. Bresson, S. Cristoloveanu, and N. H. Tolk, "Characterization of multiple Si/SiO 2 interfaces in silicon-on-insulator materials via second-harmonic generation," *Appl. Phys. Lett.*, vol. 85, no. 15, pp. 3095–3097, 2004.

[33] M. L. Alles, R. Pasternak, X. Lu, N. H. Tolk, R. D. Schrimpf, D. M. Fleetwood, R. P. Dolan, and R. W. Standley, "Second harmonic generation for noninvasive metrology of silicon-on-insulator wafers," *IEEE Trans. Semicond. Manuf.*, vol. 20, no. 2, pp. 107–112, 2007.

[34] G. Lüpke, "Characterization of semiconductor interfaces by second-harmonic generation," *Surf. Sci. Rep.*, vol. 35, no. 3, pp. 75–161, 1999.

[35] G. Hamaide, F. Allibert, H. Hovel, and S. Cristoloveanu, "Impact of free-surface passivation on silicon on insulator buried interface properties by pseudotransistor characterization," *J. Appl. Phys*, vol. 101, pp. 114513–317, 2007.

[36] P. A. Franken, A. E. Hill, C. W. Peters, and G. Weinreich, "Generation of Optical Harmonics," *Phys. Rev. Lett.*, vol. 7, no. 4, pp. 118–119, 1961.

[37] D. A. Kleinman, "Nonlinear Dielectric Polarization in Optical Media," *Phys. Rev.*, vol. 126, no. 6, 1962.

[38] C. H. Lee, R. K. Chang, and N. Bloembergen, "Nonlinear electroreflectance in silicon and silver," *Phys. Rev. Lett.*, vol. 18, no. 5, pp. 167–170, 1967.

[39] N. Bloembergen, R. K. Chang, S. S. Jha, and C. H. Lee, "Optical Second-Harmonic Generation in Refiection from Media with Inversion Symmetry," vol. 174, no. 3, 1968.

[40] P. N. Butcher and D. Cotter, *The Elements of Nonlinear Optics*. Cambridge University Press, 1991.

[41] Y. R. Shen, *The Principles of Nonlinear Optics*. John Wiley & Sons, 1984.

[42] J. E. Sipe, D. J. Moss, and H. M. Van Driel, "Phenomenological theory of optical second-and third-harmonic generation from cubic centrosymmetric crystals," *Phys. Rev. B*, vol. 35, no. 3, pp. 15–1987.

[43] J. J. H. Gielis, P. M. Gevers, I. M. P. Aarts, M. C. M. van de Sanden, and W. M. M. Kessels, "Optical second-harmonic generation in thin film systems," *J. Vac. Sci. Technol. A*, vol. 26, no. 6, p. 1519, 2008.

[44] H. W. K. Tom, T. F. Heinz, and Y. R. Shen, "Second-harmonic reflection from silicon surfaces and its relation to structural symmetry," *Phys. Rev. Lett.*, vol. 51, no. 21, pp. 1983–1986, 1983.

[45] J. E. Sipe, D. J. Moss, and H. M. Vandriel, "Phenomenological Theory of Optical 2nd-Harmonic and 3rd-Harmonic Generation from Cubic Centrosymmetric Crystals," *Phys. Rev. B*, vol. 35, no. 3, pp. 1129–1141, 1987.

[46] P. Guyot-Sionnest, W. Chen, and Y. R. Shen, "General considerations on optical second-harmonic generation from surfaces and interfaces," *Phys. Rev. B*, vol. 33, no. 12, pp. 8254–8263, 1986.

[47] P. Guyot-Sionnest and Y. R. Shen, "Bulk contribution in surface second-harmonic generation," *Phys. Rev. B*, vol. 38, no. 12, pp. 7985–7989, 1988.

[48] O. A. Aktsipetrov, I. M. Baranova, L. V Grigor'eva, K. N. Evtyukhov, E. D. Mishina, T. V Murzina, and I. V Chernyĭ, "Second harmonic generation at a semiconductor–electrolyte interface and investigation of the surface of silicon by the nonlinear electroreflection method," *Sov. J. Quantum Electron.*, vol. 21, no. 8, pp. 854–859, Aug. 1991.

[49] O. A. Aktsipetrov, A. A. Fedyanin, A. V Melnikov, E. D. Mishina, A. N. Rubtsov, M. H. Anderson, P. T. Wilson, M. Ter Beek, X. F. Hu, J. I. Dadap, and M. C. Downer, "dc-electric-field-induced and low-frequency electromodulation second-harmonic generation spectroscopy of Si(001)/SiO2 interfaces."

[50] J. Dadap, Z. Xu, X. Hu, M. Downer, N. Russell, J. Ekerdt, and O. Aktsipetrov, "Second-harmonic spectroscopy of a Si(001) surface during calibrated variations in temperature and hydrogen coverage," *Phys. Rev. B*, vol. 56, no. 20, pp. 13367–13379, 1997.

[51] Y. Q. An, R. Carriles, and M. C. Downer, "Absolute phase and amplitude of second-order nonlinear optical susceptibility components at Si(001) interfaces," *Phys. Rev. B*, vol. 75, no. 24, pp. 1–4, 2007.

[52] C. H. Bjorkman, "Influence of surface roughness on the electrical properties of Si–SiO2 interfaces and on second-harmonic generation at these interfaces," *J. Vac. Sci. Technol. B*, vol. 11, no. 4, p. 1521, 1993.

[53] J. I. Dadap, B. Doris, Q. Deng, M. C. Downer, J. K. Lowell, and a. C. Diebold, "Randomly oriented Angstrom-scale microroughness at the Si(100)/SiO2 interface probed by optical second harmonic generation," *Appl. Phys. Lett.*, vol. 64, no. 16, pp. 2139–2141, 1994.

[54] S. T. Cundiff, W. H. Knox, F. H. Baumann, K. W. Evans-Lutterodt, M.-T. Tang, M. L. Green, and H. M. Van Driel, "Si/SiO interface roughness: Comparison between surface second harmonic generation and x-ray scattering," *Appl. Phys. Lett.*, vol. 70, 1997.

[55] J. H. Zhao, W. Su, Q. D. Chen, Y. Jiang, Z. G. Chen, G. Jia, and H. B. Sun, "Strain at Native Sio2/Si(111) interface characterized by strain-scanning second-harmonic generation," *IEEE J. Quantum Electron.*, vol. 47, no. 1, pp. 55–59, 2011.

[56] W. Daum, H.-J. Krause, U. Reichel, and H. Ibach, "Identification of Strained Silicon Layers at Si-Sio2 Interfaces and Clean Si Surfaces by Nonlinear Optical Spectroscopy," vol. 71, no. 8.

[57] I. L. Lyubchanskii, N. N. Dadoenkova, M. I. Lyubchanskii, T. Rasing, J.-W. Jeong, and S.-C. Shin, "Second-harmonic generation from realistic film–substrate interfaces: The effects of strain," *Appl. Phys. Lett*, vol. 76, p. 1848, 2000.

[58] Y. Cho, F. Shafiei, B. S. Mendoza, M. Lei, T. Jiang, P. S. Ho, and M. C. Downer, "Second-harmonic microscopy of strain fields around through-silicon-vias," *Appl. Phys. Lett*, vol. 108, 2016.

[59] J. J. H. Gielis, P. M. Gevers, a. a. E. Stevens, H. C. W. Beijerinck, M. C. M. van de Sanden, and W. M. M. Kessels, "Spectroscopic second-harmonic generation during Ar-ion bombardment of Si(100)," *Phys. Rev. B*, vol. 74, no. 16, p. 165311, 2006.

[60] H. Wang, E. C. Y. Yan, E. Borguet, and K. B. Eisenthal, "Second harmonic generation from the surface of centrosymmetric particles in bulk solution," *Chem. Phys. Lett.*, vol. 259, no. 1–2, pp. 15–20, 1996.

[61] A. Rumpel, B. Manschwetus, G. Lilienkamp, H. Schmidt, and W. Daum, "Polarity of space charge fields in second-harmonic generation spectra of Si (100)/SiO2 interfaces," *Phys. Rev. B*, vol. 74, p. 081303(R), 2006.

[62] G. Erley, R. Butz, and W. Daum, "Second-harmonic spectroscopy of interband excitations at the interfaces

of strained Si(100)-Si 0.85 Ge 0.15-SiO2 heterostructures," 1998.

[63] O. A. Aktsipetrov, A. A. Fedyanin, E. D. Mishina, A. N. Rubtsov, C. W. Van Hasselt, M. A. C. Devillers, and T. Rasing, "Probing the silicon-silicon oxide interface of Si(111)-SiO2-Cr MOS structures by DC-electric-field-induced second harmonic generation," *Surf. Sci.*, vol. 352–354, pp. 1033–1037, 1996.

[64] C. Ohlhoff, G. Lü, C. Meyer, and H. Kurz, "Static and high-frequency electric fields in silicon MOS and MS structures probed by optical second-harmonic generation," *Phys. Rev. B*, vol. 55, no. 7, pp. 4596–4606, 1997.

[65] P. Godefroy, W. De Jong, C. W. Van Hasselt, M. A. C. Devillers, and T. Rasing, "Electric field induced second harmonic generation spectroscopy on a metal-oxide- silicon structure," *Appl. Phys. Lett.*, vol. 68, 1996.

[66] J. I. Dadap, X. F. Hu, M. H. Anderson, M. C. Downer, J. K. Lowell, and O. A. Aktsipetrov, "Optical second-harmonic electroreflectance spectroscopy of a Si (001) metal-oxide-semiconductor structure," *Phys. Rev. B*, vol. 53, no. 12, pp. R7607-7609, 1996.

[67] D. Xiao, E. Ramsay, D. T. Reid, B. Offenbeck, and N. Weber, "Optical probing of a silicon integrated circuit using electric-field-induced second-harmonic generation," *Appl. Phys. Lett.*, vol. 88, no. 11, p. 114107, 2006.

[68] J. L. Alay and M. Hirose, "The valence band alignment at ultrathin SiO2/Si interfaces," *J. Appl. Phys.*, vol. 81, no. 3, pp. 1606–1608, 1997.

[69] W. Wang, G. Lüpke, M. Ventra, S. Pantelides, J. Gilligan, N. Tolk, I. Kizilyalli, P. Roy, G. Margaritondo, and G. Lucovsky, "Coupled Electron-Hole Dynamics at the Si/SiO2 Interface," *Phys. Rev. Lett.*, vol. 81, no. 19, pp. 4224–4227, 1998.

[70] J. G. Mihaychuk, J. Bloch, Y. Liu, and H. M. Van Driel, "Time-dependent second-harmonic generation from the Si – SiO2 interface induced by charge transfer," *Opt. Lett.*, vol. 20, no. 20, pp. 2063–2065, 1995.

[71] J. Bloch, J. Mihaychuk, and H. van Driel, "Electron Photoinjection from Silicon to Ultrathin SiO2 Films via Ambient Oxygen," *Phys. Rev. Lett.*, vol. 77, no. 5, pp. 920–923, 1996.

[72] V. Fomenko, E. P. Gusev, and E. Borguet, "Optical second harmonic generation studies of ultrathin high-k dielectric stacks," *J. Appl. Phys.*, vol. 97, no. 8, pp. 1–8, 2005.

[73] Z. Marka, R. Pasternak, S. N. Rashkeev, Y. Jiang, S. T. Pantelides, N. H. Tolk, P. K. Roy, and J. Kozub, "Band offsets measured by internal photoemission-induced second-harmonic generation.", *Phys. Rev. B*, vol. 67, p. 045302, 2003.

[74] J. G. Mihaychuk, N. Shamir, and H. M. Van Driel, "Multiphoton photoemission and electric-field-induced optical second-harmonic generation as probes of charge transfer across the Si/SiO2 interface," *Phys. Rev. B*, vol. 59, no. 3, pp. 2164–2173, 1999.

[75] B. S. Wherrett, "Scaling rules for multiphoton interband absorption in semiconductors," *J. Opt. Soc. Am. B*, vol. 1, no. 1, p. 67, 1984.

[76] V. Nathan, S. S. Mitra, and A. H. Guenther, "Review of multiphoton absorption in crystalline solids," *J. Opt. Soc. Am. B*, vol. 2, no. 2, p. 294, 1985.

[77] N. Shamir, J. G. Mihaychuk, H. M. Van Driel, and H. J. Kreuzer, "Universal Mechanism for Gas Adsorption and Electron Trapping on Oxidized Silicon," *Phys. Rev. Lett.*, vol. 82, no. 2, pp. 359–361, 1999.

[78] J. L. Fiore, V. V Fomenko, D. Bodlaki, and E. Borguet, "Second harmonic generation probing of dopant type and density at the Si/SiO2 interface," *Appl. Phys. Lett*, vol. 98, p. 041905, 2011.

[79] H. Park, J. Qi, Y. Xu, K. Varga, S. M. Weiss, B. R. Rogers, G. Lüpke, and N. Tolk, "Characterization of boron charge traps at the interface of Si/SiO2 using second harmonic generation," *Appl. Phys. Lett.*, vol. 95, 2009.

[80] H. Park, J. Qi, Y. Xu, K. Varga, S. M. Weiss, B. R. Rogers, G. Lüpke, and N. Tolk, "Boron induced charge traps near the interface of Si/SiO2 probed by second harmonic generation," *Phys. Status Solidi*, vol. 247, no. 8, pp. 1997–2001, 2010.

[81] H. Park, B. Choi, A. Steigerwald, K. Varga, and N. Tolk, "Annealing effect in boron-induced interface charge traps in Si/SiO2 systems," *J. Appl. Phys.*, vol. 113, p. 023711, 2013.

[82] T. Scheidt, E. G. Rohwer, P. Neethling, H. M. Von Bergmann, and H. Stafast, "Ionization and shielding of interface states in native p + -Si/ SiO 2 probed by electric field induced second harmonic generation," *J. Appl. Phys.*, vol. 104, no. 083712, 2008.

[83] T. Scheidt, E. G. Rohwer, H. M. von Bergmann, and H. Stafast, "Charge-carrier dynamics and trap generation in native Si/SiO2 interfaces probed by optical second-harmonic generation," *Phys. Rev. B*, vol. 69, no. 16, p. 165314, Apr. 2004.

[84] O. A. Aktsipetrov, A. A. Fedyanin, E. D. Mishina, A. N. Rubtsov, C. W. Van Hasselt, M. A. C. Devillers, and T. Rasing, "dc-electric-field-induced second-harmonic generation in Si(111)-SiO2-Cr metal-oxide-semiconductor structures," *Phys. Rev. B*, vol. 54, no. 3, pp. 1825–1832, 1996.

[85] E. Hecht, *Optics*, 4th ed. Addison-Wesley, 2002.

[86] D. J. Griffiths, *Introduction to Electrodynamics*. Pearson, 2013.

[87] J. D. Jackson, *Classical Electrodynamics*. John Wiley & Sons, 2007.

[88] N. Bloembergen and P. S. Pershan, "Light Waves at the Boundary of Nonlinear Media," *Phys. Rev.*, vol. 128, pp. 606–622, 1962.

[89] V. Mizrahi and J. E. Sipe, "Phenomenological treatment of surface second-harmonic generation," *J. Opt. Soc. Am. B*, vol. 5, no. 3, p. 660, 1988.

[90] O. S. Heavens, *Optical properties of thin solid films*. Courier Corporation, 1965.

[91] J. E. Sipe, "New Green-function formalism for surface optics," *J. Opt. Soc. Am. B*, vol. 4, no. 4, p. 481, 1987.

[92] M. A. Green, "Self-consistent optical parameters of intrinsic silicon at 300 K including temperature coefficients," *Sol. Energy Mater. Sol. Cells*, vol. 92, pp. 1305–1310, 2008.

[93] M. Falasconi, L. C. Andreani, A. M. Malvezzi, M. Patrini, V. Mulloni, and L. Pavesi, "Bulk and surface contributions to second-order susceptibility in crystalline and porous silicon by second-harmonic generation," *Surf. Sci.*, vol. 481, no. 1–3, pp. 105–112, Jun. 2001.

[94] L. V Rodríguez-de Marcos, J. I. Larruquert, J. A. Méndez, J. A. Aznárez, E. A. West, J. G. Porter, J. M. Davis, G. A. Gary, M. W. Noble, M. Lewis, R. J. Thomas, J. Kolbe, H. Kessler, T. Hofmann, F. Meyer, H. Schink, and D. Ristau, "Self-consistent optical constants of SiO2 and Ta2O5 films," *Opt. Mater. Express*, vol. 6, no. 11, pp. 3622–3637, 2016.

[95] "Femtometrix." www.femtometrix.com.

[96] S. Baldovino, S. Nokhrin, G. Scarel, M. Fanciulli, T. Graf, and M. S. Brandt, "Investigation of point defects at the high-k oxides/Si(100) interface by electrically detected magnetic resonance," *J. Non. Cryst. Solids*, vol. 322, pp. 168–173, 2003.

[97] A. Stesmans and V. V Afanas'ev, "Si dangling-bond-type defects at the interface of (100)Si with ultrathin layers of SiOx, Al2O3, and ZrO2," *Appl. Phys. Lett.*, vol. 80, no. 11, pp. 1957–1959, 2002.

[98] F. Grunthaner and P. Grunthaner, "Chemical and electronic structure of the SiO 2/Si interface," *Mater. Sci. reports*, vol. 1, no. 2, pp. 65–160, 1986.

[99] G. J. Gerardi, E. H. Poindexter, P. J. Caplan, and N. M. Johnson, "Interface traps and Pb centers in oxidized (100) silicon wafers," *Appl. Phys. Lett.*, vol. 49, pp. 348–350, 1986.

[100] N. M. Terlinden, *Second-harmonic generation spectroscopy for interface studies of dielectric thin films on silicon*. PhD thesis, 2012.

[101] R. Cabal, "Procédés innovants d'élaboration de cellules photovoltaïques silicium haut rendement adaptés aux substrats silicium minces," PhD thesis, 2010.

[102] G. Dingemans, R. Seguin, P. Engelhart, M. C. M. van den Sanden, and W. M. M. Kessels, "Silicon Surface Passivation by ultrathin Al2O3 films synthesized by thermal and plasma atomic layer deposition," *Phys.*

Status Solidi, vol. 1–2, no. 1, pp. 10–12, 2010.

[103] K. Matsunaga, T. Tanaka, T. Yamamoto, and Y. Ikuhara, "First-principles calculations of intrinsic defects in Al2O3," *Phys. Rev. B*, vol. 68, no. 8, p. 085110, 2003.

[104] J. R. Weber, A. Janotti, and C. G. Van De Walle, "Native defects in Al2O3 and their impact on III-V/Al2O3 metal-oxide-semiconductor-based devices," *J. Appl. Phys.*, vol. 109, p. 033715, 2011.

[105] J. Price, M. Lei, P. S. Lysaght, G. Bersuker, and M. C. Downer, "Charge trapping defects in Si/SiO2/Hf (1−x)SixO2 film stacks characterized by spectroscopic second-harmonic generation," *J. Vac. Sci. Technol. B Microelectron. Nanom. Struct.*, vol. 29, p. 04D101, 2011.

[106] J. J. H. Gielis, B. Hoex, M. C. M. Van De Sanden, and W. M. M. Kessels, "Negative charge and charging dynamics in Al2O3 films on Si characterized by second- harmonic generation," *J. Appl. Phys.*, vol. 104, p. 073701, 2008.

[107] N. M. Terlinden, G. Dingemans, M. C. M. Van De Sanden, and W. M. M. Kessels, "Role of field-effect on c-Si surface passivation by ultrathin (2-20 nm) atomic layer deposited Al2O3," *Appl. Phys. Lett.*, vol. 96, no. 11, pp. 2008–2011, 2010.

[108] G. Dingemans, N. M. Terlinden, D. Pierreux, H. B. Profijt, M. C. M. Van De Sanden, and W. M. M. Kessels, "Influence of the Oxidant on the Chemical and Field-Effect Passivation of Si by ALD Al2O3," *Electrochem. Solid-State Lett.*, vol. 14, no. 1, pp. H1–H4, 2011.

[109] B. Hoex, J. J. H. Gielis, M. C. M. Van De Sanden, and W. M. M. Kessels, "On the c-Si surface passivation mechanism by the negative-charge-dielectric Al2O3," *J. Appl. Phys.*, vol. 104, no. 11, 2008.

[110] G. Dingemans, N. M. Terlinden, M. a. Verheijen, M. C. M. Van De Sanden, and W. M. M. Kessels, "Controlling the fixed charge and passivation properties of Si(100)/Al2O3 interfaces using ultrathin SiO2 interlayers synthesized by atomic layer deposition," *J. Appl. Phys.*, vol. 110, no. 9, p. 093715, 2011.

[111] N. M. Terlinden, G. Dingemans, V. Vandalon, R. H. E. C. Bosch, and W. M. M. Kessels, "Influence of the SiO2 interlayer thickness on the density and polarity of charges in Si/SiO2/Al2O3 stacks as studied by optical second-harmonic generation," *J. Appl. Phys.*, vol. 115, no. 3, 2014.

[112] J. Benick, A. Richter, T.-T. A. Li, N. E. Grant, K. R. McIntosh, Y. Ren, K. J. Weber, M. Hermle, and S. W. Glunz, "Effect of a post-deposition anneal on Al2O3/Si interface properties," in *2010 35th IEEE Photovoltaic Specialists Conference*, 2010, pp. 000891–000896.

[113] D. K. Schroder, "Carrier lifetimes in silicon," *IEEE Trans. Electron Devices*, vol. 44, no. 1, pp. 160–170, 1997.

[114] K. B. Jinesh, J. L. Van Hemmen, M. C. M. Van De Sanden, F. Roozeboom, J. H. Klootwijk, W. F. A. Besling, and W. M. M. Kessels, "Dielectric Properties of Thermal and Plasma-Assisted Atomic Layer Deposited Al2O3 Thin Films," *J. Electrochem. Soc.*, vol. 158, no. 2, pp. G21–G26, 2011.

[115] G. Dingemans, F. Einsele, W. Beyer, M. C. M. Van de Sanden, and W. M. M. Kessels, "Influence of annealing and Al2O3 properties on the hydrogen-induced passivation of the Si/SiO2 interface," *J. Appl. Phys.*, vol. 111, no. 9, p. 93713, 2012.

[116] W. M. Werner, "The work function difference of the MOS-system with aluminium field plates and polycrystalline silicon field plates," *Solid. State. Electron.*, vol. 17, pp. 769–775, 1974.

[117] G. Dingemans, W. Beyer, M. C. M. van de Sanden, and W. M. M. Kessels, "Hydrogen induced passivation of Si interfaces by Al2O3 films and SiO2/Al2O3 stacks," *Appl. Phys. Lett.*, vol. 97, no. 15, p. 152106, 2010.

[118] O. A. Aktsipetrov, A. A. Fedyanin, V. N. Golovkina, and T. V. Murzina, "Optical second-harmonic generation induced by a dc electric field at the Si–SiO2 interface," *Opt. Lett.*, vol. 19, no. 18, p. 1450, Sep. 1994.

[119] S. Cristoloveanu, "Silicon films on sapphire," *Rep. Prog. Phys*, vol. 50, pp. 327–371, 1987.

[120] K. Izumi, M. Doken, and H. Ariyoshi, "C.M.O.S. devices fabricated on buried SiO2 layers formed by oxygen implantation into silicon," *Electron. Lett.*, vol. 14, no. 18, p. 593, 1978.

[121] K. Izumi, “Historical overview of SIMOX,” *Vacuum*, vol. 42, no. 5–6, pp. 333–340, 1991.

[122] K. Mitani and U. M. Gosele, “Wafer Bonding Technology for Silicon-on-Insulator Applications: A Review,” *J. Electron. Mater.*, vol. 21, no. 7, pp. 669–676, 1992.

[123] T. Yonehara, K. Sakaguchi, and N. Sato, “Epitaxial layer transfer by bond and etch back of porous Si,” *Appl. Phys. Lett.*, vol. 64, no. 16, pp. 2108–2222, 1994.

[124] M. Bruel, “Silicon on insulator material technology,” *Electron. Lett.*, vol. 31, no. 14, pp. 1201–1202, 1995.

[125] SOITEC, “SmartCut process.” https://www.soitec.com/en/products/smart-cut.

[126] L. Pirro, “Caractérisation et modélisation électrique de substrats SOI avancés,” PhD thesis, 2016.

[127] S. Cristoloveanu, D. Munteanu, and M. S. T. Liu, “A review of the pseudo-MOS transistor in SOI wafers: Operation, parameter extraction, and applications,” *IEEE Trans. Electron Devices*, vol. 47, no. 5, pp. 1018–1027, 2000.

[128] S. Cristoloveanu and S. S. Li, *Electrical Characterization of Silicon-on-Insulator Materials and Devices*. Boston: Kluwer Academic Publishers, 1995.

[129] D. C. Mayer, “Modes of Operation and Radiation Sensitivity of Ultrathin SOI Transistors,” *IEEE Trans. Electron Devices*, vol. 37, no. 5, pp. 1280–1288, 1990.

[130] D. K. Schroder, “Negative bias temperature instability: What do we understand?,” 2006.

[131] J.-Y. Cheng, C. W. Yeung, and C. Hu, “Extraction of Front and Buried Oxide Interface Trap Densities in Fully Depleted Silicon-On-Insulator Metal-Oxide-Semiconductor Field-Effect Transistor,” *ECS Solid State Lett.*, vol. 2, no. 5, pp. 32–34, 2013.

[132] L. Brunet, X. Garros, A. Bravaix, A. Subirats, F. Andrieu, O. Weber, P. Scheiblin, M. Rafik, E. Vincent, and G. Reimbold, “Impact of backside interface on hot carriers degradation of thin film FDSOI Nmosfets,” *IEEE Int. Reliab. Phys. Symp. Proc.*, no. 1, pp. 3–7, 2012.

[133] M. L. Alles, R. D. Schrimpf, D. M. Fleetwood, R. Pasternak, N. H. Tolk, and R. W. Standley, “Experimental Evaluation of Second Harmonic Generation for Non-Invasive Contamination Detection in SOI Wafers,” in *The 17th Annual SEMI/IEEE ASMC Conference*, pp. 1–6, 2006.

[134] M. C. Kryger, J. P. Changala, and M. L. Alles, “Non-Destructive Contamination Detection in Thick and Extremely-Thin SOI Wafers Using Optical Second Harmonic Generation,” in *International Symposium for Testing and Failure Analysis*, 2015.

[135] V. Koldyaev, M. C. Kryger, J. P. Changala, M. L. Alles, D. M. Fleetwood, R. D. Schrimpf, and N. Tolk, “Rapid Non-Destructive Detection Of Sub-Surface Cu in Silicon-On-Insulator Wafers by Optical Second Harmonic Generation Advanced Metrology, Defect Inspection and Reduction.” *The 26th Annual SEMI/IEEE ASMC Conference*, 2015.

[136] B. Jun, R. D. Schrimpf, D. M. Fleetwood, Y. V. White, R. Pasternak, S. N. Rashkeev, F. Brunier, N. Bresson, M. Fouillat, S. Cristoloveanu, and N. H. Tolk, “Charge trapping in irradiated SOI wafers measured by second harmonic generation,” *IEEE Trans. Nucl. Sci.*, vol. 51, no. 6, pp. 3231–3237, Dec. 2004.

[137] Z. Xu, X. F. Hu, D. Lim, J. G. Ekerdt, and M. C. Downer, “Second harmonic spectroscopy of Si(001) surfaces: Sensitivity to surface hydrogen and doping, and applications to kinetic measurements,” *J. Vac. Sci. Technol. B Microelectron. Nanom. Struct.*, vol. 15, no. 4, p. 1059, 1997.

[138] Filmetrics, “https://www.filmetrics.com/reflectance-calculator.” .

[139] N. Shamir, J. G. Mihaychuk, and H. M. van Driel, “Trapping and detrapping of electrons photoinjected from silicon to ultrathin SiO2 overlayers. I. In vacuum and in the presence of ambient oxygen,” *J. Appl. Phys.*, vol. 88, no. 2, p. 896, 2000.

[140] G. Hamaide, F. Allibert, F. Andrieu, K. Romanjek, and S. Cristoloveanu, “Mobility in ultrathin SOI MOSFET and pseudo-MOSFET: Impact of the potential at both interfaces,” *Solid State Electron.*, vol. 57, pp. 83–86, 2011.

[141] A. Toriumi, J. Koga, H. Satake, and A. Ohata, “Performance and reliability concerns of ultra-thin SOI and ultra-thin gate oxide MOSFETs,” in *Proceedings of International Electron Devices Meeting*, pp. 847–850.

[142] Y. Mori, “TXRF for semiconductor applications,” *Adv. X-ray Anal.*, vol. 45, pp. 523–532, 2002.

[143] J. I. Dadap, B. Doris, Q. Deng, M. C. Downer, J. K. Lowell, and A. C. Diebold, “Randomly oriented Angstrom-scale microroughness at the Si(100)/SiO2 interface probed by optical second harmonic generation,” *Appl. Phys. Lett.*, vol. 64, pp. 2139–2484, 1994.

[144] C. Chen, J. Lue, and C. Wu, “A study of surface and interlayer structures of epitaxially grown group-III nitride compound films on Si (111) substrates by second-harmonic generation,” *J. Phys. Condens. Matter*, vol. 15, pp. 6537–6548, 2003.

List of Publications

Journals

[1] D. Damianos, G. Vitrant, A. Kaminski, D. Blanc-Pelissier, G. Ghibaudo, M. Lei, J. Changala, A. Bouchard, X. Mescot, M. Gri, S. Cristoloveanu, I. Ionica, "Field-effect passivation of Si by ALD Al_2O_3: Second Harmonic Generation monitoring and simulation", *Journal of Applied Physics 124 (12), 125309 (2018)*

[2] D. Damianos, G. Vitrant, M. Lei, J. Changala, A. Kaminski-Cachopo, D. Blanc-Pelissier, S. Cristoloveanu, I. Ionica, "Second harmonic generation characterization of SOI wafers: Impact of layer thickness and interface electric field", *Solid State Electronics 143, pp. 90-96 (2017)*

[3] D. Damianos, L. Pirro, G. Soylu, I. Ionica, V. Nguyen, G. Vitrant, A. Kaminski-Cachopo, D. Blanc-Pelissier, L. Onestas, J. Changala, M. Kryger, S. Cristoloveanu, "Second harmonic generation for contactless non-destructive characterization of silicon on insulator wafers", *Solid State Electronics 115, pp. 237-243 (2016)*

International conferences with proceedings

[1] D. Damianos, I. Ionica, J. Changala, M. Lei, A. Kaminski-Cachopo, D. Blanc-Pelissier, S. Cristoloveanu, G. Vitrant, "Layer thickness impact on Second Harmonic Generation Characterization of SOI wafers", *IEEE, International EuroSOI – ULIS Conference Proceedings (2017)*, **Poster**

[2] I. Ionica (invited speaker), **D. Damianos**, A. Kaminski-Cachopo, G. Vitrant, D. Blanc-Pelissier J. Changala, M. Kryger, C. Barbos, S. Cristoloveanu, "Non-Destructive Characterization of Dielectric-Semiconductor Interfaces by Second Harmonic Generation", *ECS Transactions **72** (2), pp. 139-151 (2016)*, **Oral**

[3] D. Damianos, I. Ionica, A. Kaminski-Cachopo, G. Vitrant, S. Cristoloveanu, D. Blanc-Pelissier, M. Kryger, J. Changala, "Transient second harmonic generation and correlation with Ψ-MOSFET in SOI wafers", *IEEE, International EuroSOI – ULIS Conference Proceedings (2016)*, **Poster**

Participation in national workshops/meetings

[1] D. Damianos, I. Ionica, A. Kaminski-Cachopo, D. Blanc-Pelissier, J. Changala, M. Lei, S. Cristoloveanu, G. Vitrant, "Second Harmonic as a contactless probe of Al_2O_3 passivation quality", *PHOTOVOLTAÏQUE: couches minces et concepts avancés*, Grenoble (Mai 2017), **Poster**

[2] D. Damianos, I. Ionica, A. Kaminski-Cachopo, D. Blanc-Pelissier, S. Cristoloveanu, G. Vitrant, "Second Harmonic Generation for dielectric/semiconductor interface analysis", *ARC6 : Technologies de l'information et de la communication et usages informatiques innovants*, Lyon (Nov. 2016), **Poster**

[3] D. Damianos, I. Ionica, A. Kaminski-Cachopo, D. Blanc-Pelissier, S. Cristoloveanu, "Second Harmonic Generation for SOI interface/surface analysis", *ARC6 : Technologies de l'information et de la communication et usages informatiques innovants*, Grenoble (Nov. 2015), **Poster**

Génération de seconde harmonique (SHG) pour la caractérisation des interfaces entre diélectriques et semiconducteurs

(Résumé en français)

Chapitre 1: Introduction générale et contexte

Dans le monde d'aujourd'hui, la microélectronique et le photovoltaïque sont de plus en plus présents dans nos vies grâce à leur nombreuses applications (électronique grand publique, énergie, santé, environnement…). Ces applications sont basés sur des dispositifs élémentaires tels que les transistors MOSFET (Metal-Oxide-Semiconductor field effect transistors) ou les cellules solaires. Dans les deux cas, au niveau matériaux, nous trouvons des empilements diélectriques (SiO_2, high-k) sur silicium. Dans les transistors [1] ces diélectriques sont utilisés en tant qu'oxyde de grille, ou encore oxyde enterré dans les substrats SOI (Silicon-on-Insulator) [3], tandis que dans les cellules solaires [2] ils servent de couche de passivation.

Les hautes performances nécessaire pour les applications implique l'utilisation des matériaux et interfaces d'excellente qualité (structurale et électrique). Les propriétés électriques sont principalement reliées à la présence des défauts [4], tels que des contaminations à la surface et au volume de l'oxyde et du semi-conducteur, des liaisons pendantes à la surface du silicium, ainsi que des charges d'oxyde et des pièges à l'interface. Les principaux paramètres qui rendent compte de la qualité électrique d'une interface diélectrique – semiconducteur sont la densité de charges fixes dans l'oxyde (Q_{ox}) et la densité d'états interface (D_{it}). Des informations complémentaires peuvent être rajoutées par la durée de vie de porteurs minoritaires (τ_{eff})

Jusqu'à présent, la caractérisation de propriétés électriques des empilements de diélectrique sur Si était effectuée à l'aide de techniques telles que les mesures de capacité CV [5], de décroissance de photoconductivité µPCD [6] ou encore de charge Corona, COCOS [7].

Chacune de ces techniques présente certains avantages et inconvénients:

- La CV permet l'extraction de Q_{ox} et D_{it}, mais c'est une technique invasive, car un dépôt de métal est nécessaire.
- La µPCD est non invasive, mais il n'est pas possible d'extraire Q_{ox} et D_{it}; seule la durée de vie effective du porteur minoritaire τ_{eff} est obtenue.
- Le COCOS est également non invasif et l'extraction Q_{ox}/D_{it} est possible, mais il est difficile de déposer des charges uniformes dans de grandes zones afin de caractériser la totalité d'une plaque; de plus après chaque mesure il faut évacuer les charges déposées.

Dans cette thèse, nous utilisons la génération de seconde harmonique (SHG), comme technique de caractérisation complémentaire des autres techniques existantes. Pour la SHG, un laser de haute intensité est incident sur l'empilement diélectrique-semi-conducteur. Sous des conditions spécifiques, une lumière de seconde harmonique est générée à partir de l'échantillon et est ensuite détectée. Le SHG est une technique de caractérisation non invasive qui s'appuie sur un balayage rapide du laser sur la surface des plaques. La SHG est sensible aux champs électriques présents aux interfaces et le but de cette thèse est d'obtenir des informations sur Q_{ox} et D_{it} en exploitant le champ électrique E_{dc}, contenu dans le signal SHG.

Chapitre 2: Introduction à la SHG

Ce chapitre présente les bases théoriques de la génération de seconde harmonique (SHG) et donne quelques exemples de son utilisation pour la caractérisation des matériaux et des interfaces. L'élément clé est que pour des matériaux centrosymetrique (dans l'approximation dipolaire), l'intensité SHG provient principalement de l'interface et contient le champ électrique qui s'y trouve[8], [9]:

$$I_{2\omega}(t) = \left|\chi^{(2)} + \chi^{(3)}\left[E_{dc}(0) + E_{dc}(t)\right]\right|^2 I_{\omega}^2$$

$\chi^{(2)}$ et $\chi^{(3)}$sont les susceptibilités du 2ème et 3ème ordre respectivement. La contribution du champ électrique E_{dc} à l'SHG est appelée EFISH (Electric Field Induced Second Harmonic) [24]–[31]. Le terme constant de ce champ $E_{dc}(0)$ fournit des informations sur les charges fixes dans l'oxyde (Q_{ox}) et les défauts initialement chargés. Le terme $E_{dc}(t)$ dépendant du temps révèle les mécanismes de charge/piégeage à l'interface SiO_2/Si.

Notons également que la SHG est une technique optique et donc les intensités I_{ω} et $I_{2\omega}$ subissent des phénomènes de propagation optique dans les systèmes à couches minces. Afin d'extraire des informations sur E_{dc} uniquement (donc Q_{ox} et D_{it}), il est nécessaire d'anticiper l'impact de ces effets optiques (absorption, réflexions multiples interférences). Pour cela nous avons eu besoin de développer un simulateur, décrit dans le chapitre suivant.

Chapitre 3 : Modélisation optique de la SHG

Le calcul de l'intensité SHG en sortie d'un échantillon s'appuie sur deux éléments:

1. la propagation dans les couches: elle concerne à la fois le faisceau fondamental et la SHG. La seule différence entre les deux faisceaux est de faire les calculs avec les coefficients d'absorption adaptés à la longueur d'onde respective.

2. la transmission aux niveaux des interfaces. Le traitement du faisceau fondamental implique l'utilisation des équations de Maxwell sans termes sources et on évalue le champ électrique transmis d'une couche à l'autre. Pour la SHG générée justement au niveau des interfaces, les équations contiennent également des termes «source» faisant intervenir la polarisation des matériaux, comme réponse au champ électrique de l'excitation fondamentale. Notons qu'en présence d'un champ électrique «statique» E_{DC} au niveau de l'interface, la polarisation en sera modifiée.

Notre programme calcule les champs électriques à la fréquence fondamentale et à la fréquence double en tout point de la structure. L'intensité SHG sortante est évaluée en rajoutant des conditions limite «physiques» réelles du problème (pas de lumière ω et 2ω réfléchie du fond du substrat - absorbant semi-infini - et pas la lumière incidente 2ω (car elle est uniquement générée à l'intérieur de l'empilement).

Notre outil de simulation a été vérifié à l'aide de données expérimentales pour plusieurs configurations SiO_2/Si en faisant varier des paramètres tels que l'angle d'incidence, la polarisation en entrée, etc… La Figure 1 montre un exemple de SHG en fonction de la polarisation incidente provenant de Si recouvert de SiO_2 natif. Une bonne corrélation a été observée entre les expériences (Fig. 1a) et les simulations (Fig.1b). L'outil de simulation validé ici, est utilisé extensivement dans les chapitres suivants pour l'alumine et le SOI.

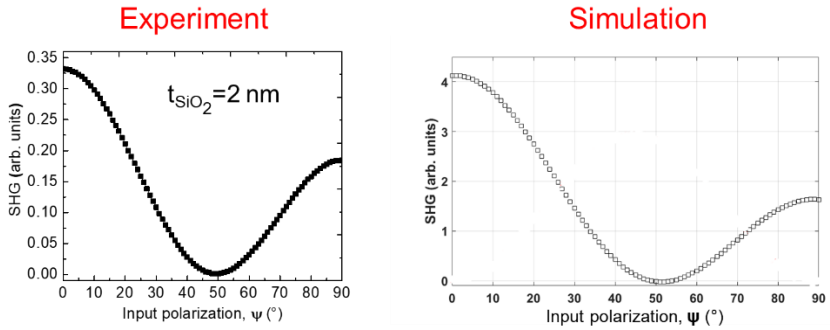

Figure 1: Intensité expérimentale et simulée du SHG en fonction de la polarisation d'entrée pour une lumière SH polarisée P pour Si recouvert d'oxyde natif de 2 nm.

Chapitre 4 : Caractérisation de couches Al_2O_3 sur Si par SHG

Al_2O_3 est connu pour fournir une excellente passivation de surface du silicium cristallin, ce qui est critique pour la performance de dispositifs tels que les photodétecteurs et les cellules solaires à haute efficacité [19]. Deux mécanismes de passivation sont combinés:

- passivation chimique attribuée à la diffusion de H présent dans Al_2O_3 vers l'interface avec le silicium [19].

- passivation par effet de champ par charges négatives [19], liées aux lacunes d'aluminium (V_{Al}) et aux oxygènes interstitiels (O_i) [20], [21].

Le défi de la caractérisation de la passivation par Al_2O_3 est de distinguer la passivation chimique de la passivation par effet de champ. C'est la raison pour laquelle les recherches des techniques de caractérisation restent un point critique. Dans ce chapitre, nous étudions la capacité de SHG à inspecter la passivation à effet de champ produite par une couche atomique déposée d'alumine sur Si.

Des échantillons avec différentes charges d'oxydes (Q_{ox}) et densités d'états d'interface (D_{it}) ont été fabriqués dans différentes conditions. Les mesures conventionnelles de µPCD et de CV ont donné accès respectivement à la durée de vie des porteurs minoritaires (τ_{eff}) et à la densité de piège d'interface (D_{it}) ainsi qu'à la densité de charge d'oxyde fixe (Q_{ox}). Le champ électrique statique (E_{dc}) à l'interface entre Si et Al_2O_3 a été estimé. Les mesures de SHG ont montré une corrélation entre les valeurs de SHG initiales et les paramètres obtenus à partir des techniques de caractérisation conventionnelles:

d) Le recuit des échantillons provoque une augmentation de la durée de vie et de l'intensité du SHG, en raison de l'augmentation de Q_{ox} (passivation à effet de champ) [22]–[25]. La même tendance est observée avec les valeurs de SHG initiales (Fig. 2a), ce qui corrobore la possibilité de sondage par SHG sans contact du champ électrique à l'interface entre Al_2O_3 et Si.

e) Nous avons montré que la racine carrée de l'intensité du SHG évolue linéairement avec la valeur du champ électrique (extraite des mesures de CV) comme prévu théoriquement: $\sqrt{I_{2\omega}} \propto \left|\chi^{(2)} + \chi^{(3)} E_{dc}\right| I_{\omega}$ (Fig. 2b). Cela implique que l'étalonnage devrait être possible.

f) Les variations des champs électriques à l'intérieur du Si sont utilisées dans les simulations SHG et permettent de reproduire les données expérimentales SHG en fonction de l'angle d'incidence (AOI) (Fig. 2c).

Ces résultats montrent la possibilité de calibrer la SHG en fonction de AOI pour mettre en place des analyses quantitatives des champs électriques et par conséquent des charges se trouvant à l'interface alumine/Si.

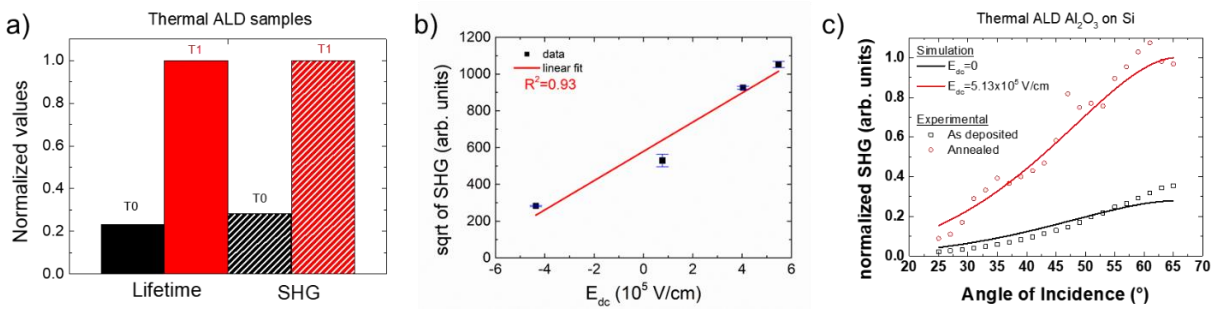

Figure 2: a) Durée de vie des porteurs normalisée, mesurée par µPCD et signaux SHG initiaux normalisés pour des échantillons après dépôt (T0) et après recuit (T1). La normalisation a été effectuée pour chaque ensemble avec le maximum respectif de chaque technique de mesure. b) Racine carrée de la valeur initiale du signal SHG en fonction du champ électrique statique calculée à partir de Q_{ox} extrait des mesures C-V. c) Intensité normalisée du SHG en fonction de l'angle d'incidence. Les symboles noir et rouge sont les données expérimentales pour les échantillons après dépôt et après recuit respectivement. Les lignes noires et rouges représentent les données

simulées d'une variation du champ électrique à l'interface, calculées à partir du décalage V_{FB} des courbes C-V. Une normalisation est effectuée en divisant chaque ensemble (expérimental et simulé) avec ses valeurs maximales correspondantes.

Chapitre 5: Caractérisation de substrats SOI par SHG

Le silicium-sur-isolant (SOI) est un excellent substrat pour des applications microélectroniques à faible consommation. Le SOI est constitué par une couche supérieure en silicium (film), séparée du substrat par une couche isolante (oxyde enterré ou buried oxide, BOX) qui permet un bon contrôle électrostatique sur le futur dispositif. Les trois interfaces («air»/film de Si, film de Si/BOX, BOX/substrat) présentent des champs électriques qui, suivant la géométrie du SOI, peuvent être couplés et qui auront un impact important sur le futur transistor. Leur caractérisation électrique est donc un enjeu d'autant plus important que pour les SOI ultra-minces actuels les techniques classiques sous pointes abiment le BOX rendant la caractérisation impossible. Dans ce chapitre, le SHG a été utilisé comme méthode non destructive pour évaluer la qualité des plaquettes SOI. De plus, la simulation a été utilisée afin de comprendre l'impact des différentes interfaces sur le signal SHG total.

Une première étude nous a permis d'identifier les paramètres expérimentaux conduisant à un fort signal SHG pour le SOI de 88nm épaisseur de film et 145 nm épaisseur de BOX: polarisation incidente P, polarisation SHG P, angle d'incidence de 45° et un angle de rotation (azimuthal) de l'échantillon de 0°.

Les interférences multiples dans les multicouches influence la réponse en SHG et compliquent la tâche d'accéder uniquement aux champs électriques. Nous avons mis en évidence l'effet des interférences en corrélant la SHG avec les épaisseurs du film et de la BOX. La Figure 3 montre les résultats expérimentaux qui sont alignés sur les courbes simulées tracées avec notre outil. Dans ces simulations, aucun champ E_{dc} n'a été utilisé; les variations sont uniquement dues aux phénomènes de propagation dans les multicouches.

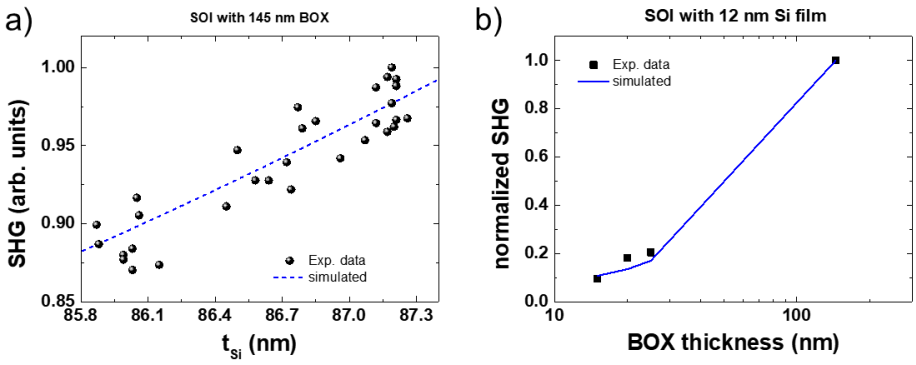

Figure 3: a) Comparaison entre modèle (ligne) et mesure du signal SHG par rapport à l'épaisseur du couche Si. Une normalisation a été effectuée en divisant chaque ensemble (expérimental et simulé) par la valeur maximale correspondante. Différents points ont été mesurés sur une plaque de SOI de 300mm de diamètre. L'épaisseur du film de Si a été mesurée au même temps sur les mêmes points par réflectométrie b) SHG en fonction de l'épaisseur de la BOX (données expérimentales et simulation pour lesquelles aucun E_{dc} n'a été pris en compte).

La profondeur de pénétration du rayonnement SH dans Si [13]) est de l'ordre de 70nm. Cela implique que pour des SOI ultra minces (avec films inférieurs à 70nm) toutes les interfaces contribuent au SHG. Dans ce cas, il faut identifier la contribution de chaque champ électrique au signal SHG total. Pour cette raison, nous avons étudié un SOI avec un film de Si très mince (12 nm), permettant aux interfaces enterrées de contribuer au SHG total. Dans l'outil de simulation nous avons modifié séparément le champ E_{dc} à chaque interface et observé l'effet sur les graphes SHG vs AOI (Fig. 4). La Figure 4 montre l'intensité SHG vs AOI lorsque:

a) on fait varier le champ E_1 (entre le film de Si et le SiO_2 supérieur –natif ou de passivation) tandis que les autres champs ont une valeur 0.

b) on fait varier le champ E_2 (film de Si/BOX) tandis que les autres champs ont une valeur 0.

c) on fait varier le champ E_3 (BOX/substrat) tandis que les autres champs ont une valeur 0.

La simulation montre que le champ électrique E_1 domine la réponse totale du SHG. Ceci a également été observé expérimentalement à partir d'échantillons passivés et non passivés, ayant intrinsèquement différents E_{dc} à l'interface entre SiO_2 supérieur et couche Si. L'interface à qualifier dans le SOI en vue des applications est notamment celle entre le film et le BOX, or sa contribution semble masquée par E_1. Nous avons montré par des simulations qu'il est possible d'envisager une méthode de calibration qui, à interface supérieure constante, donnerait accès au champ E_2 à l'interface entre le film et le BOX et conduirait à la caractérisation des états d'interface (D_{it}) et au contrôle de la qualité des plaquettes SOI.

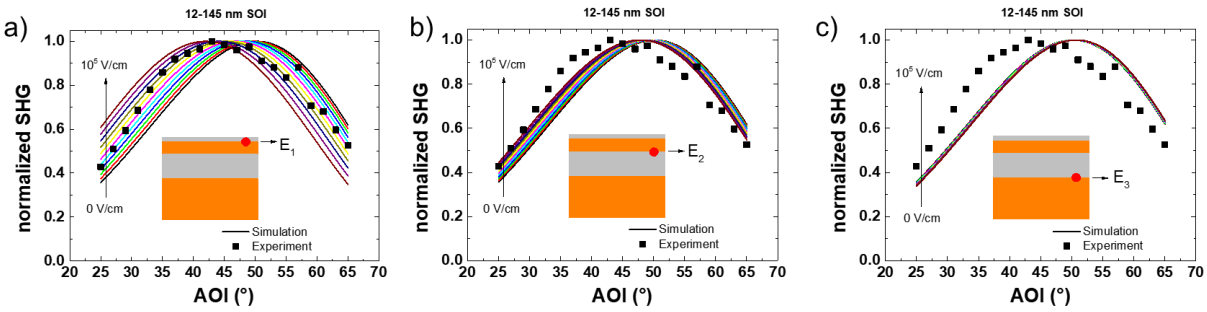

Figure 4: SHG simulé en fonction de l'angle d'incidence pour une structure SOI de 12 nm/145 nm. a) variable E_1, $E_2 = E_3 = 0$. b) variable E_2, $E_1 = E_3 = 0$. c) variable E_3, $E_1 = E_2 = 0$.

Conclusions & Perspectives

Le SHG est une méthode très intéressante et non invasive qui pourrait être intégrée dans les lignes de fabrication pour la surveillance en temps réel de paramètres électriques tels que les charges fixes dans les oxydes (Q_{ox}) et les pièges à interface (D_{it}). Le SHG étant une technique optique, les intensités optiques à la fréquence fondamentale et à la fréquence double sont impactées par des phénomènes de

propagation optique dans les systèmes à couches minces, tels que l'absorption et les réflexions multiples provoquant des interférences. Nous avons correctement rendu compte de ces effets optiques en développant un simulateur que nous avons validé en utilisant des données expérimentales de Si recouvertes de SiO_2 natif. Les mesures SHG couplées aux simulations ont été appliqué pour caractériser (1) la passivation par effet de champ obtenue par l'alumine sur Silicium, et (2) la qualité des interfaces des substrats SOI. Quelques perspectives de notre travail seraient:

- concernant la simulation, on pourrait prendre en compte des phénomènes supplémentaires qui sont présents en réalité dans les structures: a) la distribution du champ électrique dans la zone de charge d'espace du Si, b) les sources de rayonnement SH à partir de quelques nm (~ profondeur de fuite du SHG) à l'intérieur du Si volumique, c) les chargements/déchargements qui donne une dépendance temporelles au champ électrique à l'interface.
- la méthodologie développée pour l'alumine peut être étendue aux autres diélectriques high-k sur Si (HfO_2, SiN_x, etc.).
- pour le SOI, on pourrait faire des études en modifiant le champ à l'interface film BOX par une tension appliqué sur le bulk, comme dans un Ψ-MOSFET sans contact.

References

[1] E. R. Fossum, S. Mendis, and S. E. Kemeny, "ACTIVE PIXEL SENSOR WITH INTRA-PIXEL CHARGE TRANSFER," 5471515, 1995.

[2] A. G. Aberle, "Surface passivation of crystalline silicon solar cells: a review," *Prog. Photovoltaics Res. Appl.*, vol. 8, no. 5, pp. 473–487, 2000.

[3] O. Kononchuk and B.-Y. Nguyen, Eds., *Silicon-on-insulator (SOI) Technology: Manufacture and Applications*. Woodhead Publishing, 2014.

[4] C. R. Helms and E. H. Poindexter, "The silicon-silicon-dioxide system: its microstructure and imperfections," *Rep. Prog. Phys*, vol. 57, pp. 791–852, 1994.

[5] E. H. Nicollian and J. R. Brews, *MOS (Metal Oxide Semiconductor) Physics and Technology*. New York, USA: John Wiley & Sons, 1982.

[6] Dieter K Schroder, *Semiconductor Material and Device Characterization*, 3rd ed. Wiley & Sons, 2006.

[7] M. Wilson, J. Lagowski, L. Jastrzebski, A. Savtchouk, and V. Faifer, "COCOS (corona oxide characterization of semiconductor) non-contact metrology for gate dielectrics," *AIP Conf. Proc.*, vol. 550, p. 220, 2001.

[8] T. F. Heinz, "Second-Order Nonlinear Optical Effects at Surfaces and Interfaces," *Nonlinear Surface Electromagnetic Phenomena*. pp. 353–416, 1991.

[9] B. Jun, Y. V. White, R. D. Schrimpf, D. M. Fleetwood, F. Brunier, N. Bresson, S. Cristoloveanu, and N. H. Tolk, "Characterization of multiple Si/SiO 2 interfaces in silicon-on-insulator materials via second-harmonic generation," *Appl. Phys. Lett.*, vol. 85, no. 15, pp. 3095–3097, 2004.

[10] J. L. Alay and M. Hirose, "The valence band alignment at ultrathin SiO2/Si interfaces," *J. Appl. Phys.*, vol. 81, no. 3, pp. 1606–1608, 1997.

[11] S. M. Sze, *Physics of Semiconductor Devices Physics of Semiconductor Devices*, 3rd ed. Wiley & Sons, 2007.

[12] H. Park, J. Qi, Y. Xu, K. Varga, S. M. Weiss, B. R. Rogers, G. Lüpke, and N. Tolk, "Characterization of boron charge traps at the interface of Si/SiO2 using second harmonic generation," *Appl. Phys. Lett.*, vol. 95, 2009.

[13] Z. Marka, R. Pasternak, S. N. Rashkeev, Y. Jiang, S. T. Pantelides, N. H. Tolk, P. K. Roy, and J. Kozub, "Band offsets measured by internal photoemission-induced second-harmonic generation."

[14] J. G. Mihaychuk, J. Bloch, Y. Liu, and H. M. Van Driel, "Time-dependent second-harmonic generation from the Si – SiO2 interface induced by charge transfer," *Opt. Lett.*, vol. 20, no. 20, pp. 2063–2065, 1995.

[15] J. Bloch, J. Mihaychuk, and H. van Driel, "Electron Photoinjection from Silicon to Ultrathin SiO2 Films via Ambient Oxygen," *Phys. Rev. Lett.*, vol. 77, no. 5, pp. 920–923, 1996.

[16] J. L. Fiore, V. V Fomenko, D. Bodlaki, and E. Borguet, "Second harmonic generation probing of dopant type and density at the Si/SiO2 interface," *Appl. Phys. Lett*, vol. 98, p. 041905, 2011.

[17] C. Ohlhoff, G. Lü, C. Meyer, and H. Kurz, "Static and high-frequency electric fields in silicon MOS and MS structures probed by optical second-harmonic generation," *Phys. Rev. B*, vol. 55, no. 7, pp. 4596–4606, 1997.

[18] J. E. Sipe, D. J. Moss, and H. M. Van Driel, "Phenomenological theory of optical second-and third-harmonic generation from cubic centrosymmetric crystals," *Phys. Rev. B*, vol. 35, no. 3, pp. 15–1987.

[19] G. Dingemans and W. M. M. Kessels, "Status and prospects of Al2O3-based surface passivation schemes for silicon solar cells," *J. Vac. Sci. Technol. A*, vol. 30, p. 040802, 2012.

[20] K. Matsunaga, T. Tanaka, T. Yamamoto, and Y. Ikuhara, "First-principles calculations of intrinsic defects in Al2O3," *Phys. Rev. B*, vol. 68, no. 8, p. 085110, 2003.

[21] J. R. Weber, A. Janotti, and C. G. Van De Walle, "Native defects in Al2O3 and their impact on III-V/Al2O3 metal-oxide-semiconductor-based devices," *J. Appl. Phys.*, vol. 109, p. 033715, 2011.

[22] F. Kersten, A. Schmid, S. Bordihn, J. W. M??ller, and J. Heitmann, "Role of annealing conditions on surface passivation properties of ALD Al2O3 films," *Energy Procedia*, vol. 38, no. 3494, pp. 843–848, 2013.

[23] G. Dingemans, R. Seguin, P. Engelhart, M. C. M. van den Sanden, and W. M. M. Kessels, "Silicon Surface Passivation by ultrathin Al2O3 films synthesized by thermal and plasma atomic layer deposition," *Phys. Status Solidi*, vol. 1–2, no. 1, pp. 10–12, 2010.

[24] G. Dingemans, F. Einsele, W. Beyer, M. C. M. Van de Sanden, and W. M. M. Kessels, "Influence of annealing and Al2O3 properties on the hydrogen-induced passivation of the Si/SiO2 interface," *J. Appl. Phys.*, vol. 111, no. 9, p. 93713, 2012.

[25] C. Barbos, D. Blanc-Pelissier, A. Fave, E. Blanquet, A. Crisci, E. Fourmond, D. Albertini, A. Sabac, K. Ayadi, P. Girard, and M. Lemiti, "Characterization of Al2O3 thin films prepared by thermal ALD," *Energy Procedia*, vol. 77, pp. 558–564, 2015.